# Growth Laws in Morphoelasticity


Alexander Erlich
Christ Church College
University of Oxford

A thesis submitted for the degree of
*Doctor of Philosophy*
May 2017

# Abstract

Many living biological tissues are known to grow in response to their mechanical environment, such as changes in the surrounding pressure. This growth response can be seen, for instance, in the adaptation of heart chamber size and arterial wall thickness to changes in blood pressure. Moreover, many living elastic tissues actively maintain a preferred level of mechanical internal (residual) stress, called the mechanical homeostasis. The tissue-level feedback mechanism by which changes of the local mechanical stresses affect growth is called a growth law within the theory of morphoelasticity, a theory for understanding the coupling between mechanics and geometry in growing and evolving biological material. The goal of this thesis is to develop mathematical techniques to analyse growth laws that are biologically plausible, and to explore issues of heterogeneity and growth stability.

Firstly, we review attempts based on the Second Law of Thermodynamics (Coleman-Noll procedure) concluding that they cannot universally restrict the mathematical form of growth laws. In light of these results we focus on the phenomenological concept of homeostasis. We hypothesize that growth laws are functions of homeostatic stress (homeostasis-driven growth).

Secondly, we demonstrate that for a static residually stressed network made of elastic bars connected in series and parallel, the network response has the same functional form as the response of individual bars (similarly to electrical circuits). For a dynamically evolving network, on the other hand, the macroscopic network response is a nonlinear function of microscopic homeostasis-driven growth laws with no electrical counterpart. We characterise the macroscopic growth dynamics as non-monotonic and non-oscillatory.

Thirdly, we discuss the growth dynamics of tubular structures, which are very common in biology (e.g. arteries, plant stems, airways). We model the homeostasis-driven growth dynamics of tubes which produces spatially inhomogeneous residual stress. We show that the stability of the homeostatic state nontrivially depends on the anisotropy of the growth response. The key role of anisotropy may provide a foundation for experimental testing of homeostasis-driven growth laws.

Fourthly, we apply our theoretical framework to the growth of Ammonites' seashells. We demonstrate how homeostasis-driven growth produces seashell morphology that is consistent with observation and that cannot readily be captured with previous models.

# Acknowledgements

First of all I would like to thank my supervisors, Alain Goriely and Derek Moulton. Working with these masters has been a formative experience and I can only hope to have assimilated some of their brilliance by—if nothing else—osmosis. I have developed a deep admiration for Alain and Derek. Everyone who knows Alain has experienced his sharp wit and often incisive criticism, which cuts through formalism directly to the heart of a problem. The single most important thing I hope to have learned from Alain is to focus on the single most important thing and fade out everything else. Derek's advice and guidance during my time at Oxford were invaluable, and his high benchmark for academic writing helped me greatly with my thesis. The single most important thing I hope to have learned from Derek is to explain my mathematics amply and clearly with not only equations but words and pictures—something that does not always come easy to me. I highly appreciate this brilliant duo of advisors. Thank you A&D.

I would like to thank my grandparents for their kindness and mental support, and the sense of prioritising education which they have instilled in me from an early age. Also, I would like to thank my mother and my little sister. In her childish way of rebelling against my futile attempts to work while at home in Germany my little sister always kept reminding me of how valuable family time is.

Nobody has experienced my thesis tantrums quite like my significant other. Thank you, Dao, for not collecting a penny from me every time you heard the phrase "I really have to finish writing this today!". I thank you for all your support and patience and for nodding along to my stories about radial and hoop stress.

Thank you Siddharth for being a great friend and mentor, and for making my time at Oxford so much more funny and crazy through your personality and your circle of friends which reflects your personality. It would take until 3017 to tell even half the funny stories that happened when you, myself, Thanasis, Felix, Fahd et al. were in the same room. I won't even get started. Suffice it to say that Siddharth is a creature to be trusted! It has been an honour being your apprentice.

I would like to thank many post-docs and research fellows for great conversations about maths, academia and life, many of which happened in the late hours of the day, in which the Mathematical Institute becomes a productive and serenely peaceful place. First of all Thomas Lessinnes, for taking the time to regularly discuss my research questions with me in an early stage of the project and for helping me grasp concepts of growth dynamics. I thank Cameron Hall for many discussions throughout my D.Phil., in particular

microscale models of morphoelasticity and multiple scales analysis. I thank Fabian, Matteo, Pierre, Julian and Jeevan for the many warm and open discussions about research, academia and career paths in our field.
A few words of appreciation for my friends and fellow D.Phil. students. Thank you Felix for many insightful discussions over dinner at Christ Church, and for some healthy competition with virtual machine guns at the Graduate Common Room afterwards. Thank you Andrey for the many challenging discussions about our related D.Phil. research topics on the whiteboard, and for many uniquely funny moments at the Mathematical Institute—you are a legend. Thank you Nick for many unforgettable laughs, like our semi-serious attempt at breaking down the plot of Inception. Thank you Ben for introducing me to TRON and for sharing your passion about your greatest heroes of mathematics. Thank you Ousmane for our shared appreciation of the old fashioned things, like great books about physics and physicists. Thank you Lukas sharing a desire to merge art and science, and for our ongoing discussions. Thank you Georgina and Stephen for guiding me through some of the hoops of being a D.Phil. student. Many others are on my mind, you know who you are—I am grateful for having crossed paths with many great people.

I thank the Doctoral Training Centre for providing an interesting overview over biology in the first year of my D.Phil., and for putting me into a room with interesting characters from all disciplines, many of whom I have become good friends with. I thank Christ Church for financial support when I most needed it, which was towards the end of my D.Phil. I also thank the EPSRC and OCCAM for their generous support. Most of all, I thank my family for saving me when my patchwork of funding grew thin.

# Contents

# Chapter 1

# Introduction

In 1926, the zoologist John S. Haldane began his essay "On being the right size" [37] with the sharp statement:

> "The most obvious differences between different animals are differences of size, but for some reason the zoologists have paid singularly little attention to them."

In his playful language, he goes on to discuss how physics imposes constraints on the proportion of animals, humans, and their organs. The relationship between mechanics and biology was perhaps most deeply researched and most clearly articulated by D'Arcy Thompson, who wrote in the Introduction to his epic and inspiring 1917 monograph On Growth And Form [71]

> "If we tried building ships, palaces or temples of enormous size, yards, beams and bolts would cease to hold together; nor can Nature grow a tree nor construct an animal beyond a certain size, while retaining the proportions and employing the materials which suffice in the case of a smaller structure."

The point these authors in the pre-genetics era are making is that living organisms are constrained in their size and proportions (among other aspects) by their mechanical environment. In the hundred years after Thompson's 1917 publication, geneticists have uncovered many of the biomechanical pathways involved in growth and size regulation [13], modern microscopy techniques have allowed insights in the elastic nature of the cytoskeleton of the cell and even the elastic properties of its constituents (microtubuli and

actin filaments), and tissue level experimentation has allowed detailed understanding of the large-scale response of some living tissues and provided a variety of constitutive laws. But attempts to bridge these gaps from the biochemical up to the tissue level still leave basic questions unanswered, such as how mechanics is involved in regulating growth, and how cells integrate the information of their mechanical environment to decide when it is time to stop growing and "being the right size".

To put these ambitious but perhaps abstract questions into a more modern and practical setting, we consider two examples from the study of properties of bones: astronauts, after return from space flights, have a lower bone density [28]. On a related note, X-ray analysis of the humerus bone in tennis players reveal increased bone density in the playing arm [70]. Similarly to bone, soft living tissues are documented to respond to changes in the mechanical environment by localised growth. There are countless documented examples, many of which are spectacular or anecdotal, or of practical everyday relevance. Wound closure is a response to a change of tension in skin tissue caused by injury [8]. More extremely, in some animals severed limbs regrow [48]. In response to high blood pressure, human cardiac tissue thickens the walls to withstand the increased pressure [25]. And, as hinted in Thompson's quote, trees grow more stubby in windy areas [15].

Our aim in this thesis is to develop a mathematical framework to describe the growth evolution over time of a soft elastic material as a response to its internal and external mechanical environment. One of the difficulties is that soft tissues often exhibit surprising responses to mechanical stimuli. This is in part due to the non-linear constitutive response of soft material to large geometric deformations, and in part due to the availability of pre-existing mechanical stresses in the tissue known as residual stress. The latter is discussed in more detail in Section 1.1.

Another challenge is to understand how living tissues respond dynamically to mechanical changes in their environment, such as changes in loading conditions (which may be as simple as switching off gravity, as in the case of the astronaut example described above). Growth dynamics is discussed in Section 1.2.

Experimental data on the temporal evolution of living tissue (including residual stress distributions) is extremely sparse. The thermodynamic openness of living tissue to exchange of energy with their environment (e.g. nutrients in the extracellular

fluid) makes fundamental physical treatments of growth dynamics challenging, limiting the insights such approaches allow into the inner workings of growth-mechanical interactions (see Section 1.6 for a detailed discussion of a thermodynamical approach). Another difficulty is the integration of micromechanical analysis with tissue level modeling. Mircomechanical analysis is the attempt to build models based on microscopic properties, such as the elastic properties of microtubuli and actin filaments of the cell cytoskeleton (estimated in [29]). However, such models are difficult to integrate to the tissue level via homogenisation techniques [10], in part due to the lack of lattice periodicity and crystal symmetry in biological tissue. Such a description of elastomers, however, does not do justice to modern microscopic cell models and macroscopic growth evolution laws, which are reviewed in Section 1.5.4.

Phenomenological models are of great help within the context of these difficulties to obtain a fundamental description of growth-mechanical interaction. The most common of such phenomenological approaches to modelling the growth and evolution of soft tissues is to assume that tissues have a preferred mechanical state (called homeostasis) which is regulated through growth and remodeling during regular physiological conditions. The concept of homeostasis is further explained in Section 1.2, formally introduced in Section 1.5.5, and homeostasis type models are reviewed in Section 1.5.4.

## 1.1 Residual stress in living systems

A key aspect that plays an important role in many living tissues is residual stress. This is an internal stress that remains when all external loads of an originally unloaded configuration are removed. Tissues actively build these internal stresses both during morphogenesis (when they rapidly change shape and add mass) and in the mature physiological state (when mass and volume changes serve the purpose of maintenance and are comparatively small). It arises in biological tissues as material is added or lost in a non-uniform manner, forcing neighboring tissue to incorporate the newly added material through elastic deformation. Geometrically, this concept is known as incompatibility and is discussed in Section 1.5.1 in a more formal setting.

The mechanism behind the creation of residual stresses in biological tissue is known as differential growth, in which the living tissue adds mass and volume heterogeneously,

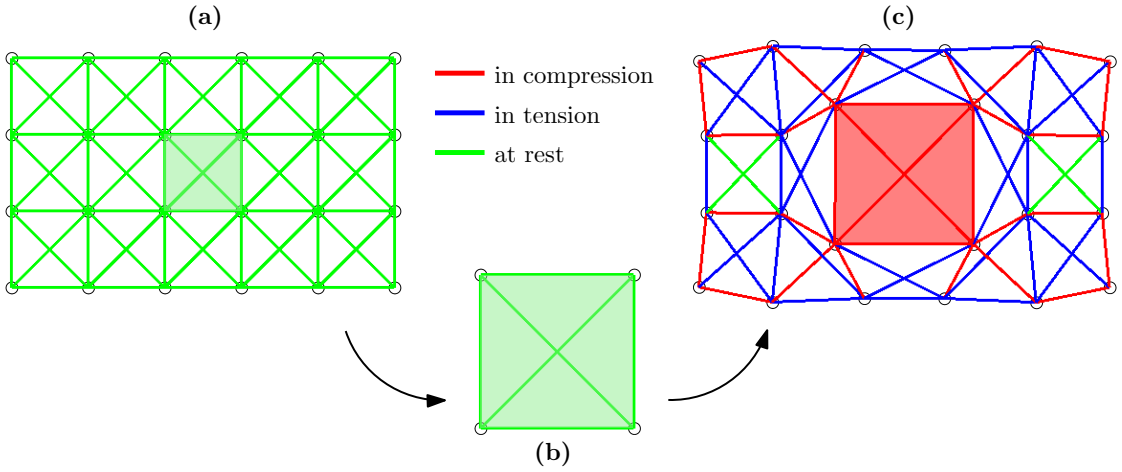


Figure 1.1: Illustrative schematic of residual stress forming through differential growth. A 2D lattice of linear Hookean springs is attached to equal mass points (circles), with no forces applied at the domain boundary. In the unstressed reference configuration (a), the system is force-free (green) and all springs have the same length as their rest length. In (b), the rest lengths of the highlighted cell are grown by a factor of 2, but the rest of the lattice is left unchanged. This local change (emulating differential growth) propagates through the whole system, introducing stress on the whole domain. In the stressed configuration (c), the red springs are in compression (as is the grown cell), the blue springs in tension. The tissue is now residually stressed.

which leads to mechanical stresses globally. A basic illustrative[1] schematic of this idea is presented in Figure 1.1, showing how local growth in two selected regions causes the formation of stresses in a piece of model tissue.

A classic example is the residual stress in arteries, which has been theoretically and experimentally described by Fung and others [23, 72]. The observation is that arteries, when radially cut, open up due to compressive stress built in the hoop (circumferential) direction. The opening angle can be used to quantify residual stress [23]. Experiments also suggest that arteries are residually stressed in the axial direction [31]. In a series of seminal studies, Fung and co-workers demonstrated residual stress in other physiological systems such as the heart [61], veins [75], and the trachea [41]. Other investigators identified residual stress in physiological tissues and organs such as the oesophagus

[1]Note that Figure 1.1 serves as a visual schematic of residual stress, but all modeling in this thesis is done with continuum models, not lattice models. This is because the research question is focused on characterising macroscopic growth response laws rather than characterising microstructure. Ultimately, forming a connection between micromechamical models and macroscopic descriptions such as growth laws is essential for a theory of mechanics and growth. This is usually mathematically very challenging. Microscopic lattice models are typically not straightforward to homogenise to continuum mechanical theories, and are often highly dependent on elementary cell geometry [10]. Reviews of agent-based soft-tissue models, including lattice based models, can be found in [46, 30].

[33], the aorta [5], the brain [9], bones [76], and the developing embryo [6]. It was also found in pathological tissue such as solid tumors [4]. This list of examples of residual stress in physiological tissue is not exhaustive, and the plant kingdom also offers a rich pool of examples of residually stressed systems, of which the review of Taber [67] (physiological tissue) and the book by Goriely [30] (physiological and plant tissue) offer comprehensive descriptions.

## 1.2 Stress as a regulatory feedback mechanism for growth

Differential growth produces residual stress. But of equal important is that stress can serve as a regulatory mechanism for growth. This idea of mechanical stresses locally informing differential growth, and differential growth in turn producing residual stress and changing the mechanical environment, is an informal description of the main problem studied in this thesis, which we will formally introduce via mathematical growth laws in Section 1.5.4 below. Experimental evidence of such mutual interactions between growth and mechanics can be found at many length scales. At the cellular level, it has been shown that axons can be grown by applying tension [43]. Another example is the stress developed by fibroblast cells on a silicone substrate, as demonstrated by Harris and co-workers: initially, the cultured cell does not deform the soft substrate, but after a while the substrate wrinkles, suggesting that the grown fibroblast has developed tension through growth [42].

The mechanism of mechanical feedback and growth has proven difficult to break down to universally applicable rules. As we will discuss in more detail in Section 1.6, thermodynamical attempts to derive clear rules for mechanical feedback mechanisms have been rather unsuccessful. We will focus on a helpful phenomenological principle called homeostasis [14]. This principle states that organisms have the ability to self-regulate some of their properties to adapt the conditions for its optimal function in a physiological state, such as the ability of mammals to maintain a constant body temperature. An example of homeostasis is the maintenance of constant internal temperature of mammals. In some biological cases, homeostatically regulated systems appear to adjust to the host animal (baboon livers transplanted into humans grow to the size of

human livers, and the inverse holds for transplantation into smaller animals [74]); in other cases, regulation appears to occur independently of the host (salamander limbs transplanted into smaller or larger salamanders grow to the normal size of the donor animal, [74]). The mechanism by which the proportions of the host organism inform the size of homeostatically regulated subsystems is unknown, and lies very much at the heart of the question of growth and size raised by Haldane and Thompson in the introductory quotes.

In the context of mechanics, homeostasis can be understood as a living tissue's ability to grow and remodel to accommodate a preferred (homeostatic) stress, i.e. to reshape itself to reduce the difference between its actual stress and the a priori known or genetically encoded homeostatic stress. At homeostasis, the preferred mechanical environment within a tissue or an organ is present so that the tissue can function at its optimal level. Growth evolves to keep the difference between the actual and homeostatic stress field as small as possible, so that growth reaches an equilibrium state and the tissue reaches its final observed size and morphology once the homeostatic stress is fully accommodated.

Examples of mechanobiological homeostasis are arteries and their regulation of wall thickness in response to pressure changes (Thomas' Law), bones and their trabecular remodeling in response to loading (Wolff's Law), and the heart and its ability to regulate wall thickness and chamber size in response to volume and pressure overload (Wood's Law). These historic observations ('Laws'), as well as modern insights, are discussed in [30, 67].

## 1.3 Accretive growth of seashells

In the previous examples, elastic tissues undergo bulk deformations. A different type of growth, in which mechanical feedback can play an equally important part, is accretive growth [24, 65]. Among other processes, it underlies the formation of hard surfaces, such as seashells, horns and teeth. A particularly iconic example of accretive growth is the seashell. The growth of the hard mineralised shells of gastropod mollusks is the result of a repeated secretion process of material via a soft elastic organ called the mantle. The secreted material subsequently calcifies in the shape of the mantle. The form

and pigmentation patterning of seashells have been studied from many perspectives, such as descriptive kinematics for shell geometry [63, 53], reaction-diffusion models for pigmentation patterning [22, 34] and mechanics [38, 39]. In seashells, mechanical interactions underlie a secondary structure called 'ornamentation' on a primary coiled structure such as a logarithmic spiral. The two basic mechanical ornamentation types are commarginal and antimarginal ornamentation (see Section 4.1.3).

Ammonites are an extinct group of cephalopods with a nearly perfect logarithmic spiral as their primary structure, and with secondary commarginal ornamentation with a very good ribbing regularity. To uncover the mechanism behind the emergence of commarginal ornamentation of Ammonite shells, Moulton and co-workers [57] developed a model based on physical interactions underlying mollusc shell secretion, building on the stress regulating idea of [38]. A limitation of this model was that the growth process was modulated within a fixed circular geometry of the growing shell edge. In [21], we extended this model in multiple ways, including the situation of elliptical geometry, and interpreted the effects of shell expansion (i.e. properties of observed logarithmic spirals on Ammonites) and cross section curvature (i.e. circular vs. ellipse shaped) in the context of evolutionary developmental biology. This work serves as a foundation for the investigation of growth-mechanical feedback which we present in Chapter 4. Our results show that mechanical feedback has a noticeable effect on the commarginal ribbing pattern in Ammonites which cannot readily be captured with previous models. In the presence of mechanical feedback, the juvenile stages of Ammonite morphogenesis are more ribbed then the adult stages, which is consistent with observation.

## 1.4 The time scales of elasticity, growth and homeostasis

In this work, our focus is the characterisation of long-term behaviour of growth dynamics, neglecting the relatively slow inertial and viscous effects. This approach is common for the study of biological materials and is justified when observing the time scales of elastodynamics (inertial effects) vs. growth dynamics (growth-mechanical feedback). Elastodynamic effects, which are typically characterised by the velocity of wave propagation, have a timescale that is very short when compared to growth. To illustrate

this point, let us assume that most tissues and organs have a typical lengthscale of $\chi = 10\text{cm}$ and typical wave propagation velocities $c$ in the order 10-100m/s. With these assumptions, the time scale $\tau = \chi/c$ of elasto-dynamics will range between $10^{-2}$s and $10^{-3}$s. While there is great variety in the elastic properties of biological tissue, this range can serve as a starting point for comparison with the timescale of growth. The latter varies from minutes (doubling time of *Escherichia coli*) to years (slow growing tumours), and is therefore typically several orders of magnitude larger than the timescale of elasto-dynamics (see [30] for a detailed discussion of time scales of growth compared to various elastic time scales). Upon neglecting inertial effects, growth dynamics can be considered as a series of elastic equilibrium states. This quasistatic simplification is formalised in [32] and will form the foundation for our growth dynamical approach in Chapters 2–4. Note also the excellent paper by Vandiver [73] and Chapter 14.6 of Goriely's book [30] for detailed analysis of growth-dynamical systems.

It is also worth noting that homeostatic stresses may evolve on a much slower time scale than growth. In fact, the homeostatic stress may in general be an inadmissible quantity, that is it may not satisfy the boundary conditions of the mechanical problem (the term stress in 'homeostatic stress' may be considered somewhat misleading). Homeostatic stress should be thought of as a preferred mechanical state of the system, genetically prescribed or otherwise informed (e.g. through chemical fields). During the growth process, we assume that homeostatic stress may be spatially varying but is temporally constant field.

To summarise, the timescales are related to each other as follows:

$$\underbrace{\text{elasticity (milliseconds)}}_{\text{very short: quasi-static}} \ll \boxed{\underbrace{\text{growth (days to years)}}_{\text{focus of this study}}} \ll \underbrace{\text{homeostasis (years)}}_{\text{very long: parameter variation}} \tag{1.1}$$

Within the community of morphoelasticity and related biomechanical growth theories ([67, 46, 30, 1]), the study of growth in biology is typically subdivided into growth (mass change), remodeling (property change), and morphogenesis (shape change). In the context of the community of morphoelasticity and related biomechanics, bone is the preferred context of remodelling. In bones, trabeculae re-orientate, changing the internal bone structure without much affecting mass. Our work offers no detailed analysis of remodeling (we refer to classical work by [16]) but focuses on morphogenesis

and growth. We refer to morphogenesis as significant change in shape and mass over an individual's lifetime (ontogenetic development process). Finally, we refer to growth as a moderate change in mass in order to sustain a physiological state of adult tissue. This work proposes models for the study of growth (Chapters 2 and 3) and morphogenesis (Chapter 4). As we will demonstrate, homeostasis is a powerful concept that can play a vital role in growth (Chapters 2, 3) and morphogenesis (Chapter 4).

## 1.5 Morphoelasticity and volumetric growth

To model the growth response to mechanical stimuli at the tissue level, and to incorporate concepts like homeostasis into the modelling, the framework of continuum mechanics is essential [36, 27]. Furthermore, to incorporate the nonlinear response of biological material to mechanical loading, nonlinear elasticity is essential [59, 45]. To incorporate the effects of growth and the associated local changes in volume and mass of tissues and to differentiate their influence on the observed morphology from purely elastic deformations, extra care must be taken. In their seminal paper, Rodriguez et al. [64] proposed a multiplicative decomposition of the deformation gradient into contributions for growth and elasticity.

Their work was based on similar ideas from plasticity: The Kröner-Lee decomposition ([47, 50]) splits the deformation gradient into an elastic and a plastic part. In this chapter, we formally introduce the theory of morphoelasticity, which is an evolution of Rodriguez' deformation gradient decomposition. This introduction, much like a text on traditional nonlinear solid mechanics, will include a part on kinematics (geometric deformation, i.e. the study of strains, see Section 1.5.1), balance laws (balance of forces and other physical quantities, see Section 1.5.2) and constitutive relationships (which relate strains to stresses, see Section 1.5.3).

A challenging aspect of morphoelasticity is that (as opposed to traditional nonlinear solid mechanics) morphoelastic systems can be open to fluxes of mass, energy, momentum and entropy. These quantities must be accounted for carefully. This will be the subject of Section 1.5.2. It will result in a continuum formulation of the second law of thermodynamics known as the Clausius-Duhem inequality. This formalism will be picked up in Section 1.6 where we will derive a statement about growth laws based

on this inequality.

### 1.5.1 Kinematics

In traditional continuum mechanics, it is common to consider the body in two different configurations, the *initial reference configuration* and the *current configuration*. The initial reference configuration describes the body in its initial state at $t = 0$ (i.e. before deformation) and it is required to be *stress-free*. The current configuration describes the deformed body at time $t$. Mathematically, they are subsets of Euclidean space, denoted $\mathcal{B}_0 \subset \mathbb{E}^3$ and $\mathcal{B}_t \subset \mathbb{E}^3$, respectively. Material points in $\mathcal{B}_0$ are described by the the vector $\mathbf{X}$ which are mapped to $\mathbf{x}$ in $\mathcal{B}_t$. This deformation map is is

$$\boldsymbol{\varphi} : \ \mathcal{B}_0 \to \mathcal{B}_t \qquad \mathbf{X} \mapsto \mathbf{x} = \boldsymbol{\varphi}(\mathbf{X}, t) \tag{1.2}$$

for which we assume the inverse $\boldsymbol{\varphi}^{-1}$ to exist. Strain, the geometric deformation of a body $\mathcal{B}_t$ with respect to its reference state in $\mathcal{B}_0$, is quantified through the deformation gradient $\mathbf{F}$. The latter is defined as the gradient of the deformation map with respect to initial reference coordinates

$$\mathbf{F}(\mathbf{X}, t) = \nabla_{\mathbf{X}} \boldsymbol{\varphi}(\mathbf{X}, t) = \frac{\partial \mathbf{x}}{\partial \mathbf{X}}(\mathbf{X}, t) \tag{1.3}$$

As mentioned in the introduction, in morphoelasticity we decompose the deformation gradient $\mathbf{F}$ into a tensor field $\mathbf{G}$ and an elastic deformation gradient $\mathbf{A}$:

$$\mathbf{F}(\mathbf{X}, t) = \mathbf{A}\mathbf{G} \tag{1.4}$$

This requires the introduction of the virtual reference configuration $\mathcal{B}_r$, which is said to be incompatible, which means that a body cannot be put into a one-to-one correspondence with points in a region in Euclidean space, i.e. the body has holes and overlaps see Figure 1.2).

We define the determinants of the tensor fields $\mathbf{F}$, $\mathbf{A}$ and $\mathbf{G}$ as $J := \det \mathbf{F}$, $J_A := \det \mathbf{A}$ and $J_G := \det \mathbf{G}$ and of course we have $J = J_A J_G$. If the deformation is incompressible (i.e. locally volume preserving), $J_A = 1$.

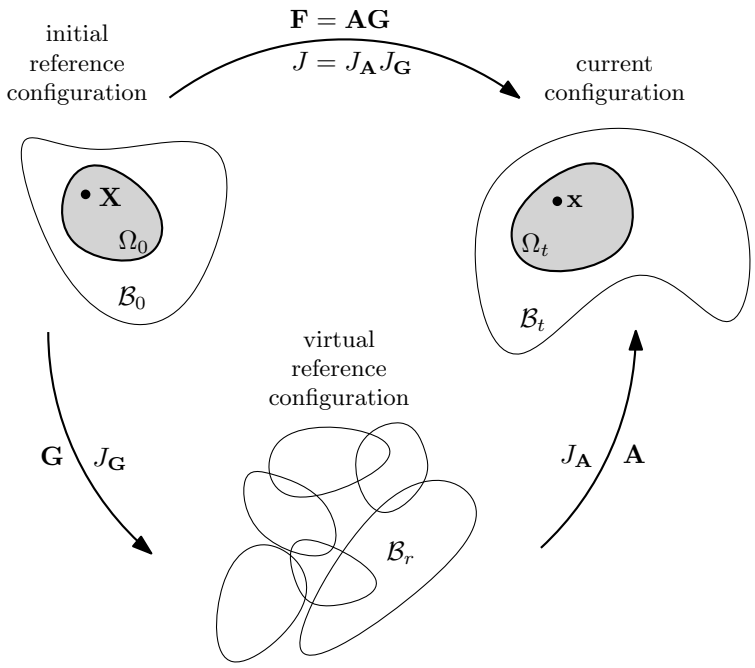


Figure 1.2: Deformation gradient decomposition. The fact that the virtual reference configuration $\mathcal{B}_r$ does not fit into Euclidean space is highlighted.

Formally[2], $\mathbf{G}$ maps vectors from $\mathcal{B}_0$ to $\mathcal{B}_r$ and $\mathbf{A}$ maps from $\mathcal{B}_r$ to $\mathcal{B}_t$ and their composition $\mathbf{F} = \mathbf{AG}$ maps vectors from $\mathcal{B}_0$ to $\mathcal{B}_t$. On a physical level, the decomposition can be interpreted as follows. Growth (geometrically speaking) is a map from a stress-free configuration $\mathcal{B}_0$ to another stress-free configuration $\mathcal{B}_r$, but the latter will in general not fit into Euclidean space as the grown material will overlap or (if locally $\det \mathbf{G} < 1$, i.e. resorption) have holes. That is, $\mathbf{G}$ can break the continuity of the tissue. The purpose of the elastic deformation is to restore continuity of the tissue, filling the holes at the expense of introducing tensile stress, and moving apart the overlapping regions at the expense of introducing compressive stress. For this reason, the current configuration $\mathcal{B}_t$ is no longer stress free, even when it is unloaded. Stress that remains even in the absence of loads is called residual stress.

The configuration $\mathcal{B}_r$ is not physically realised in a growing biological tissue, and for this reason we refer to it as the virtual reference configuration. Because of overlaps of tissue, a bijective deformation map of the kind (1.2) cannot be defined between $\mathcal{B}_0$ and $\mathcal{B}_r$ (i.e. it is impossible to keep track of material points if $\mathcal{B}_r$ is Euclidean) and $\mathbf{G}$ cannot be defined as a gradient of a deformation map in the fashion of (1.3)—things are somewhat different if $\mathcal{B}_r$ is assumed non-Euclidean, see footnote 2 for literature on

[2]A more detailed differential geometric treatment of traditional continuum mechanics can be found in [51]. Growth theories are presented in a differential geometric framework in [77] and [30].

differential geometric growth theories.

### 1.5.2 Balance laws

In this section we state the balance laws for mass, linear momentum, angular momentum, energy and the entropy imbalance. The energy balance and the entropy imbalance are continuum formulations of the first and second law of thermodynamics, which will lead to the Clausius-Duhem formulation of the second law. This section should not only serve as a thorough study of morphoelasticity and the openness (with respect to mass, momentum, energy and entropy flow) of the systems it is intended for, but will also pave the way for Section 1.6 of the present work. In this chapter, we will use the framework of rational thermodynamics, in particular the Coleman-Noll procedure, to draw conclusions about growth laws based on the Clausius-Duhem inequality stated in 1.5.2.7.

Generalising the conservation equations of traditional continuum mechanics to morphoelasticity and open systems requires careful balance and the correct interpretation of source terms. These equations have been studied by several authors and we will keep our notation relatively close to [19].

Note that the overdot denotes derivatives with respect to the time variable. For some quantity $a$, we denote the time derivative $\dot{a} = \mathrm{d}a/\mathrm{d}t$. Also note that spatial differentiation (divergence, gradient) is always implied with respect to the current variable $\mathbf{x} \in \mathcal{B}_t$ (unless specified otherwise in the subscript of the nabla operator, for instance in the definition of the deformation gradient $\mathbf{F} = \nabla_{\mathbf{X}}\varphi$, see (1.3)).

#### 1.5.2.1 Slow growth assumptions of morphoelasticity

Having stated the kinematic assumptions of morphoelasticity in the previous section, we now introduce some mechanical assumptions.

1. **Separation of timescales**: The timescale of growth is much slower than that of elasticity.

2. Mass is added from the initial reference configuration $\mathcal{B}_0$ to the virtual reference configuration $\mathcal{B}_r$ and is constant throughout the elastic deformation (which maps from $\mathcal{B}_r$ to $\mathcal{B}_t$).

3. Mass is added through a **volumetric source** (i.e. no mass boundary flux).

The first assumption is discussed in detail in Section 1.4.

We will now briefly explore a consequence of the second assumption and explore the third assumption when stating the mass balance. We assume that mass is added in the growth process from $\mathcal{B}_0$ to $\mathcal{B}_r$, but no mass is added during the elastic deformation from $\mathcal{B}_r$ to $\mathcal{B}_t$. To investigate the consequences of this assumption, suppose $\mathrm{d}M_r = \rho_r \mathrm{d}V_r$ is a mass element in the virtual reference configuration $\mathcal{B}_r$, where $\rho_r$ is the virtual reference mass density and $\mathrm{d}V_r$ is a virtual reference volume element. Similarly, let $\mathrm{d}M_t = \rho \mathrm{d}V_t$ where $\rho$ is the current density. Earlier, we introduced $\mathbf{F} = \mathbf{AG}$ and $J = \det \mathbf{F}$, $J_A = \det \mathbf{A}$ and $J_G = \det \mathbf{G}$. Since no mass is added from $\mathcal{B}_r$ to $\mathcal{B}_t$, $\mathrm{d}M_t = \mathrm{d}M_r$, and with appropriate coordinate transform $\mathrm{d}V_t = J_A \mathrm{d}V_r$ we obtain

$$J_A \, \rho = \rho_r. \tag{1.5}$$

We now make the additional assumption that $\rho_r$ is constant in time. This implies that the new, grown mass has the same density (locally) as the surrounding pregrown tissue. This assumption allows for a simple coupling between the mechanics and geometry of growth, as we will see in the statement of mass balance.

#### 1.5.2.2 Mass balance

We think of a growing tissue as a collection of cells which take nutrients from the extracellular fluid. In our continuum modeling approach, the tissue has a density (mass per volume) $\rho(\mathbf{x}, t)$ in $\mathcal{B}_t$. Nutrient uptake contributes a volumetric growth rate function $\rho(\mathbf{x}, t)\,\gamma(\mathbf{x}, t)$ in $\mathcal{B}_t$. Physical laws are most naturally stated in the current configuration. We will present the mass balance for a volume $\Omega_t \subset \mathcal{B}_t$. The mass balance takes the form

$$\frac{\mathrm{d}}{\mathrm{d}t} \int_{\Omega_t} \rho \mathrm{d}V_t = \int_{\Omega_t} \rho\gamma \mathrm{d}V_t \tag{1.6}$$

We now transform this balance equation which is integrated over $\Omega_t$ into a local, pointwise statement at $\mathbf{x}$, $t$. Since $\Omega_t$ is a region which evolves with time, it will prove useful to transform to the corresponding region $\Omega_0 \subset \mathcal{B}_0$ and evaluate time derivatives in this

static region. Volume elements and area elements transform as

$$\int_{\Omega_t} \mathrm{d}V_t = \int_{\Omega_0} J \mathrm{d}V_0 \tag{1.7}$$

Evaluating time derivatives in $\mathcal{B}_0$ and taking into account that $J_A\,\rho$ is constant in time leads us to the local, pointwise statement

$$\gamma = \mathrm{tr}\left(\dot{\mathbf{G}}\mathbf{G}^{-1}\right) \tag{1.8}$$

The assumption that $\rho_r$ is constant allows for a simple coupling between the mechanics and the geometry of growth: The last equation relates the change in mass of a body to properties of the growth deformation tensor.

#### 1.5.2.3 Compatible and incompatible sources

In the following, we will present the integral statements over $\Omega_t$ for the remaining laws (energy, linear and angular momentum, entropy) and then the localised (pointwise) statements of the same laws.

As we have discussed regarding the slow growth assumption, new mass (with the same density as the surrounding material) enters the tissue with the local growth rate $\rho\gamma$. This material will come with its own momentum, energy and entropy which may or may not diverge from the surrounding tissue. One possibility is that indeed the new material has the same properties as (locally) the surrounding tissue. We call these type of sources compliant, using the terminology of [19], and they balance out and do not appear in the local statements of the laws. Alternatively, the new material may have sources that are different from the pregrown material, having for instance locally a higher energy density than the surrounding tissue, or due to microscopic organisation possibly a lower entropy. We call these sources non-compliant, and they do appear in the local statements. We denote non-compliant sources with an overbar.

#### 1.5.2.4 Linear momentum balance

This is the balance between change in linear momentum and the forces that cause it. We introduce the volumetric body force density (force per volume) $\mathbf{b}$, the surface traction (force per area) $\mathbf{t}$ which according to Cauchy's postulate can be decomposed

into the Cauchy stress $\mathbf{T}$ times the surface normal $\mathbf{n}$, i.e. $\mathbf{t} = \mathbf{T}\mathbf{n}$. The non-compliant momentum source (force per volume) is $\overline{\mathbf{p}}$:

$$\frac{\mathrm{d}}{\mathrm{d}t}\int_{\Omega_t}\rho\mathbf{v}dV_t = \underbrace{\int_{\Omega_t}\mathbf{b}\mathrm{d}V_t + \int_{\partial\Omega_t}\mathbf{T}\mathbf{n}\mathrm{d}A_t}_{\text{body and traction forces}} + \underbrace{\int_{\Omega_t}\gamma\rho\mathbf{v}\mathrm{d}V_t}_{\text{compliant}} + \underbrace{\int_{\Omega_t}\bar{\mathbf{p}}\mathrm{d}V_t}_{\text{non-compliant}} \tag{1.9}$$

The local (pointwise) statement is

$$\rho\dot{\mathbf{v}} = \mathbf{b} + \nabla\cdot\mathbf{T} + \bar{\mathbf{p}} \tag{1.10}$$

#### 1.5.2.5 Angular momentum balance

This is the balance between change in angular momentum and the moments (sometimes also called torques) that balance it. Without loss of generality, we state moments with respect to the coordinate system origin. Since the non-compliant linear momentum source $\overline{\mathbf{p}}$ enters the angular momentum balance, we require no additional non-compliant angular momentum source (it could be included into $\overline{\mathbf{p}}$).

$$\frac{\mathrm{d}}{\mathrm{d}t}\int_{\Omega_t}\rho\mathbf{x}\times\mathbf{v}\mathrm{d}V_t = \underbrace{\int_{\Omega_t}\mathbf{x}\times\mathbf{b}\mathrm{d}V_t + \int_{\partial\Omega_t}\mathbf{x}\times\mathbf{T}\mathbf{n}\mathrm{d}A_t}_{\text{moments through body and traction forces}} + \underbrace{\int_{\Omega_t}\gamma\rho\mathbf{x}\times\mathbf{v}\mathrm{d}V_t}_{\text{compliant}} + \underbrace{\int_{\Omega_t}\mathbf{x}\times\overline{\mathbf{p}}\mathrm{d}V_t}_{\text{non-compliant}} \tag{1.11}$$

From localising the angular momentum balance, we can derive symmetry of the Cauchy stress tensor $\mathbf{T} = \mathbf{T}^T$.

#### 1.5.2.6 Energy balance (first law of thermodynamics)

This is the balance between the change in the total energy of the body and contributions from mechanical power and heat. The total energy is made up of internal energy $\mathcal{E}$ (i.e. elastic and chemical energy) and kinetic energy $\mathcal{K}$. The mechanical power $\mathcal{P}$ is the work per time which the body is exposed to through body force forces $\mathbf{b}$ and surface traction $\mathbf{t}$, introduced in the context of linear momentum balance. The heating $\mathcal{Q}$ is composed of a volumetric heat source $r$ (for radiation) and a surface flux $\mathbf{q}$ called the Fourier heat flux. Apart from $\overline{\mathbf{p}}$, the non-compliant energy source $\overline{\varepsilon}$ enters the balance

equation:

$$\underbrace{\frac{\mathrm{d}}{\mathrm{d}t}\int_{\Omega_t}\rho\left(\varepsilon+\frac{1}{2}\left|\mathbf{v}\right|^2\right)\mathrm{d}V_t}_{\dot{\mathcal{E}}(\Omega_t)+\dot{\mathcal{K}}(\Omega_t)} = \underbrace{\int_{\Omega_t}\mathbf{b}\cdot\mathbf{v}\mathrm{d}V_t+\int_{\partial\Omega_t}\mathbf{n}\cdot\mathbf{T}\mathbf{v}\mathrm{d}A_t}_{\mathcal{P}(\Omega_t)}+\underbrace{\int_{\Omega_t}\rho r\,\mathrm{d}V_t+\int_{\partial\Omega_t}\mathbf{q}\cdot\mathbf{n}\mathrm{d}A_t}_{\mathcal{Q}(\Omega_t)}$$
$$+\underbrace{\int_{\Omega_t}\gamma\rho\left(\varepsilon+\frac{1}{2}\left|\mathbf{v}\right|^2\right)\mathrm{d}V_t}_{\text{compliant}}+\underbrace{\int_{\Omega_t}\overline{\varepsilon}+\overline{\mathbf{p}}\cdot\mathbf{v}\mathrm{d}V_t}_{\text{non-compliant}} \tag{1.12}$$

The local (pointwise) statement is

$$\rho\dot{\varepsilon}=\mathbf{T}:\dot{\mathbf{F}}\mathbf{F}^{-1}+\rho r-\nabla\cdot\mathbf{q}+\bar{\varepsilon} \tag{1.13}$$

Note that to successfully derive this local form, the term $\mathbf{b}\cdot\mathbf{v}$ should be replaced through the linear momentum balance according to (1.10), which is why $\overline{\mathbf{p}}$ does not appear in the local statement.

#### 1.5.2.7 Entropy / free energy imbalances (second law of thermodynamics)

We will only be concerned with stating the entropy imbalance here. In Section 1.6, we will discuss it from the perspective of rational thermodynamics, which we will apply to obtain restrictions to constitutive relationships.

According to the entropy imbalance, the change in entropy density $\eta$ is greater than the heat supply (as defined in the energy balance) divided by the temperature density $\theta$. The non-compliant energy source $\bar{\varepsilon}$ and the entropy source $\overline{\eta}$ also enter the imbalance.

$$\frac{\mathrm{d}}{\mathrm{d}t}\int_{\Omega_t}\rho\eta\mathrm{d}V_t\geq\underbrace{\int_{\Omega_t}\frac{\rho r}{\theta}\mathrm{d}V_t-\int_{\partial\Omega_t}\frac{\mathbf{q}\cdot\mathbf{n}}{\theta}\mathrm{d}A_t}_{\mathcal{Q}(\Omega_t)/\Theta(\Omega_t)}+\underbrace{\int_{\Omega_t}\gamma\rho\eta\mathrm{d}V_t}_{\text{compliant}}+\underbrace{\int_{\Omega_t}\frac{\bar{\varepsilon}-\bar{\eta}}{\theta}\mathrm{d}V_t}_{\text{non-compliant}} \tag{1.14}$$

which locally takes the form

$$\rho\dot{\eta}\geq\frac{\rho r}{\theta}-\nabla\cdot\left(\frac{\mathbf{q}}{\theta}\right)+\frac{\bar{\varepsilon}-\bar{\eta}}{\theta} \tag{1.15}$$

For our analysis of constitutive relationships, it is useful to Legendre transform to the

free energy density $\psi = \varepsilon - \theta\eta$. After applying the time derivative and substituting (1.13) for the internal energy, we obtain the free energy imbalance

$$\rho\dot{\psi} \leq \mathbf{T} : \dot{\mathbf{F}}\mathbf{F}^{-1} - \rho\dot{\theta}\eta - \frac{\mathbf{q} \cdot \nabla_{\mathbf{x}}\theta}{\theta} + \overline{\eta} \tag{1.16}$$

This formulation of the second law of thermodynamics is known as the Clausius-Duhem inequality in terms of the free energy density.

### 1.5.3 Constitutive relationships

In the context of nonlinear elasticity, a constitutive law or constitutive relationship relates strains to stresses[3]. For a hyperelastic material, stresses can be derived from a scalar field called the strain energy density $W$. Its independent variables depend on the modeling assumptions at hand. Typical assumptions in the context of modelling biological tissues are:

1. **Hyperelastic** and **isothermal** materials, i.e. strain energy density depends only on the elastic deformation gradient, $W = W(\mathbf{A})$.

2. **Incompressible** materials, $\det(\mathbf{A}) = 1$.

For incompressible, isothermal, hyperelastic materials the Cauchy stress $\mathbf{T}$ can be derived from the strain energy density as

$$\mathbf{T}(\mathbf{A}) = \frac{\partial W}{\partial \mathbf{A}}\mathbf{A}^T - p\mathbf{1} \tag{1.17}$$

where $p$ is a Lagrange multiplier which enforces incompressibility. Incompressibility is a typical assumption for soft biological tissues.

There is generally very little information on constitutive relationships in soft biological tissues (see e.g. concluding remarks in [67]), and neo-Hookean materials have proven very useful as modeling starting points. The strain-energy density function of a neo-Hookean solid in three dimensions is $W(\mathbf{A}) = \mu(I_1 - 3)$ where $\mu$ is a material parameter and $I_1$ is the first principal invariant of the right Cauchy-Green strain tensor $\mathbf{C} = \mathbf{A}^T\mathbf{A}$ for which $I_1 = \operatorname{tr}\mathbf{C} = \alpha_1^2 + \alpha_2^2 + \alpha_3^2$ where $\alpha_i$, $i = 1, 2, 3$ are the three

[3]Note that in the context of rational thermodynamics, the notion of constitutive relationships carries a wider meaning. This will be discussed in Section 1.6.

principal elastic stretches. We obtain

$$W(\alpha_1, \alpha_2, \alpha_3) = \mu\left(\alpha_1^2 + \alpha_2^2 + \alpha_3^2 - 3\right). \tag{1.18}$$

### 1.5.4 Growth laws and literature review

In morphoelasticity, the evolution of growth is described as a differential equation in time

$$\dot{\mathbf{G}} = \mathcal{G}(\mathbf{T}, \mathbf{F}, \mathbf{G}, \boldsymbol{\mu}; t, \mathbf{x}, \mathbf{X}) \tag{1.19}$$

where the dot denotes time differentiation. Here, $\mathbf{F}$ is the deformation gradient and $\mathbf{G}$ is the growth tensor field as described above, $\mathbf{T}$ is the Cauchy stress, $\boldsymbol{\mu}$ can be biochemical or other fields and $\mathbf{x}$ and $\mathbf{X}$ describe positions in the undeformed and deformed body, respectively. The growth law $\dot{\mathbf{G}} = \mathcal{G}$ describes an active growth process which requires energy and adds material, whereas the elastic accommodation (geometrically described by $\mathbf{A}$) is passive, adds no mass and consumes no energy (unless plasticity is involved). The difficulty in stating growth laws is that the observed evolving form and mass of the body are a result of both growth and its elastic accommodation. There is a lack of data for constitutive relationships of biological tissues, let alone successfully retrieved growth deformations $\mathbf{G}$, which makes the growth law $\dot{\mathbf{G}}$ particularly difficult to access. Making restrictive statements about the form of $\mathcal{G}$ from first principles in physics is the goal of Section 1.6.

The study of growth laws is in its infancy. Even the question of whether stress or strain drives growth is not settled; every major review contains a debate on this topic ([67, 1, 46]). Here we take the view that growth laws should be functions of stress $\dot{\mathbf{G}} = \mathcal{G}(\mathbf{T})$ so that a stress-free configuration can be chosen as reference (a reference configuration for strain is less obvious).

The simplest stress-dependent growth law which incorporates the idea of homeostasis is a linear coupling with Cauchy stress

$$\dot{\mathbf{G}} = \mathbf{K}(\mathbf{T} - \mathbf{T}^*)\,\mathbf{G} \tag{1.20}$$

where $\mathbf{K}$ is a matrix of constant coefficients and $\mathbf{T}^*$ is the homeostatic stress. This

was studied in [62]. The authors ran finite element simulations on variations of two-dimensional beams glued in parallel, finding that (depending on choices of $\mathbf{K}$ and $\mathbf{T}^*$) the system either equilibrates or does not. Further, they studied a delay differential equation version of (1.20) by replacing $\mathbf{T}(\mathbf{x}, t)$ with $\mathbf{T}(\mathbf{x}, t-\tau)$ where $\tau$ is a small delay, finding that depending on the delay and the stiffness ratio of beams glued in parallel, either no oscillations, stress oscillations or both stress and curvature oscillations of the beams occur. Finally, the authors studied invagination of cylindrical and spherical, fluid-filled or empty shells. Again, they used a finite-element simulation in which the shell consists of passive material with a small striped active region in the shell driving the invagination. Overall, their analysis shows that (1.20) either leads to stationary states of the growing system, or to unrealistic ever-growing systems, depending on the choice of $\mathbf{K}$ and $\mathbf{T}^*$, but stability is not analysed systematically.

In [68, 69], the previous growth law is modified by adding evolution equations for the target stress:

$$\dot{\mathbf{G}}\mathbf{G}^{-1} = \mathbf{A}(\mathbf{T} - \mathbf{T}^*) \qquad \dot{\mathbf{T}}^* (\mathbf{T}^*)^{-1} = \mathbf{B}(\mathbf{T} - \mathbf{T}^*) \tag{1.21}$$

where $\mathbf{A}, \mathbf{B}$ are fourth-order tensors with constant entries. The systems analysed in these papers are practically the same as in [62] and the conclusions are similar: For some parameter choices of $\mathbf{A}, \mathbf{B}, \mathbf{T}^*(t=0)$ actually $\mathbf{T}$ and $\mathbf{T}^*$ converge to the same equilibrium value. In other cases, they converge to different equilibrium values, and in yet other cases the stresses diverge, reaching no equilibrium at all.

Based on the thermodynamic argument briefly discussed above, and discussed in more detail in Section 1.6, a growth law driven by Eshelby stress is proposed in [2]

$$\dot{\mathbf{G}} = \mathbf{K}(\mathbf{E} - \mathbf{E}^*)\mathbf{G} \tag{1.22}$$

where $\mathbf{E}$ and $\mathbf{E}^*$ are Eshelby stress and homeostatic Eshelby stress, respectively, and $\mathbf{K}$ is a matrix of constant coefficients. The proposition that Eshelby stress drives is supported by thermodynamical arguments ([20, 2, 3]).

In [3], the authors take as their starting point a growth law inspired by cardiovascular mechanics, in which $\mathbf{G}$ is diagonal (i.e. no shear) and involves only the circumferential components of Cauchy stress. For diagonal $\mathbf{G}$ and small deformations, they

show that (1.22) coincides with (1.20) up to a sign. By showing results of particular numerical simulations (but without a general stability result), the authors achieve convergence to the homeostatic stress in the case of displacement boundary conditions but obtain a divergent (ever-growing) in the case of prescribed load. Finally, they show that by adding passive layers (analysing a three rather than one-layered system, with inner and outer layers passive), convergence towards homeostasis is also possible when the load is prescribed.

### 1.5.5 Formal description of homeostatic evolution laws

The growth law (1.20) is consistent with our assumptions about homeostasis and the various time scales of the problem. However, even for growth dynamics cases with homogeneous deformations, stating the growth law in terms of second order tensors proves too restrictive (see Chapter 3). For this reason we generalise (1.20) to

$$\dot{\mathbf{G}} = \boldsymbol{K} : (\mathbf{T} - \mathbf{T}^*)\,\mathbf{G} \tag{1.23}$$

where $\boldsymbol{K}$ is a fourth-order tensor [30, 67]. In an orthonormal basis, the components are

$$\dot{G}^{ij} = K^{ikmn}\,[T^{mn} - (T^*)^{mn}]\,G^{kj}. \tag{1.24}$$

To elucidate the nature of the fourth order tensor $\boldsymbol{K}$, we shall introduce basis vectors in this section which are different for $\mathcal{B}_0$, $\mathcal{B}_r$ and $\mathcal{B}_t$. Let the set of basis vectors in $\mathcal{B}_0$ be denoted by $\{\mathbf{E}^i\}$, basis vectors in $\mathcal{B}_r$ be $\{\boldsymbol{\varepsilon}^i\}$ and basis vectors in $\mathcal{B}_t$ be $\{\mathbf{e}^i\}$ where $i \in \{r, \theta, z\}$. As the deformation gradient $\mathbf{F}$ maps $\mathbf{F} : \mathcal{B}_0 \to \mathcal{B}_t$, it has a mixed basis, taking the form $\mathbf{F} = F^{ij}\mathbf{e}^i \otimes \mathbf{E}^j$. The elastic deformation gradient $\mathbf{A}$ maps $\mathbf{A} : \mathcal{B}_r \to \mathcal{B}_t$, taking the form $\mathbf{A} = A^{ij}\mathbf{e}^i \otimes \boldsymbol{\varepsilon}^j$. The growth tensor field $\mathbf{G}$ maps $\mathbf{G} : \mathcal{B}_0 \to \mathcal{B}_r$, taking the form $\mathbf{G} = G^{ij}\boldsymbol{\varepsilon}^i \otimes \mathbf{E}^j$.

To satisfy the equality (1.23), the fourth order tensor $\mathcal{K}$ must have the form

$$\boldsymbol{\mathcal{K}} = \mathcal{K}^{ijkl}\boldsymbol{\varepsilon}^i \otimes \boldsymbol{\varepsilon}^j \otimes \mathbf{e}^k \otimes \mathbf{e}^l. \tag{1.25}$$

Note that summation over repeated indices is implied and all indices are elements of the same index set as $i$.

## 1.6 Thermodynamic restrictions of growth laws

In Section 1.5.2, we have stated balance laws for various quantities. As opposed to traditional continuum mechanics, in which conservation of mass, momentum, energy can be granted, in the context of morphoelasticity we are dealing with open systems. For open systems, the various quantities are no longer conserved and sources of mass, linear momentum and energy enter the equations, transforming conservation equations into balance equations. Balance equations with sources present are given in 1.5.2, and it is in this section that we will make full use of them, attempting to exploit the second law of thermodynamics (in the Clausius-Duhem formulation) to derive restrictions to and make statements about growth laws.

The standard procedure for for deriving restrictions to constitutive laws is known as the Coleman-Noll procedure [12]. It was developed in the framework of rational thermodynamics. While it is very appealing for its axiomatic buildup and mathematical elegance, some of its assumptions are rather unorthodox and have been criticised as e.g. *'adventurous'* ([52]) and *'out of touch with physical reality'* ([49]). However, for the treatment of thermoelastic solids, rational thermodynamics is quite elegant and produces equations that are consistent with elasticity and traditional (equilibrium) thermodynamics. For this reason, rational thermodynamics is widely used in the continuum mechanics community ([36]) and has found application to growing soft biological tissues.

### 1.6.1 Relevant ideas from rational thermodynamics

In the following presentation, we will briefly describe the most relevant ideas and assumptions of rational thermodynamics for our purpose, also briefly highlighting some of its problems.

The most important and useful objective of rational thermodynamics is to place restrictions on the constitutive relationships for free energy $\widehat{\Psi}$, entropy, $\widehat{\eta}$, Cauchy stress $\widehat{\mathbf{T}}$ and Fourier heat flux $\widehat{\mathbf{q}}$ by means of the Clausius-Duhem inequality in the form (1.16). The difference between the previously defined fields $\psi$, $\eta$, $\mathbf{T}$ $\mathbf{q}$ (without hats) and hatted fields $\widehat{\Psi}$, $\widehat{\eta}$, $\widehat{\mathbf{T}}$, $\widehat{\mathbf{q}}$ is that the latter specifically refer to the constitutive relationship. The standard procedure by which restrictions of the constitutive relationships are achieved

is the Coleman-Noll procedure. Its objective is to restrict the constitutive relationships

$$\widehat{\Psi}\left(\mathbf{A},\theta,\nabla\theta\right) \qquad \widehat{\eta}\left(\mathbf{A},\theta,\nabla\theta\right) \qquad \widehat{\mathbf{T}}\left(\mathbf{A},\theta,\nabla\theta\right) \qquad \widehat{\mathbf{q}}\left(\mathbf{A},\theta,\nabla\theta\right). \tag{1.26}$$

It should be said that typically in solid mechanics literature unrelated to thermodynamics, the term 'constitutive relationship' relates to how strains are related to stresses, which is the terminology we use in Section 1.5.3. For hyperelastic materials, as described in Section 1.5.3, the constitutive relationship $\widehat{\mathbf{T}}\left(\mathbf{A}\right)$ can in fact be derived from a strain energy density $W\left(\mathbf{A}\right)$. This is not assumed a priori in rational thermodynamics, but instead will be a result of the treatment of thermoelastic solids[4]. In the context of rational thermodynamics, constitutive relationships characterise a given material response. The Clausius-Duhem inequality, (1.16), with the constitutive assumptions incorporated and multiplied by $J$, is

$$J\rho\dot{\widehat{\Psi}} \leq J\widehat{\mathbf{T}} : \dot{\mathbf{F}}\mathbf{F}^{-1} - J\rho\dot{\theta}\widehat{\eta} - \frac{J}{\theta}\widehat{\mathbf{q}}\cdot\nabla\theta + J\overline{\eta} \tag{1.27}$$

It would be fair to ask at this point: If in this context the Fourier heat flux $\widehat{\mathbf{q}}$ is considered a constitutive relationship, i.e. a material response, then why does this not apply to the heat source $r$ in (1.12)? After all, $r$ is a volumetric heat source ($r$ stands for radiation) and $\widehat{\mathbf{q}}$ represents heat entering through a volume boundary, see 1.12. Similarly, if $\widehat{\mathbf{T}}$ is a constitutive relationship, why not the body force $\widehat{\mathbf{b}}$ in (1.9)? The answer is that rather than prescribing $\mathbf{b}$ and $r$ as constitutive relationships about which restrictions are to be inferred, they are *defined* in terms the linear momentum balance (1.9) and energy balance (1.12), respectively. In other words, $\mathbf{b}$ and $r$ are free parameters making sure that the momentum and energy balance are always satisfied, ruling them out of the restriction process of constitutive laws. As $r$ and $\mathbf{b}$ are usually supplied in applications ($\mathbf{b}$ might be gravity, for instance), rational thermodynamics takes a somewhat *'perplexing attitude'*, in the words of [49], with regard to these balance laws.

To complete the chain of ideas of the Coleman-Noll procedure, we point out that

[4]Both the fact that $\widehat{\Psi}$, $\widehat{\eta}$, $\widehat{\mathbf{T}}$ and $\widehat{\mathbf{q}}$ have the same arguments and the fact that $\nabla\theta$ appears as a constitutive argument (in addition to the obvious thermo-elastic parameters $\theta$, $\mathbf{A}$) are the results of Truesdell's *principle of equipresence*. In the words of G. A. Maugin, "This is simply a precautionary measure to avoid missing any significant dependence or coupling" ([52], p. 65). See also [36] p. 230 for a comment on equipresence.

(1.27) is expected to hold for all admissible thermodynamic processes, which means that it must hold for arbitrary deformation tensors and temperature fields. Since the momentum and energy balance laws are ruled out by the argument in the previous paragraph, the fact that (1.27) must hold for all $\mathbf{A}$ and $\theta$ puts restrictions on the constitutive relationships (1.26).

### 1.6.2 Coleman-Noll procedure for morphoelasticity

We now use the constitutive assumptions (1.26) to evaluate the Clausius-Duhem inequality (1.27). Let us separately analyse two important terms, $\dot{\widehat{\Psi}}$ and $J\widehat{\mathbf{T}} : \dot{\mathbf{F}}\mathbf{F}^{-1}$. By chain rule, we obtain

$$\dot{\widehat{\Psi}}\left(\mathbf{A}, \theta, \nabla\theta\right) = \frac{\partial\widehat{\Psi}}{\partial\mathbf{A}} : \dot{\mathbf{A}} + \frac{\partial\widehat{\Psi}}{\partial\theta}\dot{\theta} + \frac{\partial\widehat{\Psi}}{\partial\nabla\theta} \cdot \dot{\overline{\nabla\theta}}. \tag{1.28}$$

Evaluating $J\widehat{\mathbf{T}} : \dot{\mathbf{F}}\mathbf{F}^{-1}$ with $\mathbf{F} = \mathbf{A}\mathbf{G}$, we obtain

$$J\widehat{\mathbf{T}} : \dot{\mathbf{F}}\mathbf{F}^{-1} = J\widehat{\mathbf{T}}\mathbf{A}^{-T} : \dot{\mathbf{A}} + J\mathbf{A}^{T}\mathbf{T}\mathbf{A}^{-T} : \dot{\mathbf{G}}\mathbf{G}^{-1} \tag{1.29}$$

We now regroup the terms and divide by $J_G$, taking into account $J_A\rho = \rho_r$ and $J = J_A J_G$. We obtain

$$\left(\rho_r\frac{\partial\widehat{\boldsymbol{\Psi}}}{\partial\mathbf{A}} - J_A\widehat{\mathbf{T}}\mathbf{A}^{-T}\right) : \dot{\mathbf{A}} + \rho_r\left(\frac{\partial\widehat{\Psi}}{\partial\theta} + \eta\right)\dot{\theta} + \rho_r\frac{\partial\widehat{\Psi}}{\partial\nabla\theta} \cdot \dot{\overline{\nabla\theta}} \tag{1.30}$$

$$\leq \mathbf{A}^{T}\left(J_A\widehat{\mathbf{T}}\mathbf{A}^{-T}\right) : \dot{\mathbf{G}}\mathbf{G}^{-1} - \frac{J_A}{\theta}\widehat{\mathbf{q}} \cdot \nabla\theta + J_A\overline{\eta} \tag{1.31}$$

We have made the assumption of a constant reference density (see comment after 1.5), which without loss of generality allows us to define $\rho_r := 1$ e.g. by rescaling mass or volume.

As pointed out in Section 1.6.1, the expression (1.31) is expected to hold for all deformation tensors and all temperature fields. But it easy to construct a deformation gradient $\mathbf{A}$ and a temperature field $\theta$ which at a particular point and time $\mathbf{X}_0, t_0$ take values $\mathbf{A}\left(\mathbf{X}_0, t_0\right)$, $\dot{\mathbf{A}}\left(\mathbf{X}_0, t_0\right)$, $\theta\left(\mathbf{X}_0, t_0\right)$, $\dot{\theta}\left(\mathbf{X}_0, t_0\right)$, $\nabla\theta\left(\mathbf{X}_0, t_0\right)$, $\dot{\overline{\nabla\theta}}\left(\mathbf{X}_0, t_0\right)$ that are independent[5]. For this reason, the coefficients of $\dot{\mathbf{A}}$, $\dot{\theta}$ and $\dot{\overline{\nabla\theta}}$ must vanish. Taking

[5]This is easy to show. Let us denote the values of $\mathbf{A}$, $\dot{\mathbf{A}}$, $\theta$, $\dot{\theta}$, $\nabla\theta$, $\dot{\overline{\nabla\theta}}$ at the point $\mathbf{X}_0$, $t_0$ by

into account $\rho_r = 1$, it follows

$$\mathbf{P}_r := J_A \widehat{\mathbf{T}} \mathbf{A}^{-T} = \frac{\partial \widehat{\mathbf{\Psi}}}{\partial \mathbf{A}} \qquad \eta = -\frac{\partial \widehat{\Psi}}{\partial \theta} \qquad \frac{\partial \widehat{\Psi}}{\partial \nabla\theta} = 0 \tag{1.34}$$

In this result rational thermodynamics shows itself from its most elegant side. It shows how the first Piola-Kirchhoff $\mathbf{P}_r$ stress and the entropy are derived from the thermodynamic potential $\widehat{\Psi}$ which is consistent with traditional nonlinear elasticity and thermodynamics. The Piola-Kirchhoff stress is given with respect to the stress-free configuration $\mathcal{B}_r$, as one would expect from traditional elasticity. It also shows that the free energy density is independent of the temperature gradient, suggesting (by equipresence, see footnote 4) that (1.26) should be updated to $\widehat{\Psi}(\mathbf{A}, \theta)$, $\widehat{\eta}(\mathbf{A}, \theta)$, $\widehat{\mathbf{T}}(\mathbf{A}, \theta)$, $\widehat{\mathbf{q}}(\mathbf{A}, \theta)$.

Taking into account (1.34), for (1.31) we obtain[6]

$$0 \leq \mathbf{M}_r : \dot{\mathbf{G}}\mathbf{G}^{-1} + \frac{J_A}{\theta} \widehat{\mathbf{q}} \cdot \nabla\theta + J_A \overline{\eta} \tag{1.35}$$

where we introduced the Mandel stress $\mathbf{M}_r := \mathbf{A}^T \mathbf{P}_r$.

---

underlined symbols $\underline{\mathbf{A}}$, $\underline{\dot{\mathbf{A}}}$, $\underline{\theta}$, $\underline{\dot{\theta}}$, $\underline{\nabla\theta}$, $\underline{\dot{\nabla\theta}}$. We dropped the subscript $m$ in $\theta$ for simplicity. The gradient is understood with respect to the reference variable $\mathbf{X}$, which we also dropped. Then

$$\mathbf{A}(\mathbf{X}, t) = \underline{\mathbf{A}} + (t - t_0)\underline{\dot{\mathbf{A}}} \qquad \theta(\mathbf{X}, t) = \underline{\theta} + (t - t_0)\,\underline{\dot{\theta}} + \left[\underline{\nabla\theta} + (t - t_0)\,\underline{\dot{\nabla\theta}}\right](\mathbf{X} - \mathbf{X}_0) \tag{1.32}$$

With this choice of $\mathbf{A}$ and $\theta$, it simply follows

$$\mathbf{A}(\mathbf{X}_0, t_0) = \underline{\mathbf{A}} \qquad \dot{\mathbf{A}}(\mathbf{X}_0, t_0) = \underline{\dot{\mathbf{A}}} \qquad \theta(\mathbf{X}_0, t_0) = \underline{\theta} \qquad \nabla\theta(\mathbf{X}_0, t_0) = \underline{\nabla\theta} \qquad \dot{\nabla\theta}(\mathbf{X}_0, t_0) = \underline{\dot{\nabla\theta}} \tag{1.33}$$

This shows that at $\mathbf{X}_0$, $t_0$, the quantities$\mathbf{A}$, $\dot{\mathbf{A}}$, $\theta$, $\dot{\theta}$, $\nabla\theta$, $\dot{\nabla\theta}$ can be chosen to have independent values $\underline{\mathbf{A}}$, $\underline{\dot{\mathbf{A}}}$, $\underline{\theta}$, $\underline{\dot{\theta}}$, $\underline{\nabla\theta}$, $\underline{\dot{\nabla\theta}}$.

[6]Note that another way of arriving at (1.35) is to consider the constitutive relationship of the free energy density as a function of the growth field, $\hat{\Psi} = \hat{\Psi}(\mathbf{A}, \theta, \mathbf{G})$. By the equipresence (see Footnote 4), the other constitutive relationships $\widehat{\eta}$, $\widehat{\mathbf{T}}$ and $\widehat{\mathbf{q}}$ would depend on the same fields. This requires us to treat $\mathbf{G}$ as an *internal* state variable, whereas $A$ and $\theta$ are *external* state variables. Internal variables are associated with configurational forces, which are the result of inflow of free energy [35]. The configurational force associated with growth is related to the Mandel stress, $\partial\hat{\Psi}/\partial\mathbf{G} = \mathbf{M}_r\mathbf{G}^{-T}$ (see [19]). Configurational forces associated with internal variables (such as $\mathbf{G}$) produce additional terms in the Clausius-Duhem inequality. To summarise, while our analysis leading to (1.35) is close to the treatment of thermoelastic solids of Coleman and Noll [12], one can arrive at the same result by treating the growth field as an internal state variable. In the latter case, the term $\mathbf{M}_r : \dot{\mathbf{G}}\mathbf{G}^{-1}$ in (1.35) arises as a configurational force associated with growth (see [19]).

### 1.6.3 Interpreting result of Coleman-Noll procedure

For simplicity, we assume that temperature is spatially homogeneous, such that the $\widehat{\mathbf{q}} \cdot \nabla\theta$ term drops out, which leaves

$$\mathbf{M}_r : \dot{\mathbf{G}}\mathbf{G}^{-1} + J_A\overline{\eta} \geq 0. \tag{1.36}$$

In the spirit of rational thermodynamics, restrictive statements about the growth law should only be the result of considering all possible deformations. We illustrate with the simple growth law

$$\dot{\mathbf{G}} = \left(\widehat{\mathbf{T}} - \mathbf{T}^*\right)\mathbf{G} \tag{1.37}$$

how such a restriction can be useful. Let us assume that $\mathbf{G}$, $\dot{\mathbf{G}}$, $\widehat{\mathbf{T}}$ and $\mathbf{T}^*$ are diagonal and the material is incompressible ($J_A = 1$). In this case, the Mandel stress coincides with the Cauchy stress, $\mathbf{M}_r = \mathbf{T}$. Evaluating (1.36) yields

$$\widehat{\mathbf{T}} : \left(\widehat{\mathbf{T}} - \mathbf{T}^*\right) + \overline{\eta} = \left(\widehat{t}_1^2 + \widehat{t}_2^2\right) + \left(\widehat{t}_1 t_1^* + \widehat{t}_2 t_2^* + \overline{\eta}\right) \geq 0. \tag{1.38}$$

The first bracketed term is positive or zero for any deformation and therefore it cannot contribute to a violation of the Clausius-Duhem inequality. In the second bracketed term, however, $\widehat{t}_1 t_1^* + \widehat{t}_2 t_2^*$ can potentially become negative at some point in space and time $\mathbf{X}_0, t_0$, and therefore requires an external source or sink of entropy to satisfy the Clausius-Duhem inequality. This could be provided by some biochemically driven self-organisation process. This suggests that a growth law of the form $\dot{\mathbf{G}} = \widehat{\mathbf{T}}\mathbf{G}$ is in principle microscopically achievable at every time and position in the tissue without further input or supporting mechanisms. However, no microscopic physical process could achieve the contribution $-\mathbf{T}^*\mathbf{G}$ without further supply of information.

### 1.6.4 Conclusion on Thermodynamics

Thermodynamics recovers the usual constitutive law for stress, but can contribute little to the search for growth laws. The difference between the great success of rational thermodynamics to restrict evolution laws in fields like plasticity and thermoelasticity [36] compared to the lack of success to achieve the same for growth laws in living elastic tissues is due to the openness of these systems: the entropy sink $-\overline{\eta}$ is an unknown field.

It defies the entropy increase by processing information at the cellular level, possibly through genetically pre-programmed response. Living systems take up energy through nutrients in the extracellular fluid in order to power such active (energy consuming) processes. This idea is at the core of the study of self-assembly, i.e. the creation of highly ordered structures via local entropy sinks in a system with global entropy increase. This is the main difference between living tissues and artificial materials such as rubber, elastomers or gels, which (in general) do not consume energy at the microscale (passive processes). For such processes the Clausius-Duhem dissipation inequality yields meaningful restrictions of evolution laws. In the context of biological solid mechanics, the rational thermodynamics approach allows to identify Mandel stress as a key quantity, but ultimately provides no compelling argument for growth laws of the type (1.22).

## 1.7 An overview of this thesis

As the review of growth laws presented in Section 1.5.4 reveals, most authors have taken the ability of growing systems to reach homeostasis for granted, but the consequences of this assumption have never been carefully investigated mathematically. In this thesis, we first investigate in detail the modelling of homeostasis for volumetric growth models (Chapters 2 & 3). The goal is to uncover the exact conditions under which growth dynamical systems striving for homeostasis are mechanically stable or unstable. Stability describes the physiological state of a living biological tissue, whereas instability could be interpreted as a failure of the homeostasis mechanism leading to pathological scenarios such as tumour growth or cell apoptosis. In addition to addressing these conceptual questions mathematically, we also investigate in detail a direct application of the description of growth and mechanical feedback to the morphology of Ammonites' seashells (Chapter 4).

In Chapter 2, we propose a model of pieces of elongated elastic tissue connected in series and in parallel. An inspiration is the filamentary structure of muscle, for example in cardiac muscle cells cardiomyocytes. A fascinating experimental observation is that cardiomyocytes grow through the deposition of additional sarcomeres (elongated bundles of actin/myosin) either in series or in parallel. Deposition of sarcomeres in

series makes cardiomyocytes longer and the volume of the heart chambers larger and has been observed as a response to a particular change in mechanical conditions of the heart (volume overload), whereas deposition of additional sarcomeres in parallel thickens the ventricular walls in response to pressure overload ([25], [67]). Inspired by these observations, we consider an idealised model of growth driven by homeostasis in a network of elongated morphoelastic tissues (we simply call them bars). Any number of bars can be connected in series or in parallel to other bars. These interconnected bars contribute to the elastic and dynamical behaviour of the entire network. In Section 2.1, we establish rules to compute the effective elastic properties from individual network components. Finally, in Section 2.3, we analyse the dynamical behaviour of the effective network as a function of its individual parts.

Chapter 3 extends the idea of growth driven by a mechanism accommodating homeostatic stress to a setting of cylindrical geometry, inspired by the many tubular structures in biology, such as airways, arteries or axons. In particular, a motivating factor is to understand the size of such systems (i.e. the radius and wall thickness) not simply as residually stressed passive tubes, but as dynamically growing actively evolving structures. The observed size of a tubular structure can then be understood as a stable equilibrium of a dynamical system in which the homeostatic stress is accommodated by the system. The hope is that such a study can provide a foundational framework to explain the observed size of tubular structures (modernising studies such as [17] in the context of nonlinear elasticity and deformation gradient decomposition), and to offer a dynamical interpretation to various insights and hypotheses linking residual stress in arteries to structural optimisation. In [23] it was hypothesized that the function of residual stress is to flatten the circumferential stress profile across the arterial wall. The lower the circumferential stress gradient is across arterial walls, the less structural damage the tissue will suffer from shear forces between the cylindrical layers, avoiding tissue separation. Residual stress also contributes to keeping axial strain nearly constant under different pressure values to avoid structural damage when blood pressure fluctuates [31].

An additional complication of tubular structures is that wall stress is inhomogeneously distributed, leading to considerably different stress levels at the inner and outer walls of tubes. A key idea of Chapter 3 is to propose a discretisation scheme

which simplifies the dynamics of the system and enables the application of standard techniques form dynamical systems theory to investigate the stability of the homeostatic stress equilibrium. At the same time, we expect our discretised approach to represent the true behaviour of the full inhomogeneous system if the discretisation is sufficiently fine.

Chapter 4 shifts the focus from a conceptual perspective to a specific biological application, the growth of Ammonites' seashells. The focus of Chapter 4 is on the implications of a homeostasis-like growth-mechanical feedback mechanism on the morphology of Ammonites' shells. To isolate the influence of mechanical feedback, we first focus on known morphological features of the shells and the underlying soft elastic mechanism behind the oscillatory ribbing pattern that can be seen on Ammonites, as presented previously by Moulton and co-workers [57]. As part of the study of these morphological features, which are summarised succinctly as Buckman's Law, we extend the previous work to incorporate a wider class of morphologies. We published these results in [21]. Chapter 4 describes the results in [21], and also extends the system to stress-driven growth, which we show to have a clear effect on the shell morphology that cannot be replicated by the previous modelling results of [57] and [21], and which is consistent with observed morphological trends in Ammonites.

# Chapter 2

# Growth dynamics of elastic networks

Physics has often provided intriguing systems for the study of mathematics, and this chapter is inspired by electric circuits and the simple rules with which relevant properties (resistance, voltage, current...) can be extracted. It also provides an insight into the complexity of growth dynamics, showing that even simple systems can exhibit intricate dynamics due to constitutive and/or geometric nonlinearities.

In electric circuits, there is a very simple way of computing an effective or total resistance from a given arrangement of resistors. For a series circuit, the effective resistance is computed as the sum of resistances. For a parallel circuit, on the other hand, the rule is similar but involves a sum of reciprocal resistances. In analogy to electric circuits, for soft tissues the question suggests itself: if we arrange a number of homogeneous pieces of soft elastic tissue with individual properties (in particular, an individual homeostatic stress), how will they contribute to the behaviour of the total arrangement? The most interesting quantity for collective behaviour is the homeostatic stress: Could there be a rule of computing an effective homeostatic stress $t^*$ at dynamic equilibrium from a set of individual homeostatic stresses $t^*$ in a similar manner to the electric resistance?

To answer this question, we study networks of soft elastic growing bars. To exclude unnecessary complications such as buckling or torque, we assume that the bars deform only in one dimension. In Section 2.1, we focus on an algebraic description of static elastic networks. Static means that there is no growth dynamics; however these networks nevertheless have a complex mechanical behaviour because they are locally stressed. The general description of such networks in Section 2.1 states clear rules on

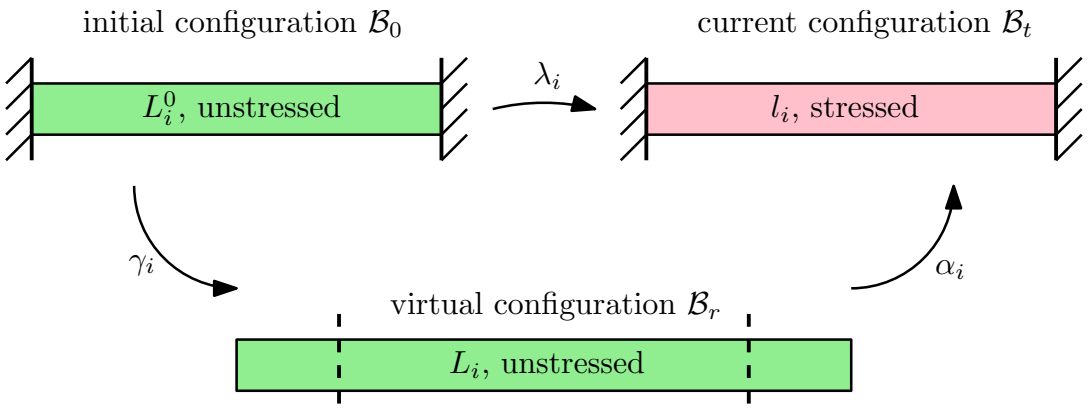


Figure 2.1: Illustration of morphoelastic decomposition. In the virtual configuration $\mathcal{B}_r$, the bar is grown but not compatible with the physical environment, which in this case means it does not fit between the walls. Elasticity restores the compatibility in $\mathcal{B}_t$, fitting the bar back between walls.

how such networks can be constructed.

In the following section, Section 2.2, we continue with an analysis of static networks but turn our attention to the case of small deformations, i.e. deformations near the undeformed initial state of the network. This allows us to vastly simplify and analyse the static description of our networks, and to suggest a homogenisation approach towards computing an effective Hooke's Law for the entire network, in which we heavily draw inspiration from electrical networks. We show an analogy between Ohm's Law and Hooke's Law, and propose an elastic analogy to Kirchhoff's Laws for electrical circuits.

Finally, in Section 2.3, we consider growth dynamics. In this section we build on the foundation established in our study of static networks with small deformations, and propose a mechano-sensitive growth law which drives the individual network elements towards their homeostatic levels. We analyse the dynamics both from an algebraic approach (similarly to Section 2.1), as well as an inductive, electrical circuit-like approach similarly to Section 2.2. We attempt to establish rules to compute the effective homeostatic stress of a dynamical network where individual network elements compete to reach their own homeostasis.

## 2.1 Static networks

### 2.1.1 Individual morphoelastic bars

Our network consists of $n$ morphoelastic bars, which are labeled by an index $i = 1, \ldots, n$. In this section, we consider one of those bars in isolation.

We assume that every bar is morphoelastic. Its initial state is described by the initial reference configuration $\mathcal{B}_0$, in which the $i$-th bar has length $L_i$ and is stress free (no forces). The post-growth state of the bar is called the virtual reference configuration $\mathcal{B}_r$, in which the bar has[1] the post-grown length $L_i$. Finally, the current and physically realised state of the bar is described by the current configuration $\mathcal{B}_t$, in which the bar has length $l_i$. The configurations are illustrated in Fig. 2.1. In summary, the lengths in $\mathcal{B}_0$, $\mathcal{B}_r$ and $\mathcal{B}_t$ are, respectively

$$\text{initial length } L_i^0, \quad \text{reference length } L_i, \quad \text{and} \quad \text{current length } l_i. \tag{2.1}$$

The stress $t_i$ in $\mathcal{B}_t$ of an individual bar is described by a constitutive relationship $h_i$, which is a function of the elastic stretch $l_i/L_i$ (see eq. 2.4 below):

$$t_i = h_i\left(\frac{l_i}{L_i}\right) \tag{2.2}$$

We assume that the constitutive relationship $h_i$ is a monotonically increasing function of $l_i/L_i$ and that $h_i(1) = 0$ (i.e. no elastic strain deformation produces zero stress). We call the quantity

$$\mu_i = h_i'(1) \tag{2.3}$$

the Young's Modulus of the $i$-th bar.

All bars are homogeneous, which means that the stretches and stresses throughout every individual bar are constant ($\mathrm{d}t_i/\mathrm{d}x = 0$), but can be different from bar to bar ($t_i \neq t_j$). For completeness, the homogeneity of the bars allows us to define the elastic stretches $\alpha_i$, growth stretches $\gamma_i$ and morphoelastic stretches $\lambda_i$ as

$$\alpha_i = \frac{l_i}{L_i}, \quad \gamma_i = \frac{L_i}{L_i^0}, \quad \lambda_i = \frac{l_i}{L_i^0}. \tag{2.4}$$

[1] Note: We are *not* using Einstein summation convention (summation over repeated indices) in this text.

The kinematic and mechanical setup is summarised in Figure 2.1.

### 2.1.2 A network of morphoelastic bars

In the previous Section, we discussed individual morphoelastic bars, which are described by their lengths in the respective configuration and their constitutive behaviour (2.2). We now connect these individual bars together in the form of an elastic network, which will allow us to study their effective elastic properties. We start by considering a simple case of three bars connected as shown in Figure 2.2. The bars have initial reference lengths $L_1^0$, $L_2^0$, $L_3^0$, current lengths $l_1$, $l_2$, $l_3$, and forces $t_1$, $t_2$, $t_3$. This network has a total length of $l_\Sigma$ and a total force of $t_\Sigma$. In this setup, every bar can only deform in horizontal direction, buckling and torques are not possible. The height of the bars does not influence the physics but only serves as an illustration of the linking. The thickly drawn vertical walls balance the forces purely in horizontal direction.

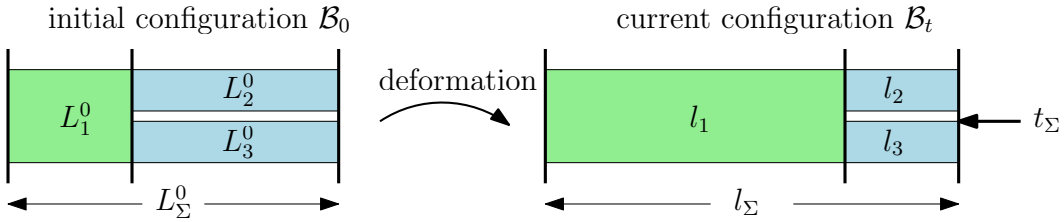


Figure 2.2: A schematic of the initial configuration $\mathcal{B}_0$ and the current configuration $\mathcal{B}_t$ of an example system with $n = 3$ bars.

We can now discuss how the individual bars of this network are connected to the effective properties of the network, i.e. its total length $l_\Sigma$ and total force $t_\Sigma$. Bars 2 and 3 are connected in parallel, and they are also connected in series with bar 1. Bars connected in parallel share the same length ($l_2 = l_3$) and bars connected in series share the same force ($t_1 = t_2 + t_3$). The length and force balance of the network is fully described by

$$l_1 + l_2 = l_\Sigma, \quad l_1 + l_3 = l_\Sigma, \quad t_1 = t_\Sigma, \quad t_2 + t_3 = t_\Sigma\,. \tag{2.5}$$

In this section, it will be our goal to present a consistent framework to describe the length and force balance of similar networks with any number of series and parallel connections. At the centre of this description are the matrices $A$ and $B$. The matrix $A$ describes how individual lengths of the bars connect to the effective length of the network. The matrix $B$ describes how individual forces add up to the effective force of

the network

In this Subsection we will define $A$ and $B$ formally, thus presenting a description of networks as algebraic equations between lengths and forces. In Subsection 2.1.3, we present a way of obtaining the matrices $A$ and $B$ through a series of horizontal and vertical cuts of a single initial bar. As the constitutive behaviour of the individual bars, eq. (2.2) allows for nonlinear couplings between length and force, a mathematical analysis of the networks presented in this section requires additional simplifying assumptions. We will discuss such simplifications and perform a mathematical analysis of both static networks ($\dot{L}_i = 0$) and growing networks ($\dot{L}_i \neq 0$) in Subsections 2.2 and 2.3, respectively.

### Notation

Let us consider a quantity $q_i$ relating to the bar with index $i$. For instance, this could be the current length $l_i$ or force $t_i$. We note that as the domain of deformation is one-dimensional, despite their different unity we use the words stress and force interchangeably in this chapter.

We denote an $n$-vector of the quantity $q_i$ with a bold letter notation as $\boldsymbol{q}$:

$$\mathbf{q} = \begin{pmatrix} q_1 \\ \vdots \\ q_n \end{pmatrix} . \tag{2.6}$$

We will frequently require this quantity in the form of an $n \times n$ diagonal matrix, which we denote by $D_q$, putting the appropriate vector quantity in the subscript:

$$D_q = \operatorname{diag}(q_1, \ldots, q_n) . \tag{2.7}$$

Furthermore, we define $\boldsymbol{v}^p$ as a $p$-vector of ones where $p$ is an integer $p < n + 1$. In components, this means that

$$v_i^p = 1 \tag{2.8}$$

for all $i \in \{1, \ldots, p\}$. For example, $\boldsymbol{v}^2 = (1, 1)^T$ and $\boldsymbol{v}^5 = (1, 1, 1, 1, 1)^T$.

### Network description

Now we consider a network of single bars. The network is described by the quantities

$$\textit{total} \text{ initial length } L_\Sigma^0, \qquad \textit{total} \text{ reference length } L_\Sigma, \quad \text{and} \quad \textit{total} \text{ current length } l_\Sigma \,. \tag{2.9}$$

These quantities are defined further below in terms of the initial, reference and current lengths of the individual bars (see (2.1)). The geometric connections are described by a matrix $A$ and the force connections by matrix $B$, which are matrices of ones and zeros,

$$A \in \{0,1\}^{r\times n}\,, \qquad B \in \{0,1\}^{s\times n}\,, \tag{2.10}$$

that is $A$ and $B$ are matrices of zeros and ones which satisfy the following relationship:

$$r + s = n + 1\,. \tag{2.11}$$

The matrices $A$, $B$ satisfy the following linear systems:

$$l_\Sigma = \sum_{j=1}^{n} A_{ij} l_j \quad \forall i \in \{1,\dots,r\} \quad \text{and} \quad t_\Sigma = \sum_{j=1}^{n} B_{ij} t_j \quad \forall i \in \{1,\dots,s\}\,. \tag{2.12}$$

Note that the subscript $\Sigma$ refers to the summation over any given row of the network. The entries of all matrix coefficients are either 0 or 1, that is $A_{ij} \in \{0,1\}$ and $B_{ij} \in \{0,1\}\,\forall i,j$. Alternatively, we can write the linear systems (2.12) in matrix form as

$$A\boldsymbol{l} = l_\Sigma \boldsymbol{v}^r \quad \text{and} \quad B\boldsymbol{t} = t_\Sigma \boldsymbol{v}^s \tag{2.13}$$

where $\boldsymbol{v}$ is defined in (2.8).

The equations $(2.12)_1$ and $(2.13)_1$ show how the *total* current length $l_\Sigma$ of the network is a sum of all current lengths $l_i$ of the individual bars over a given row of the network. A similar summation holds for the total initial length $L_\Sigma^0$, which is the sum over all initial lengths $L_i^0$ of individual bars:

$$A\boldsymbol{L}^0 = L_\Sigma^0 \boldsymbol{v}^r. \tag{2.14}$$

A reference length $L_\Sigma$ will be defined further below.

When considering a network, there is a simple rule to connect the formal notation laid out in this section with intuition. The matrix $A$ can be obtained by summing up the lengths of individual bars for every individual row. Similarly, the matrix $B$ can be obtained by evaluating the force balance at every force transmitting (i.e. vertical) wall. Throughout this chapter, such force transmitting walls are highlighted as bold vertical lines in drawings.

We can now return to the three bar example presented in Figure 2.2 and re-interpret the system through the formalism developed here. The matrices $A$ and $B$ for the three bar example are

$$A = \begin{pmatrix} 1 & 1 & 0 \\ 1 & 0 & 1 \end{pmatrix}, \qquad B = \begin{pmatrix} 1 & 0 & 0 \\ 0 & 1 & 1 \end{pmatrix}. \tag{2.15}$$

As can be easily verified, the linear systems (2.13) reproduce the force and length balance (2.5).

### 2.1.3 Constructing networks through cutting a single bar multiple times

This section explores construction rules that give rise to networks consistent with the description in the previous section. Consider, for instance, the network presented in Figure 2.3.

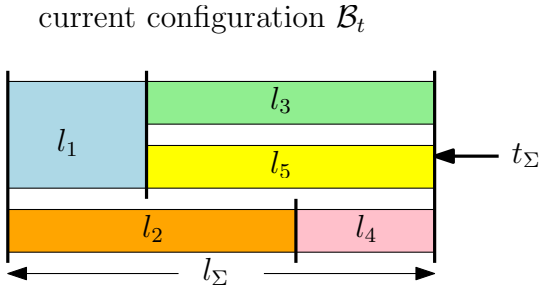


Figure 2.3: Network with $n = 5$ bars.

By following the rules of the previous section, we can construct the matrices $A$ and

$B$ for this network:

$$A = \begin{pmatrix} 1 & 0 & 1 & 0 & 0 \\ 0 & 1 & 0 & 1 & 0 \\ 1 & 0 & 0 & 0 & 1 \end{pmatrix}, \qquad B = \begin{pmatrix} 1 & 1 & 0 & 0 & 0 \\ 0 & 1 & 1 & 0 & 1 \\ 1 & 0 & 0 & 1 & 0 \end{pmatrix}. \tag{2.16}$$

This is an $n = 5$ bar network. The matrices $A$ and $B$ for larger networks quickly become very cumbersome to assemble manually. In this Section, we change the viewpoint: How can a network like (2.16) be obtained from simple construction principles? At the centre of our approach is the idea of cutting a single elementary network element, i.e. a single bar, into pieces. More specifically, we cut a single bar with $n - 1$ subsequent cuts, to obtain a network with $n$ bars in total. Every cut is either horizontal or vertical. We formalise this idea of cuts by defining maps that append columns and rows to the matrices $A$ and $B$ depending on the type of cut (horizontal or vertical). To do this, we first make precise the notion of adding a column and appending a row in this particular context, and then show how these maps are integrated to form maps that define cuts. In Figure 2.3, we demonstrate a step by step cutting process which begins with one original bar 2.4 and produces the network (2.16). In Figure 2.3 at every step of the iteration we provide a visual representation of the network (similarly to Figure 2.3) as well as the matrices $A$ and $B$.

We end this section with a note about degrees of freedom of the kinematic description of such networks which are *not* included in $A$ and $B$. These degrees of freedom are the initial reference lengths of the bars, of which $n - r$ are independent. We provide an example of an $n = 7$ network with given matrices $A$ and $B$ and demonstrate two initial reference configurations compatible with this network.

### Notation setup

We consider an $m \times n$ matrix

$$M \in \{0, 1\}^{m \times n} . \tag{2.17}$$

We also introduce the indices

$$a \in \{1, 2, \ldots, m + 1\} \qquad \text{and} \qquad b \in \{1, 2, \ldots, n + 1\} \tag{2.18}$$

which we use to label matrix elements, as well as the fixed indices

$$p \leq m, \quad k \leq n \tag{2.19}$$

which are not summed over and which label a specific fixed row ($p$) and column ($k$). In the next subsection, we use these conventions to define operations on $A$ and $B$, which will be used to define cutting operations (as described above) in the Section thereafter, thus giving the basic building blocks to generate networks.

### Matrix operations

**Add column** We introduce a map $C_k(M)$ which duplicates the $k$-th column of $M$, thus producing a matrix $\tilde{M}$ with $n+1$ columns:

$$\begin{aligned} C_k : \{0,1\}^{m\times n} &\rightarrow \{0,1\}^{m\times(n+1)} \\ M &\mapsto \tilde{M} = C_k(M) \end{aligned}$$

where $\tilde{M} = C_k(M)$ is defined as follows:

$$\tilde{M}_{ab} = \begin{cases} M_{ab} & \text{for } a = 1,\ldots,m+1;\ b = 1,\ldots,n \\ M_{ak} & \text{for } a = 1,\ldots,m+1;\ b = n+1 \end{cases} . \tag{2.20}$$

In matrix block notation, this can be expressed as

$$\tilde{M}_{ab} = \left( M_{ab} \,|\, M_{ak} \right) . \tag{2.21}$$

Example: Application of $C_k$

$$M = \begin{pmatrix} 1 & 0 \\ 0 & 1 \end{pmatrix}, \qquad C_1(M) = \begin{pmatrix} 1 & 0 & 1 \\ 0 & 1 & 0 \end{pmatrix}, \qquad C_2(M) = \begin{pmatrix} 1 & 0 & 0 \\ 0 & 1 & 1 \end{pmatrix} . \tag{2.22}$$

**Add row** We introduce a map $R_k(M)$ which duplicates the $p$-th row of $M$. The index $p$ is a function of the column number $k$, and $p$ is defined as the lowest value of $a$

for which $M_{ak}$ is 1:

$$p = \min \{a \in \{1, 2, \ldots, m\} \, | M_{ak} = 1\} \, . \tag{2.23}$$

The map $R_k(M)$ produces a matrix $\tilde{M}$ with $m+1$ rows and $n+1$ columns:

$$\begin{aligned} R_k : \{0,1\}^{m \times n} &\rightarrow \{0,1\}^{(m+1)\times(n+1)} \\ M &\mapsto \tilde{M} = R_k(M) \end{aligned} \tag{2.24}$$

where $\tilde{M} = R_k(M)$ is defined as follows:

$$\tilde{M}_{ab} = \begin{cases} M_{ab} & \text{for } a = 1, \ldots, m;\ b = 1, \ldots, n \\ M_{pb}(1 - \delta_{bk}) & \text{for } a = m+1;\ b = 1, \ldots, n \\ \delta_{a,\, m+1} & \text{for } a = 1, \ldots, m+1;\ b = n+1 \end{cases} \tag{2.25}$$

where $\delta$ is the Kronecker Delta. In matrix block notation, this can be expressed as

$$\tilde{M}_{ab} = \left( \begin{array}{c|c} \multirow{2}{*}{$M_{ab}$} & \begin{matrix} 0 \\ \vdots \\ 0 \end{matrix} \\ & \\ \hline M_{pb}(1 - \delta_{bk}) & 1 \end{array} \right) . \tag{2.26}$$

Example: Application of $R_k$

We consider the following matrix $M$:

$$M = \begin{pmatrix} 1 & 1 & 0 \\ 0 & 1 & 1 \end{pmatrix} . \tag{2.27}$$

In the following results for $R_1(M)$, $R_2(M)$ and $R_3(M)$ we highlight with a small box the pivotal element $\tilde{M}_{pk}$, where $p$ is computed according to (2.23).

$$R_1(M) \overset{p=1}{=} \begin{pmatrix} \boxed{1} & 1 & 0 & 0 \\ 0 & 1 & 1 & 0 \\ 0 & 1 & 0 & 1 \end{pmatrix}, \qquad R_2(M) \overset{p=1}{=} \begin{pmatrix} 1 & \boxed{1} & 0 & 0 \\ 0 & 1 & 1 & 0 \\ 1 & 0 & 0 & 1 \end{pmatrix}, \tag{2.28}$$

$$R_3(M) \overset{p=2}{=} \begin{pmatrix} 1 & 1 & 0 & 0 \\ 0 & 1 & \boxed{1} & 0 \\ 0 & 1 & 0 & 1 \end{pmatrix} . \tag{2.29}$$

### Network operations

Networks are generated by taking a single bar and cutting it horizontally or vertically. To increase the number of network elements, it is necessary to decide which bar to operate on, and whether the operation is a horizontal or vertical cut. The definition of these cuts relies on the maps $C_k$ and $R_k$ introduced in the previous section.

The vertical cut of the $k$-th network element (i.e. $k$-th bar) is the map $V_k(A, B)$, which is defined as

$$V_k : \{A, B\} \;\mapsto\; \{C_k(A), R_k(B)\} . \tag{2.30}$$

In other words, $V_k$ take takes the network composition (stored in $A$ and $B$) and applies a column addition map (as defined in eq. 2.20) to $A$ and a row addition map (as defined in eq. 2.25) to $B$.

The horizontal cut of the $k$-th bar $H_k(A, B)$ reverses this relationship, applying

row addition to $A$ and column addition to $B$:

$$H_k : \{A, B\} \quad \mapsto \quad \{R_k(A), C_k(B)\} \,. \tag{2.31}$$

**Application to an example network**

We now return to our original example at the top of this subsection in Figure 2.3. The network operations (2.30) and (2.31) provide us with the tools to express the five bar network as a series of four cuts. To show how this works, let us first consider a single morphoelastic bar expressed in the networks formalism: It simply reads $A = (1)$, $B = (1)$. In terms of the horizontal and vertical cut maps (eq. 2.30 and 2.31, respectively) we can obtain the network from Figure 2.3 as

$$H_3 \circ V_2 \circ V_1 \circ H_1 (A, B) \,. \tag{2.32}$$

Every step of the composition, that is $H_1(A, B)$, $V_1 \circ H_1(A, B)$ etc. is shown in Figure 2.4. The network is given in terms of $A$ and $B$ at every step, and also in visual form. Note that the pivot $p$ (2.23) is also shown at every step.

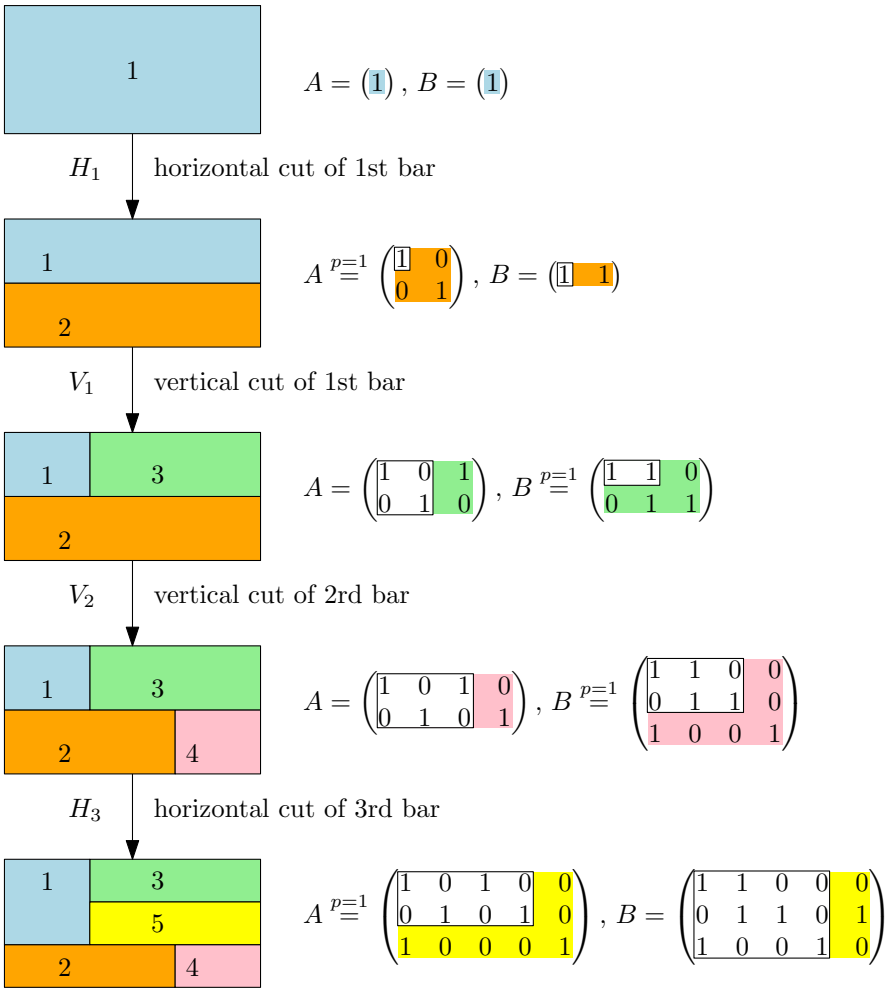


Figure 2.4: Every cut adds a new cell, which we draw in a new colour. The part of the matrices $A$, $B$ which contains information on the new bar is highlighted in the same color, whereas the unchanged part of the matrix is shown in a white box. Note that the final result is consistent with (2.16).

### Input and output variables for full kinematic and mechanical description of networks

The result (2.14) provides a description of the force and length balance of networks in a mechanical equilibrium. Here, we briefly describe what the input and output variables are, and which constraints they are subjected to.

**Inputs and outputs** The kinematic input parameters are $n$ initial reference lengths $L_i^0 > 0$ and $n$ post-grown reference lengths $L_i > 0$ for $i = 1, \dots, n$. As we note below, however, only $n - r$ of the $L_i^0$ are independent. The mechanical input parameters are the Young's Modulus values $\mu_i > 0$ for $i = 1, \dots, n$. Finally, to close the system, we require a functional relationship between the total length of the system $l_\Sigma$ and its stress

at the boundary $t_\Sigma$. The most common boundary conditions are prescribed length $l_\Sigma$, or alternatively prescribed pressure $t_\Sigma = P$ at the boundary. With the constitutive relationships (2.2), we can compute the current lengths $l_i$ for $i = 1, \ldots, n$ of the system, which automatically satisfy (2.13).

**Constraints on initial lengths** The input variables are the $n$ initial reference lengths $\boldsymbol{L}^0$ which must satisfy the $r$ constraints (2.14), which ensures that the lengths are compatible (i.e. all network rows have the same length). This leaves $n - r$ of the $L_i > 0$ independent. To illustrate this point, we consider the following example.

**Example: Sampling initial reference values for a 7 bar network**

Consider an $n = 7$ bar system,

$$A = \begin{pmatrix} 1 & 0 & 0 & 1 & 1 & 1 & 0 \\ 1 & 0 & 0 & 1 & 1 & 0 & 1 \\ 0 & 1 & 0 & 1 & 1 & 0 & 1 \\ 0 & 0 & 1 & 1 & 1 & 0 & 1 \end{pmatrix}. \tag{2.33}$$

For this system, $r = 4$. Through Gaussian elimination, identify the $n - r = 3$ independent variables as $L_1^0$, $L_4^0$, $L_5^0$: which have the following dependence to the remaining unknowns:

$$L_2^0 = L_1^0, \quad L_3^0 = L_1^0, \quad L_6^0 = L_\Sigma^0 - L_1^0 - L_4^0 - L_5^0, \quad L_7^0 = L_\Sigma^0 - L_1^0 - L_4^0 - L_5^0. \tag{2.34}$$

The following two configurations are compatible with these constraints:

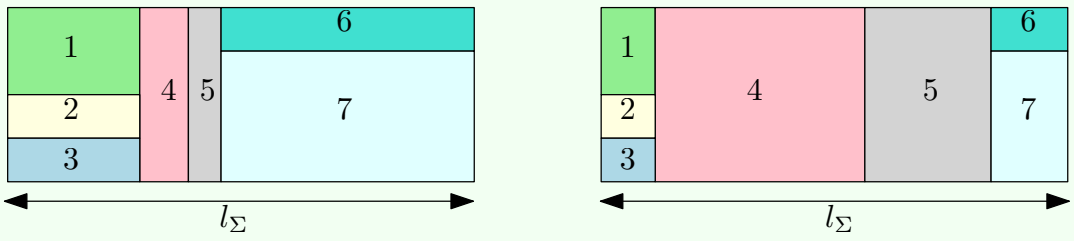

## 2.2 Linear Analysis of static networks

### 2.2.1 Small deformations

In this Section, we focus on small deformations of the static network, i.e. deformations close to its (unstressed) initial reference state. This will allow us to formulate a single linear system which describes the static network completely, taking into account both the geometric constraints and the mechanical constraints (see eq. 2.13). The benefit of such an analysis is the possibility to formulate a homogenisation theory for this system, i.e. treating the elastic network as one single entity with an effective length and an effective stress. In fact, the linear formulation allows to relate the effective length and force in a constitutive law which is analogous to Hooke's Law for the effective, homogenised network.

A powerful aspect of the linear treatment is that the elastic network can be analysed from two perspectives, which mutually enrich each other. We first take an algebraic perspective, which allows us to compute the effective properties of the network (the effective Young's Modulus $\mu_\Sigma$ and effective unloaded length $L_\Sigma$) as functions of the network connections $A$, $B$ and its boundary conditions $l_\Sigma$, $t_\Sigma$. This analysis naturally leads to a particular choice of a reference configuration for the homogenised network, which we call the unloaded configuration. The unloaded configuration is residually stressed, but unstressed at its boundaries (unloaded).

We explore another perspective to analysing the linear elastic network, which is based on induction, and shares strong analogies with how electric circuits are traditionally studied. The idea here is to isolate a connection of two bars in series, as well as a connection of two bars in parallel. Computing the effective quantities based on such a pair of bars reveals a rule for that can be applied recursively to the whole network. A similar problem appears in the study of electric networks, specifically networks with resistors and batteries. A series connection of resistors can be treated as one effective resistance, with a resistance value equal to the sum of the individual resistance values. Similarly, in a parallel connection, the effective resistance is calculated from a reciprocal sum of individual resistances. In this Section we show how these ideas apply to elastic networks, make explicit the analogy between electric circuits (described by voltage, current and resistance) and elastic networks (described by length, force and

Young's Modulus) and show how the unloaded reference configuration (which we discuss explicitly in the context of our algebraic approach) naturally re-appears in this induction based approach.

**Kinematics**

We now consider the deformations of all individual bars to be small, in the sense that their current length $l_i$ and reference length $L_i$ are close to their initial length $L_i^0$:

$$l_i = L_i^0 + \varepsilon \tilde{l}_i + \mathcal{O}\left(\varepsilon^2\right) \quad \text{and} \quad L_i = L_i^0 + \varepsilon \tilde{L}_i + \mathcal{O}\left(\varepsilon^2\right) \tag{2.35}$$

where $\varepsilon \ll 1$ is a small parameter, and the quantities

$$\text{reference displacement } \tilde{L}_i \quad \text{and} \quad \text{current displacement } \tilde{l}_i \tag{2.36}$$

of the $i$-th bar. As the individual bars are close to their respective initial lengths, we assume the same for the total network, which means that its *total* reference length $L_\Sigma$ and total current length $l_\Sigma$ are close to the total initial length $L_\Sigma^0$ defined in (2.14):

$$L_\Sigma = L_\Sigma^0 + \varepsilon \tilde{L}_\Sigma + \mathcal{O}\left(\varepsilon^2\right) \quad \text{and} \quad l_\Sigma = L_\Sigma^0 + \varepsilon \tilde{l}_\Sigma + \mathcal{O}\left(\varepsilon^2\right) \tag{2.37}$$

where we have introduced the

$$\textit{total} \text{ reference displacement } \tilde{L}_\Sigma \quad \text{and} \quad \textit{total} \text{ current displacement } \tilde{l}_\Sigma\,. \tag{2.38}$$

We note that the the linear system $(2.12)_1$ allows us to write the total current length of the network in terms of the current lengths of the individual bars. By using the expansion $(2.35)_1$ and $(2.37)_2$, we can similarly define the total current displacement in terms of individual current displacements

$$A\tilde{\boldsymbol{l}} = \tilde{l}_\Sigma \boldsymbol{v}^r\,. \tag{2.39}$$

**Mechanics**

Given the assumption of small displacements presented in the previous subsection, the stresses of individual bars are

$$t_i = h_i\left(\frac{l_i}{L_i}\right) = \varepsilon\mu_i\left(\frac{\tilde{l}_i - \tilde{L}_i}{L_i^0}\right) + \mathcal{O}\left(\varepsilon^2\right) \tag{2.40}$$

where we used the property $h_i(1) = 0$ of constitutive relationships, as well as Young's Modulus $\mu_i = h_i'(1)$. We also define the modified Young's Modulus

$$\tilde{\mu}_i = \frac{\mu_i}{L_i^0}. \tag{2.41}$$

In analogy with (2.36), we define a linearised force

$$\tilde{t}_i = \tilde{\mu}_i\left(\tilde{l}_i - \tilde{L}_i\right). \tag{2.42}$$

This is a Hookean stress-strain relationship, which is offset by a reference displacement $\tilde{L}_i$ due to growth. For simplicity, we will refer to this simply as Hooke's Law.

In analogy to the total current displacement (2.39), we define a total small force as

$$B\tilde{\boldsymbol{t}} = \tilde{t}_\Sigma \boldsymbol{v}^s. \tag{2.43}$$

### 2.2.2 A homogenised Hooke's Law for networks

As we have seen previously, for small deformations of individual bars the stress-strain relationship is (2.42). In this Section, we establish a homogenised Hooke's Law, which approximates the network's effective stress response $\tilde{t}_\Sigma$ to a displacement $\tilde{l}_\Sigma$:

$$\tilde{t}_\Sigma = \tilde{\mu}_\Sigma\left(\tilde{l}_\Sigma - \tilde{L}_\Sigma\right) \tag{2.44}$$

It has the same form as Hooke's Law for an individual bar (2.42) if one replaces the index $i$ of an individual bar by the subscript $\Sigma$ denoting the effective system. Previously, we defined effective stress response $\tilde{t}_\Sigma$ in (2.43) and the effective displacement $\tilde{l}_\Sigma$ in (2.39). However, the form of the effective reference length $\tilde{L}_\Sigma$ and effective Young's Modulus $\tilde{\mu}_\Sigma$ for a given network are not clear at this point. We will define these quantities as functions of the other network properties. This will allow us to return to the example network introduced in Figure 2.2 and compute its effective Hooke's Law.

We now consider the linear systems (2.12) and rewrite them in terms of current

displacement and small force:

$$A\tilde{\boldsymbol{l}} = \tilde{l}_\Sigma \boldsymbol{v}^r \quad \text{and} \quad BD_{\tilde{\mu}}\tilde{\boldsymbol{l}} = \tilde{t}_\Sigma \boldsymbol{v}^s + BD_{\tilde{\mu}}\tilde{\boldsymbol{L}}\,. \tag{2.45}$$

This allows us to write a single linear system

$$M\tilde{\boldsymbol{l}} = \boldsymbol{m} \tag{2.46}$$

where the matrix $M$ and vector $\boldsymbol{m}$ are of the following dimensions:

$$M \in \mathbb{R}^{(n+1)\times n} \quad \text{and} \quad \boldsymbol{m} \in \mathbb{R}^{n+1}\,. \tag{2.47}$$

The matrix $M$ is defined as

$$M = \begin{pmatrix} A \\ BD_{\tilde{\boldsymbol{\mu}}} \end{pmatrix} \quad \text{and} \quad \boldsymbol{m} = \begin{pmatrix} \tilde{l}_\Sigma \boldsymbol{v}^r \\ \tilde{t}_\Sigma \boldsymbol{v}^s + BD_{\tilde{\boldsymbol{\mu}}} D_{\tilde{\boldsymbol{L}}} \end{pmatrix} \tag{2.48}$$

Note that unlike $A$ and $B$, some entries of $M$ and $\boldsymbol{m}$ are dimensional. According to Fredholm's Alternative, for a solution of $M\tilde{\boldsymbol{l}} = \boldsymbol{m}$ to exist, there must exist an $n+1$ dimensional null space vector $\boldsymbol{\xi}$ such that $M^T\boldsymbol{\xi} = 0$, from which it follows that

$$\boldsymbol{\xi} \cdot \boldsymbol{m} = 0\,. \tag{2.49}$$

This condition, which establishes an equation between the applied small force $\tilde{t}_\Sigma$ and the displacement of the network $\tilde{l}_\Sigma$, plays the role of Hooke's Law for the elastic network.

The null space vector $\boldsymbol{\xi}$ has the dependence $\xi_i = \xi_i\,(A, B, \tilde{\boldsymbol{\mu}})$. We can evaluate the scalar product (2.49) explicitly:

$$0 = \boldsymbol{\xi} \cdot \boldsymbol{m} = \tilde{l}_\Sigma \left( \sum_{k=1}^{r} \xi_k \right) + \tilde{t}_\Sigma \left( \sum_{k=r+1}^{n+1} \xi_k \right) + \sum_{k=r+1}^{n+1} \xi_k \left( \sum_{j=1}^{n} B_{k-r,\,j} \tilde{\mu}_j \tilde{L}_j \right)\,. \tag{2.50}$$

This result is consistent with Hooke's Law in the form (2.44) and allows us to identify the effective Young's Modulus $\tilde{\mu}_\Sigma$ and effective reference displacement $\tilde{L}_\Sigma$

$$\tilde{\mu}_\Sigma = -\frac{\sum_{k=1}^{r} \xi_k}{\sum_{k=r+1}^{n+1} \xi_k}, \qquad \tilde{L}_\Sigma = -\frac{\sum_{k=r+1}^{n+1} \xi_k \left( \sum_{j=1}^{n} B_{k-r,\,j} \tilde{\mu}_j \tilde{L}_j \right)}{\sum_{k=1}^{r} \xi_k}\,. \tag{2.51}$$

To provide some intuition for how $\tilde{\mu}$ and $\tilde{L}_\Sigma$ are computed for a given network, we return to the example network introduced in Figure 2.2 and compute its effective Hooke's Law.

**Effective Hooke's Law for an example network**

For the system presented in Figure 2.2, the matrices $A$ and $B$ are given in (2.15). With this in mind, the $M$ and $\boldsymbol{m}$ can be computed by evaluating (2.48):

$$M = \begin{pmatrix} 1 & 1 & 0 \\ 1 & 0 & 1 \\ \tilde{\mu}_1 & 0 & 0 \\ 0 & \tilde{\mu}_2 & \tilde{\mu}_3 \end{pmatrix}, \qquad \boldsymbol{m} = \begin{pmatrix} \tilde{l}_\Sigma \\ \tilde{l}_\Sigma \\ \tilde{t}_\Sigma + \tilde{\mu}_1 \tilde{L}_1 \\ \tilde{t}_\Sigma + \tilde{\mu}_2 \tilde{L}_2 + \tilde{\mu}_3 \tilde{L}_3 \end{pmatrix} \tag{2.52}$$

The null space vector $\boldsymbol{\xi}$ which satisfies $\boldsymbol{\xi} \cdot \boldsymbol{m} = 0$ is

$$\boldsymbol{\xi} = \left( -\tilde{\mu}_2, -\tilde{\mu}_3, -\frac{-\tilde{\mu}_2 - \tilde{\mu}_3}{\tilde{\mu}_1}, 1 \right). \tag{2.53}$$

With this knowledge, the effective Young's Modulus $\tilde{\mu}_\Sigma$ and effective reference length $\tilde{L}_\Sigma$ can be obtained from (2.51):

$$\boxed{\tilde{\mu}_\Sigma = \frac{\tilde{\mu}_1 \left( \tilde{\mu}_2 + \tilde{\mu}_3 \right)}{\tilde{\mu}_1 + \tilde{\mu}_2 + \tilde{\mu}_3}} \quad \text{and} \quad \tilde{L}_\Sigma = \tilde{L}_1 + \frac{\tilde{\mu}_2 \tilde{L}_2}{\tilde{\mu}_2 + \tilde{\mu}_3} + \frac{\tilde{\mu}_3 \tilde{L}_3}{\tilde{\mu}_2 + \tilde{\mu}_3}. \tag{2.54}$$

This provides all the pieces needed to obtain the effective Hooke's Law of the network given by (2.44).

### 2.2.3 Unloaded reference configuration

In this Section we re-visit the morphoelastic decomposition $\boldsymbol{F} = \boldsymbol{AG}$, and how it applies to the specific demands of our homogenisation problem. For this, we consider the schematic 2.5. In an elastic network, the initial, post-grown and current configurations correspond to Figure 2.5(a), (b) and (d). These are perfectly in line with the configurational picture drawn and explained in the introductory section. However, since our goal is to describe the effective system as a morphoelastic single bar, we require a suitable post-grown virtual configuration for the effective bar. The traditional morphoelastic

post-grown configuration $\mathcal{B}_r$ (see Figure 2.5b) is incompatible and can therefore not satisfy this role.

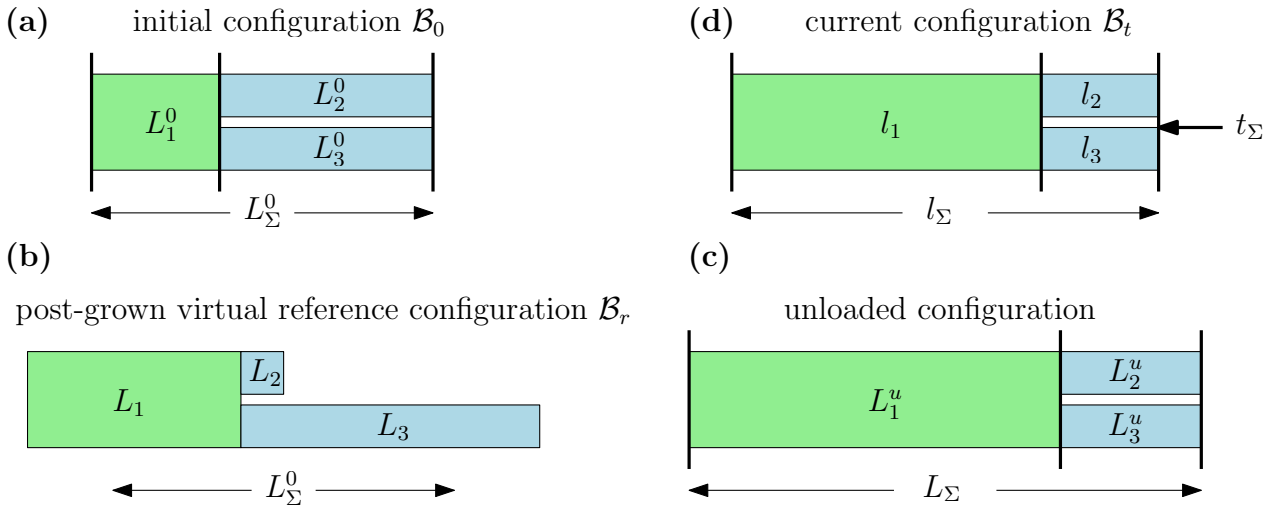


Figure 2.5: Schematic drawings of the various configurations explained in the text. **(a)** The initial reference configuration is unloaded and unstressed. **(b)** The virtual reference configuration is unloaded and unstressed. In general, it is also incompatible with the boundary conditions of the system. **(c)** The unloaded configuration is residually stressed if growth is present, i.e. $L_i \neq 0$. **(d)** The current configuration is physically realised. In general it is both residually stressed and loaded (i.e. exposed to a pressure at the boundary, $t_\Sigma = P$).

To provide a compatible reference configuration, we define the unloaded configuration as the post-grown compatible configuration 2.5(d), which in the presence of growth will in general be residually stressed. The lengths of individual bars in this configuration is denoted by $L_i^u$ for $i = 1, \ldots, n$. Their sum for every is $L_\Sigma$:

$$A\boldsymbol{L}^u = L_\Sigma \boldsymbol{v}^r \,. \tag{2.55}$$

The unloaded reference length provides a helpful quantity to understand the relationship between growth and residual stress in the context of Hooke's Law (2.44). We note that according to (2.51), if the system is not grown, $L_i^0 = L_i$ and $L_\Sigma^0 = L_\Sigma$, that is the initial reference configuration and the unloaded configuration coincide. In this particular case, Hooke's law reduces to

$$\tilde{t}_\Sigma = \tilde{\mu}_\Sigma \tilde{l}_\Sigma \,. \tag{2.56}$$

In this case, when the current deformation vanishes ($\tilde{l}_\Sigma = 0$), there is no force at the boundary of the network ($\tilde{t}_\Sigma$). On the other hand, when growth is present ($L_i^0 \neq L_i$ and $L_\Sigma^0 \neq L_\Sigma$), the effective system (2.44) is stress-free at the boundary (also called "unloaded") in the presence of a nonzero current deformation,

$$l_\Sigma = L_\Sigma. \tag{2.57}$$

This statement defines the unloaded configuration presented in 2.5(d). This configuration is a well-defined virtual configuration for the homogenised system and has a clear role in Hooke's law to introduce residual stress.

### 2.2.4 An iterative approach to computing effective network quantities

This section introduces an alternative approach to computing effective properties of a static linear network. In the previous Section, we computed the effective network quantities $\mu_\Sigma$ (Young's Modulus) and $L_\Sigma$ (length of unloaded system) by integrating all available information about the network ($A$, $B$, $\mu_i$ and $L_i^0$ for all $i = 1 \dots n$) in one single step.The present section provides an alternative way of computing the effective quantities based on an iterative approach. This method is inspired by the study of electrical networks, to which we establish a formal analogy in a Section to establish the computation of effective length and Young's Modulus between any two bars for both connection types (series and parallel), which we do in the next subsections on parallel and series connections. These rules can then be recursively applied to every subsystem in the network, producing the effective quantities $\tilde{\mu}_\Sigma$ and $\tilde{L}_\Sigma$, which we discuss in the subsection thereafter. We end this section by applying these rules to the network given in Figure 2.2. We will show that the results match our previously computed the effective quantities $\tilde{\mu}_\Sigma$ and $\tilde{L}_\Sigma$ from (2.54).

**Series connections**

We consider a setup of two bars connected in series, with current displacements $\tilde{l}_1$ and $\tilde{l}_2$, and total current displacement

$$\tilde{l}_\Sigma = \tilde{l}_1 + \tilde{l}_2 \,. \tag{2.58}$$

Similarly, the bars have reference displacements $\tilde{L}_1$ and $\tilde{L}_2$, as well as a total reference displacement $\tilde{L}_\Sigma$ which is to be determined. The total (small) force applied to the the system is $\tilde{t}_\Sigma$, which is equal in both bars connected in series,

$$\tilde{t}_\Sigma = \tilde{t}_1 = \tilde{t}_2 \,. \tag{2.59}$$

The bars have stress-strain relationships

$$\tilde{t}_1 = \tilde{\mu}_1 \left( \tilde{l}_1 - \tilde{L}_1 \right) \quad \text{and} \quad \tilde{t}_2 = \tilde{\mu}_2 \left( \tilde{l}_2 - \tilde{L}_2 \right) . \tag{2.60}$$

We also postulate that the total system has the same form of stress-strain relationship,

$$\tilde{t}_\Sigma = \tilde{\mu}_\Sigma \left( \tilde{l}_\Sigma - \tilde{L}_\Sigma \right) , \tag{2.61}$$

and it is our goal to find $\tilde{\mu}_\Sigma$ and $\tilde{L}_\Sigma$ for series connections.

We consider the total displacement $\tilde{l}_\Sigma = \tilde{l}_1 + \tilde{l}_2$ (see2.58). To replace replace $\tilde{l}_1$, $\tilde{l}_2$ in terms $t_1$, $\tilde{t}_2$, we rearrange (2.60) to obtain $\tilde{l}_1 = \tilde{t}_1/\tilde{\mu}_1 + \tilde{L}_1$ and $\tilde{l}_2 = \tilde{t}_2/\tilde{\mu}_2 + \tilde{L}_2$. This allows us to write the total displacement as

$$\tilde{l}_\Sigma = \tilde{l}_1 + \tilde{l}_2 = \frac{\tilde{t}_1}{\tilde{\mu}_1} + \tilde{L}_1 + \frac{\tilde{t}_2}{\tilde{\mu}_2} + \tilde{L}_2 \,. \tag{2.62}$$

Taking into account that $\tilde{t}_\Sigma = \tilde{t}_1 = \tilde{t}_2$ (see 2.59), and that $\tilde{l}_\Sigma = \tilde{t}_\Sigma/\tilde{\mu}_\Sigma + \tilde{L}_\Sigma$ (as a simple rearrangement of 2.61), we obtain

$$\tilde{l}_\Sigma = \frac{\tilde{t}_\Sigma}{\tilde{\mu}_\Sigma} + \tilde{L}_\Sigma = \underbrace{\left( \frac{1}{\tilde{\mu}_1} + \frac{1}{\tilde{\mu}_2} \right)}_{1/\tilde{\mu}_\Sigma} \tilde{t}_\Sigma + \underbrace{\tilde{L}_1 + \tilde{L}_2}_{\tilde{L}_\Sigma} . \tag{2.63}$$

This means, in summary, that

$$\boxed{\frac{1}{\tilde{\mu}_\Sigma} = \frac{1}{\tilde{\mu}_1} + \frac{1}{\tilde{\mu}_2}} \quad \text{and} \quad \boxed{\tilde{L}_\Sigma = \tilde{L}_1 + \tilde{L}_2}. \tag{2.64}$$

**Parallel connections**

This setup is similar to the previous one, except that this time two bars are connected in parallel. Their displacements satisfy

$$\tilde{l}_\Sigma = \tilde{l}_1 = \tilde{l}_2 \,. \tag{2.65}$$

Their forces satisfy

$$\tilde{t}_\Sigma = \tilde{t}_1 + \tilde{t}_2 \,. \tag{2.66}$$

The individual bars have stress-strain relationships (2.60) and we also postulate a similar stress-strain relationship for the total system (2.61). Once again our goal is to find $\tilde{\mu}_\Sigma$ and $\tilde{L}_\Sigma$ for parallel connections.

We consider the total (small) force $\tilde{t}_\Sigma = \tilde{t}_1 + \tilde{t}_2$ (see 2.66). We replace $\tilde{t}_1$, $\tilde{t}_2$ in terms $\tilde{l}_1$, $\tilde{l}_2$ by using Hooke's law for individual bars (see 2.60). This allows us to write the total force as

$$\tilde{t}_\Sigma = \tilde{t}_1 + \tilde{t}_2 = \tilde{\mu}_1 \left(\tilde{l}_1 - \tilde{L}_1\right) + \tilde{\mu}_2 \left(\tilde{l}_2 - \tilde{L}_2\right) . \tag{2.67}$$

Taking into account that $\tilde{l}_\Sigma = \tilde{l}_1 = \tilde{l}_2$ (see 2.65), and that $\tilde{t}_\Sigma = \tilde{\mu}_\Sigma \left(\tilde{l}_\Sigma - \tilde{L}_\Sigma\right)$ (see 2.61), we obtain

$$\tilde{t}_\Sigma = \tilde{\mu}_\Sigma \left(\tilde{l}_\Sigma - \tilde{L}_\Sigma\right) = \underbrace{(\tilde{\mu}_1 + \tilde{\mu}_2)}_{\tilde{\mu}_\Sigma} \tilde{l}_\Sigma - \underbrace{\left(\tilde{\mu}_1 \tilde{L}_1 + \tilde{\mu}_2 \tilde{L}_2\right)}_{\tilde{\mu}_\Sigma \tilde{L}_\Sigma} . \tag{2.68}$$

Solving for $\tilde{L}_\Sigma$, this allows us to write

$$\boxed{\tilde{\mu}_\Sigma = \tilde{\mu}_1 + \tilde{\mu}_2} \quad \text{and} \quad \boxed{\tilde{L}_\Sigma = \frac{\tilde{\mu}_1 \tilde{L}_1 + \tilde{\mu}_2 \tilde{L}_2}{\tilde{\mu}_\Sigma}} . \tag{2.69}$$

A formal analogy between electrical and elastic networks is established in Section A.2.

**A numerical example for two bars in parallel**

Here we provide a numerical example for computing effective quantities from two bars in parallel, and give the explicit lengths and Young's Modulus values for both the individual and homogenised system.

Let us consider two bars in parallel. We assume that the two bars have the same Young's Modulus,

$$\mu_1 = \mu_2 = \mu. \tag{2.70}$$

The initial reference lengths of the bars are

$$L_\Sigma^0 = L_1^0 = L_2^0 = \lambda \tag{2.71}$$

and the virtual reference lengths are

$$L_1 = 2\lambda, \qquad L_2 = \frac{\lambda}{2}. \tag{2.72}$$

Finally, the system is under external loading

$$t_1 + t_2 = P = \frac{\mu}{2} \quad \text{(tensile)}. \tag{2.73}$$

In a parallel connection, we have

$$\mu_\Sigma = 2\mu, \qquad L_\Sigma = \frac{5}{4}\lambda. \tag{2.74}$$

The current lengths are

$$l_1 = l_2 = l_\Sigma = \frac{t_\Sigma L_\Sigma^0}{\mu_\Sigma} + L_\Sigma = \left(\frac{P}{2\mu} + \frac{5}{4}\right)\lambda = \frac{3}{2}\lambda \tag{2.75}$$

The lengths of the bars (both individual and homogenised) are sketched in Figure (2.6) in their respective configurations. We note that, as expected, the total lengths of initial and current configurations in (a) and (b) coincide. As discussed in Figure 2.5, the pre-grown configuration in (a) is unstressed and incompatible, whereas the distinctly different unloaded configuration in (b) is residually stressed and compatible.

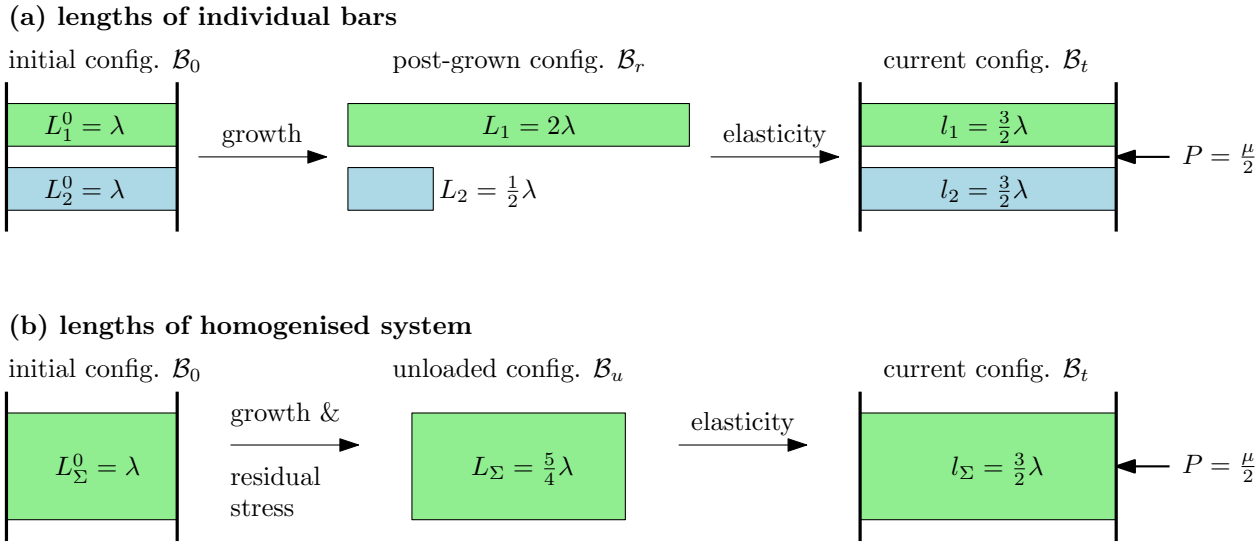


Figure 2.6: Individual and effective lengths for two bars in parallel. The first column **(a)** provides the lengths of the individual bars in initial, pre-grown and current configuration. The second column **(b)** provides the lengths of the homogenised system. Note that the configurations are initial, unloaded and current.

## 2.3 Growth of networks

In the previous sections, we formulated a framework for studying static networks. We described the connection between bars in networks through the matrices $A$ and $B$, so that the length and force balance can be given by the linear systems (2.12). The difficulty of studying such systems arises from the fact that length and force are in general non-linearly related through constitutive laws 2.2. To better understand elastic networks, we considered small deformations in which case all bars are close in lengths to the undeformed network (see (2.35), (2.37)) and in which all forces in the network are small and the constitutive laws are linear (see (2.42)). This linearisation near the undeformed state permitted us to formalise both the length and force constraints of the system into a single linear system (2.46), which lead us to a stress-strain relationship (2.49) for the entire network system which plays the role of Hooke's Law for the network.

In this section, we incorporate growth dynamics into the network. The growth dynamics is driven by a homeostasis mechanism in which the individual have growth rates which are proportional to the difference between current stress and a homeostatic stress level, which is consistent with the description of growth laws discussed in Section 1.5.4. We note that because of the one-dimensionality of the problem, we use force and

stress interchangeably in this chapter.

We pursue two major trains of thought related to growth dynamics. The first idea is related to the homogenisation of the network dynamics. In Section 2.3.4, we attempt to homogenise the growth dynamics in a similar manner to our successful homogenisation of static networks in Section 2.2.4. Given that an effective Hooke's Law allows us to describe elastic properties of the network as one effective bar, is it also possible to describe the growth dynamics of the network as the dynamics of a single bar? This question is answered in Section 2.3.4.

We also consider the stability of growth dynamics networks in Section 2.3.1. Extending the framework of networks near the undeformed state of Section 2.2, we describe the network dynamics as a linear set of ordinary differential equations and analyse the stability in detail, focusing on an example system.

### 2.3.1 Network description of growth dynamics

To describe the dynamics of the network, we assume that every bar grows according to the following growth law

$$\dot{L}_i = k_i L_i \left(t_i - t_i^*\right), \quad i = 1, \ldots, n \tag{2.76}$$

where $k_i$ are the growth rates, $t_i$ are the stresses of the bars and $t_i^*$ are the homeostatic stresses. The homeostatic stresses are assumed to satisfy the constraint $(2.13)_2$:

$$B\boldsymbol{t}^* = t_\Sigma \boldsymbol{v}^s. \tag{2.77}$$

In the growth law (2.76), the growth rate $\dot{L}_i/L_i$ of the bars is proportional to the difference between their current stress $t_i$ and their homeostatic stress $t_i^*$, which is consistent with the description of homeostasis-driven growth in Section 1.5.4. The growth law (2.76) is in general a dynamical system which is nonlinear in $L_i$ because of the nonlinear dependence of $t_i$ on $L_1, L_2, \ldots, L_n$. To make analysis of (2.76) feasible, we assume that $L_i$ and $l_i$ are in the neighborhood of the unstressed, ungrown network (see (2.35), (2.37)), which implies that the stresses are of the order of the small parameter, (see (2.40)). To ensure that the homeostatic level is consistent with small deformations

and small stresses, we require that it is

$$t_i^* = \varepsilon \tilde{t}_i^* + \mathcal{O}\left(\varepsilon^2\right). \tag{2.78}$$

The assumption of small deformations and small stresses implies that we can use the linear system (2.46) to encode all network constraints.

We impose as a boundary condition that the total length of the network $l_\Sigma$ is a prescribed constant. With the assumption of a Hookean stress-strain relationship of the network $\tilde{t}_\Sigma = \tilde{\mu}_\Sigma \left(\tilde{l}_\Sigma - \tilde{L}_\Sigma\right)$ (see (2.44)), $\boldsymbol{m}$ (see $(2.48)_2$) takes the form

$$\boldsymbol{m} = \begin{pmatrix} \tilde{l}_\Sigma \boldsymbol{v}^r \\ \tilde{\mu}_\Sigma \left(\tilde{l}_\Sigma - \tilde{L}_\Sigma\right) \boldsymbol{v}^s + B D_{\tilde{\boldsymbol{\mu}}} \tilde{\boldsymbol{L}} \end{pmatrix}. \tag{2.79}$$

The system $M\tilde{\boldsymbol{l}} = \boldsymbol{m}$ consists of $n+1$ equations of which $n$ are linearly independent. We can therefore obtain a reduced linear system in which $M$ is a full rank $n \times n$ matrix, and write $M\tilde{\boldsymbol{l}} = \boldsymbol{m}$ in the form

$$M_r \tilde{\boldsymbol{l}} = P_r \tilde{\boldsymbol{L}} + \boldsymbol{q}_r \tag{2.80}$$

where $P_r$ and $\boldsymbol{q}_r$ are constant coefficient matrices independent of $\tilde{\boldsymbol{l}}$ or $\tilde{\boldsymbol{L}}$.

As $M_r$ is invertible, it is possible to solve (2.80) for $\tilde{\boldsymbol{l}}$ and to express the stress-strain relationship (2.2) as

$$\tilde{\boldsymbol{t}} = D_{\tilde{\boldsymbol{\mu}}} \left(\tilde{\boldsymbol{l}} - \tilde{\boldsymbol{L}}\right) = D_{\tilde{\boldsymbol{\mu}}} \left[\left(M_r^{-1} P_r - 1\right) \tilde{\boldsymbol{L}} + M_r^{-1} \boldsymbol{q}_r\right]. \tag{2.81}$$

The growth dynamics (2.76) can be expressed as

$$\dot{\tilde{\boldsymbol{L}}} = S \tilde{\boldsymbol{L}} + \boldsymbol{w}, \tag{2.82}$$

where

$$S = D_k D_{L^0} D_{\tilde{\mu}} \left(M_r^{-1} P_r - 1\right) \qquad \text{and} \qquad \boldsymbol{w} = D_k D_{L^0} \left(D_{\tilde{\mu}} M_r^{-1} \boldsymbol{q}_r - \tilde{\boldsymbol{t}}^*\right). \tag{2.83}$$

We note that $S$ and $\boldsymbol{w}$ are constants. The stability of (2.82) is encoded in the eigen-

values of $S$. Note that $S$ does not depend on the homeostatic stress, suggesting that the stability of (2.82) is independent of $\tilde{t}_i^*$.

### 2.3.2 Example system: Three bar network

At the beginning of this chapter, we introduced a three bar system (see Figure 2.2). We provided the matrices $A$ and $B$ for force and length balance in (2.15), as well as the matrices $\boldsymbol{m}$ and $M$ of the linearised system (2.52).

In this section we extend the previous analysis of the network (2.15) to growth dynamics, providing $S$ and $\boldsymbol{w}$ for the system (2.83), as well as $P_r$ and $\boldsymbol{q}_r$ which are required for the construction of (2.83):

$$P_r = \frac{1}{\tilde{\mu}_1+\tilde{\mu}_2+\tilde{\mu}_3}\begin{pmatrix} 0 & 0 & 0 \\ \tilde{\mu}_1^2 & -\tilde{\mu}_1\tilde{\mu}_2 & -\tilde{\mu}_1\tilde{\mu}_3 \\ -\tilde{\mu}_1\left(\tilde{\mu}_2+\tilde{\mu}_3\right) & \tilde{\mu}_2\left(\tilde{\mu}_2+\tilde{\mu}_3\right) & \tilde{\mu}_3\left(\tilde{\mu}_2+\tilde{\mu}_3\right) \end{pmatrix},$$

$$\boldsymbol{q}_r = \frac{\tilde{l}_\Sigma}{\tilde{\mu}_1+\tilde{\mu}_2+\tilde{\mu}_3}\begin{pmatrix} \tilde{\mu}_1+\tilde{\mu}_2+\tilde{\mu}_3 \\ \tilde{\mu}_1\left(\tilde{\mu}_2+\tilde{\mu}_3\right) \\ \tilde{\mu}_1\left(\tilde{\mu}_2+\tilde{\mu}_3\right) \end{pmatrix}.$$

According to (2.83), $S$ and $\boldsymbol{w}$ can be constructed from $P_r$, $\boldsymbol{q}_r$ and $M_r$. The latter is obtained by dropping the first row in (2.52). The values of $S$ and $\boldsymbol{w}$ are

$$S = \frac{D_k D_{L^0} D_{\tilde{\mu}}}{\tilde{\mu}_1+\tilde{\mu}_2+\tilde{\mu}_3}\begin{pmatrix} -\tilde{\mu}_2-\tilde{\mu}_3 & -\tilde{\mu}_2 & -\tilde{\mu}_3 \\ -\tilde{\mu}_1 & -\tilde{\mu}_1-\tilde{\mu}_3 & \tilde{\mu}_3 \\ -\tilde{\mu}_1 & \tilde{\mu}_2 & -\tilde{\mu}_1-\tilde{\mu}_2 \end{pmatrix}, \qquad \boldsymbol{w} = \begin{pmatrix} \frac{\tilde{\mu}_1(\tilde{\mu}_2+\tilde{\mu}_3)\tilde{l}_\Sigma}{\tilde{\mu}_1+\tilde{\mu}_2+\tilde{\mu}_3} - \tilde{t}_1^* \\ \frac{\tilde{\mu}_1\tilde{\mu}_2\tilde{l}_\Sigma}{\tilde{\mu}_1+\tilde{\mu}_2+\tilde{\mu}_3} - \tilde{t}_2^* \\ \frac{\tilde{\mu}_1\tilde{\mu}_3\tilde{l}_\Sigma}{\tilde{\mu}_1+\tilde{\mu}_2+\tilde{\mu}_3} - \tilde{t}_3^* \end{pmatrix}. \tag{2.84}$$

We note that $S$ is not full rank, in fact $\operatorname{rk} S = 2$. The vector $\boldsymbol{\lambda}$ of eigenvalues of $S$ has the form

$$\boldsymbol{\lambda} = \frac{1}{-2\left(\tilde{\mu}_1+\tilde{\mu}_2+\tilde{\mu}_3\right)}\begin{pmatrix} 0 \\ \rho+\sqrt{\Delta} \\ \rho-\sqrt{\Delta} \end{pmatrix} \tag{2.85}$$

where

$$\begin{aligned}\rho := \quad & L_1^0 k_1 \tilde{\mu}_1 \left(\tilde{\mu}_2 + \tilde{\mu}_3\right) \\ & + L_2^0 k_2 \tilde{\mu}_2 \left(\tilde{\mu}_1 + \tilde{\mu}_3\right) \\ & + L_3^0 k_3 \tilde{\mu}_3 \left(\tilde{\mu}_1 + \tilde{\mu}_2\right).\end{aligned} \tag{2.86}$$

and

$$\begin{aligned}\Delta := \rho^2 - 4\tilde{\mu}_1\tilde{\mu}_2\tilde{\mu}_3 \left(\tilde{\mu}_1 + \tilde{\mu}_2 + \tilde{\mu}_3\right) \left[k_2 k_3 L_2^0 L_3^0 \right. \\ \left. + k_1 k_2 L_1^0 L_2^0 + k_1 k_3 L_1^0 L_3^0\right].\end{aligned} \tag{2.87}$$

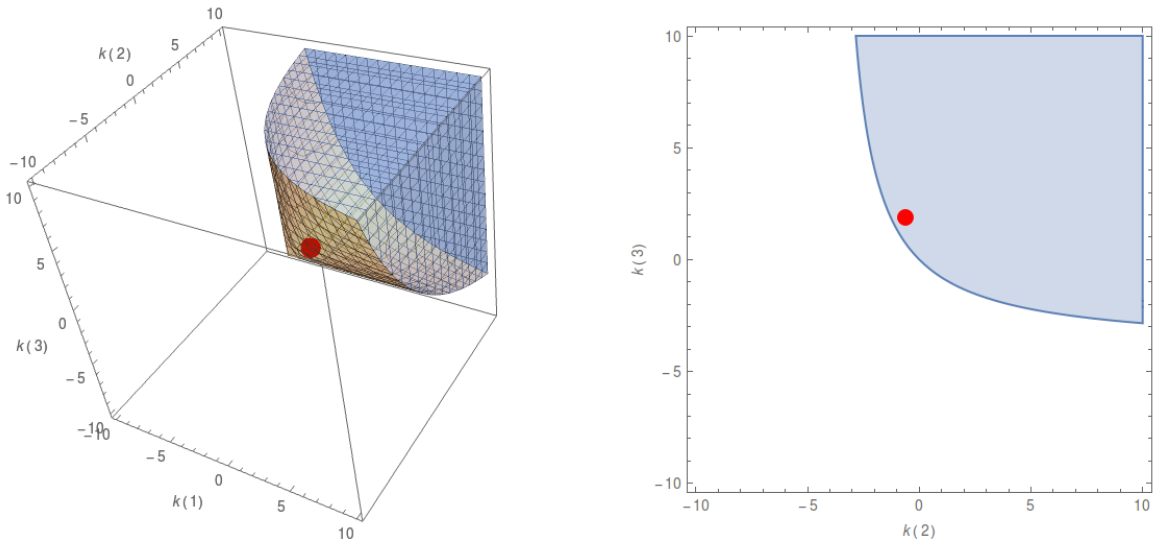


Figure 2.7: Region of $\boldsymbol{k}$-values in which the dynamics is stable, i.e. the eigenvalues of $S$ are $\lambda_1 < 0$, $\lambda_2 < 0$, $\lambda_3 = 0$ (as $\operatorname{rk} S = 2$). The red dot corresponds to the choice of $\boldsymbol{k}$ values eq. (A.5). We can see that the red point lies inside the blue region, indicating stable growth dynamics. We show the full region plot on the left hand side, and the plane $k_1 = 2.51$ (on which the point eq. A.5 lies).

We further explore the dynamics of the network (2.15) by analysing the eigenvalues of $S$ given by (2.85). Figure 2.7 shows the region of $\boldsymbol{k}$ values for which the dynamics of (2.82) is stable, i.e. $\operatorname{Re}\lambda_1 < 0$ and $\operatorname{Re}\lambda_2 < 0$ (note that $\lambda_3 = 0$ because $\operatorname{rk} S = 2$). We notice that the stability of (2.82) is highly dependent on the growth inhomogeneity of the growth law (2.76). The growth inhomogeneity is encoded in the growth rates $k_1$, $k_2$, $k_3$.

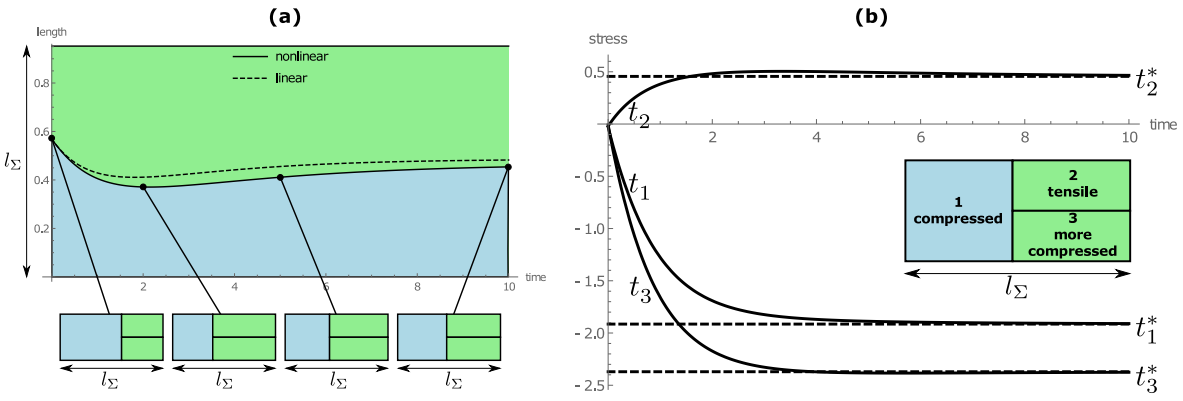


Figure 2.8: **(a)** Interface dynamics. In blue, we plot the evolution of $l_1(t) = L_1^0 + \varepsilon \tilde{l}_1$ and in green we plot $l_2(t) = l_3(t)$. The total length of the system is $l_1 + l_2 = l_1 + l_3 = l_\Sigma$, which is guaranteed by the constraint $A\tilde{\boldsymbol{l}} = \tilde{l}_\Sigma \boldsymbol{v}^r$. Notice how the linear and nonlinear solutions agree well despite the large value $\varepsilon = 0.5$. As predicted by Fig. 2.7, the dynamics is stable near the undeformed equilibrium. **(b)** We plot the nonlinear stress $t_i$ and we can see that the homeostatic stress of every individual bar is achieved ($t_1^*$ and $t_3^*$ are negative i.e. compressive, $t_2^* > 0$ is tensile).

An example trajectory of the dynamics is given in Figure 2.8(a). The trajectory is shown for values of $\boldsymbol{k}$ for which the dynamics (2.82) is stable. We note that the trajectories are non-monotonic and non-oscillatory, which we will further discuss in Section 2.3.3.

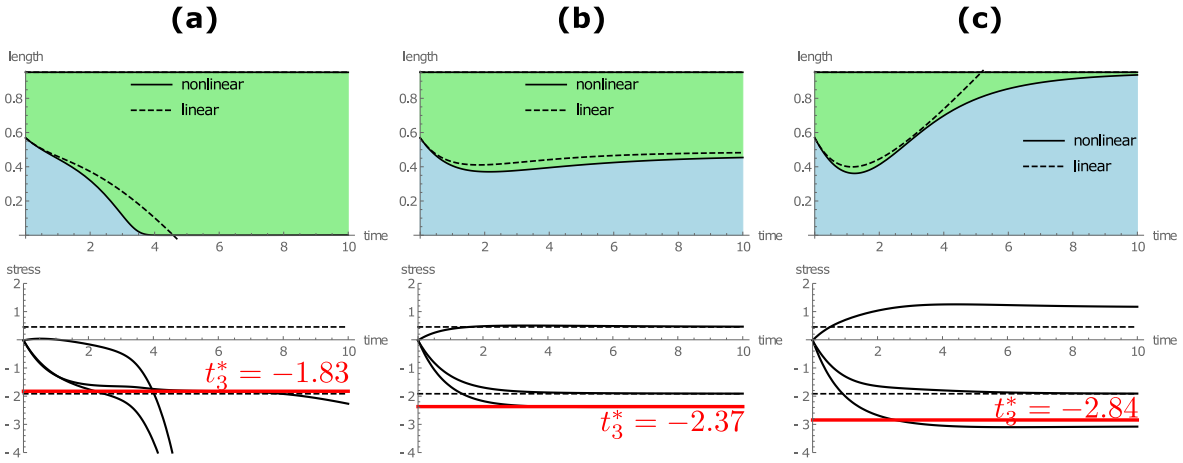


Figure 2.9: Divergent dynamics due to inadmissible homeostatic stress. Simulation parameters are provided in Section A.1.

The dashed trajectory in Figure 2.8(a) represents the linear growth dynamics according to (2.82). The linear dynamics is compared with the nonlinear case (solid line), which is computed from (2.76) with a constitutive relationship $t_i = \mu_i \log(l_i/L_i)$, see (2.2). As expected, the stresses $t_i$ converge towards their homeostatic stresses, as demonstrated in Figure 2.8(b). We note that if the homeostatic stress is not consistent

with the constraints of the network, i.e. if the homeostatic state is not a physically realisable state and (2.77) is not satisfied, the dynamics cannot converge to the homeostatic stress. In case of divergence, comparison between the linear and nonlinear solution is demonstrated in Figure 2.9. In particular, in the divergent cases either one bar takes over the whole network domain (Figure 2.9(c)) or shrinks to zero length (a). The case Figure 2.9(b) is identical with (2.8)(a).

The studies presented in Figure 2.9 and (2.8) provide an intuition for the complexity of growth dynamics for growing elastic networks for deformations in the neighborhood of the undeformed network. They also demonstrate that trajectories can be non-monotonic and raise the question of the possibility of oscillatory solutions, which we address in Section 2.3.3. The numerical values for the simulations of Figures 2.9 and (2.8) are given in Section A.1.

### 2.3.3 Can the system $\dot{\tilde{\boldsymbol{L}}} = S\tilde{\boldsymbol{L}} + \boldsymbol{w}$ have oscillatory solutions?

A natural question about the $S$ matrix is: Are oscillations possible in the dynamics of $\dot{\tilde{\boldsymbol{L}}} = S\tilde{\boldsymbol{L}} + \boldsymbol{w}$, i.e. can $S$ have imaginary eigenvalues? Given the complex algorithm in which $S$ is composed (see Subsection 2.1.3), as well as the constraint placed on the initial reference lengths (2.14), we have no way of answering this question in a straightforward analytical way. However, a numerical approach can provide some preliminary results.

In order to search for imaginary eigenvalues, we conducted a preliminary numerical study. In this study we tested if there are any imaginary eigenvalues based on randomly chosen simulation parameters for increasingly complex networks. The study was based on a total of seven different networks: One $N = 15$ bar network, one $N = 10$ bar network, one $N = 7$ bar network, two $N = 4$ bar networks and two $N = 3$ bar networks. For each network, we ran 100 simulations for a force length prescribed as well as force prescribed boundary condition each —that is, 200 simulations in total for every of the seven networks. In each simulation, the following 9 parameters were drawn from a uniform distribution:

$$L_i^0, \mu_i \in [0, 20]\,, \qquad k_i \in [-10, 10]\setminus 0 \quad \text{for} \quad i = 1, 2, 3. \tag{2.88}$$

For each simulation, the matrix $S$ was constructed and its eigenvalues were tested to have nonzero imaginary parts (any value below $10^{-12}$ was considered zero). Throughout all $7 \times 200$ simulations, not a single imaginary eigenvalue was detected. While this preliminary study cannot be considered exhaustive, its results lead us to suspect that oscillations are not possible in the system $\dot{\tilde{\boldsymbol{L}}} = S\tilde{\boldsymbol{L}} + \boldsymbol{w}$.

### 2.3.4 Inductive description of mechano-sensitive growth law

In this Section we expand the two setups for a series connection of two bars as described in Section 2.2.4, and a parallel connection of two bars described in Section 2.2.4. In these previous Sections, we obtained an effective Young's modulus $\tilde{\mu}_\Sigma$ and an effective reference length $\tilde{L}_\Sigma$ for the system of two bars connected in series and in parallel, which gives us an effective Hooke's law $\tilde{t}_\Sigma = \tilde{\mu}_\Sigma \left(\tilde{l}_\Sigma - \tilde{L}_\Sigma\right)$ to describe the system as one bar.

Here, we add a growth dynamical description to the individual bars of these connections, introducing growth rates $k_1$, $k_2$ as well as homeostatic stresses $\tilde{t}_1^*$, $\tilde{t}_2^*$ for the individual bars. We investigate whether is possible to obtain an effective growth rate $k_\Sigma$ and an effective homeostatic stress $\tilde{t}_\Sigma^*$ to describe the dynamics of one effective bar.

We assume that the growth dynamics of the two individual bars is described by the growth law

$$\dot{\tilde{L}}_1 = k_1 \left(\tilde{t}_1 - \tilde{t}_1^*\right) \quad \text{and} \quad \dot{\tilde{L}}_2 = k_2 \left(\tilde{t}_2 - \tilde{t}_2^*\right) \tag{2.89}$$

and we postulate a growth law of the same form same for the total bar,

$$\dot{\tilde{L}}_\Sigma = k_\Sigma \left(\tilde{t}_\Sigma - \tilde{t}_\Sigma^*\right) . \tag{2.90}$$

#### Series connections

We consider the same setup as described in 2.2.4, so that the addition of lengths, forces, and Hooke's law for individual and total bar (see (2.58)–(2.61)) are unchanged. The effective quantities $\tilde{\mu}_\Sigma$ and $\tilde{L}_\Sigma$ are given in (2.64).

We consider the time derivative of the total reference length $\dot{\tilde{L}}_\Sigma$, which according to (2.64) and (2.89) is

$$\dot{\tilde{L}}_\Sigma = \dot{\tilde{L}}_1 + \dot{\tilde{L}}_2 = k_1 \left(\tilde{t}_1 - \tilde{t}_1^*\right) + k_2 \left(\tilde{t}_2 - \tilde{t}_2^*\right) . \tag{2.91}$$

Given that $\tilde{t}_\Sigma = \tilde{t}_1 = \tilde{t}_2$ (see (2.59)) this can be rewritten as

$$\dot{\tilde{L}}_\Sigma = \underbrace{(k_1 + k_2)}_{k_\Sigma} \tilde{t}_\Sigma - \underbrace{\left(k_1 \tilde{t}_1^* + k_2 \tilde{t}_2^*\right)}_{k_\Sigma \tilde{t}_\Sigma^*} . \tag{2.92}$$

This means that two bars connected in series can indeed be written as one bar with growth dynamics described by (2.90), for which the effective growth rate $k_\Sigma$ and effective homeostatic stress $\tilde{t}_\Sigma^*$ are

$$\boxed{k_\Sigma = k_1 + k_2} \quad \text{and} \quad \boxed{\tilde{t}_\Sigma^* = \frac{k_1 \tilde{t}_1^* + k_2 \tilde{t}_2^*}{k_1 + k_2}} . \tag{2.93}$$

**Parallel connections**

We consider the same setup as described in 2.2.4, so that the addition of lengths and forces is described by (2.65)–(2.66). The effective quantities $\tilde{\mu}_\Sigma$ and $\tilde{L}_\Sigma$ are given in (2.69).

We consider once again the time derivative of the total reference length, $\dot{\tilde{L}}_\Sigma$, which according to (2.69) and (2.89) is

$$\dot{\tilde{L}}_\Sigma = \frac{\tilde{\mu}_1 \dot{\tilde{L}}_1 + \tilde{\mu}_2 \dot{\tilde{L}}_2}{\tilde{\mu}_\Sigma} = \frac{\tilde{\mu}_1 k_1 \left(\tilde{t}_1 - \tilde{t}_1^*\right) + \tilde{\mu}_2 k_2 \left(\tilde{t}_2 - \tilde{t}_2^*\right)}{\tilde{\mu}_\Sigma} . \tag{2.94}$$

We note that in the case of parallel connections, $\tilde{t}_\Sigma = \tilde{t}_1 + \tilde{t}_2$ (see eq. 2.66) this expression can only be reduced to the form $\dot{\tilde{L}}_\Sigma = k_\Sigma \left(\tilde{t}_\Sigma - \tilde{t}_\Sigma^*\right)$ if

$$\boxed{\tilde{\mu}_1 k_1 = \tilde{\mu}_2 k_2} . \tag{2.95}$$

In this case, $\dot{\tilde{L}}_\Sigma$ can be rewritten as

$$\dot{\tilde{L}}_\Sigma = \underbrace{\frac{\tilde{\mu}_1 k_1}{\tilde{\mu}_\Sigma}}_{k_\Sigma} [\tilde{t}_\Sigma - \underbrace{\left(\tilde{t}_1^* + \tilde{t}_2^*\right)}_{\tilde{t}_\Sigma^*}] \tag{2.96}$$

In summary, two bars connected in parallel cannot be reduced to one effective bar (in the sense (2.90)) unless the growth dynamics of individual bars (2.89) is constrained by (2.95). In this special case, the effective growth rate $k_\Sigma$ and effective homeostatic

stress $\tilde{t}^*_\Sigma$ are

$$\boxed{k_\Sigma = \frac{\tilde{\mu}_1 k_1}{\tilde{\mu}_\Sigma} = \frac{\tilde{\mu}_2 k_2}{\tilde{\mu}_\Sigma}} \quad \text{and} \quad \boxed{\tilde{t}^*_\Sigma = \tilde{t}^*_1 + \tilde{t}^*_2}. \tag{2.97}$$

We also considered the following strain-dependent growth laws: $\dot{\tilde{L}}_i = k_i \left(\tilde{L}_i - \tilde{L}^*_i\right)$ in which growth is driven by reference strain and $\dot{\tilde{L}}_i = k_i \left(\tilde{l}_i - \tilde{l}^*_i\right)$ in which growth is driven by current strain. We note that homogenisation (in the sense that microscopic and macroscopic growth law have the same form) is only possible if strong restrictions similarly to (2.97) are imposed.

## 2.4 Conclusion

In this Chapter, we have explored properties of growing elastic networks. These networks are governed by simple rules: Each row of the network must add up to the same current length, and each column must add up to the same force. Our first result concerns static networks, by which we mean that the networks do not evolve in time, but can be locally stressed if growth is present in the system. We found that for small deformations of such networks, it is possible to describe elastic properties of the network as a whole, homogenised object. This homogenised elastic bar has an effective Young's Modulus $\tilde{\mu}_\Sigma$, and (if residual stress is present in the network) an effective nonzero displacement of the unloaded configuration $\tilde{L}_\Sigma$ (if no residual stress is present, $\tilde{L}_\Sigma = 0$). This allows us to state an effective Hooke's Law for the network (we are reproducing eq. 2.44 here),

$$\tilde{t}_\Sigma = \tilde{\mu}_\Sigma \left(\tilde{l}_\Sigma - \tilde{L}_\Sigma\right) . \tag{2.98}$$

The homogenised quantities $\tilde{\mu}_\Sigma$ and $\tilde{L}_\Sigma$ can be computed from the individual network elements $\tilde{\mu}_i$, $\tilde{L}_i$ according to eq. (2.51).

This conclusion, that homogenisation of the network elements towards one effective elastic bar is possible in the form described above, can be reached from a different perspective: By looking at the two possible connections between bars (series and parallel) separately and stating rules for computing the effective Young's Modulus $\tilde{\mu}_\Sigma$ and effective displacement of the unloaded configuration $\tilde{L}_\Sigma$ for both of the two connection types as functions of the properties of individual bars. These rules can then be applied recursively to the entire network. The rules for computing the effective effective

Young's Modulus $\tilde{\mu}_\Sigma$ from a series and parallel connection, respectively, are

$$\frac{1}{\tilde{\mu}_\Sigma} = \frac{1}{\tilde{\mu}_1} + \frac{1}{\tilde{\mu}_2} \qquad \text{and} \qquad \tilde{\mu}_\Sigma = \tilde{\mu}_1 + \tilde{\mu}_2 \,. \tag{2.99}$$

We reproduced $(2.64)_1$ and $(2.69)_1$ here. The rules for computing the effective displacement of the unloaded configuration $\tilde{L}_\Sigma$ as a function of $\tilde{L}_1, \tilde{L}_2$ are similar and can be found in $2.64_2$ and $2.69_2$.

With these conclusions regarding static network in mind, we analysed the dynamics of networks, in which every individual bar is growing towards its individual homeostasis according to the growth law

$$\dot{L}_i = k_i L_i \left(t_i - t_i^*\right) \,. \tag{2.100}$$

We reproduced eq. (2.76) here. We focus on a growth law with a linear relationship between growth rate and stress, which allows us to distill its dynamics near the undeformed state into a set of ordinary differential equations for the reference displacements of individual bars

$$\dot{\tilde{\boldsymbol{L}}} = S\tilde{\boldsymbol{L}} + \boldsymbol{w} \,. \tag{2.101}$$

We reproduced eq. (2.82) here. The matrix $S$ is always a matrix of constant coefficients determined by the network, Young's Modulus and growth rates, whereas the vector $\boldsymbol{w}$ can be a function of time and encodes the boundary conditions and homeostatic stress.

We also investigate whether the dynamics near the undeformed state can produce oscillatory solutions. After a preliminary numerical study we suspect that oscillations are not possible in the system $\dot{\tilde{\boldsymbol{L}}} = S\tilde{\boldsymbol{L}} + \boldsymbol{w}$. The parameters which decide the stability of the growing system, i.e. if an equilibrium close to the undeformed state is achieved, are the growth rates $\boldsymbol{k}$ and the homeostatic stress $\boldsymbol{t}^*$, which are both assumed to be vectors of constant values.

Finally, we extend the question of homogenising a static network towards dynamic networks. In the static case, we showed how to obtain an effective Young's Modulus $\tilde{\mu}_\Sigma$ and an effective displacement of the unloaded configuration $\tilde{L}_\Sigma$. In the context of growth, this question extends to finding an effective growth rate $k_\Sigma$ and an effective homeostatic stress $\tilde{t}^*_\Sigma$. We show how in the case of two bars connected in series, these

quantities can be obtained as

$$k_\Sigma = k_1 + k_2 \quad \text{and} \quad \tilde{t}^*_\Sigma = \frac{k_1 \tilde{t}^*_1 + k_2 \tilde{t}^*_2}{k_1 + k_2} \,. \tag{2.102}$$

We reproduced eq. (2.93) here. However, in the case of a parallel connection of two bars, such a homogenisation is not possible unless one assumes a particular dependence $\tilde{\mu}_1 k_1 = \tilde{\mu}_2 k_2$ between the growth rates of the two bars connected in parallel, which a severe restriction. Only with this restriction is a homogenisation in which one obtains effective dynamical quantities for the entire network possible.

# Chapter 3

# A discrete model for growth dynamics of multiple layered cylinders

In this chapter, we present a mathematical framework to study the growth dynamics and stability of tubular structures, which are very common in biology. In the context of biomechanics, tubular and cylindrical structures and their stresses are rarely considered in a dynamical context but mostly analysed at a particular time $t_0$. For example Fung's opening angle method (see [23]) is a well-known method to compute residual stress at the time $t_0$ of the cut, and Wapas ("Killer Trees") explode because the residual stress present at time $t_0$ is suddenly released ( see [46, 30]). The presence of residual stress at $t_0$ is typically attributed to differential growth, its history is usually irrelevant. The model presented in this Chapter adds an additional layer of description in which the observed stress at $t_0$ (as well as residual stress and growth) are emergent features of the homeostasis-driven growth dynamics of tubular structures.

Compared to growth dynamics on a one-dimensional domain (as discussed in Chapter 2), growth on a cylindrical domain introduces a considerable complication: In cylindrical geometry stress is spatially inhomogeneous. The study of the growth dynamics and stability of a cylindrical structure becomes that of a partial differential equation (PDE). While the numerical solution of such a system is relatively straightforward by the method of lines (as demonstrated in Section 3.1.4), linear stability analysis becomes intractable, as the homeostatic stress tensor is no longer a value but a nontrivial spatially varying tensor field. Our goal in this chapter is to address the inhomogeneity of the system through a discretisation, which transforms the PDE to a system of

ordinary differential equations (ODEs) and allows the application of rigorous methods from dynamical systems theory like linear stability analysis. At the same time, our goal is to show the conclusions reached about the stability of the discrete system remain unchanged as the discretisation is further refined. One of the inspirations behind our discretisation approach is the observation that many biological tubular systems have a distinct number of well-defined layers, each with e.g. distinct material properties. With the discretisation approach outlined in this chapter, by construction every discrete system is a self-contained physical system in its own right, and can be used as a toy model for layered biological tubular structures with as low as $N = 2$ layers. Even a system composed of as low as two layers shows remarkably rich dynamical behaviour as we demonstrate in Section 3.2.

We approach the study of growth on a cylindrical domain in three parts. Firstly, in Section 3.1, we present a boundary value problem and demonstrate by numerical solution of the spatially continuous PDE the difficulty of characterising stability. Next, in Section 3.2, we introduce our discretisation scheme and study in detail the growth dynamics of a two layer system, finding very rich dynamics. Finally, in Section 3.3, we generalise the discretisation to $N$ layers and characterise the stability of the dynamics, which does not change for sufficiently large $N$ .

## 3.1 Continuous growth dynamics in cylindrical geometry

### 3.1.1 Kinematics

We consider a cylindrical tube. The inner wall of the tube is attached to an unmoving solid nucleus, whereas the outer wall is movable (see Figure 3.1). We assume that the tube is made from an incompressible isotropic material, does not grow in the axial direction, and is not exposed to any external fields (body forces). We also demand that the tube's centreline remains unchanged, which implies that buckling in axial direction is impossible, and we also do not permit buckling in the radial direction. Further, we do not permit twisting of the cylinder, which means that there is no shear stress.

As a consequence of these assumptions, we can limit the analysis of the elastic tube

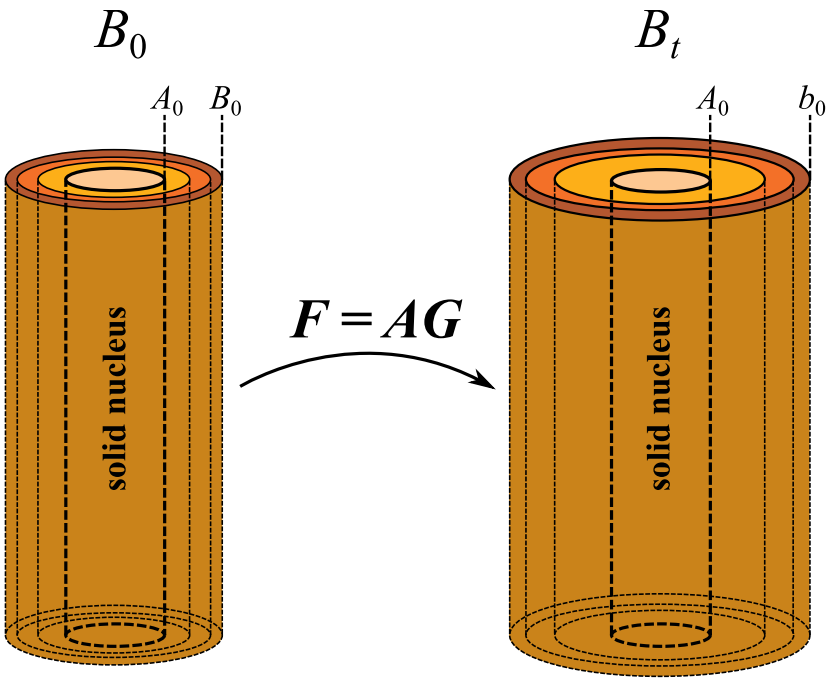


Figure 3.1: Sketch of kinematic setup.

to its cross section without loss of generality. Geometrically, we describe the cross section in a planar polar orthonormal coordinate basis $\left\{\mathbf{e}^R, \mathbf{e}^\theta\right\}$ where $\mathbf{e}^R$ denotes the radial and $\mathbf{e}^\theta$ the circumferential basis unit vector. We use the same basis vectors in initial and current configurations. We refer to the elastic soft tissue attached to the nucleus as a disk, annulus or layer (we will consider several layers attached to each other in later sections).

In analogy to (1.2), the deformation map of an annulus is

$$\mathbf{x} = r\left(R^0\right)\mathbf{e}^R\,. \tag{3.1}$$

The deformation gradient in a polar coordinate basis is

$$\mathbf{F} = r'\left(R^0\right)\mathbf{e}^R \otimes \mathbf{e}^R + r/R^0\mathbf{e}^\theta \otimes \mathbf{e}^\theta \tag{3.2}$$

where the prime denotes total derivative with respect to $R^0$. The kinematic setup is sketched in Figure 3.1.

The elastic deformation gradient is

$$\mathbf{A} = \alpha^R\mathbf{e}^R \otimes \mathbf{e}^R + \alpha^\theta\mathbf{e}^\theta \otimes \mathbf{e}^\theta. \tag{3.3}$$

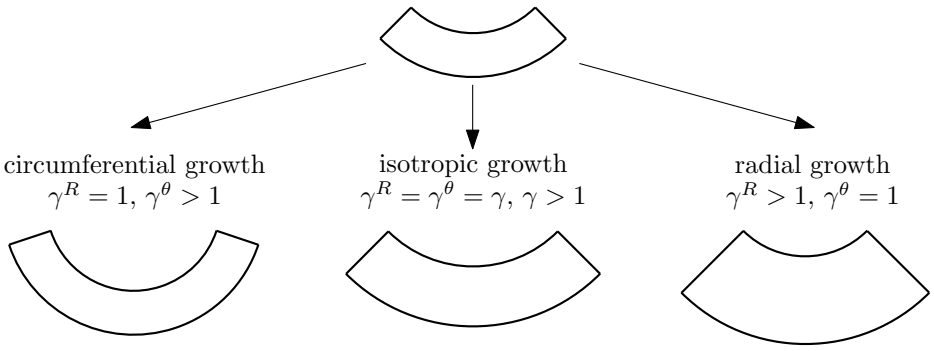


Figure 3.2: Illustration of isotropic and anisotropic growth.

Since $\mathbf{A}$ is isochoric ($\det \mathbf{A} = 1$), we define $\alpha := \alpha^\theta$. The isochoric deformation then requires that $\alpha^{-1} = \alpha^r$. The growth tensor field is

$$\mathbf{G} = \gamma^R \mathbf{e}^R \otimes \mathbf{e}^R + \gamma^\theta \mathbf{e}^\theta \otimes \mathbf{e}^\theta. \tag{3.4}$$

Whenever we use matrix notation, the basis $\left\{\mathbf{e}^R, \mathbf{e}^\theta\right\}$ is implied. The tensor fields that make up the morphoelastic decomposition (see 1.4) are

$$\mathbf{F} = \begin{pmatrix} \frac{\mathrm{d}r}{\mathrm{d}R^0} & 0 \\ 0 & \frac{r}{R^0} \end{pmatrix}, \qquad \mathbf{A} = \begin{pmatrix} \alpha^{-1} & 0 \\ 0 & \alpha \end{pmatrix}, \qquad \mathbf{G} = \begin{pmatrix} \gamma^r & 0 \\ 0 & \gamma^\theta \end{pmatrix}. \tag{3.5}$$

An illustration of anisotropic growth for an annulus is shown in Figure 3.2. Note that we use superscripts to denote the coordinate basis index and associated vector and tensor components. Subscripts are reserved for the layer index which is relevant in later sections.

In the initial reference configuration $\mathcal{B}_0$, the inner cylinder wall is located at $R^0 = A_0$ and the outer wall is located at $R^0 = A_1$. Evaluating the morphoelastic decomposition $\mathbf{F} = \mathbf{AG}$, we find $r' = \gamma^R/\alpha$ and $r/R^0 = \alpha\gamma^\theta$. By eliminating $\alpha$, we obtain

$$r\left(R^0\right) r'\left(R^0\right) = \gamma^R\left(R^0\right) \gamma^\theta\left(R^0\right) R^0, \qquad r\left(A_0\right) = A_0\,, \tag{3.6}$$

in which the boundary condition $r\left(A_0\right) = A_0$ represents the unmoving solid nucleus (i.e. unmoving inner cylinder wall). We can integrate (3.6) as

$$r = \sqrt{A_0^2 + 2\int_{A_0}^{R^0} \gamma^R(\tilde{R})\gamma^\theta(\tilde{R})\tilde{R}\mathrm{d}\tilde{R}}. \tag{3.7}$$

### 3.1.2 Mechanics

Given that all deformations are diagonal in the coordinate basis considered here, (1.17) implies that the Cauchy stress will also be diagonal,

$$\mathbf{T} = T^{RR}\mathbf{e}^R \otimes \mathbf{e}^R + T^{\theta\theta}\mathbf{e}^\theta \otimes \mathbf{e}^\theta. \tag{3.8}$$

The strain energy density describing the elastic energy density in terms of principal stretches is $W\left(\alpha^R, \alpha^\theta\right)$. The Cauchy stress tensor is given by

$$T^{RR} = \alpha^r \frac{\partial W}{\partial \alpha^r} - p\,, \qquad T^{\theta\theta} = \alpha^\theta \frac{\partial W}{\partial \alpha^\theta} - p\,, \tag{3.9}$$

where $p$ is the Lagrange multiplier enforcing incompressibility. Cauchy's equation (1.10) in a cylindrical coordinate basis takes the form

$$\frac{\partial T^{RR}}{\partial r} = \frac{T^{\theta\theta} - T^{RR}}{r} \tag{3.10}$$

We define $\widehat{W}(\alpha) := W(\alpha^{-1}, \alpha)$. Then

$$T^{\theta\theta} - T^{RR} = \alpha \mathrm{d}\widehat{W}/\mathrm{d}\alpha. \tag{3.11}$$

For a neo-Hookean strain energy density

$$\widehat{W}(\alpha) = \frac{\mu}{2}\left(\alpha^2 + \alpha^{-2} - 2\right)\,, \tag{3.12}$$

and (3.10) becomes

$$\begin{aligned} \frac{\mathrm{d}T^{RR}}{\mathrm{d}R^0} &= \frac{2\mu\gamma^R}{R^0\gamma^\theta}\left[1 - \frac{\left(R^0\right)^4\left(\gamma^\theta\right)^4}{r^4}\right] \\ T^{RR}(A_1) &= 0 \end{aligned} \tag{3.13}$$

The boundary condition $T^{RR}(A_1) = 0$ means that there is no pressure on the outer cylinder wall for all time. Note that (3.6) and (3.13) together form a boundary value problem, which we have broken down into two initial value problems, since (3.6) can be independently integrated from Cauchy stress according to (3.7). Once the radial stress component $T^{RR}$ has been integrated, the circumferential component can be obtained

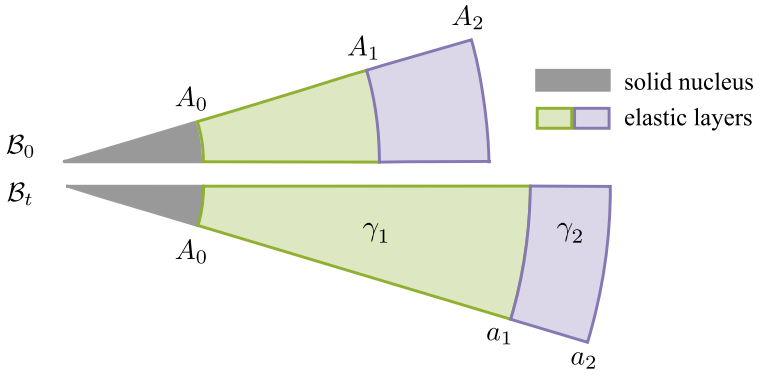


Figure 3.3: Kinematic setup two layer system. The innermost layer is attached to an unmoving nucleus ($a_0 = A_0$) and the boundary condition at the outer layer is no pressure $T^{RR}(A_2) = 0$.

as

$$T^{\theta\theta} = T^{RR} + \frac{2\mu r^2}{(R^0)^2 (\gamma^\theta)^2} \left[1 - \frac{(R^0)^4 (\gamma^\theta)^4}{r^4}\right] . \tag{3.14}$$

### 3.1.3 Growth law

To be consistent with the above assumptions, all tensor fields must have diagonal form in the coordinate basis $\{\mathbf{e}^R, \mathbf{e}^\theta\}$. Let the non-vanishing components of the fourth order tensor $\boldsymbol{K}$ be $K^{RR} := \mathcal{K}^{RRRR}$, $K^{R\theta} := \mathcal{K}^{RR\theta\theta}$, $K^{\theta R} := \mathcal{K}^{\theta\theta RR}$, $K^{\theta\theta} := \mathcal{K}^{\theta\theta\theta\theta}$. Then the growth law takes the form

$$\begin{aligned} \dot{\gamma}^R &= \left\{ K^{RR} \left[T^{RR} - \left(T^{RR}\right)^*\right] + K^{R\theta} \left[T^{\theta\theta} - \left(T^{\theta\theta}\right)^*\right] \right\} \gamma^R , \\ \dot{\gamma}^\theta &= \left\{ K^{\theta R} \left[T^{RR} - \left(T^{RR}\right)^*\right] + K^{\theta\theta} \left[T^{\theta\theta} - \left(T^{\theta\theta}\right)^*\right] \right\} \gamma^\theta . \end{aligned} \tag{3.15}$$

The growth rates $K^{RR}$, $K^{R\theta}$, $K^{\theta R}$ and $K^{\theta\theta}$ are constant in space and time.

### 3.1.4 Numerical simulation of inhomogeneous growth

In this section, we simulate the growth dynamics of the fully inhomogeneous system (PDE) by the method of lines. We study a circumferentially driven growth law that leads to stable behaviour, and a radially driven growth law that leads to unstable behaviour. The growth tensor $\boldsymbol{G}$ here is anisotropic ($\gamma^R \neq \gamma^\theta$). This demonstrates the difficulty of predicting the PDE stability and motivates a discretisation approach presented in the following sections.

We separate the soft tissue into two layers attached to each other: The inner layer

is attached to the nucleus and is growing actively, while the outer layer is a passive elastic material attached to the inner inner layer. In the initial reference configuration $\mathcal{B}_0$, the inner layer is defined by the region $A_0 \leq R^0 \leq A_1$ with growth $\gamma_1 \neq 1$ (active layer), while the outer layer is $A_1 < R^0 \leq A_2$ with growth $\gamma_2 = 1$ (passive layer).

The necessity of the passive layer is rooted in the boundary condition (3.13), which specifies that the radial Cauchy stress component must vanish at the outer boundary of the tube. In the absence of passive material at the outer boundary, the term $T^{RR} - \left(T^{RR}\right)^*$ at the outer boundary in the growth law (3.15) would be nonvanishing unless $\left(T^{RR}\right)^* = 0$. As a consequence, growth dynamics for nonvanishing homeostatic stress could never reach an equilibrium because the outer wall would grow perpetually. The addition of passive material mediates this problem.

The kinematic setup for a two-layered system is sketched in Figure 3.3. Here, specifically, note that the inner layer is an inhomogeneously growing active layer, that is $\dot{\gamma}_1 \neq 0$, $\mathrm{d}\gamma_1/\mathrm{d}R^0 \neq 0$. The outer layer is passive, that is $\gamma_2 = 1$ for all $R^0$ and $t$.

#### 3.1.4.1 Kinematic, mechanical and growth dynamical setup

We have the following growth tensor components

$$\gamma^R\left(R^0\right) = \begin{cases} \gamma_1^R\left(R^0\right) & \text{if } A_0 \leq R^0 \leq A_1 \\ 1 & \text{if } A_1 < R^0 \leq A_2 \end{cases} \tag{3.16}$$

$$\gamma^\theta\left(R^0\right) = \begin{cases} \gamma_1^\theta\left(R^0\right) & \text{if } A_0 \leq R^0 \leq A_1 \\ 1 & \text{if } A_1 < R^0 \leq A_2 \end{cases} \tag{3.17}$$

Evaluating the radial map (3.7) piecewise over the appropriate region with initial condition $r\left(A_0\right) = A_0$, we obtain:

$$r\left(R^0\right) = \begin{cases} r_1\left(R^0\right) := \sqrt{A_0^2 + 2\int_{A_0}^{R^0} \gamma_1^R(\tilde{R})\gamma_1^\theta(\tilde{R})\tilde{R}\mathrm{d}\tilde{R}} & \text{if } A_0 \leq R^0 \leq A_1 \\ r_2\left(R^0\right) := \sqrt{r_1^2\left(A_1\right) + \left(R^0\right)^2 - A_1^2} & \text{if } A_1 < R^0 \leq A_2 \end{cases} \tag{3.18}$$

Similarly, we evaluate the linear momentum balance (3.13)

$$\frac{\mathrm{d}T^{RR}}{\mathrm{d}R^0} = \begin{cases} \frac{\mathrm{d}T_1^{RR}}{\mathrm{d}R^0} = \frac{2\mu}{R^0}\left[1 - \frac{\left(R^0\right)^4\left(\gamma_1^\theta\right)^4}{r_1^4}\right]\frac{\gamma_1^R}{\gamma_1^\theta} & \text{if } A_0 \leq R^0 \leq A_1 \\ \frac{\mathrm{d}T_2^{RR}}{\mathrm{d}R^0} = \frac{2\mu}{R^0}\left[1 - \frac{\left(R^0\right)^4}{r_2^4}\right] & \text{if } A_1 < R^0 \leq A_2 \end{cases} \tag{3.19}$$

$$T^{RR}\left(A_2\right) = 0. \tag{3.20}$$

Once the radial stress component $T^{RR}$ has been integrated, the circumferential component $T^{\theta\theta}$ can be computed from (3.14). Note that while there is no growth in the passive layer $A_1 < R^0 \leq A_2$, the growth in the inner layer builds residual stress in the outer layer, that is $T_2^{RR} \neq 0$, $T_2^{\theta\theta} \neq 0$.

Next, the growth law becomes

$$\dot{\gamma}_1^R = \gamma_1^R\left\{K^{RR}\left[T_1^{RR} - \left(T_1^{RR}\right)^*\right] + K^{R\theta}\left[T_1^{\theta\theta} - \left(T_1^{\theta\theta}\right)^*\right]\right\} \quad \text{for } A_0 \leq R^0 \leq A_1 \tag{3.21}$$

$$\dot{\gamma}_1^\theta = \gamma_1^\theta\left\{K^{\theta R}\left[T_1^{RR} - \left(T_1^{RR}\right)^*\right] + K^{\theta\theta}\left[T_1^{\theta\theta} - \left(T_1^{\theta\theta}\right)^*\right]\right\} \quad \text{for } A_0 \leq R^0 \leq A_1 \tag{3.22}$$

#### 3.1.4.2 Growth dynamics simulations

The growth dynamics of the problem (3.21) and (3.22) is anisotropic and inhomogeneous. It depends on many parameters, including four weighting coefficients $K^{RR}$, $K^{R\theta}$, $K^{\theta R}$ and $K^{\theta\theta}$. It is beyond the scope of this work to obtain any general results about its growth dynamics. But we can nevertheless study interesting features by numerical example, such as the influence of radial vs. circumferential stress contributions on the dynamics.

**Growth dynamics driven by circumferential stress** We first focus on the case of growth dynamics driven purely by circumferential stress, that is $K^{RR} = K^{\theta R} = 0$ and $K^{R\theta} = K^{\theta\theta} = 1$. The growth dynamics takes the form

$$\begin{aligned} \dot{\gamma}_1^R &= \gamma_1^R\left[T_1^{\theta\theta} - \left(T_1^{\theta\theta}\right)^*\right], \\ \dot{\gamma}_1^\theta &= \gamma_1^\theta\left[T_1^{\theta\theta} - \left(T_1^{\theta\theta}\right)^*\right], \end{aligned} \tag{3.23}$$

for $A_0 \leq R^0 \leq A_1$.

Next, we must specify an initial condition for $\gamma_1^R\left(t = 0, R^0\right)$ and $\gamma_1^\theta\left(t = 0, R^0\right)$,

which is the initial inhomogeneous growth deformation. We choose a small oscillation near the unit growth tensor

$$\begin{aligned} \gamma_1^R &= 1 + a \sin\left(2\pi N \hat{R}\right), \\ \gamma_1^\theta &= 1 + a \cos\left(2\pi M \hat{R}\right), \end{aligned} \tag{3.24}$$

where $\hat{R} = \left(R^0 - A_0\right) / \left(A_1 - A_0\right)$ for $A_0 \leq R^0 \leq A_1$. Here, $0 < a \ll 1$ is a small amplitude of the perturbation and $M$, $N$ are integer values.

As for the homeostatic stress, we choose a Gaussian with mean 1.25 and standard deviation 0.05 and height 0.1 subtracted from the base value -0.5, that is

$$\left(T_1^{\theta\theta}\right)^* = -0.5 + 0.1 e^{\frac{\left(R^0 - 1.25\right)^2}{0.005}} \quad \text{for } A_0 \leq R^0 \leq A_1 \tag{3.25}$$

In Figure 3.4(a), we show the numerical results of the growth dynamics of the system (3.23) with initial conditions (3.24) and homeostatic stress profile (3.25) of the active layer. We repeated the growth dynamics simulation for several values of $a$, $M$ and $N$. While running the simulation repeatedly with changing initial conditions cannot be considered a full stability analysis, this method reduces the likelihood for numerical fluctuations. It is clear from the plots that the circumferential stress converges towards its inhomogeneous target stress profile.

**Growth dynamics driven by radial stress** Next, we demonstrate an example of dynamics driven by radial stress which does not converge. The growth rates are $K^{RR} = K^{\theta R} = 1$ and $K^{R\theta} = K^{\theta\theta} = 0$. The growth dynamics takes the form

$$\dot{\gamma}_1^R = \gamma_1^R \left[T_1^{RR} - \left(T_1^{RR}\right)^*\right], \tag{3.26}$$

$$\dot{\gamma}_1^\theta = \gamma_1^\theta \left[T_1^{RR} - \left(T_1^{RR}\right)^*\right] \tag{3.27}$$

for $A_0 \leq R^0 \leq A_1$.

For initial conditions $\gamma_1^R\left(t = 0, R^0\right)$ and $\gamma_1^\theta\left(t = 0, R^0\right)$, we take the final state of the previous system, with the addition of a small perturbation similar to (3.24) to ensure that the initial state of the system is compatible with the boundary conditions of the

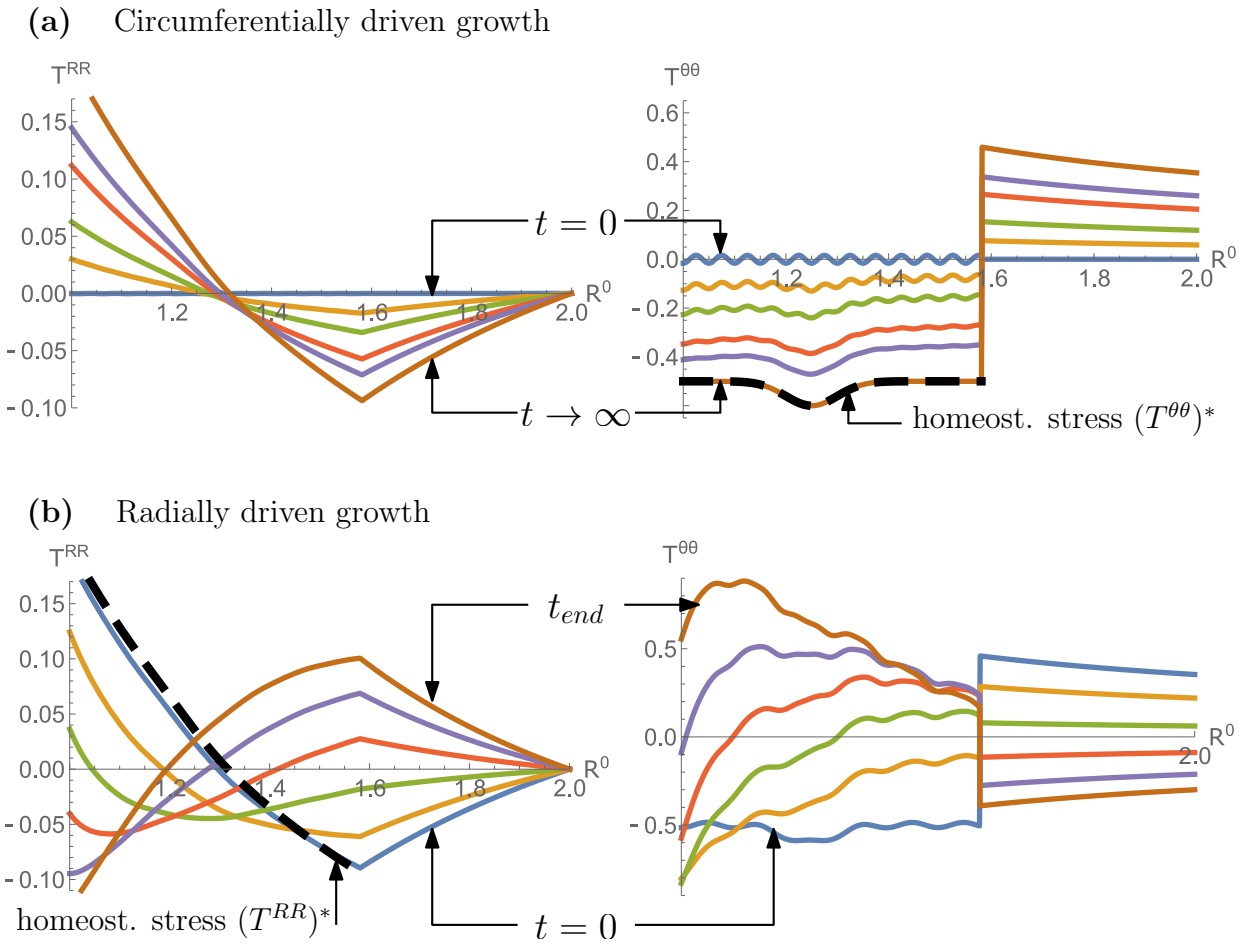


Figure 3.4: Dynamics of circumferentially and radially driven growth in inner layer, with passive outer layer. (a) Circumferentially driven growth. The simulation starts with $T^{RR}$ and $T^{\theta\theta}$ nearly zero and evolves to an equilibrium state for $t \to \infty$. The homeostatic stress (dashed black) is fully accommodated at equilibrium. Parameters for (3.24) are $a = 0.002$, $N = M = 20$. (b) Radially driven growth. The initial state of this simulation is the final state of the circumferentially driven growth simulation, with a small sinusoidal perturbation added to it. The dynamics does not converge to the homeostatic stress (black dashed curve). Parameters for (3.24) are $a = 0.002$, $N = M = 10$.

system. As for the homeostatic stress $\left(T_1^{RR}\right)^*$, we take the final stress $\lim_{t\to\infty} T^{RR}$ of the previous system.

The initial conditions chosen here imply that the initial stresses are close to the homeostatic stresses. As previously, we repeat the simulation for various values of $a$, $M$ and $N$. However, consistently over many simulations, the dynamics does not reach an equilibrium. The results of numerical simulations of this growth dynamics problem are shown in Figure 3.4(b).

However, as this type of numerical investigation cannot be expected to hold generally we introduce in the next sections a discretisation approach with which various questions about stability can be answered exactly.

## 3.2 Stability of spatially discretised growth dynamics with $N = 2$ layers

The central idea of this model is to simplify the complex growth dynamics of the previous model, while preserving the principal idea of growth driven by stress which attempts to accommodate its homeostasis. For this purpose, we propose a modified version of the growth law (3.15). Unlike in the previous model, we no longer consider inhomogeneous radial and circumferential stress as the driving forces of growth dynamics. Instead, we consider their averaged values over the respective layer. The averaging implies that throughout the process of growth dynamics, the growth deformation tensor also remains homogeneous within the respective layers. Overall, the inhomogeneity of the previous model is replaced by a piecewise homogeneous model. This preserves the key idea of inhomogeneity (allowing, for instance, circumferential growth to be higher near the nucleus than far away from it). But at the same time, this model is tractable and allows precise statements about its long-term dynamics, such as tracing the influence of radial vs. circumferential stress contributions on the stability of the system.

### 3.2.1 Kinematics

There are two soft layers attached to a solid nucleus. In the initial reference configuration $\mathcal{B}_0$, the inner wall has the radial coordinate $R^0 = A_0$, the middle wall at $R^0 = A_1$

and the outer wall at $R^0 = A_2$. In the current configuration $\mathcal{B}_t$, the radial coordinates are $r(A_0) = A_0$, $r(A_1) = a_1$ and $r(A_2) = a_2$, respectively.

We assume that in the initial reference configuration the two rings enclose the same area $\pi\Delta^2$ . The initial reference radii of the two rings satisfy

$$\Delta^2 = A_2^2 - A_1^2 = A_1^2 - A_0^2 \,. \tag{3.28}$$

The tensor fields of the morphoelastic decomposition are

$$\mathbf{F} = \begin{pmatrix} \frac{\mathrm{d}r}{\mathrm{d}R^0} & 0 \\ 0 & \frac{r}{R^0} \end{pmatrix} , \qquad \mathbf{A} = \begin{pmatrix} \alpha^{-1} & 0 \\ 0 & \alpha \end{pmatrix} , \qquad \mathbf{G} = \gamma \mathbf{I} \,, \tag{3.29}$$

where $\gamma(R)$ is a piecewise homogeneous function

$$\gamma\left(R^0\right) = \begin{cases} \gamma_1 & \text{if } A_0 \leq R^0 \leq A_1 \\ \gamma_2 & \text{if } A_1 < R^0 \leq A_2 \,. \end{cases} \tag{3.30}$$

That is, growth is homogeneous within every individual layer, and piecewise homogeneous overall: $\mathrm{d}\gamma_1/\mathrm{d}R^0 = 0$, $\mathrm{d}\gamma_2/\mathrm{d}R^0 = 0$. Note that growth is chosen to be isotropic, that is $\gamma_1 = \gamma_1^r = \gamma_1^\theta$ and $\gamma_2 = \gamma_2^r = \gamma_2^\theta$ (we recall that the upper index denotes the basis direction and the lower index identifies the layer). The kinematics of this model is summarised in Figure 3.3.

To obtain the deformation map (3.1), we integrate (3.7) over the appropriate layers, in which the growth deformation tensor takes the values (3.30). The solid nucleus initial condition is $r(A_0) = A_0$. We obtain

$$r\left(R^0\right) = \begin{cases} r_1(R^0) := \sqrt{A_0^2 + \gamma_1^2\left[(R^0)^2 - A_0^2\right]} & \text{if } A_0 \leq R^0 \leq A_1 \,, \\ r_2(R^0) := \sqrt{A_0^2 + \gamma_1^2\Delta^2 + \gamma_2^2\left[(R^0)^2 - A_1^2\right]} & \text{if } A_1 \leq R^0 \leq A_2 \,. \end{cases} \tag{3.31}$$

Note that at $R^0 = A_1$ we obtain $r = \sqrt{A_0^2 + \gamma_1^2\Delta^2}$ making $r$ continuous but not differentiable.

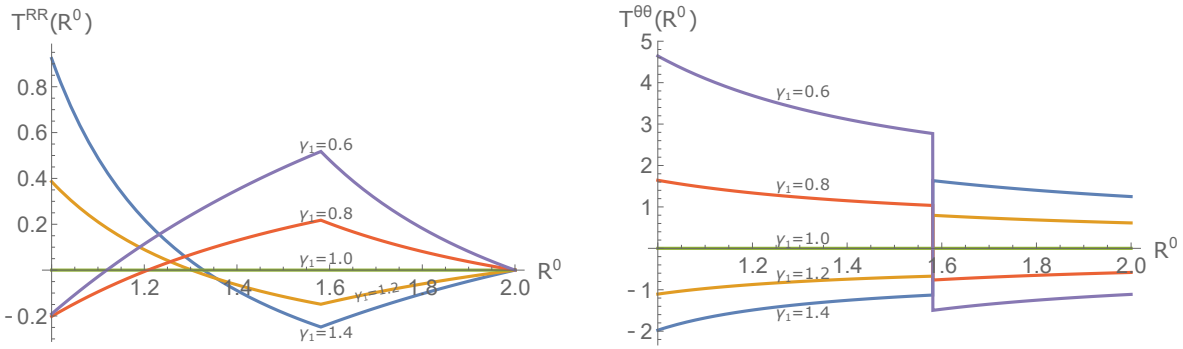


Figure 3.5: Radial (left) and circumferential (right) components of Cauchy stress for $A_0 = 1$, $A_1 = \sqrt{5/2}$, $A_2 = 2$, $\Delta = \sqrt{5/2}$, $\mu = 1$, $\gamma_2 = 1$ and $\gamma_1$ as indicated. Computed from (3.32) and (3.33).

### 3.2.2 Mechanics

The stress balance (3.13) can be integrated to obtain a result for radial stress $T^{RR}(R^0)$:

$$T^{RR}\left(R^0\right) = \begin{cases} T_1^{RR}(R^0) := T_1^{RR}(A_1) + \mu \int_{A_1}^{R^0} \frac{2}{\tilde{R}} \left(1 - \frac{\tilde{R}^4 \gamma_1^4}{r_1^4}\right) \mathrm{d}\tilde{R} & \text{if } A_0 \leq R^0 \leq A_1\,, \\ T_2^{RR}(R^0) := \underbrace{T_2^{RR}(A_2)}_{0} + \mu \int_{A_2}^{R^0} \frac{2}{\tilde{R}} \left(1 - \frac{\tilde{R}^4 \gamma_2^4}{r_2^4}\right) \mathrm{d}\tilde{R} & \text{if } A_1 \leq R^0 \leq A_2\,. \end{cases} \tag{3.32}$$

By (3.14), we obtain the circumferential stress $T^{\theta\theta}(R^0)$:

$$T^{\theta\theta}\left(R^0\right) = \begin{cases} T_1^{\theta\theta}(R^0) := T_1^{RR}(R^0) + \mu \frac{2r_1^2}{\gamma_1^2 (R^0)^2} \left[1 - \frac{\left(R^0\right)^4 \gamma_1^4}{r_1^4}\right] & \text{if } A_0 \leq R^0 \leq A_1\,, \\ T_2^{\theta\theta}(R^0) := T_2^{RR}(R^0) + \mu \frac{2r_2^2}{\gamma_2^2 (R^0)^2} \left[1 - \frac{\left(R^0\right)^4 \gamma_2^4}{r_2^4}\right] & \text{if } A_1 \leq R^0 \leq A_2\,. \end{cases} \tag{3.33}$$

The expressions $T_1^{RR}$ and $T_2^{RR}$ as well as $T_1^{\theta\theta}$ and $T_2^{\theta\theta}$ can be determined analytically as functions of $A_0$, $A_1$, $A_2$, $\mu$, $\gamma_1$ and $\gamma_2$. An example is shown in Figure 3.5.

### 3.2.3 Averaging

We define the average stresses $\overline{T_1}$ and $\overline{T_2}$ (this applies to both radial and circumferential stress) as

$$\overline{T_1} = \frac{2}{\Delta^2} \int_{A_0}^{A_1} T_1\left(\tilde{R}\right) \tilde{R} \mathrm{d}\tilde{R}\,, \qquad \overline{T_2} = \frac{2}{\Delta^2} \int_{A_1}^{A_2} T_2\left(\tilde{R}\right) \tilde{R} \mathrm{d}\tilde{R}\,, \tag{3.34}$$

in the regions $A_0 \leq R^0 \leq A_1$ and $A_1 \leq R^0 \leq A_2$, respectively.

### 3.2.4 Growth law

We study the growth law

$$\begin{aligned}\dot{\gamma}_1 &= \gamma_1 \left\{ K^{RR} \left[ \overline{T_1^{RR}} - \left(T_1^{RR}\right)^* \right] + K^{\theta\theta} \left[ \overline{T_1^{\theta\theta}} - \left(T_1^{\theta\theta}\right)^* \right] \right\} \quad \text{if } A_0 \leq R^0 \leq A_1 \,, \\ \dot{\gamma}_2 &= \gamma_2 \left\{ K^{RR} \left[ \overline{T_2^{RR}} - \left(T_2^{RR}\right)^* \right] + K^{\theta\theta} \left[ \overline{T_2^{\theta\theta}} - \left(T_2^{\theta\theta}\right)^* \right] \right\} \quad \text{if } A_1 \leq R^0 \leq A_2 \,.\end{aligned} \tag{3.35}$$

While these equations appear superficially similar to the growth law presented in Section 3.1.3, there are a few differences we want to emphasise. The growth law (3.15) is anisotropic and all fields are functions of the position $R^0$. The growth law (3.35), on the other hand, is isotropic ($\gamma^R = \gamma^\theta$). Growth in (3.35) is a function of stress averages over a given layer. The spatial dependence of growth and stress is encoded in the location of the layers, which are indexed with the subscript 1 and 2. Compared to the anisotropic model (3.15), the isotropy in (3.35) enforces $K^{RR} = K^{\theta R}$ and $K^{\theta\theta} = K^{R\theta}$, which is why only two (rather than four) growth rates $K^{RR}$ and $K^{\theta\theta}$ are present in (3.35).

We make the additional assumption that the homeostatic radial stress values are the same in layer 1 and 2, that is

$$\left(T^{RR}\right)^* := \left(T_1^{RR}\right)^* = \left(T_2^{RR}\right)^* \qquad \text{and} \qquad \left(T^{\theta\theta}\right)^* := \left(T_1^{\theta\theta}\right)^* = \left(T_2^{\theta\theta}\right)^* \,. \tag{3.36}$$

We emphasise that while $\overline{T_i^{RR}}$ and $\overline{T_i^{\theta\theta}}$ for $i = 1, 2$ are averages over actual stresses according to (3.34), the homeostatic values $\left(T_i^{RR}\right)^*$ and $\left(T_i^{\theta\theta}\right)^*$ for $i = 1, 2$ are prescribed values. The latter should be seen as genetically encoded or otherwise informed values, but are not necessarily averages over physically realisable stresses which satisfy the boundary conditions of the system.

To facilitate the analysis, we rescale time $t$ according to $\tilde{t} := t\, K^{\theta\theta}$ and introduce

$$\tilde{K} := K^{RR}/K^{\theta\theta} \qquad \text{and} \qquad T^* := \tilde{K} \left(T^{RR}\right)^* + \left(T^{\theta\theta}\right)^* \,. \tag{3.37}$$

The parameter $\tilde{K}$ is a measure of anisotropy of the mechanical feedback, i.e. a weighting of the contribution of radial vs. circumferential stress to the growth response of the soft tissue. We emphasise here that $\tilde{K}$ characterises the anisotropy of the growth *response*

— the growth tensor itself is isotropic. The rescaled growth law is:

$$\begin{aligned}\dot{\gamma}_1 &= \gamma_1 \left[\tilde{K}\overline{T_1^{RR}} + \overline{T_1^{\theta\theta}} - T^*\right] \\ \dot{\gamma}_2 &= \gamma_2 \left[\tilde{K}\overline{T_2^{RR}} + \overline{T_2^{\theta\theta}} - T^*\right]\end{aligned} \tag{3.38}$$

In the last equation, and from here for the rest of this Section, we have re-defined the overdot as a total derivative with respect to rescaled time: $\dot{f} := \mathrm{d}f/\mathrm{d}\tilde{t}$ for all scalar functions $f$. Note that all stress averages depend nonlinearly on $\gamma_1$ and $\gamma_2$, but not on the spatial coordinate $R^0$, as it has been integrated out. The growth dynamics is described by two coupled nonlinear ordinary differential equations (3.38). We can now apply traditional methods of stability analysis to quantify the long-term behaviour of this system.

### 3.2.5 Stability analysis

To investigate the growth dynamics of (3.38), we consider the following questions: How many equilibria ($\dot{\gamma}_1 = 0$ and $\dot{\gamma}_2 = 0$) does the system have? What is their stability?

To address the first question, we define an equilibrium state $\{\gamma_1^{\mathrm{eq}}, \gamma_2^{\mathrm{eq}}\}$ of (3.38) by $\dot{\gamma}_1^{\mathrm{eq}} = 0$, $\dot{\gamma}_2^{\mathrm{eq}} = 0$. The nonlinear nature of the dependence of $\overline{T_1^{RR}}$, $\overline{T_2^{RR}}$, $\overline{T_1^{\theta\theta}}$ and $\overline{T_2^{\theta\theta}}$ on $\gamma_1$, $\gamma_2$ makes it difficult to predict by analytical methods the number and location of equilibrium states as a function of the parameters $\tilde{K}$ and $T^*$ and we shall use numerical methods to this end.

To address the second question, given an equilibrium state, the characterisation of its stability requires a linear expansion of the dynamical system near an equilibrium. We expand as follows:

$$\begin{aligned}\gamma_1 &= \gamma_1^{\mathrm{eq}} + \varepsilon\overline{\gamma}_1 + \mathcal{O}\left(\varepsilon^2\right), \\ \gamma_2 &= \gamma_2^{\mathrm{eq}} + \varepsilon\overline{\gamma}_2 + \mathcal{O}\left(\varepsilon^2\right),\end{aligned} \tag{3.39}$$

where $0 < \varepsilon \ll 1$ is a small parameter. Introducing $\boldsymbol{\gamma} = (\gamma_1, \gamma_2)$ to describe the state of the system (3.38), its linearly expanded version (to order $\varepsilon$) takes the form

$$\dot{\overline{\boldsymbol{\gamma}}} = \mathbf{J}\overline{\boldsymbol{\gamma}} \tag{3.40}$$

where the Jacobian has entries

$$J_{ij} = \left[\frac{\partial \dot{\gamma}_i}{\partial \gamma_j}\right]_{\boldsymbol{\gamma}=\boldsymbol{\gamma}^{\mathrm{eq}}} \tag{3.41}$$

subscript $\boldsymbol{\gamma} = \boldsymbol{\gamma}^{\mathrm{eq}}$ means that the matrix entries are evaluated at the equilibrium state. To assess the stability of this state, the eigenvalues of $\mathbf{J}$ provide the necessary information. They are the solutions $\lambda_1$ and $\lambda_2$ to the characteristic equation

$$0 = \left[\left(\frac{\partial \dot{\gamma}_1}{\partial \gamma_1} - \lambda\right)\left(\frac{\partial \dot{\gamma}_2}{\partial \gamma_2} - \lambda\right) - \frac{\partial \dot{\gamma}_1}{\partial \gamma_2}\frac{\partial \dot{\gamma}_2}{\partial \gamma_1}\right]_{\boldsymbol{\gamma}=\boldsymbol{\gamma}^{\mathrm{eq}}} \tag{3.42}$$

We recall that an equilibrium state for which

$$\mathrm{Re}\,(\lambda_1) < 0, \quad \mathrm{Re}\,(\lambda_2) < 0, \quad \text{and} \quad \mathrm{Im}\,(\lambda_1) = \mathrm{Im}\,(\lambda_2) = 0 \tag{3.43}$$

is called a saddle node,

$$\mathrm{Re}\,(\lambda_1) > 0, \quad \mathrm{Re}\,(\lambda_2) > 0, \quad \text{and} \quad \mathrm{Im}\,(\lambda_1) = \mathrm{Im}\,(\lambda_2) = 0 \tag{3.44}$$

is called an unstable node and

$$\mathrm{Re}\,(\lambda_1) > 0, \quad \mathrm{Re}\,(\lambda_2) > 0, \quad \text{and} \quad \mathrm{Im}\,(\lambda_1) = -\mathrm{Im}\,(\lambda_2) \neq 0 \tag{3.45}$$

is known as an unstable focus. If

$$\mathrm{Re}\,(\lambda_1)\,\mathrm{Re}\,(\lambda_2) = 0, \tag{3.46}$$

no conclusion can be reached. The bifurcation analysis in the following section provides information on how many equilibrium states the system (3.38) has for a set of parameters $\left\{\tilde{K}, T^*\right\}$, and what the stability (i.e. type of node) of these equilibria is.

### 3.2.6 Bifurcation diagram

We present a bifurcation analysis of (3.38) in Figure 3.6. In the presented parameter region of $\tilde{K}$ and $T^*$ we identify four regions with unique dynamical behaviour, see Figure 3.6.

- **Region IV** has no equilibrium state.

- **Region I** has four unique equilibrium states, of which only one is a stable node. The other nodes are two saddles and either an unstable node or an unstable focus focus. In Figure 3.6(b) we show phase portraits for two selected points P1 and P2 which are contained in Region I of $\left(\tilde{K}, T^*\right)$ parameter space (see subfigure a).

- **Region II** has four unique equilibrium states: Two saddles and either two stable nodes or said stable focus and a stable node. In Figure 3.6(b) we show phase portraits for two selected points P3 and P4 which are contained in Region II of $\left(\tilde{K}, T^*\right)$ parameter space (see subfigure a). A Hopf bifurcation transforms the unstable focus into a stable focus and occurs at the interface of Regions I & II.

- **Region III** has two equilibrium states, one of which is a stable node, the other a saddle node. In Figure 3.6(b) we show phase portraits for two selected points P5 and P6 which are contained in Region III of $\left(\tilde{K}, T^*\right)$ parameter space (see subfigure a). The annihilation between a stable node and saddle node from region II to region III is a saddle-node bifurcation.

Note that while regions I, II and III contain the possibility of stable dynamics, mostly the stable equilibrium states describe a body that is shrunk ($\gamma_1^{\text{eq}}\gamma_2^{\text{eq}} < 1$). Only a small parameter region for $\tilde{K}$ and $T^*$ denoted by a dark blue island in Figure 3.6 contains the possibility of forming a grown equilibrium state $\gamma_1^{\text{eq}}\gamma_2^{\text{eq}} > 1$.

Interestingly, this suggests that stable growth is difficult to achieve as it is only occurs in a finely tuned parameter region.

In summary, we have found that tubular structures growing towards their homeostasis mostly exhibit pathological growth. Such structures may grow unbounded (like a tumour), or shrink until all cells have died. But under the right conditions, physiological (healthy) growth is possible, as shown in Figure 3.6. Our model uncovers the exact conditions under which tubular structures grow and adapt to their mechanical environment in a stable way.

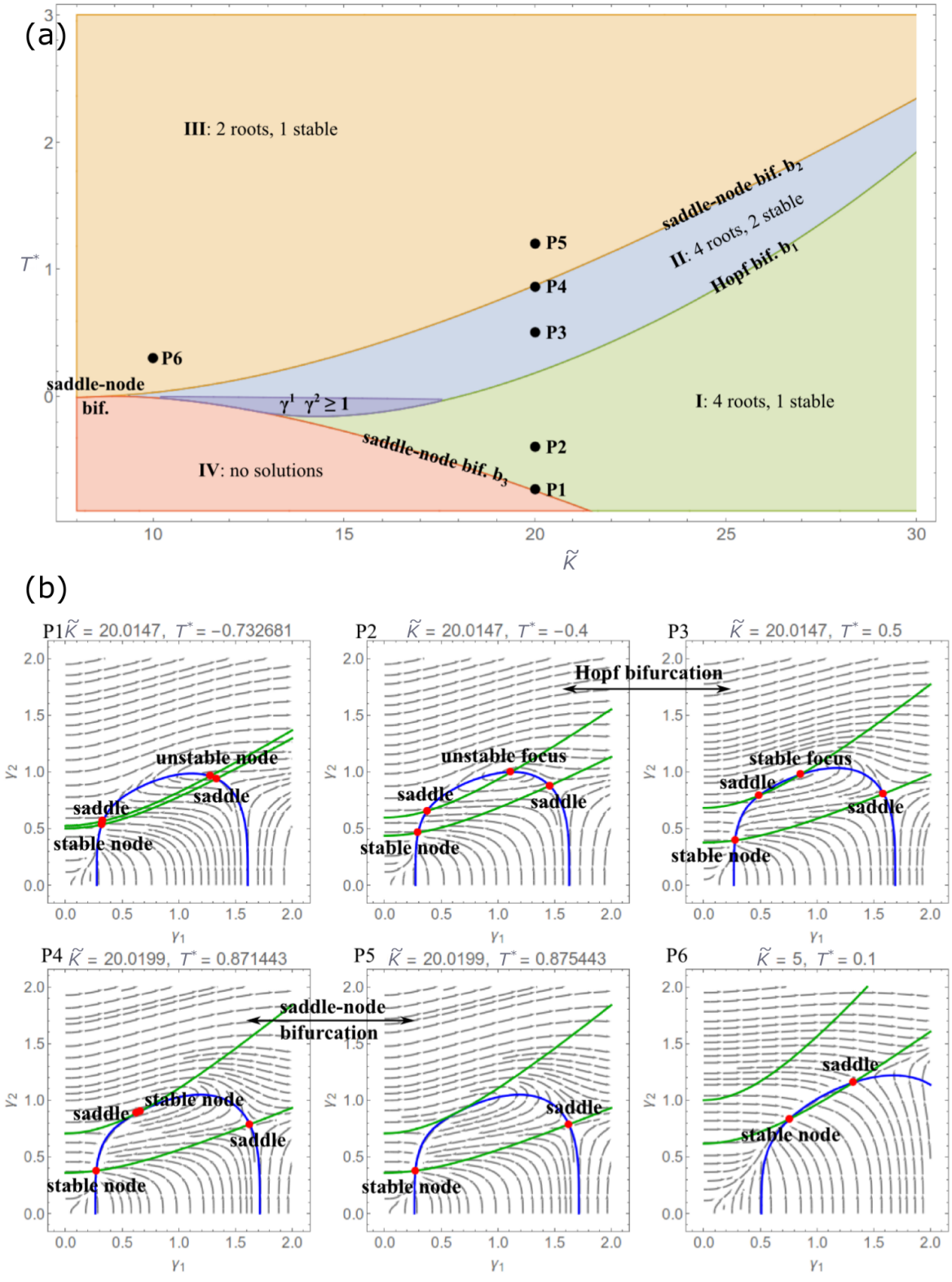


Figure 3.6: (a) Bifurcation diagram for two layered actively growing piecewise homogeneous system. (b) Equilibrium states and their dynamical characterisation.

### 3.2.7 Detailed dynamics of two layer system

**Admissible and inadmissible homeostatic values** In the Section (3.2.4), we considered the dynamics of a growth law in which the homeostatic stress values are equal in both layers (see (3.36)). As pointed out in the same section, the homeostatic value is in general not an average over a stress profile which satisfies the boundary conditions of the system. We define an admissible homeostatic value as an average over a stress field which can be physically realised, i.e. which satisfies the boundary conditions $r(A_0) = A_0$. $T^{RR}(A_2) = 0$. An admissible homeostatic value, e.g. $\overline{T_1^{RR}}(\boldsymbol{\gamma}^*)$ is a stress average (according to (3.34)) evaluated homeostatic strain values $\boldsymbol{\gamma}^* = (\gamma_1^*, \gamma_2^*)^T$. Admissible homeostatic for a two-layered system are denoted as

$$\overline{T_i^{RR}}(\boldsymbol{\gamma}^*) \qquad \text{and} \qquad \overline{T_i^{\theta\theta}}(\boldsymbol{\gamma}^*), \qquad i = 1, 2. \tag{3.47}$$

An inadmissible homeostatic value (such as discussed in Section 3.2.4) cannot be expressed as an average over actual stress, i.e. there exists no $\boldsymbol{\gamma}^*$ such that $\overline{\boldsymbol{T}}(\boldsymbol{\gamma}^*)$ equals the inadmissible homeostatic value. We use the term homeostatic stress and homeostatic value interchangeably.

**Growth law with admissible homeostatic values** We now consider a growth law with admissible homeostatic values. Because of the spatial inhomogeneity of the Cauchy stress profile in the two layer cylinder (see for instance Figure 3.5), the homeostatic values in layer 1 and 2 cannot be equal. Unlike in (3.36), the inhomogeneity of the Cauchy stress profile requires that $\overline{T_1^{RR}}(\boldsymbol{\gamma}^*) \neq \overline{T_2^{RR}}(\boldsymbol{\gamma}^*)$ and $\overline{T_1^{\theta\theta}}(\boldsymbol{\gamma}^*) \neq \overline{T_2^{\theta\theta}}(\boldsymbol{\gamma}^*)$. The growth law with admissible homeostatic values reads

$$\begin{aligned}
\dot{\gamma}_1 &= \gamma_1 \left\{ \tilde{K} \left[ \overline{T_1^{RR}}(\boldsymbol{\gamma}) - \overline{T_1^{RR}}(\boldsymbol{\gamma}^*) \right] + \left[ \overline{T_1^{\theta\theta}}(\boldsymbol{\gamma}) - \overline{T_1^{\theta\theta}}(\boldsymbol{\gamma}^*) \right] \right\} \\
\dot{\gamma}_2 &= \gamma_2 \left\{ \tilde{K} \left[ \overline{T_2^{RR}}(\boldsymbol{\gamma}) - \overline{T_2^{RR}}(\boldsymbol{\gamma}^*) \right] + \left[ \overline{T_2^{\theta\theta}}(\boldsymbol{\gamma}) - \overline{T_2^{\theta\theta}}(\boldsymbol{\gamma}^*) \right] \right\}.
\end{aligned} \tag{3.48}$$

In Figure 3.7, we show the dynamics of a strongly anisotropic growth law in which radial stress dominates mechanical feedback ($\tilde{K} = 23.5$). The contour plot in Figure 3.7(a) shows that there are in total four four equilibrium states. The streamlines and trajectory plots in Figure 3.7(b) and (c) reveal that the equilibria are a stable spiral, two saddles, and one stable node. We focus on three trajectories (red, green and blue)

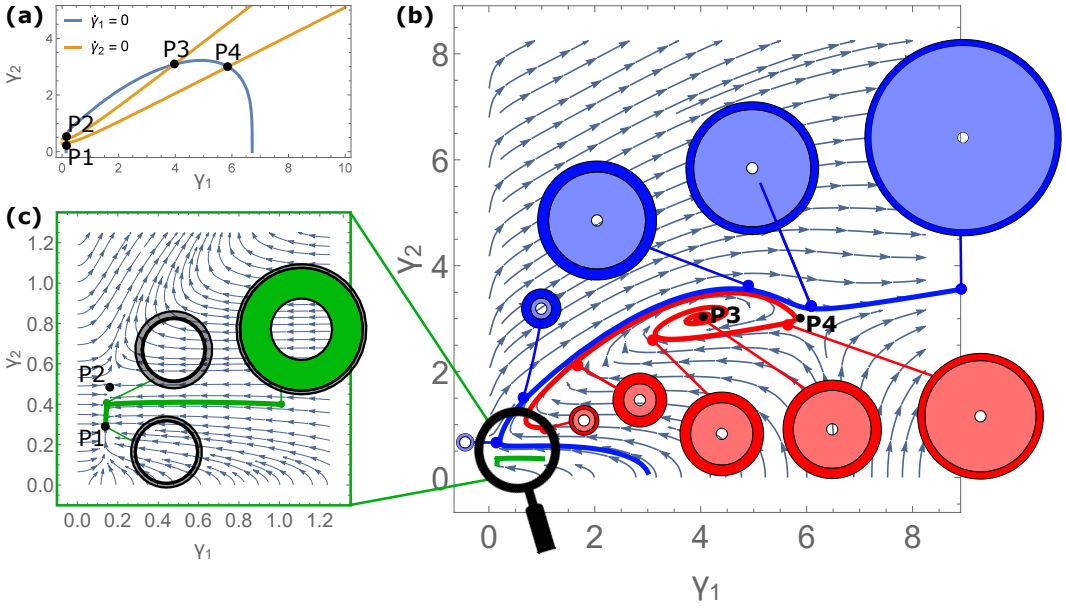


Figure 3.7: Trajectories and layer sizes for highly anisotropic growth law with admissible homeostatic state. **(a)** Contours for $\dot{\gamma}_1 = 0$ and $\dot{\gamma}_2 = 0$ for the system 3.7. As can be confirmed from the stream plots **(b)** and **(c)**, there is one stable spiral, two saddles, and one stable node. Notice the similarity to to the "P3" case in Figure 3.6. The saddle point P4 in (b) is the homeostatic equilibrium $(\gamma_1^*, \gamma_2^*)$. Parameters: $\mu = 2$, $\Delta = \sqrt{3}$ ($A_0 = 1$, $A_2 = \sqrt{7}$). $\tilde{K} = 23.5$. Homeostatic growth: $\gamma_1^* = 5.867$, $\gamma_2^* = 3$.

and plot the domain size at different times. The homeostatic equilibrium is defined by $\overline{T_i^{RR}}(\boldsymbol{\gamma}) = \overline{T_i^{\theta\theta}}(\boldsymbol{\gamma}^*)$ for $i = 1, 2$. At the homeostatic equilibrium, the average of current stress coincides with the average homeostatic stress. In Figure 3.7(b) the homeostatic equilibrium is denoted as P4 and is shown to be a saddle point (i.e. an unstable equilibrium). Note that this dynamical behaviour is analogous to a case we already discussed, that is point P3 in Figure 3.6. We conclude that in this example, the difference between an admissible homeostatic state 3.7 and an inadmissible one 3.6 does not greatly affect the dynamics.

## 3.3 Growth of discrete $N$ layer system

In this section, we generalise the dynamical system of the previous section from two to $N$ layers. This serves as a spatial discretisation, as growth and stresses are constant throughout each layer, which similarly to (3.48) allows to describe growth dynamics as a system of $N$ (rather than 2) coupled ODEs. We will analyse the stability of this system near the homeostatic equilibrium, and show to what extent these results remain unchanged as the discretisation is refined ($N$ increases), which informs the stability of

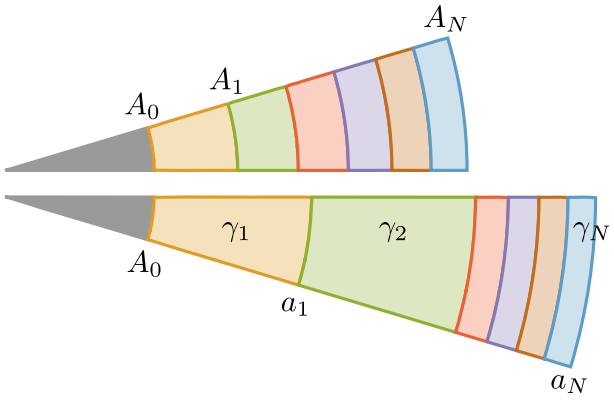


Figure 3.8: Kinematic setup for isotropically growing $N$ layered system. Consider Figure 3.3 for comparison to the two layers system.

the continuous ($N \to \infty$) system.

A major difference compared to the two layer model from Section 3.2.7 is our method to obtain homeostatic values. In Figure (3.7), they were prescribed via the homeostatic growth values $\gamma_1^*$, $\gamma_2^*$. In the present model, homeostatic values are obtained from a prescribed continuous homeostatic growth profile $\gamma^*(R^0)$. The homeostatic values $\{\gamma_i^*\}$ are obtained through averaging over the prescribed profile $\gamma^*(R^0)$ in a fashion similarly to (3.34). They are by definition admissible (see Section 3.2.7). By choosing a linear homeostatic growth profile $\gamma^*(R^0)$, we can characterise the homeostatic stress through a single parameter, the slope of $\gamma^*(R^0)$. Since the growth is taken as constant in each layer, the stresses can be determined fully analytically and a stability analysis can be performed. The stability analysis will inform under which conditions the dynamical system will relax to a homeostatic state after a small perturbation.

### 3.3.1 Kinematics

We consider $N$ perfectly connected annuli, separated by $N+1$ interfaces, which in the initial reference configuration have the radial coordinate values $\{A_0, A_1, \ldots, A_N\}$. The $K$-th annulus is defined by $A_{K-1} \leq R < A_K$ for $K \in \{1, \ldots, N\}$. The kinematic setup is sketched in Figure 3.8.

The spacing between layers satisfies

$$A_K^2 - A_{K-1}^2 := \Delta^2 = \text{const.} \tag{3.49}$$

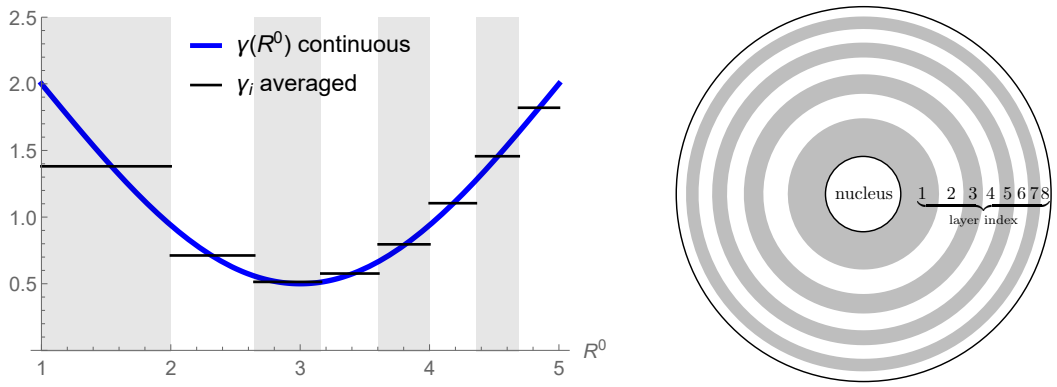


Figure 3.9: Growth $\gamma$ continuous vs. averaged. The continuous curve (3.52) is plotted in blue, and the average over a particular discretisation according to (3.51) is plotted in red. The gray shading helps to emphasise the different layers, which do not scale linearly in radius, but instead as $A_K^2 - A_{K-1}^2 = \Delta^2 = \text{const}$. This is also illustrated with the disk on the right hand side, which is limited by the nucleus at $R^0 = A_0$ and the outer boundary $R^0 = A_N$. The layers are numbered from 1 to $N = 8$. The other parameters are $A_0 = 1$, $A_N = 5$ and $\Delta = \sqrt{\left(A_N^2 - A_0^2\right)/n} = \sqrt{3}$.

This fixes the area of every layer as $\pi\Delta^2$. We can write $A_K$ explicitly as

$$A_K^2 = A_0^2 + K\Delta^2 \,. \tag{3.50}$$

Given a continuous curve $\gamma\left(R^0\right)$ we define the piecewise constant growth profile by taking the average

$$\gamma_K := \overline{\gamma\left(R^0\right)} = \frac{2}{\Delta^2}\int_{A_{K-1}}^{A_K} \gamma\left(\tilde{R}\right)\tilde{R}\mathrm{d}\tilde{R} \quad \text{for} \quad R^0 \in \left[A_{K-1}, A_K\right]. \tag{3.51}$$

The growth value $\gamma_K$ is constant for the $K$-th layer. We demonstrate the computation of the discrete profile $\{\gamma_K\}$ from the continuous profile $\gamma\left(R^0\right)$ in Figure 3.9, in which we consider as an example the continuous function

$$\gamma\left(R^0\right) = 2 - \frac{3}{2}\sin\left(\pi\frac{R^0 - A_0}{A_N - A_0}\right). \tag{3.52}$$

Once $\{\gamma_K\}$ are obtained, we compute the radial map $r_K\left(R^0\right)$ from the discrete profile $\{\gamma_K\}$. Note that while $\gamma_K$ is a constant throughout the $K$-th layer, the radial map $r_K$ is a function of the radial coordinate $R^0$:

$$r_K^2\left(R^0\right) = r_{K-1}^2\left(A_{K-1}\right) + \gamma_K^2\left[\left(R^0\right)^2 - A_{K-1}^2\right], \qquad r_0^2\left(R^0\right) = A_0^2. \tag{3.53}$$

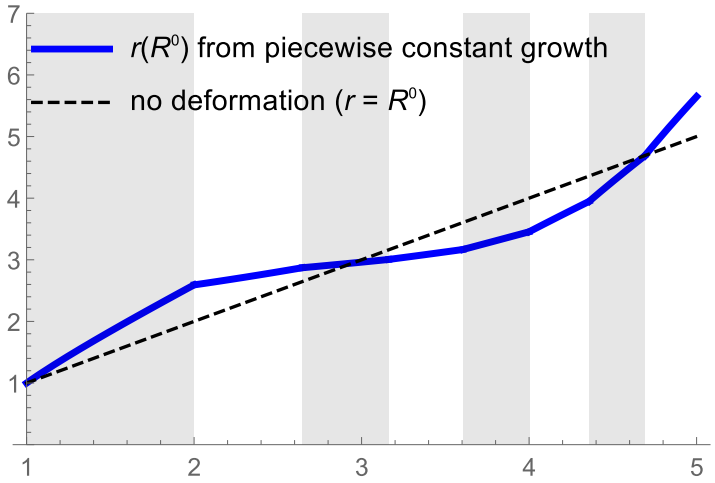


Figure 3.10: Radial function $r_K\left(R^0\right)$ for the case of discrete growth $\gamma_i$, computed according to (3.54). The dashed line represents the case of no deformation $r = R^0$; everything below the dashed line is resorption ("shrinking"), everything above this line is growth. Parameters are the same as in Fig. 3.9.

Explicitly, this implies

$$r_K^2\left(R^0\right) = A_0^2 + \left(\Delta^2 \sum_{i=1}^{K-1} \gamma_i^2\right) + \gamma_K^2 \left[\left(R^0\right)^2 - A_{K-1}^2\right]. \tag{3.54}$$

Notice that the recursive expression (3.53) and the explicit expression (3.54) are consistent with the requirement

$$r_{K-1}\left(A_{K-1}\right) = r_K\left(A_{K-1}\right), \tag{3.55}$$

which means that $r_K$ is continuous at the boundary layer $A_{K-1}$.

### 3.3.2 Mechanics

**Radial stress** In the continuous version, $T^{RR}$ is obtained from (3.13). The discrete version reads

$$\frac{\partial T_K^{RR}}{\partial R^0} = \frac{2\mu}{R^0}\left[1 - \frac{\gamma_K^4 \left(R^0\right)^4}{r_K^4\left(R^0\right)}\right], \qquad T_N^{RR}\left(A_N\right) = 0\,. \tag{3.56}$$

As required,

$$T_K^{RR}\left(A_K\right) = T_{K+1}^{RR}\left(A_K\right). \tag{3.57}$$

We define $\tau^{RR}(R^0)$ as the indefinite integral over the right hand side of (3.56) (dropping the integration constant),

$$\tau^{RR}\left(R^0\right) := -\mu\frac{r_{K-1}^2\left(A_{K-1}\right) - A_{K-1}^2\gamma_K^2}{r_K^2\left(R^0\right)} - \mu\log\left[\frac{r_K^2\left(R^0\right)}{\left(R^0\right)^2}\right]. \tag{3.58}$$

The knowledge of the explicit form of $\tau^{RR}$ allows us to express the radial stress, i.e. the solution to (3.56), in explicit form:

$$T_K^{RR}\left(R^0\right) = \tau_K^{RR}\left(R^0\right) - \tau_N^{RR}\left(A_N\right) + \sum_{i=K}^{N-1}\mu\frac{A_i^2\left(\gamma_{i+1}^2 - \gamma_i^2\right)}{r_i^2\left(A_i\right)} \tag{3.59}$$

The radial stress profile is depicted in Figure 3.11(a).

**Circumferential stress** In the continuous version, the circumferential stress $T^{\theta\theta}$ is related to the radial stress $T^{RR}$ through 3.14. The discrete version of the relationship between $T^{RR}$ and $T^{\theta\theta}$ is given by

$$T_K^{\theta\theta}\left(R^0\right) = T_K^{RR}\left(R^0\right) + \kappa_K\left(R^0\right) \tag{3.60}$$

where the function $\kappa_K$ is defined as

$$\kappa_K\left(R^0\right) := \frac{2\mu r_K^2\left(R^0\right)}{\gamma_K^2\left(R^0\right)^2}\left(1 - \frac{\gamma_K^4\left(R^0\right)^4}{r_K^4}\right). \tag{3.61}$$

The circumferential stress profile is depicted in Figure 3.11(b).

**Average radial stress** The average radial stress in the $K$-th layer $\overline{T_K^{RR}}$ is

$$\overline{T_K^{RR}} = -\tau_N^{RR}\left(A_N\right) + \sum_{i=K}^{N-1}\mu\frac{A_i^2\left(\gamma_{i+1}^2 - \gamma_i^2\right)}{r_i^2\left(A_i\right)} + \frac{2}{\Delta^2}\left[\nu_K^{rr}\left(A_K\right) - \nu_K^{rr}\left(A_{K-1}\right)\right] \tag{3.62}$$

where $\nu_K\left(R^0\right)$ is defined as

$$\nu_K^{rr}\left(R^0\right) := \mu\left[A_{K-1}^2 - \frac{r_{K-1}^2\left(A_{K-1}\right)}{\gamma_K^2}\right]\log\left[r_K^2\left(R^0\right)\right] - \frac{1}{2}\mu\left(R^0\right)^2\log\left[\frac{r_K^2\left(R^0\right)}{\left(R^0\right)^2}\right]. \tag{3.63}$$

The average radial stress is depicted as horizontal lines in the respective layers in Figure (3.11)(a).

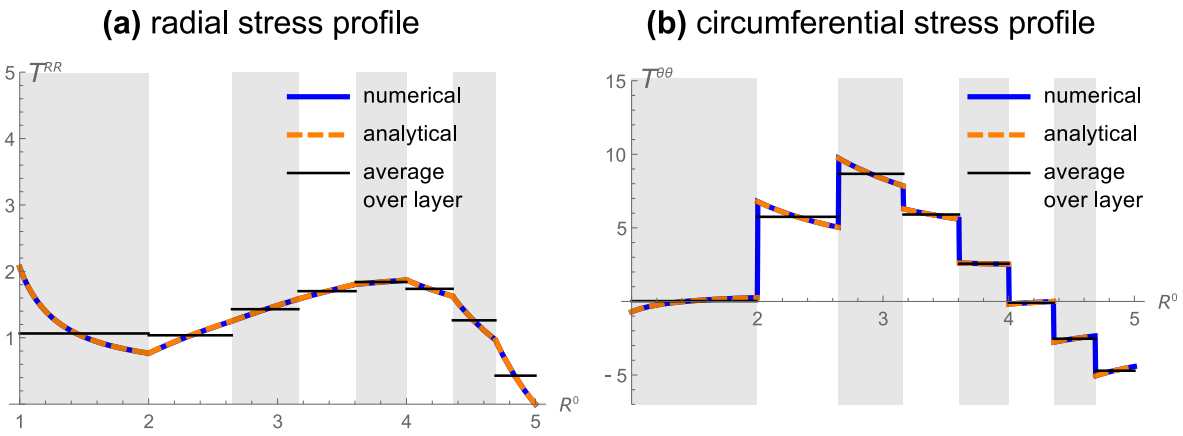


Figure 3.11: Stress profile and stress averages for piecewise growth. **(a)** Radial stress profile $T^{RR}$ and average stress profile $\overline{T^{RR}}$. The analytical curve was obtained from (3.59) and the numerical curve (for validation) was obtained from (3.13). In both the numerical and analytical case, the piecewise growth profile $\gamma_i$ according to (3.51) was used. The average stress was computed according to 3.62 with the same growth profile as the other curves. **(b)** Circumferential stress profile $T^{\theta\theta}$ and average stress profile $\overline{T^{\theta\theta}}$. The analytical curve was obtained from (3.60) and the numerical curve (for validation) was obtained from (3.14). The growth profile is as in (a) . The average stress was computed according to 3.64 with the same growth profile as the other curves. All other parameters are as in Figure 3.9, with Young's Modulus $\mu = 1$.

**Average circumferential stress** We have seen in (3.60) how the circumferential stress $T^{\theta\theta}$ relates to the radial stress $T^{RR}$. The average over that expression is

$$\overline{T_K^{\theta\theta}} = \overline{T_K^{RR}} + \overline{\kappa_K}, \tag{3.64}$$

We have presented an expression for $\kappa_K$ in (3.61). The average over $\kappa_K$ is

$$\overline{\kappa_K} = \frac{2\mu\left[r_K^2\left(A_K\right) - \gamma_K^2 A_K^2\right]}{\Delta^2 {\gamma_K}^2} \log\left[\frac{A_K^2 r_K^2\left(A_K\right)}{A_{K-1}^2 r_{K-1}^2\left(A_{K-1}\right)}\right]. \tag{3.65}$$

According to (3.64), the expression for $\overline{T_K^{\theta\theta}}$ is the sum of $\overline{\kappa_K}$ (see (3.65)) and $\overline{T_K^{RR}}$ (see (3.62)). The average circumferential stress is depicted as horizontal lines in the respective layers in Figure (3.11)(b).

### 3.3.3 Generating a homeostatic state from prescribed growth profile

We prescribe a growth profile $\gamma^*\left(R^0\right)$ from which the homeostatic stress is computed through averaging. The growth profile is linear and has a slope given by the parameter

$C_1$:

$$\gamma^*\left(R^0\right) = 1 + C_1\left(R^0 - A_0\right), \qquad C_1\left(A_N - A_0\right) < 1. \tag{3.66}$$

Note that this growth profile satisfies $\gamma^*\left(A_0\right) = 1$, i.e. no growth at the inner boundary. For $C_1 = 0$ there is no growth ($\gamma^* = 1$).

To obtain the discrete homeostatic stress profile $\{\gamma_i^*\}$ from the continuous profile $\gamma^*\left(R^0\right)$, we compute the average according to (3.51). The homeostatic stress is $\boldsymbol{T}\left(\boldsymbol{\gamma}^*\right)$ is computed from the discrete homeostatic stress profile $\{\gamma_i^*\}$ according to (3.59) and (3.60). The homeostatic values $\overline{\boldsymbol{T}}\left(\boldsymbol{\gamma}^*\right)$ are obtained as averages according to (3.62) and (3.64). It is important to note that the homeostatic stress is generated by prescribing a growth profile 3.66, which by definition makes the homeostatic stress is admissible (see Section 3.2.7). The homeostatic values are averages of a Cauchy stress profile which satisfies the system's boundary conditions.

### 3.3.4 Growth Dynamics

In this Section, we propose a growth law which is a generalisation of (3.48) from 2 to $N$ layers. Apart from the number of layers, the main difference between (3.48) and the present growth law are the values for homeostatic stress: In the present case, homeostatic stress is obtained from a linear growth profile in Section 3.3.3. The advantage of the present approach is that for any number of layers, the homeostatic stress is characterised by a single parameter $C_1$ (see (3.66)). The growth law reads

$$\dot{\gamma}_K = \gamma_K\left\{\tilde{K}\left[\overline{T_K^{RR}}\left(\boldsymbol{\gamma}\right) - \overline{T_K^{RR}}\left(\boldsymbol{\gamma}^*\right)\right] + \overline{T_K^{\theta\theta}}\left(\boldsymbol{\gamma}\right) - \overline{T_K^{\theta\theta}}\left(\boldsymbol{\gamma}^*\right)\right\}, \qquad K = 1\ldots N \tag{3.67}$$

In order to consider the stability of (3.67) in the neighborhood of the homeostatic state, we expand (similarly to eq. (3.39))

$$\gamma_K = \gamma_K^* + \varepsilon\tilde{\gamma}_K + \mathcal{O}\left(\varepsilon^2\right), \qquad K = 1, \ldots, N. \tag{3.68}$$

To linear order in $\varepsilon$, the dynamical system simplifies to

$$\dot{\tilde{\boldsymbol{\gamma}}} = J\tilde{\boldsymbol{\gamma}} \tag{3.69}$$

The eigenvalues of the Jacobian $J$ characterise the stability of (3.67) near the homeostatic state. The components of the $N \times N$ matrix $J$ are

$$J_{ij} = \left[ \gamma_i \left( \tilde{K} \frac{\partial \overline{T_i^{RR}}(\boldsymbol{\gamma})}{\partial \gamma_j} + \frac{\partial \overline{T_i^{\theta\theta}}(\boldsymbol{\gamma})}{\partial \gamma_j} \right) \right]_{\boldsymbol{\gamma}=\boldsymbol{\gamma}^*} . \tag{3.70}$$

We characterise the stability in the neighborhood of the homeostatic state as a function of two nondimensional parameters: The mechanical feedback anisotropy parameter $\tilde{K}$ and the slope of the homeostatic growth profile $C_1$. The latter appears in (3.70) through $\boldsymbol{\gamma}^*$, see 3.3.3.

Figure 3.12(a) shows a bifurcation diagram of the stability of the dynamical system (3.12) as a function of $\tilde{K}^{-1}$ and $C_1$ for $N = 9$ layers (note that unlike in Figure 3.6, here we discuss the inverse of $\tilde{K}$ to focus on large circumferential stress, see $(3.37)_2$). The regions are coloured according to the largest real part of the eigenvalues $\lambda_i$ of $J$, that is Max(Re $\lambda_1$, Re $\lambda_2$, ... Re $\lambda_N$). This quantity is simply abbreviated as $\lambda$ in the figure legend. There are three parameter regions: an unstable region (orange), a stable region (blue), and an undecidable region (green) for which $\lambda$ is within a small tolerance of zero. This relatively shallow region of $\lambda$ is further explored in Figure 3.13 and allows us to identify the clearly stable and clearly unstable regions of the diagram. Figure 3.12(b)–(e) shows that for increasing values of $N$ (that is, a refinement of the discretisation), the regions are practically unchanged (b–d), and that the largest eigenvalue of four selected points converges reliably to a finite positive (P1 & P2) or negative (P3 & P4) eigenvalue.

The green shallow region is more explicitly visualised in Figure 3.13. This plot shows in the vertical axis the value of the largest real eigenvalue computed at $\left(\tilde{K}^{-1}, C_1\right)$ from the Jacobian (3.70). The planes $\lambda = \text{tol}$ and $\lambda = -\text{tol}$ are shown in dark gray, and eigenvalues between are assumed to be in the shallow (green) region in which stability cannot be decided from an expansion of $\boldsymbol{\gamma}$ according to (3.68) to first order in $\varepsilon$.

Thus, for this example we see that in the $N$ layer growth dynamics system there exist a region of stability, and a region of instability, which both persist (for large enough $N$) independently of the discretisation. A strongly anisotropic growth law ($\tilde{K}^{-1}$ close to zero or negative) is required for the system to be unstable. We showed for a representative sample of points in the stable and unstable region that convergence

of their eigenvalues for large $N$ is very good. We expect that the stable and unstable region represent the true behaviour of the full (inhomogeneous) system discussed in section 3.1. The intermediate (green) shallow region of eigenvalues has a fine structure not expected in the full system, which is an artefact of the discretisation.

### 3.3.5 Discussion of possible model extensions

**Boundary conditions prescribing pressure** For all models presented in this chapter, we chose a setup of soft elastic annuli surrounding an unchanging nucleus, with no pressure applied at the boundary of the outer annulus (see (3.6) and (3.13)). Mathematically, fixing the deformation at the inner layer and the pressure at the outer layer has computational advantages. When the growth profile is prescribed, the boundary value problem can be separated, so that the deformation map (3.7)can be integrated independently of stress, and its result informs the stress integration (3.13). However, the boundary conditions can be relatively easily generalised without changing most of the analysis and meaning of our averaging approach to growth dynamics and stress averaging. To accommodate a wider class of problems related to biological tubes, we can set the boundary conditions of (3.7)and (3.13) to

$$T^{RR}(A) = P, \qquad T^{RR}(B) = 0, \tag{3.71}$$

where $P$ is once again a prescribed pressure (see e.g. [7] for an analysis of spherical shells in this boundary value). In the boundary value problem 3.71, the integration of $r$ can no longer be executed independently from $T^{RR}$, because the integration domain is not known a priori. In analogy to (3.7), the radial map is

$$r = \sqrt{a^2 + 2\int_A^{R^0} \gamma^r(\tilde{R})\gamma^\theta(\tilde{R})\tilde{R}\mathrm{d}\tilde{R}} \tag{3.72}$$

where $a = r(A)$ is unknown. Inserting (3.72) into (3.7) with boundary conditions (3.71) requires numerical root finding (e.g. Newton's Method) to solve for $a$. In practise, this is a very minor difference and the techniques outlined in this chapter (stress-averaging, $N$-layered cylinder) all apply unaltered — there is simply an additional calculation required to numerically find the integration domain at every time step.

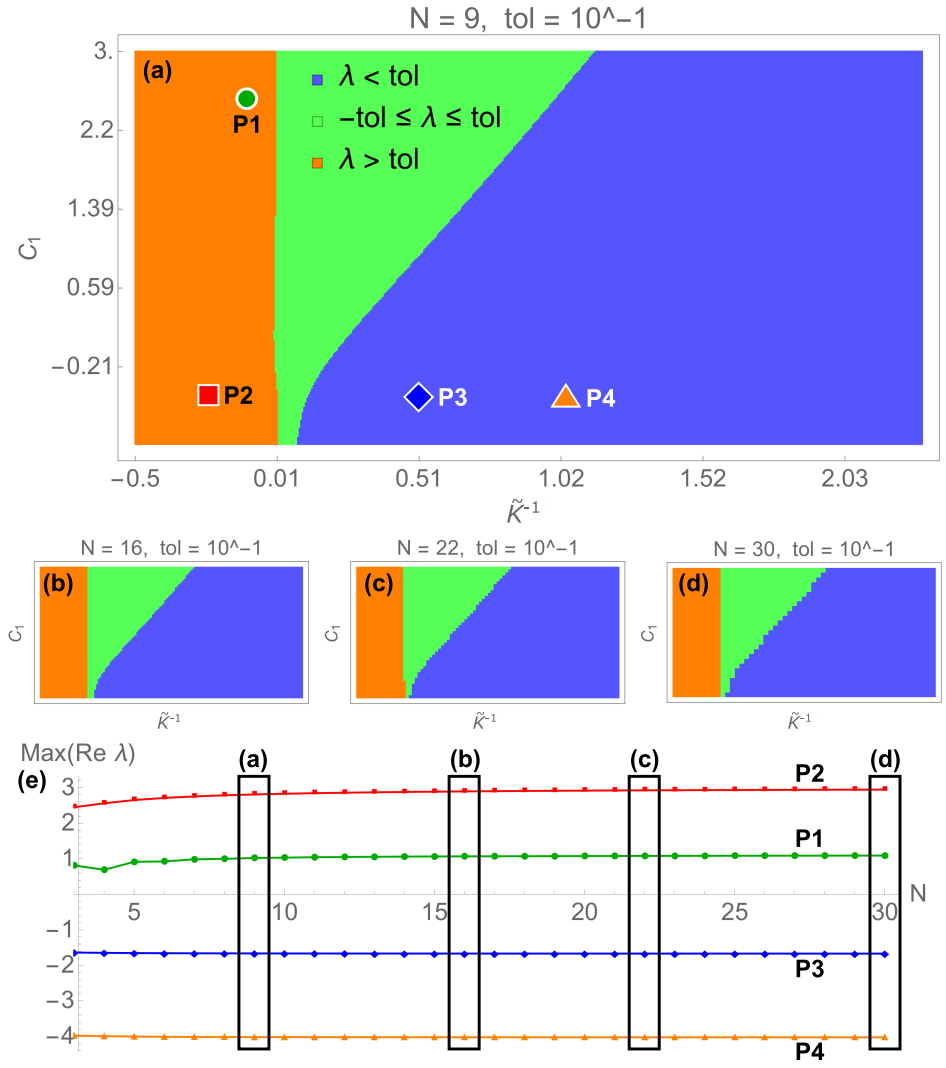


Figure 3.12: Bifurcation diagram and convergence for $N$-layered cylinder system. **(a)**–**(d)**: The unstable (orange) and stable (blue) regions retain their shape for increasing values of $N$. **(e)**: For a representative sample of points P1 to P4, the convergence of the largest eigenvalue is very good (see interpretation in text). The $\left(\tilde{K}^{-1}, C_1\right)$ coordinates are P1 $(0.1, 2.5)$, P2 $(-0.25, -0.5)$, P3 $(0.5, -0.5)$, P4 $(1, -0.5)$. Other parameters are $\mu_1 = 1$, $A_0 = 1$, $A_N = 2$.

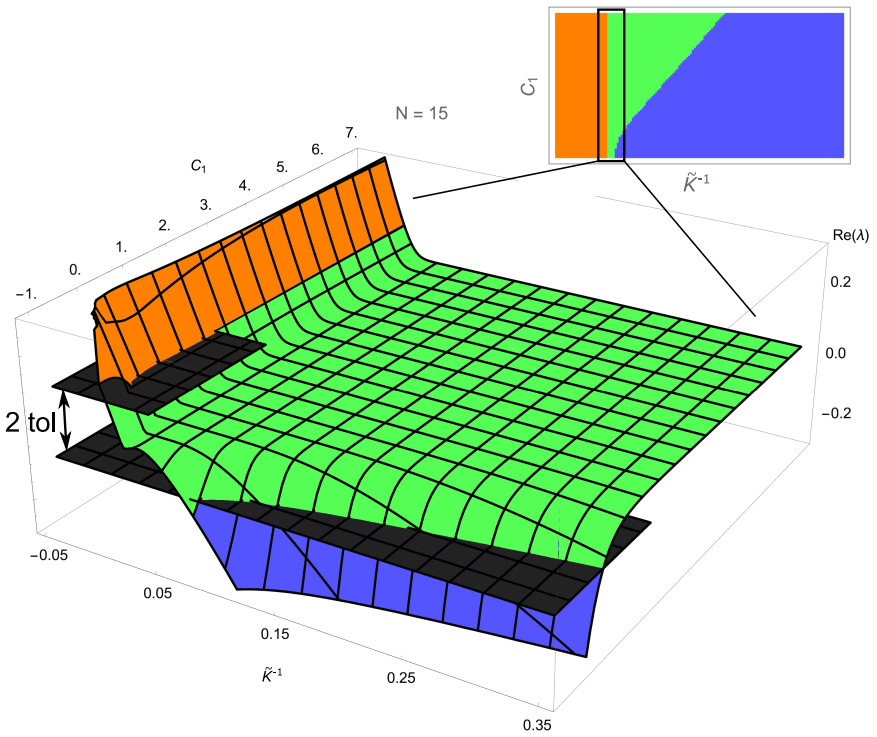


Figure 3.13: Detailed depiction of the shallow (green) region from Figure 3.12. The large shallow region has a fine structure which is an artefact of discretisation and is not expected in the full inhomogeneous system. For this reason, we choose a three colour system in Figure 3.12(a)–(d), in which the shallow region and its fine structure are merged into one region defined by $-\text{tol} \leq \lambda \leq \text{tol}$. The two planes serving as upper and lower bounds of this region are depicted in dark gray. Values above $\lambda = \text{tol}$ are stable, below $\lambda = -\text{tol}$ are unstable.

**Alternative stress-strain relationships** Another straightforward modification to the model would be the use of a different stress-strain relationship. We used the Neo-Hookean model throughout the chapter, which describes an isotropic elastomer. To incorporate for instance strain-stiffening properties observed in many biological materials [18], a Fung material would be an appropriate choice for (3.12), that is

$$\hat{W}_{\text{Fung}} = \frac{\mu}{2\beta}\left[e^{\beta\left(\alpha^2+\alpha^{-2}-2\right)}-1\right] \tag{3.73}$$

where the parameter $\beta$ controls the strain-stiffening. A comprehensive list for nonlinear constitutive laws for elastomers and soft tissues is described in [30].

**Anisotropic growth tensor in addition to anisotropic growth laws** A generalisation of the $N$-disk model to anisotropic growth would also be of interest. In the model presented in Section 3.3, the growth law is already anisotropic, whereas the growth tensor is isotropic. Allowing for an anisotropic growth tensor would increase the size of the dynamical system (3.67) from $N$ to $2N$ equations, as $\dot{\gamma}_K^{RR}$ and $\dot{\gamma}_K^{\theta\theta}$ would need to be specified for $K = 1 \dots N$. It would be interesting to see if the stability results presented in 3.12 would be strongly affected by adding anisotropic growth on top of an anisotropic growth law.

## 3.4 Conclusion

This chapter extends the ideas of growth dynamics driven by homeostasis, and its implications on the stability of such dynamical systems, from a one dimensional to a two dimensional system. The problem studied here, that of a morpho-elastic cylindrical structure, introduces the problem of spatial inhomogeneity.

Table 3.1 shows an overview of the different models presented here, and a succinct summary of the insights they allow. In Section 3.1, we demonstrate numerical solutions for growth dynamics of the full inhomogeneous problem, in which the growth law is a function of the full spatially dependent tensor field $\boldsymbol{T}$. We conclude that this approach makes general statements about stability infeasible on a continuous spatial domain. We therefore considered a simplification of the spatial domain via discretisation (Sections 3.2 and 3.2.7). The focus of these sections was to characterise the dynamics of the full

| | Sec 3.1 | Sec 3.1.4 | Sec 3.2 | Sec 3.2.7 | Sec 3.3 |
|---|---|---|---|---|---|
| **Idea** | General setup, no analysis. | Simulate dynamics numerically. General statements infeasible. | Fully capture dynamics for two layers. Include all equilibria. | Dynamics remains intricate even for admissible homeostasis. | For large $N$ stability of homeostasis has distinct parameter regions. |
| $\boldsymbol{G}$ **symmetry** | anisotropic | anisotropic | isotropic | isotropic | isotropic |
| $\boldsymbol{G}$ **spatial dependence** | $\gamma(R^0)$ continuous | $\gamma_1(R^0)$ continuous, $\gamma_2 = 1$ (passive) | $\gamma_1$, $\gamma_2$ discrete | $\gamma_1$, $\gamma_2$ discrete | $\gamma_1$, $\gamma_2$, ... $\gamma_N$ discrete |
| **Homeostatic stress admissive?** | No | No | No | Yes | Yes |

Table 3.1: Overview of model assumptions made in different sections of this chapter. Brief summary and properties of the models: Symmetry of $\boldsymbol{G}$ (isotropic $\gamma^{RR} = \gamma^{\theta\theta}$ vs anisotropic $\gamma^{RR} \neq \gamma^{\theta\theta}$), spatial dependence (continuous vs discrete, how many layers?), and admissive property of homeostatic stress (does it satisfy system boundary conditions?).

nonlinear system, and we conclude that the number of equilibria and their stability varies greatly and gives rise to highly intricate dynamics which we organise via several bifurcations. We find that only a rather narrow parameter region permits solutions where the system is stable and grown (i.e. added mass). Whether or not the homeostatic state is admissive does not appear to change this conclusion. This complexity of dynamics raises the question about stability of the homeostatic equilibrium. We address this question in Section 3.3. We analyse the dynamics near the homeostatic equilibrium, keeping the discretisation of the system ($N$) as a parameter. We show that clear regions of stability and instability persist independently of the discretisation (for sufficiently large $N$). We expect that these regions represent the true behaviour of the full inhomogeneous system. This result allows us to characterise the stability of a morphoelastic growing cylinder.

# Chapter 4

# Morphomechanics of the Ammonites' shell form

## 4.1 Introduction

In this Chapter, we apply the concept of mechanical feedback to the growth of Ammonites' shells. Their morphology has been very well studied. A set of qualitative observations known as Buckman's Law summarises how the features of the logarithmic shell spiral and the shape of the shell cross-section correlate with the oscillatory ribbing pattern. The shell cross-section is typically on a continuum between a circle and an ellipse.

Our goal in this Chapter is to uncover how a mechanical feedback mechanism similar to homeostasis-driven growth (as presented in Chapter 3) affects the morphology of Ammonites. To achieve this goal, we use as a foundation the morphomechanical model by Moulton et al. [57]. The model is capable of partially addressing Buckman's Law, but cannot address changes to the shape of the shell cross-section and models shell growth as a constant (mechanical feedback is not modeled). We extend in this chapter the model [57] to describe a wider class of morphologies and show how the model predictions are consistent with Buckman's Law. This extended morphomechanical model serves as a foundation to incorporate mechanical feedback and to explore the nuanced effect that a homeostasis-driven growth feedback mechanism has on the shell morphology. Finally, we show that the morphological effect of mechanical feedback is consistent with observation and cannot readily be captured by previous models.

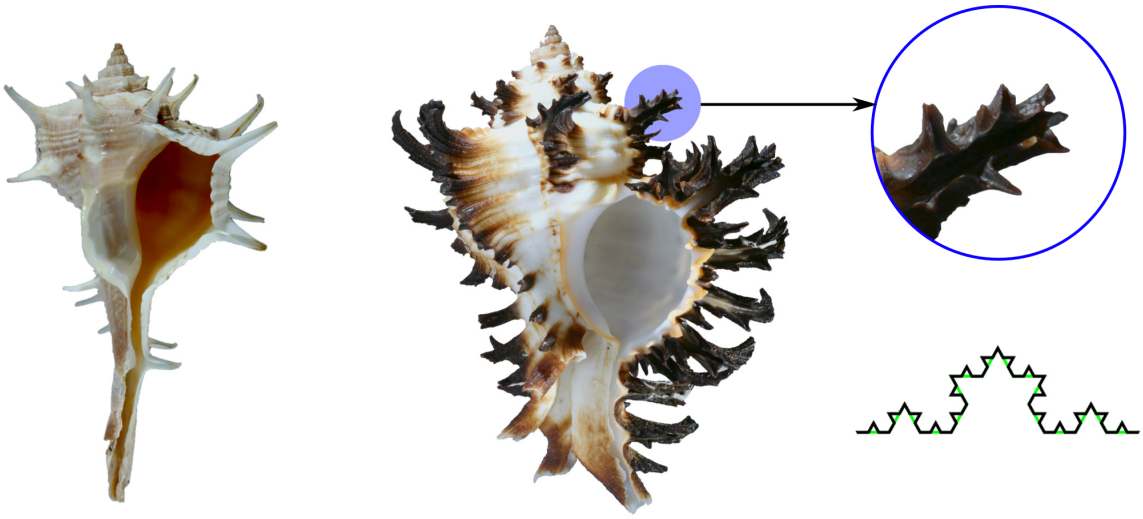

Figure 4.1: Examples of shell ornamentation. **Right**: Shell of the *Hexaplex* family. It is remarkable how the ornamentation exhibits a self-similar structure. Some of the ornamentation is similar to a Koch curve iterated up to degree four (if you consider a triangle as degree 1). **Left**: Shell of the *Chicoreus* family. The characteristic shape of the sharp and regular growth outbursts is studied in [11]. Photographs courtesy of Régis Chirat.

### 4.1.1 A natural 3D printer

Much like with 3D printers, the creation of seashells involves laying down new material in thin, thread-like layers. However, in the case of Ammonites' shells, a soft creature (mollusk) without a compass or access to mathematical software produces astonishingly detailed patterns with great regularity and geometrical precision. Such patterns involve for instance sharp spines and fractal-like ornamentation (see Fig. 4.1). This mollusk's success of building the shell does not rely on specific spatial orientation or a support mechanism for the shell it is building, and wastes no material on any redundant internal scaffolding, which 3D printers tend to do very often. Nevertheless, the rigidity of seashells is remarkable.

### 4.1.2 Seashell growth

In this Chapter we study the ornamentation, that is the ribbing patterns, of Ammonites' shells. As mentioned before, the growth of these shells occurs layer by layer, with approximately one layer created a day, over a period of time of several years to create a full seashell. The mollusk has a soft elastic organ, the mantle, which lines the inside of the shell, see Fig. 4.2. It is attached via a stiff elastic layer, the periostracum,

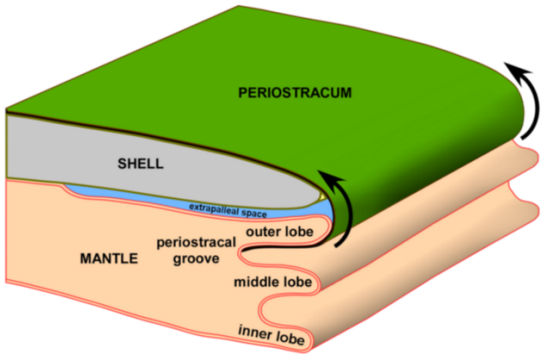


Figure 4.2: Schematic of mantle attached via the periostracum to the shell edge. Reproduced from [57] with permission.

to the already hardened (calcified) shell. For a growth increment to occur, the mantle grows slightly beyond the shell edge, where it takes a particular equilibrium shape governed by the forces in the mantle/periostracum system. In this equilibrium configuration, a chemical substance is secreted in the periostracal grove, which later calcifies into a shell increment. The mantle/periostracum system (from now on referred to as the mantle) acts as its own template in creating the seashell, where every individual shell layer can be interpreted as an elastic equilibrium of the mantle attached to the calcified seashell.

### 4.1.3 Commarginal and Antimarginal Ornamentation

Seashells can typically be described as having a primary base structure and a secondary ornamental structure. The base structure typically takes the form of a smooth coiling, and in the case of Ammonites is very similar to a logarithmic spiral. We argue in this chapter that the secondary (ornamental) structure of Ammonite shells has a mechanical basis.

Shell ornamentation is typically subdivided into commarginal and antimarginal ornamentation. Commarginal ornamentation takes the shape of an oscillatory component to the dilation of the shell aperture (the opening or edge of the shell where new material has most recently been deposited). Antimarginal ornamentation, on the other hand, are patterns that are orthogonal to the shell aperture (see examples in Fig. 4.3). The possibility of modeling antimarginal ornamentation is discussed in Section 5.2.2. In this chapter we focus on commarginal ornamentation of Ammonites.

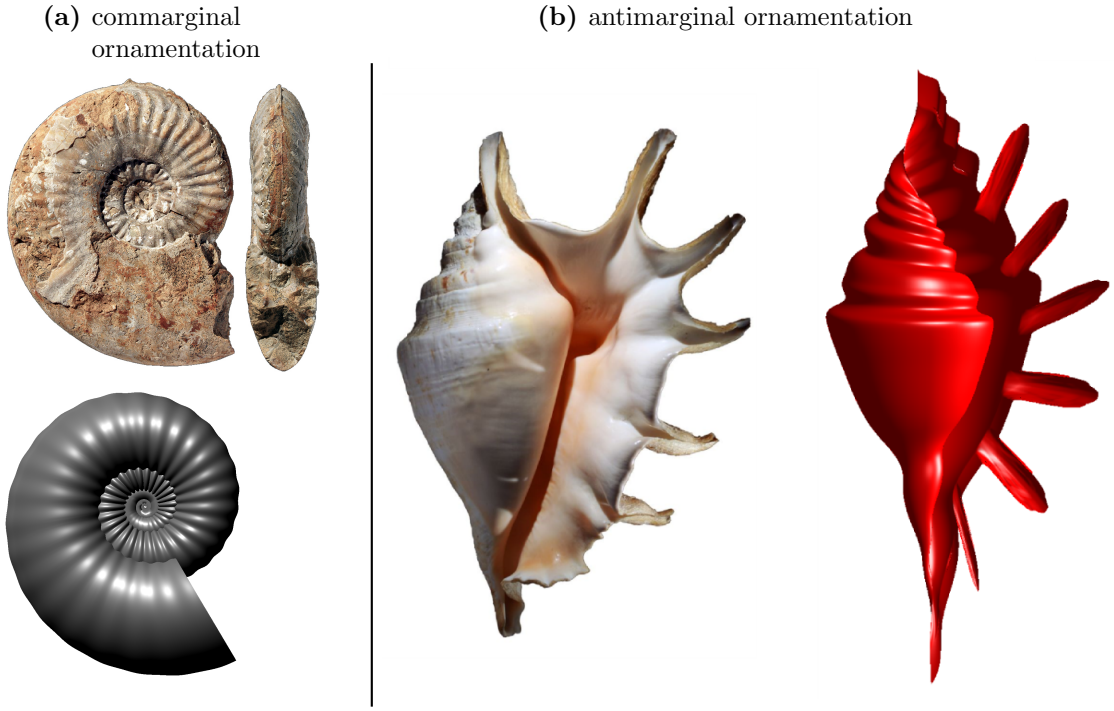


Figure 4.3: Ornamentation types. (a) Commarginal ornamentation on *Sonninia Propinquans* shell. Modelling details explored in Fig. 4.20 in Chapter 4. (b) Antimarginal ornamentation on *Lambis truncata*. The author's implementation of the surface growth framework [55, 56] applied to the model of sharp spines proposed in [11]. Photograph provided by Régis Chirat.

### 4.1.4 Buckman's Law

Ammonites' shells have a characteristic spiral shape and ornamental ribbing pattern (Fig. 4.4). They became extinct 65 million years ago (see [21]) and their form and lineages have been very well studied. A standard set of observations about Ammonites is known as Buckman's law, which relates ribbing oscillation pattern to the spiral coiling, as well as the elliptic shape of the cross-section. It has received much attention because the correlations it predicts are true not only for closely related Ammonite species, but also for distantly related ones.

Buckman's Law relates the shell coiling and shell cross-section shape to the shell ribbing pattern. To state Buckman's Law following the definition of [40], we first introduce the notions of involution and compression.

The key feature in describing the coiling of the shell is called involution. We describe this feature in terms of its opposites, evolute and involute. Evolute means that the outermost whorl (that is a $2\pi$ revolution), which is shown in red in Fig. 4.4 in red,

is relatively small compared to all inner whorls (blue). The opposite term, involute, means that the outer whorl is relatively large compared to all inner whorls.

Ammonites' shells have ellipse shaped cross-sections. The key feature in describing the cross-section shape is compression. A compressed ellipse is thin, with the long axis being in the plane of the coiled shell. On the opposite hand, the term 'circular' describes the proximity to a circular cross-section (see Fig. 4.5). Overall Buckman's statements relate compression and involution to the ribbing pattern of the seashell.

Paraphrasing [40], Buckman's Law comprises two statements:

1.The more evolute the coiling, the more ornamentation. (4.1)

2.The more circular the cross-section, the more ornamentation. (4.2)

The first statement relates the seashell spiral coiling to the ribbing pattern, the second one relates the shape of the seashell cross-section (circle vs. ellipse) to the ribbing pattern.

#### 4.1.4.1 Buckman's first statement

Let us consider the first statement of Buckman, relating coiling to ribbing. In Fig. 4.4, three Ammonite shells with varying degree of involution are depicted. Their degree of compression is approximately the same. The shell to the left is the most evolute, as can be seen from the ratio of the outer whorl (red) to the inner whorls (blue). This shell is in fact the most ornamented (for a quantitative description of ornamentation in terms of relative amplitude and wavelength, see below). In the shell to the right, on the other hand, only the outer whorl is visible at all, which makes it strongly involute. As Buckman's statement predicts, it is indeed very smooth (not ornamented).

#### 4.1.4.2 Buckman's second statement

Buckman's second statement relates compression to ribbing. In Fig. 4.5, once again three Ammonites' shells are shown, this time with varying degrees of compression and approximately equal involution. The shell to the left is the least compressed, and has the highest degree of ornamentation, as consistent with Buckman's second statement.

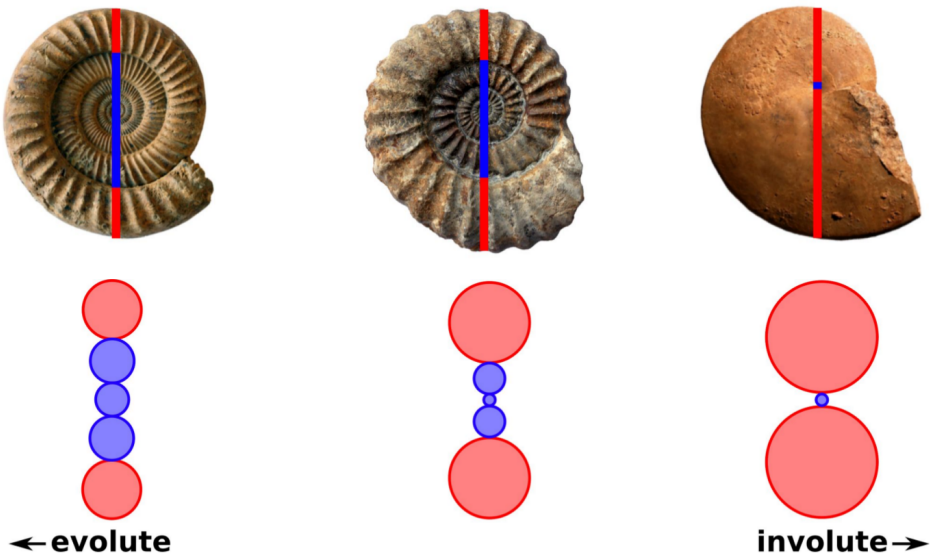


Figure 4.4: Illustration of the first statement of Buckman's law. The shell to the left is the most evolute and the most ornamented, whereas the shell to the right is the most involute and the least ornamented, i.e. the smoothest.

The shell to the right, on the other hand, is the most compressed and has the lowest degree of ornamentation, i.e. it is very smooth.

#### 4.1.4.3 Quantification of Buckman's Law

In [57], the authors proposed a morpho-mechanical model which addressed the first of Buckman's statements very successfully. The authors propose a model based on a force balance between the elastic forces in the mantle and the attachment forces of the mantle/periostracum to the calcified shell. They clearly relate the involution and ornamentation of shells to geometric and physical parameters in their model, proposing that Buckman's law is likely a consequence of fundamental principles of mechanics and growth.

However, the model [57] has some limitations preventing it from addressing Buckman's involution statement. The reason is that the model is built around a circular cross-section, which by definition prevents from any statements about compression. To overcome the limitations, we identified the energy contributions which produce a force balance consistent with the [57] model. This opens up the possibilities of treating more complicated cross-section geometries and makes it possible to incorporate an elliptic cross-section. This allowed us to address both statements of Buckman's law.

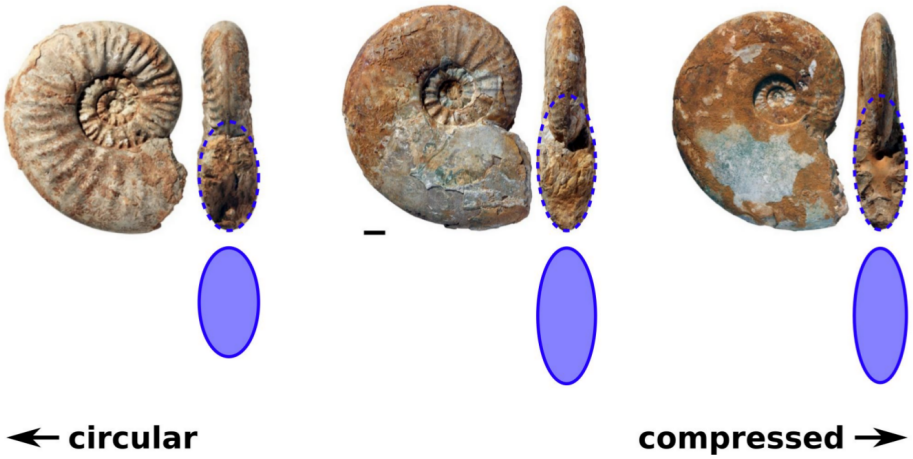


Figure 4.5: Illustration of the second statement of Buckman's law. The shell to the left is the most circular and the most ornamented, whereas the shell to the right is the most compressed and the least ornamented, i.e. the smoothest.

## 4.2 The Lagrangian framework

### 4.2.1 Morphomechanical Model

The basic physical premise for the model is illustrated in Fig. 4.6. The shape of the shell at any given point emerges as a balance between the elastic forces within the shell secreting mantle/periostracum (hereafter referred to as simply the mantle) and a generating zone force, akin to a torque spring, that describes the resistance of the generative zone to change orientation from the portion of the calcified shell to which it is continuously attached. The change to an elliptical geometry means that the stresses within the soft tissue are not constant but rather vary with position along the mantle edge. This added complexity renders a force-balance description, such as presented in [57], impractical. Rather, our approach is to use a Lagrangian energy-based description, which can be formulated in terms of three functions, two of which are independent: the semi-minor axis $b(z)$, the semi-major axis $a(z)$ and the eccentricity $e(z)$ (i.e. a measure of how much it deviates from being circular) of the aperture ellipse, all written as functions of shell arc length $z$ (details are provided in Subsections 4.2.3 and 4.2.5). In order to capture the stresses within the mantle, we also require as an input to the model the reference shape of the mantle, i.e. the shape that it would take in the absence of any interaction with the shell. In our formulation, this is accomplished by positing the functions $\hat{a}(z)$, $\hat{b}(z)$ and $\hat{e}(z)$, such that the mantle is stress-free if and only if

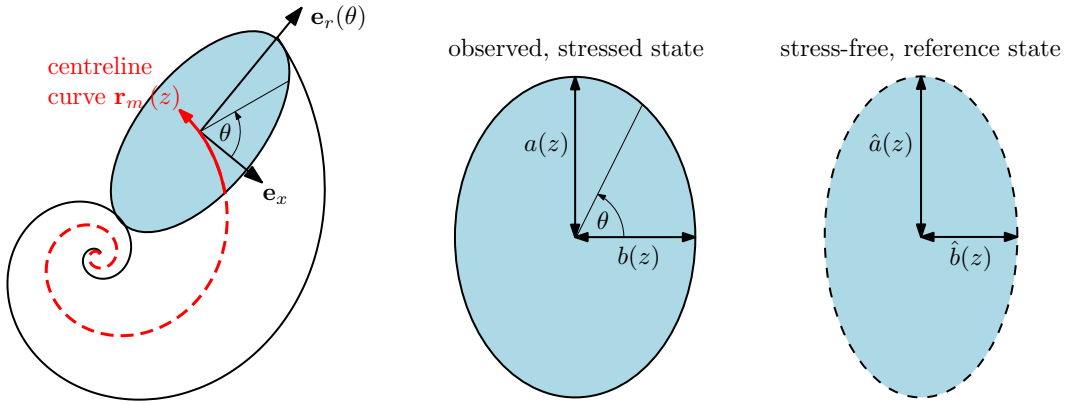


Figure 4.6: Schematic of the model. The mantle and shell aperture are assumed to have an elliptical shape, described by (semi-)major axis $a$ and (semi-)minor axis $b$ and eccentricity $e = \sqrt{1 - b^2/a^2}$, all functions of arc length $z$. The stress-free reference state (dashed ellipse) is the shape the mantle would take if it did not interact with the shell, and is described by $\hat{a}$, $\hat{b}$ and $\hat{e} = \sqrt{1 - \hat{b}^2/\hat{a}^2}$, again functions of $z$.

$a = \hat{a}$, $b = \hat{b}$ and $e = \hat{e}$. The functions $\hat{a}(z)$, $\hat{b}(z)$ and $\hat{e}(z)$ characterize the expansion of the growing mantle and allometric variation (a change in reference eccentricity). The current and reference states of the mantle are illustrated in Figure 4.6.

### 4.2.2 Lagrangian approach

In this section we derive the Lagrangian formulation governing the ornamental pattern. The shell cross section is assumed to have an elliptical shape. The governing equations are derived from an energy minimisation point of view. This leads to a formulation consistent with the previous force balance in the special case of a circle, but is more amenable to analysis in the present case of an elliptical cross-section. Exploiting the fact that the arc length of the shell aperture is much larger than the thickness of the mantle, the mantle (and the growing shell) is modelled as a planar curve, and the energy may be formulated within the framework of elastic rods [58]. The shape of the shell at each point during development is then determined by minimizing the (quasistatic) mechanical energy, arising due to a potential mismatch between the reference state of the growing mantle and the calcifying rigid shell to which it is adhered.

There are three particular contributions to the total energy $E$:

$$E = E_s + E_b + E_g. \tag{4.3}$$

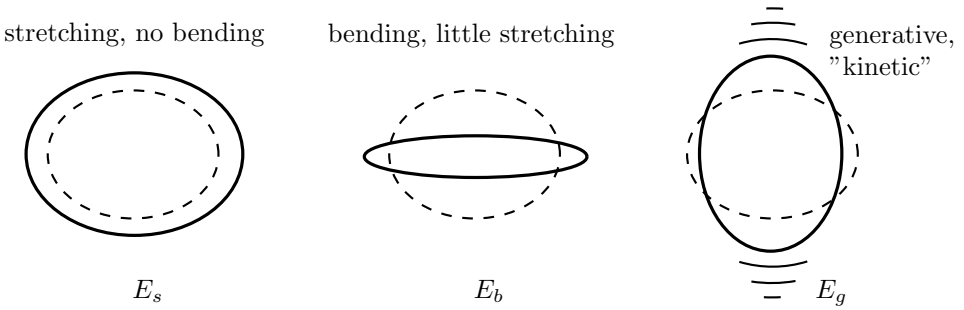


Figure 4.7: Illustration of three energy contributions. The undeformed (reference) shape is dashed. **(a)**: Stretching is tangential to the cross-section curve such that increasing the size of the ellipse builds up stretching energy $E_s$. **(b)**: High curvature points contribute greatly to the bending energy $E_b$. **(c)**: The resistance of the generative zone to change in orientation from the calcified shell is provided by the generative zone energy $E_g$. Mathematically, this contribution shares a certain analogy with the kinetic energy of a vibrating string, which accounts for inertial effects of motion.

Deformations of the mantle from its (stress free) reference shape to the current shape (attached to the shell) induce both a stretching energy $E_s$ and a bending energy $E_b$. The other energy contribution comes from the generative zone and is denoted $E_g$. This term captures the resistance of the generative zone to changes in orientation. A qualitative description of the energies is provided in Figure 4.7, whereas a quantitative description is developed below.

Note that the model takes into account the contact of the mantle with calcified shell material from the previous whorl, i.e. self-contact, creating an overlap region shown in Figure A.5. Overlap is accounted for through a geometric overlap parameter $\tau$ which is discussed in more detail in Appendix A.4.1. However, self-contact is considered in our model purely geometrically, not mechanically, i.e. self-contact is not accounted for in the energy balance. A possible extension of our model to an arbitrary aperture shape, which would allow us to explore the simultaneous formation of commarginal and antimarginal ornamentation (including self-contact), is discussed in Section 5.2.2.

### 4.2.3 Quantitative description of energy contributions

We first require a description of stretching and bending within the elliptical geometry. In planar Cartesian coordinates, an ellipse is parameterised by the curve $\mathbf{r}(\theta) = (a\cos\theta, b\sin\theta)$. An infinitesimal arc length element of this curve is $\mathrm{d}s = r\mathrm{d}\theta$ where $r(\theta) = |\mathbf{r}(\theta)|$. The semi-major axis is $r(0) = a$ and the semi-minor axis is $r(\pi/2) = b$. The base assumption in this paper is that the ribbing pattern of the Ammonites' shell

is parameterised by

$$\mathbf{r}_s(\theta, z) = (a(z)\cos\theta, b(z)\sin\theta, z), \tag{4.4}$$

where $z$ is the growth axis. Note that this description treats the growing shell as a ribbed cone or cylinder; coiling will be subsequently introduced in Sec. A.4 in order to simulate 3D shells.

The objective then is to determine the functions $a(z)$ and $b(z)$. In order to do this, we also require the reference shape, i.e. the shape of the mantle in the absence of any external forces; this is described by the ellipse $\hat{\mathbf{r}}(\theta) = \left(\hat{a}\cos\theta, \hat{b}\sin\theta\right)$ with arc length $\mathrm{d}S = \hat{r}\mathrm{d}\theta$. Explicitly,

$$\mathrm{d}s = \mathrm{d}\theta\sqrt{b^2\cos^2\theta + a^2\sin^2\theta}, \qquad \mathrm{d}S = \mathrm{d}\theta\sqrt{\hat{b}^2\cos^2\theta + \hat{a}^2\sin^2\theta}. \tag{4.5}$$

The local elastic stretch is defined as $\alpha(\theta) = \mathrm{d}s/\mathrm{d}S$ and takes the form

$$\alpha(\theta) = \sqrt{\frac{b^2\cos^2\theta + a^2\sin^2\theta}{\hat{b}^2\cos^2\theta + \hat{a}^2\sin^2\theta}}. \tag{4.6}$$

From this we introduce the quadratic stretching energy

$$E_s = \int_0^{2\pi} \frac{K_s}{2}\left[\alpha(\theta) - 1\right]^2 \mathrm{d}\theta, \tag{4.7}$$

where $K_s > 0$ is a parameter characterizing stretching stiffness. Note that when the observed system coincides with its resting state ($\mathrm{d}s \equiv \mathrm{d}S$), the stretching energy contribution is zero.

In order to define the bending energy, we first compute the Frenet curvature $\kappa$:

$$\kappa(\theta) = \left|\frac{\mathrm{d}\mathbf{r}}{\mathrm{d}\theta} \times \frac{\mathrm{d}^2\mathbf{r}}{\mathrm{d}\theta^2}\right| \Big/ \left(\frac{\mathrm{d}r}{\mathrm{d}\theta}\right)^3. \tag{4.8}$$

The Frenet curvature of an ellipse in the parameterisation $\mathbf{r}(\theta)$ is

$$\kappa(\theta) = \frac{ab}{\left(b^2\cos^2\theta + a^2\sin^2\theta\right)^{3/2}}. \tag{4.9}$$

The reference curvature $\hat{\kappa}$ is defined (as earlier) by replacing $a$ by $\hat{a}$ and $b$ by $\hat{b}$. The

bending energy is then given by

$$E_b = \int_0^{2\pi} \frac{K_b}{2} \left[\alpha(\theta)\,\kappa(\theta) - \hat{\kappa}(\theta)\right]^2 \mathrm{d}\theta \tag{4.10}$$

where $K_b > 0$ is a bending stiffness parameter. Note that if the ellipse is scaled at fixed aspect ratio (i.e. fixed eccentricity) the geometric curvature $\kappa$ decreases. However, the term $\alpha\kappa$ remains constant and ensures that a fixed aspect ratio deformation generates a stretching energy but no bending energy. Details about the Frenet curvature and the quantity $\alpha\kappa$ (the second component of the so called Darboux vector) and their relationship to each other can be found in [58].

The final component is the generative zone energy $E_g$. Its form is

$$E_g = \int_0^{2\pi} \frac{K_g}{2} r'^2 \mathrm{d}\theta, \tag{4.11}$$

where prime denotes a derivative with respect to the arc length $z$ and $K_g > 0$ is the generative zone stiffness parameter.

As discussed in Section 4.2.1, the calcified shell is connected to the not yet calcified shell edge via the mantle/periostracum system. This connecting region is the generative zone.

The generative zone acts akin to a torque spring, resisting a change in angle, so that work must be done to change its orientation with respect to the already calcified shell. It could be thought of as a penalty which becomes greater if the tangent surface of calcified shell material is misaligned with the tangent surface of the mantle.

Let us first consider the absence of generative zone energy. If $\mathrm{d}r(\theta)/\mathrm{d}z$ is constant in $z$, the generative zone is perfectly aligned with old material. In this case, the generative zone energy is $E_g = 0$ and no ribs are formed. This case is illustrated in Figure 4.8(a) if growth is absent and in Figure 4.8(b) when growth is present.

In the presence of generative zone energy ($E_g \neq 0$), $\mathrm{d}^2 r(\theta)/\mathrm{d}z^2 \neq 0$, which gives rise to oscillations, see Figure 4.8(c). The term $E_g$ captures the resistance of the generative zone to changes in orientation from the already calcified portion of the shell to which it is adhered. It provides the mechanical system with a memory of the shell orientation, and is essential to the formation of ribbing.

Another physical interpretation of the generative zone energy is described in Sec-

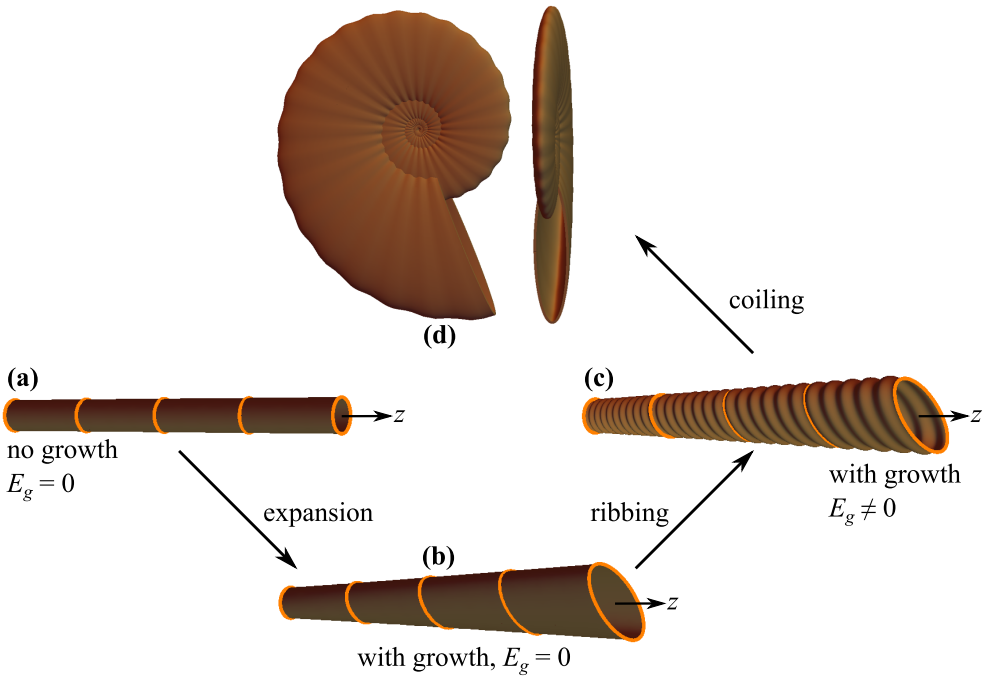


Figure 4.8: Illustration of the effect of generative zone energy $E_g$ on the seashell morphology. In the absence of generative zone energy, oscillations are not formed, even in the presence of growth, as illustrated in **(a)**–**(b)**. Ribbing is formed if $E_g \neq 0$, as shown in **(c)**. The process of transforming the expanding tube to the final morphology is coiling, see **(d)**. Coiling is discussed in detail in Section A.4.

tion 4.2.5, where an analogy between the growing shell and a vibrating elastic ring is discussed.

### 4.2.4 Explicit form of the energy contributions

Here we provide the tools for obtaining explicit forms for $E_s$, $E_b$ and $E_g$ as functions of the major axis $a(z)$, the minor axis $b(z)$ and their derivatives with respect to arc length $z$. We achieve this by expanding the expressions (4.7), (4.10) and (4.11) and by integrating over $\theta$. This allows us to present the energy contributions in a form amendable for a simpler variational approach using the Euler-Lagrange equations, which we demonstrate in the following Subsection.

We start by expanding the bending energy contribution $E_b$ according to (4.10)

$$E_b = I_b^1 + I_b^2 + I_b^3, \tag{4.12}$$

where the integrals $I_b^1$, $I_b^2$ and $I_b^3$ are

$$I_1^b = \int_0^{2\pi} \frac{a^2 b^2 K_b \csc^6\theta}{2\left(a^2+b^2\cot^2\theta\right)^2\left(\hat{a}^2+\hat{b}^2\cot^2\theta\right)}\mathrm{d}\theta, \tag{4.13}$$

$$I_2^b = \int_0^{2\pi} \frac{\hat{a}^2\hat{b}^2 K_b}{2\left(\hat{a}^2\sin^2\theta+\hat{b}^2\cos^2\theta\right)^3}\mathrm{d}\theta, \tag{4.14}$$

$$I_3^b = \int_0^{2\pi} -\frac{a\,\hat{a}\,b\,\hat{b}K_b \csc^6\theta}{\left(a^2+b^2\cot^2\theta\right)\left(\hat{a}^2+\hat{b}^2\cot^2\theta\right)^2}\mathrm{d}\theta. \tag{4.15}$$

We proceed to the generative energy $E_g$ according to (4.11)

$$E_g = I_g^1 + I_g^2 + I_g^3, \tag{4.16}$$

where the integrals $I_g^1$, $I_g^2$ and $I_g^3$ are

$$I_g^1 = \int_0^{2\pi} \frac{a^2\left(a'\right)^2 K_g\cos^2\theta}{2a^2+2b^2\tan^2\theta}\mathrm{d}\theta, \tag{4.17}$$

$$I_g^2 = \int_0^{2\pi} \frac{a\,b\,a'\,b'\,K_g}{a^2\csc^2\theta+b^2\sec^2\theta}\mathrm{d}\theta, \tag{4.18}$$

$$I_g^3 = \int_0^{2\pi} \frac{b^2\left(b'\right)^2 K_g\sin^2\theta}{2a^2\cot^2\theta+2b^2}\mathrm{d}\theta. \tag{4.19}$$

Finally, we consider the stretching energy $E_s$ according to (4.7)

$$E_s = I_s^1 + I_s^2 + I_s^3, \tag{4.20}$$

where the integrals $I_s^1$, $I_s^2$ and $I_s^3$ are

$$I_s^1 = \int_0^{2\pi} -K_s\sqrt{\frac{a^2\sin^2\theta+b^2\cos^2\theta}{\hat{a}^2\sin^2\theta+\hat{b}^2\cos^2\theta}}\mathrm{d}\theta, \tag{4.21}$$

$$I_s^2 = \int_0^{2\pi} \frac{b^2\cos^2\theta K_s}{2\hat{a}^2\sin^2\theta+2\hat{b}^2\cos^2\theta}\mathrm{d}\theta, \tag{4.22}$$

$$I_s^3 = \int_0^{2\pi} \frac{a^2\sin^2\theta K_s}{2\hat{a}^2\sin^2\theta+2\hat{b}^2\cos^2\theta}\mathrm{d}\theta. \tag{4.23}$$

Note that we neglected constant energy contributions, as these do not affect the

variational solution of energy minimisation.

The only integral to which we were unable to find a closed form solution with the *Mathematica* software is $I_s^1$. To obtain a closed form approximation, we consider an expansion in the proximity of the reference axes,

$$a = \hat{a} + \varepsilon\tilde{a} + \mathcal{O}\left(\varepsilon^2\right), \qquad b = \hat{b} + \varepsilon\tilde{b} + \mathcal{O}\left(\varepsilon^2\right). \tag{4.24}$$

This allows us to express $I_s^1$ as

$$\begin{aligned} I_s^1 = -2\pi K_s - \varepsilon \int_0^{2\pi} \frac{K_s\left(\hat{a}\tilde{a}\sin^2\theta + \hat{b}\tilde{b}\cos^2\theta\right)}{\hat{a}^2\sin^2\theta + \hat{b}^2\cos^2\theta}\mathrm{d}\theta \\ - \varepsilon^2 \int_0^{2\pi} \frac{\sin^2(2\theta)K_s\left(\hat{b}\tilde{a} - \hat{a}\tilde{b}\right)^2}{8\left(\hat{a}^2\sin^2\theta + \hat{b}^2\cos^2\theta\right)^2}\mathrm{d}\theta + \mathcal{O}\left(\varepsilon^3\right), \end{aligned} \tag{4.25}$$

and we can find closed form solutions to both integrands in *Mathematica*.

To summarise, we note that all integrals, that is $I_s^i$ (in the form (4.25)), $I_b^i$ and $I_g^i$ (where $i \in \{1,2,3\}$) are closed form functions of $a, b, a', b'$ and the reference quantities $\hat{a}, \hat{b}$. The dependence on $\theta$ can be integrated out completely. We note that in future models, it will be interesting to take into account a $\theta$-integration over less than $2\pi$ in the case of overlapping shells ($\tau > 1$, see subsection A.4).

### 4.2.5 Euler-Lagrange equations

The energies (4.7), (4.10), and (4.11) define the Lagrangian $L$, a functional of the major and minor axes $a(z)$ and $b(z)$, their rates of change along the arc length $a'(z)$ and $b'(z)$, as well as the reference functions $\hat{a}(z)$ and $\hat{b}(z)$. It has the form

$$L\left[a(z), a'(z), b(z), b'(z), z\right] = E_g - (E_s + E_b). \tag{4.26}$$

We note that we can express the Lagrangian in terms of the integrals $I_s^i$, $I_b^i$ and $I_g^i$ as

$$L = \sum_{i=1}^{3} I_g^i - \left(I_s^i + I_b^i\right). \tag{4.27}$$

The ribbing pattern is then governed by solutions to the Euler-Lagrange equations

$$\frac{\partial L}{\partial a} - \frac{\mathrm{d}}{\mathrm{d}z}\left(\frac{\partial L}{\partial a'}\right) = 0 \qquad \text{and} \qquad \frac{\partial L}{\partial b} - \frac{\mathrm{d}}{\mathrm{d}z}\left(\frac{\partial L}{\partial b'}\right) = 0\,. \tag{4.28}$$

The Lagrangian (4.26) is analogous with the dynamic mechanical problem of a vibrating ellipse-shaped string. In this analogy, $E_g$ would be identified with the kinetic energy, the arc length $z$ would be identified with time, and the term $E_s + E_b$ would describe the potential energy of the vibrating string due to stretching and bending.

The Lagrangian framework allows us to illustrate the generative zone through a classical mechanical analogy. If we replace the derivative $\mathrm{d}\left(\ldots\right)/\mathrm{d}z$ in (4.11) by a time derivative $\mathrm{d}\left(\ldots\right)/\mathrm{d}t$ (also denoted by an overdot), we obtain a Lagrangian of the form

$$L = T - V, \qquad T = \frac{K_g}{2}\dot{r}^2, \qquad V = E_s + E_b \tag{4.29}$$

where $T$ is the kinetic energy and $V$ is the potential energy (here it is the sum of bending and stretching energy, i.e. the total elastic energy of the system). The classical system (4.29) describes a vibrating elastic ring and offers the formal (albeit not necessarily physical) analogy between the generative zone energy and kinetic energy. Formally, the generative energy produces oscillations in the same way as inertia would produce oscillations, which is by transforming elastic into potential energy and vice versa. While the physical process of Ammonite morphogenesis is far too slow to be driven by inertia, the formal analogy between generative energy in a slow growing system and kinetic energy in a fast vibrating system may contribute to building intuition for the form of the generative zone energy.

## 4.3 Ribbing oscillations

In order to simplify the study and obtain a clearer picture, it is also useful to consider a reduced model, in which we make a simplifying restriction on the Lagrangian (4.26): we consider the case $e \equiv \hat{e}\,(z)$, that is, the eccentricity is prescribed as a given function of the arc length $z$. This assumption allows us to remove the effect of bending energy while preserving the elliptical geometry, enabling us to isolate the role of eccentricity in the pattern.With this assumption, there is only one independent function, so that for

example ribbing on the low curvature size automatically determines ribbing on the high curvature side ($a$ and $b$ satisfy an algebraic relation). Below, we proceed to analyse the trends predicted in the reduced model, which is more analytically tractable and enables for direction comparison with our previous results in the circular geometry [57]. We then return to the full model in Section (4.3.2) to consider synchronous variations and to demonstrate numerically that the same general trends are captured by both models.

### 4.3.1 Reduced model - prescribed eccentricity

In this section we will describe the ribbing patterns of Ammonites' shells as solutions to simplified versions of (4.28). As an initial step, we make a simplifying restriction on the Lagrangian (4.26) and consider the case $e \equiv \hat{e}(z)$. This leads to a more analytically tractable system and enables for direction comparison with [57]. This restriction is later relaxed in Section (4.3.2).

To analyse the system under the restriction $e = \hat{e}(z)$, we make the following variable transformation

$$a(z) = \frac{b(z)}{\sqrt{1-\hat{e}^2(z)}}, \qquad \text{and} \qquad \hat{a}(z) = \frac{\hat{b}(z)}{\sqrt{1-\hat{e}^2(z)}}. \tag{4.30}$$

This allows us to express the functional as

$$L\left[b(z), b'(z), z\right]. \tag{4.31}$$

#### 4.3.1.1 Constant eccentricity, linear expansion

To make further analytical progress, we first focus on the case $e = \hat{e} = \text{const}$. We also assume that the reference length of the minor axis increases linearly according to

$$\hat{b}(z) = \hat{b}_0 + \gamma_b z, \tag{4.32}$$

where $\hat{b}_0 > 0$ is the initial reference length and $\gamma_b > 0$ is the expansion rate. We also introduce the two non-dimensional constants

$$k := \frac{K_s}{K_g}, \qquad \text{and} \qquad f := \frac{2-2\hat{e}_0^2}{2-\hat{e}_0^2}. \tag{4.33}$$

With $\hat{b}(z)$ according to (4.32), the Lagrangian (4.31) takes the form

$$L = b'^2(z) - fk\left(\frac{b(z)}{\hat{b}(z)} - 1\right)^2 . \tag{4.34}$$

Taking into account that the Lagrangian (4.34) only involves a single function $b(z)$, the lone Euler-Lagrange equation $(4.28)_2$ is

$$b''(z) + \frac{fk}{\hat{b}(z)}\left(\frac{b}{\hat{b}(z)} - 1\right) = 0 . \tag{4.35}$$

For initial values, we impose for simplicity

$$b(0) = \hat{b}_0 + \delta b, \qquad \text{and} \qquad \frac{\mathrm{d}b}{\mathrm{d}z}(0) = \gamma_b, \tag{4.36}$$

which fixes the initial slope to that of the reference geometry.

The initial value problem (4.35), (4.36) can be solved exactly. Defining

$$\omega = \frac{\sqrt{4fk - \gamma_b^2}}{2\gamma_b} , \qquad A = \frac{\sqrt{1 + 4\omega^2}}{2\omega} \qquad \text{and} \qquad \nu = -\arctan\frac{1}{2\omega} , \tag{4.37}$$

we obtain the solution

$$b(z) = \hat{b}(z) + \delta b\, A\sqrt{\frac{\hat{b}(z)}{\hat{b}_0}}\cos\left(\omega \log\frac{\hat{b}(z)}{\hat{b}_0} - \nu\right) . \tag{4.38}$$

We note that in the limit $\gamma_b \to 0$ (i.e. no expansion of the reference shape) this solution takes the form

$$b(z) = \hat{b}(z) + \delta b\, \cos\left(\frac{\sqrt{kf}}{\hat{b}_0} z\right) , \tag{4.39}$$

i.e. simple harmonic motion. In the case of a circular cross-section, with $\hat{e}_0 = 0$ (for which eq. (4.33) implies $f = 1$), we find that (4.38) together with (4.37) reproduces Equations (8) and (9) of [57]. In any case, given $b(z)$, the function $a(z)$ is obtained from $(4.30)_1$.

To quantify the increase/decrease in ornamentation referred to in Buckman's Law (see Section 4.1.4), we introduce various quantities characterising the ribbing oscillation: The relative oscillation, the relative amplitude and the wavelength of the ribbing

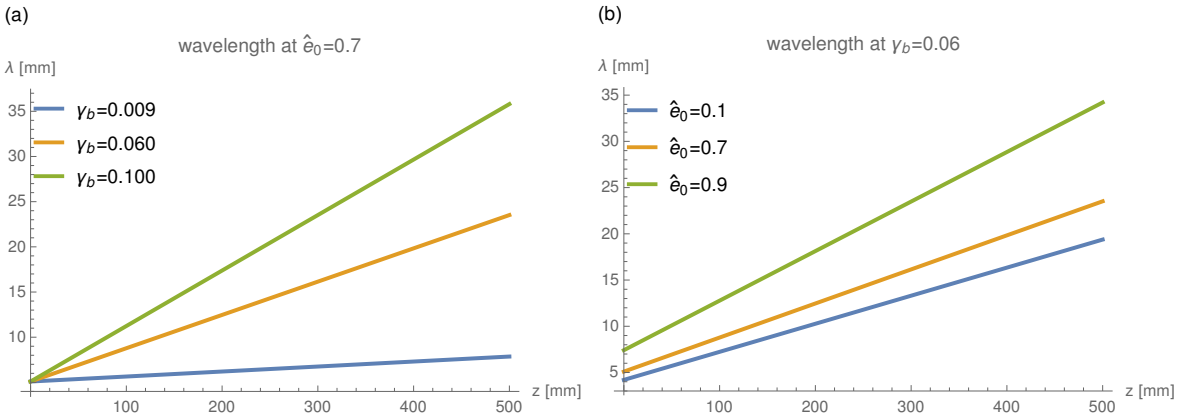


Figure 4.9: Wavelength during development for varying expansion. The wavelength increases both with the expansion rate $\gamma_b$ and the reference eccentricity $\hat{e}_0$. All simulation parameters can be found in Section A.5.

pattern.

**Relative oscillation and relative amplitude of ribbing pattern** The relative oscillation is defined as the current minor axis divided by its reference length, $b/\hat{b}$. For the model given by (4.38), the relative oscillation $b/\hat{b}$ coincides with $a/\hat{a}$. If the relative oscillation amplitude decreases over the lifetime of a shell (i.e. as a function of the arc length $z$), the 3D morphology of the shell appears smoother (less ornamented).

The relative amplitude is defined as the distance between the upper and lower enveloping curves ($\eta_+$ and $\eta_-$) of the relative oscillation. The enveloping curves can be obtained from (4.38) and have the form

$$\eta_{\pm}(z) = 1 \pm \left(\frac{\delta b\, A}{\sqrt{\hat{b}_0}}\right) \frac{1}{\sqrt{\hat{b}_0 + \gamma_b z}}\,. \tag{4.40}$$

As the expansion rate $\gamma_b$ increases, the relative amplitude decreases according to (4.40), i.e. we expect a smoother shell morphology for larger expansion rates.

### Wavelength of ribbing pattern

The wavelength $\lambda(z)$ of the oscillation $b(z)$ is $2\pi$ times the inverse of its frequency, which is the derivative of the cosine-argument of (4.38) with respect to $z$:

$$\lambda(z) = 2\pi \left[\frac{\mathrm{d}}{\mathrm{d}z}\left(\omega \ln \frac{b(z)}{\hat{b}_0} - \nu\right)\right]^{-1} = 2\pi \left[\frac{K_s}{K_g}\left(\frac{2-2\hat{e}_0^2}{2-\hat{e}_0^2}\right) - \frac{\gamma_b^2}{4}\right]^{-\frac{1}{2}} \left(\hat{b}_0 + \gamma_b z\right) \tag{4.41}$$

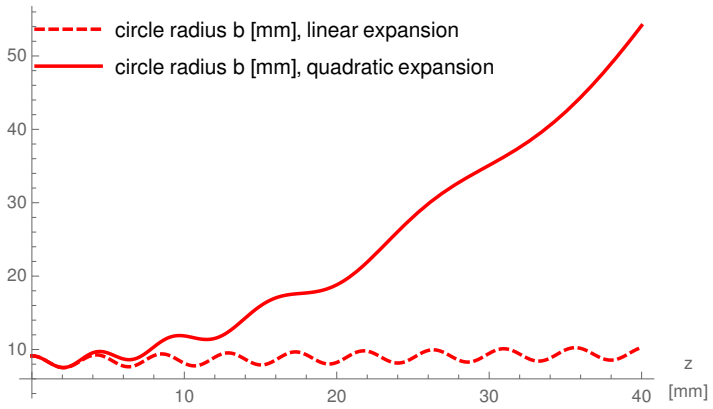


Figure 4.10: How various types of expansion influence the ribbing pattern. Comparison between linear expansion (4.32) and quadratic expansion (4.43) for a circle ($\hat{e}_0 = 0$). All simulation parameters can be found in Section A.5.

The wavelength depends linearly on the arc length $z$, but its dependence on $\gamma_b$ and $\hat{e}_0$ is nonlinear. In Figure 4.9(a), we plot the wavelength for three values of $\gamma_b$. In Figure 4.9(b), $\hat{e}_0$ is varied instead of $\gamma_b$. The wavelength increases both with the expansion rate and the reference eccentricity, which is a trend that persists even in more complex cases when the wavelength cannot be explicitly computed analytically, as we will show below. With increasing wavelength we expect a smoother shell morphology.

#### 4.3.1.2 Allometric variation

In Section 4.3.1.1 we considered a constant eccentricity. In real shells, however, the cross-section shape frequently changes over the life time of a shell, starting with a circular cross-section and ending up with a more or less compressed ellipse in the adult stages. This feature is captured in our model by allometric variation in which the eccentricity is a non-linear function of the arc length:

$$\hat{a} = \hat{a}_0 + \gamma_a z\,, \qquad \hat{b} = \hat{b}_0 + \gamma_b z\,, \qquad \text{and} \qquad \hat{e}\,(z) = \sqrt{1 - \frac{\hat{b}^2\,(z)}{\hat{a}^2\,(z)}}\,. \tag{4.42}$$

We refer to this mode of expansion as allometric variation. The Euler-Lagrange equations of the reduced model $(4.28)_1$ must be solved numerically to obtain the oscillations of minor and major axis.

#### 4.3.1.3 Constant eccentricity, nonlinear expansion

In Section (4.3.1.1) we considered a linear expansion (4.32) with constant eccentricity. This relationship may be further explored by considering a nonlinear expansion:

$$\hat{b} = \hat{b}_0 + \gamma_b z^2 \tag{4.43}$$

To simulate the ribbing pattern for nonlinear expansion, we solve the resulting Euler-Lagrange equation $(4.28)_2$ numerically for $b(z)$. Again, $a(z)$ is obtained by $(4.30)_1$.

Figure 4.10 compares the ribbing pattern of the quadratic expansion to the linearly expanding case, showing that the increase in wavelength for quadratic expansion is considerably larger compared to a linear expansion.

We extract from the linear expansion result 4.38 (which is illustrated in Figure 4.13) and from the nonlinear expansion result of Figure 4.10 the trend that an increased expansion leads to a diminished ribbing pattern. These results show that oscillations tend to damp out more quickly (decrease in relative amplitude), when expansion rate increases.

### 4.3.2 Full model

As noted in Section 4.3.1, in the reduced model the major axis $a(z)$ and minor axis $b(z)$ are not independent functions. This is due to the fact that the eccentricity is prescribed as a given function of the arc length $z$, which greatly simplifies the analysis. In this section we present the full model in which we relax the restriction of prescribed eccentricity and treat $a(z)$ and $b(z)$ as independent variables. We show that the full model displays the same general trends as the reduced model, justifying *a posteriori* the use of the reduced model. The computational results of the full model shown in Figures 4.11 and 4.12 which compare directly with Figure 4.14, which shows computational results of the reduced model

We now consider the Lagrangian of the full model (4.26) with two independent functions and compare its solutions to the reduced one degree of freedom system (4.31). The presence of bending energy (4.10) in the unconstrained Lagrangian (which is absent

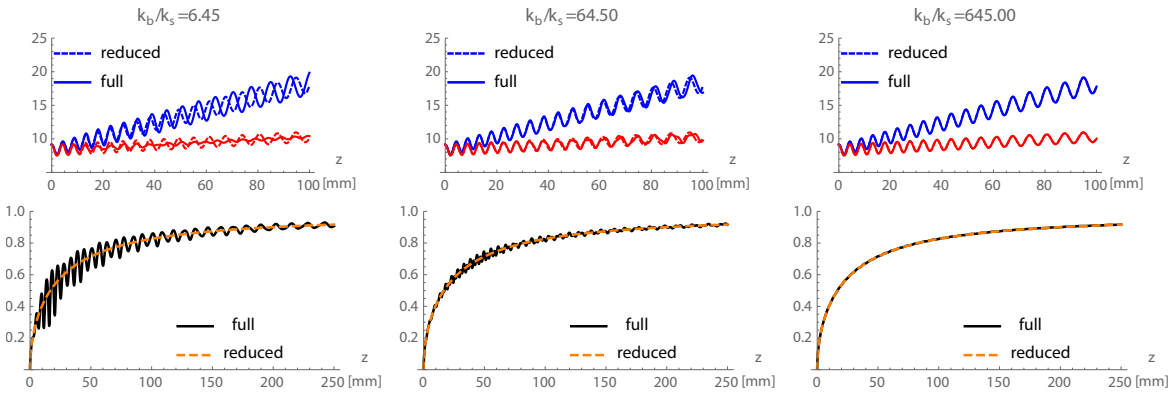


Figure 4.11: Comparison of full and reduced models for varying values of $k_b/k_s$. Other parameters are as in Figure 4.14(I.b)–(III.b), i.e. $\gamma_a = 0.1$, see 4.3.1.2. The initial conditions for the second degree of freedom are $a(0) = \hat{a}_0 + \delta a$ and $a'(0) = \gamma_a$.

for $e = \hat{e}$) requires that we introduce a new dimensionless parameter

$$k_b = \frac{K_b}{K_g} \tag{4.44}$$

in addition to $(4.33)_1$.

**Relationship between full and reduced systems** In the reduced model, there is no bending energy contribution. Hence the reduced model is obtained from the full model in the limit $k_b/k_s \to \infty$. That is, with infinite bending stiffness, the reference ellipse will only deform in a manner that avoids bending, i.e. for which $e(z) = \hat{e}(z)$. To see this numerically, we produce in Figure 4.11 a version of Figure 4.14 (centre column), comparing the full and reduced model for increasing values of $k_b/k_s$. This gives clear numerical evidence of convergence of the models with increasing $k_b/k_s$.

**General trends of full model** To demonstrate that the full model preserves the general trends of the reduced model, we plot in Figure 4.12 an analogous version of Figure 4.14, but within the unconstrained Lagrangian and with a fixed (and relatively low) value $k_b/k_s = 6.45$ throughout. Figure 4.12 shows the same trends as Figure 4.14. Namely, the full model, while less amenable to analytical progress, predicts an increase in ribbing wavelength and decrease in relative ribbing amplitude with increasing expansion rate $\gamma_a$.

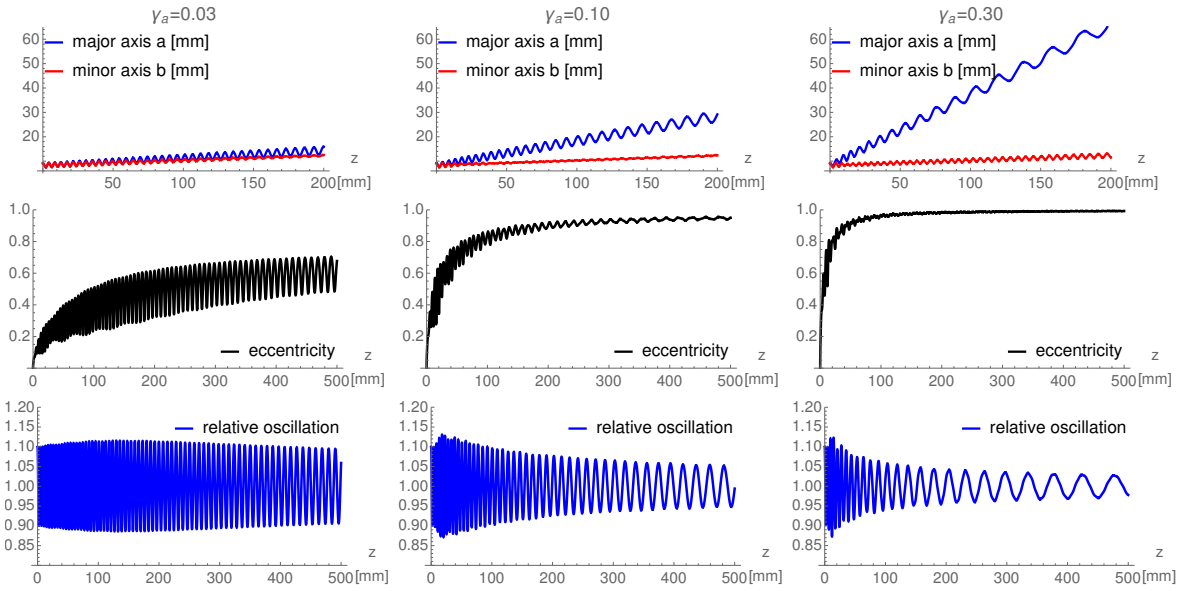


Figure 4.12: Ribbing trends predicted by full model. Parameters are as in main text Figure 4.14, see 4.3.1.2. The initial conditions for $a(z)$ are $a(0) = \hat{a}_0 + \delta a$ and $a'(0) = \gamma_a$. The value for $k_b/k_s$ is 6.45.

## 4.4 Quantification of Buckman's Law

### 4.4.1 Buckman's first statement: Relationship between expansion rate and ribbing

In this Section, we examine simulation results of the model of constant eccentricity 4.3.1.1. The ribbing oscillation of the minor axis $b(z)$ is described by (4.38), and the major axis $a(z)$ follows $b(z)$ with a larger amplitude, as can be seen from (4.30). In Figure 4.14, we show the oscillations of the major axis and minor axis plotted over the arc length $z$ of the centreline spiral. We can see from the 3D plots in Figure 4.14(III.a–III.c) that larger expansion rates $\gamma_b$ produce more evolute shells (see Figure 4.4), which allows us to identify the expansion parameter $\gamma_b$ with the involution described in the context of Buckman's Law in Section 4.1.4. For large expansion rates $\gamma_b$, the oscillation and amplitude in Figure 4.14(II.a–II.c) decreases most rapidly and the wavelength increases most rapidly. This is consistent with our findings from 4.3.1.1 where we showed the dependence of the relative amplitude enveloping curve $\eta_{\pm}(z)$ on $\gamma_b$ (see (4.40)) as well as the dependence of wavelength $\lambda_z$ on $\gamma_b$ (see (4.41)). The model simulations of Figure 4.14 are consistent with Buckman's first statement (4.1): the more evolute the shell (larger expansion rate $\gamma_b$), the less ornamented it is (faster

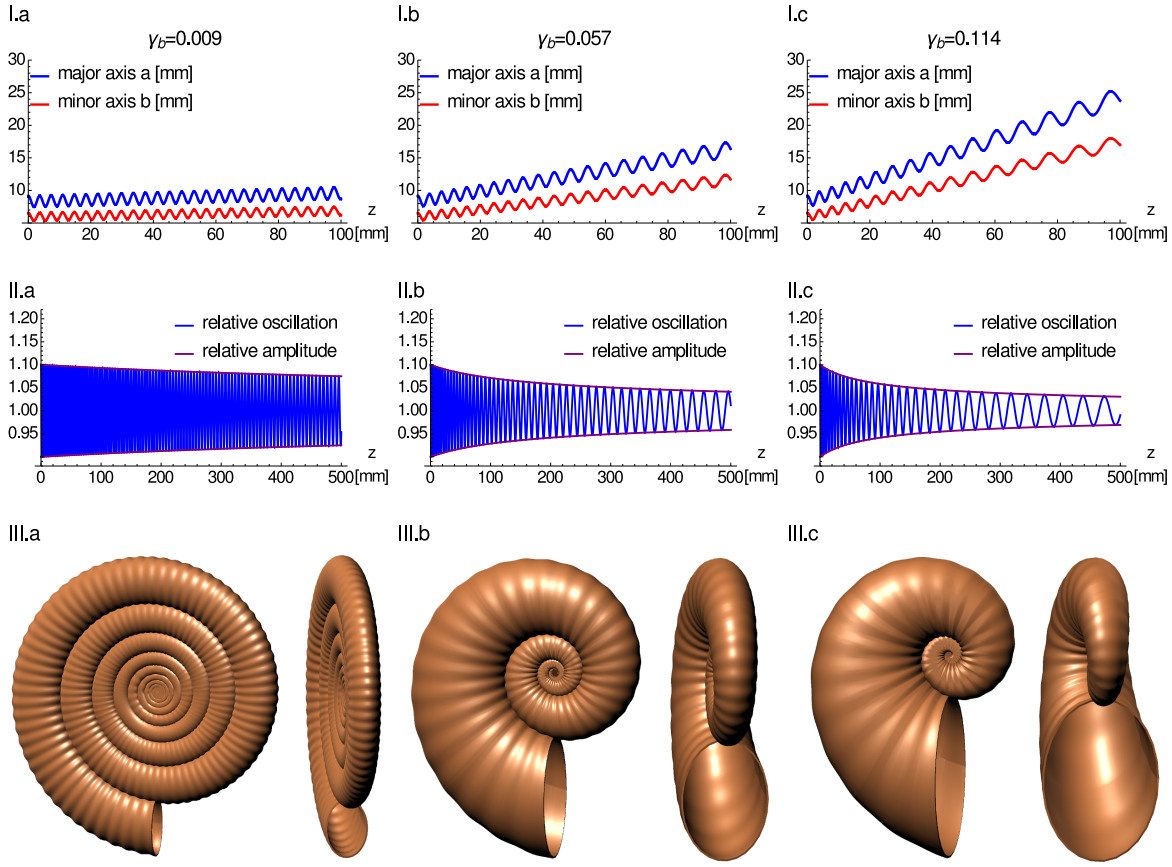


Figure 4.13: Effect of expansion rate $\gamma_b$ on the ribbing pattern at constant eccentricity. In all three cases, the material properties are identical so that the variation in ornamental pattern is purely a manifestation of the growth mechanics and the difference in geometry, that is, the expansion rate. **I.a - I.c**: Oscillations of major and minor axes. A higher expansion rate causes a faster increase in wavelength (see Fig. 4.9). **II.a - II.c**: Relative oscillation $b/\hat{b}$ (which coincides with $a/\hat{a}$), as well as relative amplitudes, which are the enveloping curves. The larger the expansion rate $\gamma_b$, the faster is the decrease in relative amplitude and increase in wavelength, leading to an increasingly smooth shell (see Section 4.3.1). **III.a - III.c**: Rendering of coiled seashell surface, in which the coiling properties result from the expansion rate (see Section A.4). All simulation parameters can be found in Section A.5.

decay of relative amplitude, increase of wavelength).

### 4.4.2 Buckman's second statement: Relationship between eccentricity and ribbing

In our examination of Buckman's first statement through our morphomechanical model, we identified the expansion rates $\gamma_b$ with involution in Buckman's first statement 4.1. Previously, we introduced the eccentricity (see Figure 4.6) to describe the shell cross-section, which is addressed in Buckman's second statement 4.2. For the simulation in Figure 4.14, we investigated the effect of the expansion rate $\gamma_b$ on the ornamentation while keeping the actual and reference constant $e \equiv \hat{e}(z) = \hat{e}_0$. Buckman's second statement can be described in our model as the opposite case in which $\gamma_b$ is held constant but $\hat{e}_0$ is varied. In Figure 4.9(b) we investigate the effect of different values of $\hat{e}_0$ on the wavelength $\lambda$ (see (4.41)). We show that the smallest value of $\hat{e}_0$ produces smallest wavelength increase and therefore the most ribbed shell. The same correlation between reference eccentricity and ribbing can be obtained by considering the relative amplitude. We note that the highest value of $\hat{e}_0$ will produce the greatest decrease in relative amplitude (i.e. the smoothest shell), as can be seen from 4.40 if $\hat{b}_0 = \hat{a}_0\sqrt{1-\hat{e}_0^2}$ is replaced according to $(4.30)_2$. Our findings regarding the amplitude and wavelength as functions of $\hat{e}_0$ are consistent with Buckman's second statement (4.2) which predicts that the most circular cross-section (lowest value of $\hat{e}_0$) will correlate with the most ornamented shell.

### 4.4.3 Conclusion: Both parts of Buckman's Law

Finally we can present a simulation in which Buckman's statements are acting together. Real Ammonites' shells have approximately circular cross-sections in their juvenile stages [21], but then over their lifetime evolve to have a compressed ellipse cross-section in their adulthood, or on the contrary remain fairly circular throughout morphogenesis. We model the evolution of the cross-section shape over the shell's lifetime through allometric variation (see Section 4.3.1.2). In Fig. 4.14, the plots II.a-II.c show the eccentricity plotted over arc length for shells with an increasing expansion rate. To be consistent with the circular cross-section in the juvenile stages, all eccen-

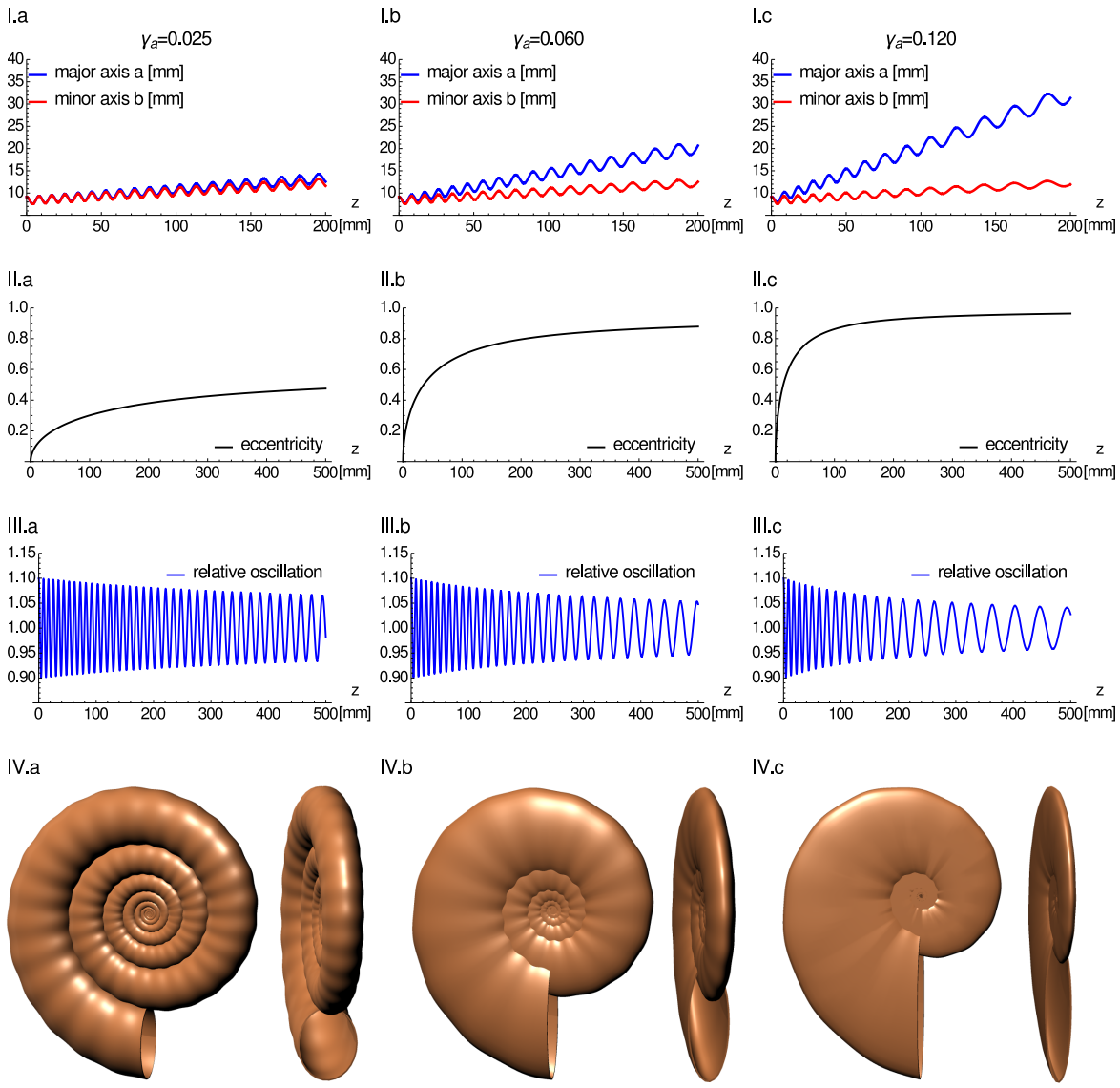


Figure 4.14: Effect of allometric increase of eccentricity $\hat{e}$ on ribbing pattern. Starting from a circular cross-section in all three cases, the reference lengths $\hat{a}$ and $\hat{b}$ increase at unequal linear rates, creating a nonlinear increase in eccentricity. The faster the eccentricity increases (see **II.a - II.c**), the faster is the increase in wavelength of the oscillations of the major and minor axis (**I.a - I.c**), the decrease in relative amplitude (**III.a - III.c**), and the stronger is the difference between high and low curvature points in the final shell cross-section (**IV.a - IV.c**). All simulation parameters can be found in Section A.5.

Figure 4.15: A series of three *Sonninia propinquans* (Lower Bajocian, France) This species shows a morphological trend commonly observed in not-closely-related species: shell ornamented in the juvenile stages tend to become smoother during development. Scale bar 10 mm.

tricities start with $\hat{e}_0 = 0$ and then allometrically increase at different rates. The 3D shells IV.a-IV.c are consistent with Buckman's law: IV.a is the most involute and also most circular shell, therefore it is most ornamented. IV.c is most evolute and most compressed, and it is therefore the smoothest shell.

We have set up a morphomechanical model which identifies the parameter expansion rate $\gamma_b$ with the involution of Buckman's first statement 4.1, and the eccentricity $\hat{e}$ with the shell cross-section in Buckman's second statement 4.2. Our model also quantifies Buckman's term "ornamentation" with the relative amplitude $\eta_\pm$ and wave length $\lambda$ of the shell ribbing pattern. The correlations in our model between $\gamma_b$ and $\eta_\pm$, $\lambda$ and between $\hat{e}$ and $\eta_\pm$, $\lambda$ are consistent with Buckman's statements 4.1 and 4.2, respectively. In the next Section, we will investigate how a mechanical feedback mechanism informed from the concept of homeostatic-driven growth (Chapter 3) affects the morphological pattern of seashells.

## 4.5 Mechanical feedback driving expansion

Buckman's Law focuses on certain features of of shells (coiling and aperture cross-section) and describes their effect on ornamentation. However, some individuals of a species have equal coiling and cross-section properties and yet exhibit different ribbing patterns. An example are the three shells presented in Figure 4.15. According to Buckman's Law, their ribbing pattern should not be significantly different, and yet differences are clearly visible. The shells in Figure 4.15. all have ribbed inner whorls,

but the outer whorls clearly exhibit some differences. The shell in Figure 4.15(a) is clearly ribbed in the outer whorl whereas the shell in Figure Figure 4.15(c) has a completely smooth outer whorl.

To address the differences of ribbing patterns of shells with equal coiling and cross-sections, we introduce mechanical feedback into the model of mechanical shell morphogenesis presented in Sections 4.2 and 4.3. In this section we study two mechanical feedback laws, which we refer to as the linear growth law and non-linear growth law, respectively.

The hypothesis behind the linear growth law is that the mantle tissue of Ammonites grows linearly in response to the force present in the mantle at the shell cross-section. In other words, the linear growth law proposes a linear coupling between growth and stress, similarly to the mechanical feedback laws presented in the previous chapters, such as $\dot{L}_i = k_i L_i \left(t_i - t_i^*\right)$ (see (2.76)) and $\dot{\mathbf{G}} = \mathbf{K}\left(\mathbf{T} - \mathbf{T}^*\right)\mathbf{G}$ (see (1.20)). The linear growth-law is discussed in detail in Section 4.5.2.

The non-linear growth law has a theoretical motivation, as it embeds the concept of growth-mechanical feedback into the Lagrangian framework discussed in Section 4.2. It allows us to establish a mathematical analogy to the system of a damped mass on a spring in classical mechanics. Details on the non-linear growth law and its relationship to Lagrangian mechanics are discussed in Section 4.5.3.

The goal of our analysis of mechanical feedback is to investigate whether mechanical feedback laws can explain the observation of different ribbing patterns of shells with equal coiling and cross-section.

### 4.5.1 Notation for shells with circular cross-section

In the previous sections, shell expansion was prescribed to be a linear function of the expansion rate linear ($\hat{b}\left(z\right) = \hat{b}_0 + \gamma_b z$, see 4.32). In this section, we explore the possibility of expansion resulting from feedback rules between growth and mechanics, rather than a prescribed linear expansion rule for growth. We refer to growth-mechanics feedback mechanisms as growth laws. In order to isolate the effects of such a feedback mechanism, we focus on shells with a circular cross-section. To be consistent with the notation of [57], we refer to the current shell radius (as a function of arc length) as

$r(z)$, i.e.

$$r(z) := a(z) \equiv b(z). \tag{4.45}$$

Similarly, we refer to the reference radius as $R(z)$ and the initial radius constant as $R_0$, i.e.

$$R(z) := \hat{a}(z) \equiv \hat{b}(z), \quad R_0 := \hat{a}_0 \equiv \hat{b}_0. \tag{4.46}$$

Finally, we refer to the expansion rate as $\gamma$, i.e.

$$\gamma := \gamma_a \equiv \gamma_b. \tag{4.47}$$

In this notation, the previously discussed case of a linearly expanding shell with no mechanical feedback is described by a linear expansion of the reference radius configuration

$$R(z) = R_0 + \gamma z \tag{4.48}$$

and the shell ribbing pattern is described by

$$r(z) = R(z) + \delta R A \sqrt{\frac{R(z)}{R_0}} \cos\left(\omega \log \frac{\hat{b}(z)}{\hat{b}_0} - \nu\right), \tag{4.49}$$

which can be obtained from (4.38) with $\hat{e}_0 = 0$ and $A$, $\omega$ and $\nu$ defined as previously (see 4.37).

### 4.5.2 Linear force-feedback law

In Chapter 2, we considered growth on a one-dimensional domain, which we described in terms of a reference length $L$. For the systems described in Chapter 2, the generic growth law is (see (2.76))

$$\dot{L} = kL(t - t^*) + \beta \tag{4.50}$$

where $t$ is the Cauchy stress, $t^*$ is the homeostatic stress and $k$ is the growth rate. In (4.50), we also introduced a new parameter $\beta$ to describe basal growth (i.e. growth of the base structure), which in Chapter 2 was not present ($\beta = 0$). In this Section, we consider a linear growth law (also referred to as force feedback law) with a related

form,

$$R'(z) = M(n - n^*) + \gamma \tag{4.51}$$

where the basal growth is $\beta = \gamma$ and $n(z)$ is the force in the shell cross-section (i.e. the force experienced by the mantle),

$$n(z) = k\left(\frac{r}{R} - 1\right). \tag{4.52}$$

To simplify the analysis we choose $n^* = 0$ for the homeostatic stress. Putting these results together, we obtain a growth law in which the expansion of the reference radius $R$ is proportional to the sum of the expansion rate $\gamma$ and the force in the cross-section:

$$R'(z) = \gamma + Mk\left[\frac{r(z)}{R(z)} - 1\right]. \tag{4.53}$$

The parameter $M$ controls the strength of the mechanical feedback. Note that for $M = 0$, we retrieve the linear expansion (4.48). Also note that the term in brackets is proportional to the force in the cross-section, $n = k(r/R - 1)$.

In order to study the influence of the mechanical term in (4.53) (which is controlled by $M$) on the ribbing pattern, we must solve the initial value problem

$$r''(z) + \frac{k}{R(z)}\left[\frac{r(z)}{R(z)} - 1\right] = 0, \qquad R'(z) = \gamma + Mk\left[\frac{r(z)}{R(z)} - 1\right] \tag{4.54}$$

and

$$r(0) = R_0 + \delta R, \qquad r'(0) = \gamma, \qquad R(0) = R_0. \tag{4.55}$$

We note that if no mechanical feedback is present, $(M = 0)$, the initial value problem (4.54) and (4.55)is solved by (4.49).

In Figure 4.16 we present 3D shells with ribbing patterns obtained as numerical solutions from (4.54) and (4.55). Note that the parameter $\varepsilon$ (which is defined in (4.60)) is proportional to the mechanical feedback coupling $M$. While higher values of $\varepsilon$ appear to make the shell surface smoother, the exact effects on amplitude and wavelength are unclear. In the next sections, we investigate these effects by means of asymptotic expansions to answer the question exactly how mechanical feedback of the

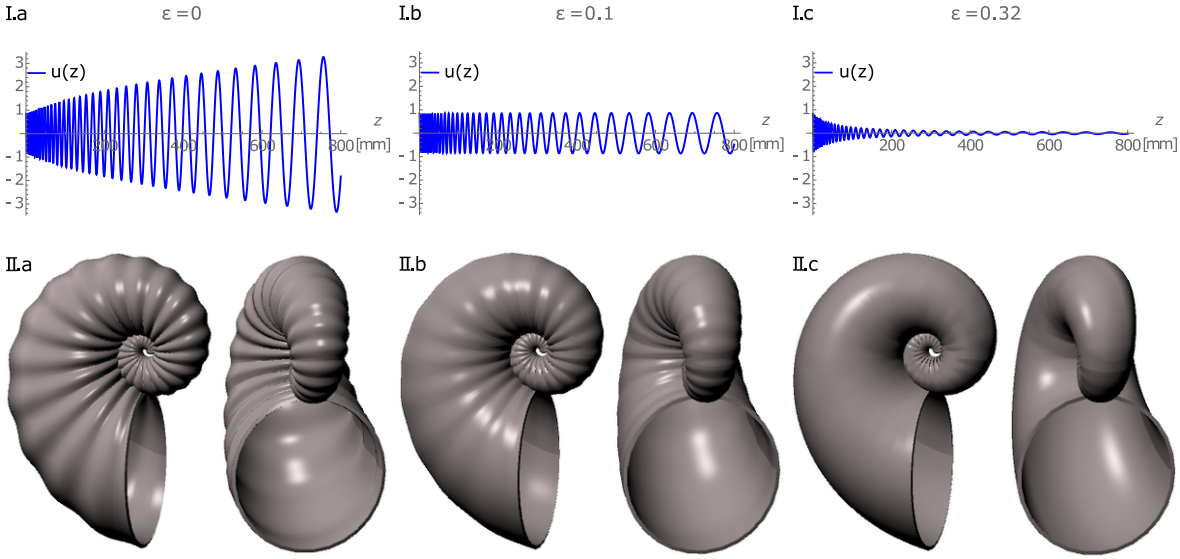


Figure 4.16: Influence of mechanical feedback parameter $\varepsilon$ on the ribbing pattern of the seashell. The higher $\tilde{\varepsilon}$, the smoother the ribbing pattern. In **(I.a)**–**(I.c)**, we show the oscillation patterns of the current radius reduced by the linear expansion, $r(z) - (R_0 + \gamma z)$, whereas **(II.a)**–**(II.c)** in we show the same for the reference radius, $R(z) - (R_0 + \gamma z)$. Note that the latter oscillates only in the presence of mechanical feedback. As previously, **(II.a)**–**(II.c)** we show 3D renderings of the coiled seashell. In In all columns, the cross-section is a circle ($e = 0$) throughout the whole development of the shell. The expansion rate is also the same for all columns. These simulations are solutions of the initial value problem (4.54) and (4.55). The simulation parameters can be found in Appendix A.5.

linear growth law influences the ribbing pattern.

#### 4.5.2.1 Displacement and non-dimensionalisation

To obtain an analytical understanding of the influence of mechanical feedback (parameter $M$) on the ribbing pattern, we transform (4.54) and (4.55) to a form better suited for analysis. First, we introduce the displacement

$$u(z) = r(z) - R(z). \tag{4.56}$$

The initial value problem (4.54) and (4.55) transforms to

$$u''(z) + R''(z) + k\frac{u(z)}{R(z)^2} = 0, \qquad R'(z) = \gamma + Mk\frac{u(z)}{R(z)}. \tag{4.57}$$

The initial conditions read

$$u(0) = \delta R, \qquad R(0) = R_0, \qquad R'(0) = \gamma + Mk\frac{\delta R}{R_0}, \qquad u'(0) = -Mk\frac{\delta R}{R_0}. \quad (4.58)$$

Next, we nondimensionalise:

$$\tilde{z} = \ln\left(1 + \frac{\gamma}{R_0}z\right), \qquad \tilde{u} = \frac{u}{\delta R}, \qquad \tilde{R} = \frac{R}{R_0}. \quad (4.59)$$

The benefit of the transformation to $\tilde{z}$ will become obvious in the perturbation analysis shown in Subsection 4.5.2.2. In short, it transforms the problem of integrating $u$ to a second order ODE with constant coefficients. As we have seen previously, in the case of linear expansion (4.48) the ribbing pattern (4.49) oscillates with $\cos\left(\omega \log\left(1 + \gamma R_0^{-1} z\right)\right)$. With $(4.59)_1$, the oscillation simplifies to $\cos(\omega\tilde{z})$. Note also that the relationship between $z$ and $\tilde{z}$ is one-to-one, which allows us to define $z = R_0\gamma^{-1}\left(e^{\tilde{z}} - 1\right)$ as the inverse of $(4.59)_1$.

To make analytical progress in solving the initial value problem (4.54) and (4.55), we introduce the assumption that mechanical feedback couples weakly to the linearly expanding model (4.48). To model the weak coupling, we assume in (4.57) that the term $Mku/R$ is relatively small compared to $\gamma$. Judging by Figure (4.16), it is reasonable to assume that displacement $u$ is relatively large such that $u/R$ is of order 1. Therefore, in the assumption of weak mechanical coupling we must have $Mk \ll \gamma$. We introduce the small nondimensional parameter $\varepsilon$ to quantify the strength of the mechanical coupling:

$$\varepsilon := \frac{Mk}{\gamma} \ll 1. \quad (4.60)$$

We also introduce the nondimensional parameter

$$\rho = \frac{\delta R}{R_0} \quad (4.61)$$

to quantify the relative initial displacement. In the new variables, (4.57) becomes

$$\begin{aligned} \tilde{u}''(\tilde{z}) - \tilde{u}'(\tilde{z}) + \rho^{-1}\left[\tilde{R}''(\tilde{z}) - \tilde{R}'(\tilde{z})\right] + e^{2\tilde{z}}\frac{k}{\gamma^2}\frac{\tilde{u}(\tilde{z})}{\tilde{R}(\tilde{z})^2} &= 0 \\ \tilde{R}'(\tilde{z}) - e^{\tilde{z}}\left[1 + \varepsilon\rho\frac{\tilde{u}(\tilde{z})}{\tilde{R}(\tilde{z})}\right] &= 0 \end{aligned} \quad (4.62)$$

with initial conditions

$$\tilde{u}(0) = \tilde{R}(0) = 1, \qquad \tilde{u}'(0) = -\varepsilon, \qquad \tilde{R}'(0) = 1 + \varepsilon\rho\,. \tag{4.63}$$

The model (4.62) has four nondimensional parameters ($\rho$, $\varepsilon$, $\gamma$, $k$) and coincides with (4.35) for $\varepsilon = \hat{e}_0 = 0$.

A perturbation series ansatz $\tilde{u} \sim \tilde{u}_0 + \varepsilon\tilde{u}_1 + \ldots$ and $\tilde{R} \sim \tilde{R}_0 + \varepsilon\tilde{R}_1 + \ldots$ does not deliver a satisfying approximation[1] because secular terms appear at $\mathcal{O}(\varepsilon)$.The presence of secular terms allows us to identify two relevant length scales: The length scale $\tilde{z}$ of fast oscillation, and the length scale $\varepsilon\tilde{z}$ of slow oscillation, at which secular terms become significant and make a regular perturbation series approximation invalid. Accordingly, we apply the method of multiple scales (see [44]).

#### 4.5.2.2 Multiple Scales Approximation

We consider two length scales,

$$z_1 = \tilde{z}, \qquad z_2 = \varepsilon\tilde{z}\,. \tag{4.64}$$

We define[2] $\tilde{u}(\tilde{z}) = \tilde{u}(z_1, z_2)$ and $\tilde{R}(\tilde{z}) = \tilde{R}(z_1, z_2)$. The first and second derivatives $\tilde{u}'(\tilde{z})$ and $\tilde{u}''(\tilde{z})$ transform as

$$\tilde{u}'(\tilde{z}) = \frac{\mathrm{d}\tilde{u}}{\mathrm{d}\tilde{z}} = \partial_1\tilde{u} + \varepsilon\partial_2\tilde{u}, \qquad \tilde{u}''(\tilde{z}) = \frac{\mathrm{d}^2\tilde{u}}{\mathrm{d}\tilde{z}^2} = \partial_1^2\tilde{u} + 2\varepsilon\partial_1\partial_2\tilde{u} + \varepsilon^2\partial_2^2\tilde{u} \tag{4.65}$$

where we used the abbreviations $\partial_1 = \partial/\partial z_1$ and $\partial_2 = \partial/\partial z_2$. Note that $(4.62)_2$ can be integrated directly at every order. Secular terms do not arise here. For this reason, derivatives of $\tilde{R}$ transform simply as

$$\tilde{R}'(\tilde{z}) = \partial_1\tilde{R}, \qquad \tilde{R}''(\tilde{z}) = \partial_1^2\tilde{R}\,. \tag{4.66}$$

[1] This is, however, not true for the nonlinear growth law, as we demonstrate in Section 4.5.3.

[2] It should be clear from the context which variable dependence of $\tilde{u}$ and $\tilde{R}$ is meant.

Then (4.62) transforms as

$$\begin{aligned}\underbrace{\left(\partial_1^2+2\varepsilon\partial_1\partial_2+\varepsilon^2\partial_2^2\right)}_{\mathrm{d}^2/\mathrm{d}\tilde{z}^2}\tilde{u}-\underbrace{\left(\partial_1+\varepsilon\partial_2\right)}_{\mathrm{d}/\mathrm{d}\tilde{z}}\tilde{u}\\ +\rho^{-1}\left(\partial_1^2\tilde{R}-\partial_1\tilde{R}\right)+e^{2z_1}\frac{k}{\gamma^2}\frac{\tilde{u}}{\tilde{R}^2}=0\end{aligned} \tag{4.67}$$

and

$$\partial_1\tilde{R}-e^{z_1}\left(1+\varepsilon\rho\frac{\tilde{u}}{\tilde{R}}\right)=0. \tag{4.68}$$

Keeping in mind that according to (4.64) $z_2$ is a function of $\varepsilon$, we now use a power series expansion

$$\begin{aligned}\tilde{u}\left(z_1,z_2\right) &= u_0\left(z_1,z_2\right)+\varepsilon u_1\left(z_1,z_2\right)+\ldots\\ \tilde{R}\left(z_1,z_2\right) &= R_0\left(z_1,z_2\right)+\varepsilon R_1\left(z_1,z_2\right)+\ldots\end{aligned}$$

**Analysis at $\mathcal{O}\left(1\right)$**

At $\mathcal{O}\left(1\right)$, $(4.62)_2$ has the form $\partial_1 R_0=e^{z_1}$ where $R_0=1$ at $z_1=0$. This can be directly integrated, obtaining $R_0=e^{z_1}$. With this solution, we obtain a homogeneous ODE with constant coefficients for $(4.62)_1$:

$$\partial_1^2 u_0-\partial_1 u_0+\frac{k}{\gamma^2}u_0=0,\qquad u_0\left(0,0\right)=1,\quad \partial_1 u_0\left(0,0\right)=0\,. \tag{4.69}$$

This has the solution

$$u_0=e^{\frac{z_1}{2}}\left[a_0\left(z_2\right)\sin\omega z_1+b_0\left(z_2\right)\cos\omega z_1\right],\qquad a_0\left(0\right)=-\frac{1}{2\omega},\quad b_0\left(0\right)=1 \tag{4.70}$$

where (in agreement with (4.37)) the frequency $\omega$ is

$$\omega=\frac{\sqrt{4k-\gamma^2}}{2\gamma}\,. \tag{4.71}$$

As required, the $\mathcal{O}\left(1\right)$ analysis reproduces the model (4.48) without mechanical feedback.

**Analysis at $\mathcal{O}(\varepsilon)$**

At $\mathcal{O}(\varepsilon)$, $(4.62)_2$ becomes

$$\partial_1 R_1 = \rho u_0, \qquad R_1(0,0) = 0 \tag{4.72}$$

The solution is

$$R_1 = -\frac{4\rho}{4\omega^2+1} + \rho e^{\frac{z_1}{2}} \left[ \left( \frac{2a_0 + 4\omega b_0}{4\omega^2+1} \right) \sin \omega z_1 + \left( \frac{2b_0 - 4\omega a_0}{4\omega^2+1} \right) \cos \omega z_1 \right]. \tag{4.73}$$

With $R_1$ we find the form of $(4.62)_1$ is

$$\partial_1^2 u_1 - \partial_1 u_1 + \frac{k}{\gamma^2} u_1 = f_1, \qquad u_1(0,0) = 0, \quad \partial_1 u_1(0,0) = -1 \tag{4.74}$$

The homogeneous equation is the same as (4.69), with the solution

$$u_1 = e^{\frac{z_1}{2}} \left[ a_1(z_2) \sin \omega z_1 + b_1(z_2) \cos \omega z_1 \right]. \tag{4.75}$$

The inhomogeneous terms are

$$\begin{aligned} f_1 \;=\; & e^{\frac{z_1}{2}} (C_1 \sin \omega z_1 + C_2 \cos \omega z_1) \\ & + e^{-\frac{z_1}{2}} (C_3 \sin \omega z_1 + C_4 \cos \omega z_1) \\ & + C_5 \sin \omega z_1 \cos \omega z_1 \\ & + C_6 \sin 2\omega z_1 + C_7 \end{aligned} \tag{4.76}$$

We note that the terms in the first line are secular terms: They satisfy the characteristic polynomial of (4.74), which contributes a particular solution term

$$z_1 e^{\frac{z_1}{2}} (K_1 \sin \omega z_1 + K_2 \cos \omega z_1) \tag{4.77}$$

with some constant coefficients $K_1$, $K_2$. A regular perturbation series approximation breaks down at lengths of the order $\varepsilon z_1$ due to secular terms. The multiple scales approximation allows us to remove the secular terms by demanding $C_1 = 0$ and $C_2 = 0$,

which gives rise to two coupled first order ODEs in $z_2$ to determine $a_0(z_2)$, $b_0(z_2)$:

$$a_0(z_2) + 2\omega b_0(z_2) + 4\omega b_0'(z_2) = 0, \qquad b_0(0) = 1 \tag{4.78}$$

$$-b_0(z_2) + 2\omega a_0(z_2) + 4\omega a_0'(z_2) = 0, \qquad a_0(0) = -\frac{1}{2\omega}. \tag{4.79}$$

The solution is

$$a_0 = \frac{e^{-\frac{z_2}{2}}}{2\omega}\left[2\omega\sin\left(\frac{z_2}{4\omega}\right) - \cos\left(\frac{z_2}{4\omega}\right)\right], \qquad b_0 = \frac{e^{-\frac{z_2}{2}}}{2\omega}\left[\sin\left(\frac{z_2}{4\omega}\right) + 2\omega\cos\left(\frac{z_2}{4\omega}\right)\right]. \tag{4.80}$$

We neglect higher order terms and summarise the results of the multiple scales approximation in the following section.

#### 4.5.2.3 Results of multiple scales approximation

After using the result (4.80) in (4.70) and (4.73), and after rearranging the terms, we obtain the approximate solution of (4.62) according to the multiple scales analysis:

$$\tilde{u} = Ae^{\frac{1}{2}\tilde{z}(1-\varepsilon)}\cos\left[\left(\omega - \frac{\varepsilon}{4\omega}\right)\tilde{z} - \nu\right] + \ldots \tag{4.81}$$

$$\tilde{R} = e^{\tilde{z}} + \varepsilon\rho\left\{-\frac{4}{4\omega^2+1} + \frac{e^{\frac{1}{2}\tilde{z}(1-\varepsilon)}}{\omega}\cos\left[\left(\omega - \frac{\varepsilon}{4\omega}\right)\tilde{z} - \phi\right]\right\} + \ldots \tag{4.82}$$

where the dots represent higher order terms in $\varepsilon$. The nondimensional constants $A$, $\nu$ (which coincide with 4.37) and $\phi$ are

$$A = \frac{\sqrt{4\omega^2+1}}{2\omega}, \qquad \nu = -\tan^{-1}\left(\frac{1}{2\omega}\right), \qquad \phi = -\tan^{-1}\left(\frac{1-4\omega^2}{4\omega}\right). \tag{4.83}$$

As we show in Fig. 4.17, dropping the higher order terms in (4.81) and (4.82) gives a very good approximation. With the parameters values from 4.17, the nondimensional constants are $\omega$, $A$, $\nu$ and $\phi$ are

$$\omega = 18.25, \qquad A = 1.00, \qquad \nu = -0.03, \qquad \phi = 1.52. \tag{4.84}$$

In the linear expansion model (4.48) described in Section (4.2.1) the mantle grows in a linear pre-programmed manner such that the reference radius is a linear function of

the expansion rate $\gamma$, see (4.48). The oscillatory ribbing pattern then arises from a balance between the elastic forces within the shell secreting mantle and a generating zone force.

The linear mechanical feedback model presented in Section (4.5.2) adds a growth response to the forces present in the shell mantle. In other words, the mantle senses the forces present and modulates its growth accordingly. Mathematically, we have modeled the growth response of the mantle as a small correction to the pre-programmed linear expansion from the model described in Section (4.2.1).

In (4.81) and (4.82), the effect of mechanical feedback is controlled by the parameter $\varepsilon$ (see 4.60). It causes a decay in amplitude by $e^{-\varepsilon\tilde{z}/2}$ and a decrease in frequency by $\varepsilon/(4\omega)$, or (equivalently) an increase in wavelength by $8\pi\omega/\varepsilon$. Figure 4.17 shows forms of the solutions $\tilde{u}(\tilde{z})$ and $\tilde{R}(\tilde{z})$ for various values of $\varepsilon$, demonstrating the effect of the mechanical feedback mechanism (4.53) on the ribbing pattern and the quality of the approximation (4.81) and (4.82) to the initial value problem (4.62) and (4.63).

#### 4.5.2.4 Comparison of amplitude and frequency shifts induced by mechanical feedback

The multiple scales analysis result (4.81) tells us how amplitude and wavelength of ribbing pattern are modified in the presence of mechanical feedback ($\varepsilon > 0$) compared to the linear expansion model (see (4.48)) with no feedback ($\varepsilon = 0$). As can be seen from Fig. 4.17, the displacement $\tilde{u}$ undergoes a rather significant qualitative change at $\varepsilon = 1$ where the enveloping curve of $\tilde{u}$ switches from exponential growth to decay. In comparison, the change in frequency is almost negligible, as the plots Fig. 4.17 are visually suggesting. Let us consider a numerical example: The seashell analysed in column b of Fig. 4.13 has the parameters $k = 155$, $\gamma_b = 0.057$, $\hat{e}_0 = 0.7$. According to $(4.37)_1$, we can calculate $\omega \approx 17.09$. The frequency change according to (4.81) is $\Delta\omega = \varepsilon/(4\omega)$, so in this example the

$$\frac{\Delta\omega}{\omega} \approx 7.7 \times 10^{-4}\varepsilon\,, \tag{4.85}$$

which makes the frequency change induced by mechanical feedback practically negligible compared to the amplitude change. In conclusion, the effect of the linear feedback law on the shell morphology is captured by the function $e^{\frac{1}{2}\tilde{z}(1-\varepsilon)}$ which acts as an

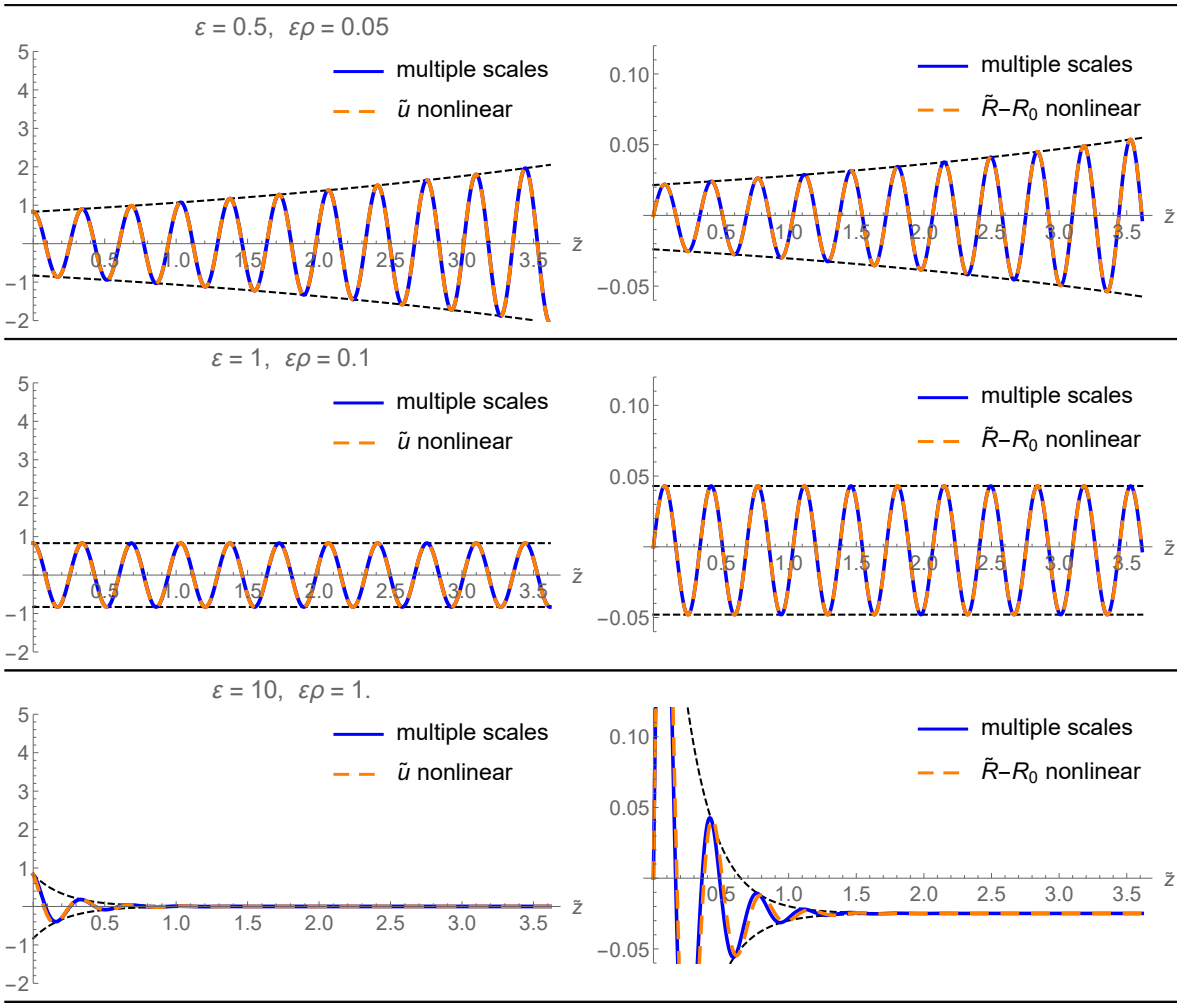


Figure 4.17: Plots of displacement $\tilde{u}$ (left column) and reference radius $\tilde{R}$ (right column), comparing the numerical solution of (4.62) and (4.63) to the multiple scales result (4.81) and (4.82). The multiple scales approximation is a very good fit even for high values of $\varepsilon$. The nondimensional parameters for this simulation are $\gamma = 0.3$, $k = 30$, $\rho = 0.1$ and $\varepsilon$ as indicated in the subfigures. Please note that in this simulation the small term is $\varepsilon\rho\tilde{u}/\tilde{R}$ (see (4.62)), i.e. at $\tilde{z} = 0$ the term $\varepsilon\rho\tilde{u}\,(0)\,/\tilde{R}\,(0) = \varepsilon\rho$ where $\rho = 0.1$.

enveloping curve for oscillations both in the displacement $\tilde{u}$ and reference radius $\tilde{R}$.

### 4.5.3 Nonlinear force-feedback law

The motivation behind the nonlinear growth law (also referred to as nonlinear force feedback law) is to embed the concept of growth-mechanical feedback into the Lagrangian framework discussed in Section 4.2. The nonlinear growth law can be derived from the Lagrangian $L$ proposed in (4.34) and a Rayleigh dissipation function $D$ (see [26]):

$$L = r'^2(z) - k\left(\frac{r(z)}{R(z)} - 1\right)^2, \qquad D = \frac{1}{\tilde{M}}\left[R'(z) - \gamma\right]^2. \tag{4.86}$$

We treat both $r$ and $R$ as generalised coordinates and apply the Euler-Lagrange formalism (as demonstrated in detail in Section 4.5.3). The Euler-Lagrange equations of (4.86) are

$$\frac{\mathrm{d}}{\mathrm{d}z}\frac{\partial L}{\partial r'} - \frac{\partial L}{\partial r} + \frac{\partial D}{\partial r'} = 0 \qquad \text{and} \qquad \frac{\mathrm{d}}{\mathrm{d}z}\frac{\partial L}{\partial R'} - \frac{\partial L}{\partial R} + \frac{\partial D}{\partial R'} = 0. \tag{4.87}$$

Explicitly, the Euler-Lagrange equations take the form

$$0 = r''(z) + \frac{k}{R(z)}\left(\frac{r(z)}{R(z)} - 1\right) \tag{4.88}$$

$$R'(z) = \gamma + \tilde{M}k\frac{r(z)}{R(z)^2}\left[\frac{r(z)}{R(z)} - 1\right]. \tag{4.89}$$

The initial conditions for this initial value problem are (4.55). The nonlinear growth law is (4.89). Note that the main difference between the linear growth law (4.53) and the nonlinear growth law (4.89) is the term $r/R^2$.

Note that while in (4.54) the parameter $M$ was dimensionless, in (4.88) the parameter $\tilde{M}$ has the dimension of length. For this reason, slightly differently from 4.60, we define the nondimensional parameter

$$\tilde{\varepsilon} = \frac{\tilde{M}k}{\gamma R_0} \tag{4.90}$$

and $\rho = \delta R/R_0$ as previously.

After transforming (4.88) to displacement (4.56) and applying the non-dimensionalisation

(4.59), in analogy to (4.62) we obtain

$$\begin{aligned} \tilde{u}'' - \tilde{u}' + \rho^{-1}\left[\tilde{R}'' - \tilde{R}'\right] + e^{2\tilde{z}}\frac{k}{\gamma^2}\frac{\tilde{u}}{\tilde{R}^2} = 0, \\ \tilde{R}' - e^{\tilde{z}}\left[1 + \tilde{\varepsilon}\rho\frac{\tilde{u}}{\tilde{R}^2} + \tilde{\varepsilon}\rho^2\frac{\tilde{u}^2}{\tilde{R}^3}\right] = 0 \end{aligned} \tag{4.91}$$

with initial conditions

$$\tilde{u}(0) = \tilde{R}(0) = 1, \qquad \tilde{u}'(0) = -\tilde{\varepsilon}(1+\rho), \qquad \tilde{R}'(0) = 1 + \tilde{\varepsilon}\rho(1+\rho)\,. \tag{4.92}$$

A multiple scales approximation similarly to Section 4.5.2.2 reveals that at least up to $\mathcal{O}(\varepsilon^2)$ no secular terms appear in (4.91). The time scale separation (4.64) is unsuitable for the non-linear feedback law. For this reason, we choose a regular perturbation series approximation

$$\tilde{u}(\tilde{z}) = u_0(\tilde{z}) + \tilde{\varepsilon}u_1(\tilde{z}) + \tilde{\varepsilon}^2 u_2(\tilde{z}) + \mathcal{O}\left(\tilde{\varepsilon}^3\right) \tag{4.93}$$

$$\tilde{R}(\tilde{z}) = R_0(\tilde{z}) + \tilde{\varepsilon}R_1(\tilde{z}) + \tilde{\varepsilon}^2 R_2(\tilde{z}) + \mathcal{O}\left(\tilde{\varepsilon}^3\right). \tag{4.94}$$

The solution of (4.91) and (4.92) at orders up to $\mathcal{O}(\varepsilon^2)$ does not result in simple corrections to the amplitude and frequency similarly to (4.81) and (4.82). We compare the series perturbation (4.93) and (4.94) to the numerical solution of the initial value problem (4.91) and (4.92) in Figure (4.18).

### 4.5.4 Comparison between growth laws

Here we compare the oscillation patterns of the linear growth law (4.54) and the nonlinear growth law (4.88). In (4.60) and (4.90), we introduced the nondimensional parameters $\varepsilon$ and $\tilde{\varepsilon}$ which are suitable for the direct comparison of the linear and nonlinear growth laws. In Figure 4.19, we plot $\tilde{u}(\tilde{z})$ for the linear (green) and nonlinear (blue) growth laws. As noted previously, because of an amplitude proportional to $e^{\frac{\tilde{z}}{2}(1-\varepsilon)}$ (see (4.81)), the linear growth law switches from expanding to decaying displacement at $\varepsilon = 1$. This is not true for the nonlinear growth law, which instead appears to develop a local minimum in its amplitude curve somewhere between $1 < \tilde{\varepsilon} < 1.5$, and appears to approximately fulfill $u(0) \approx u(\tilde{\varepsilon})$ (which appears to hold approximately true even

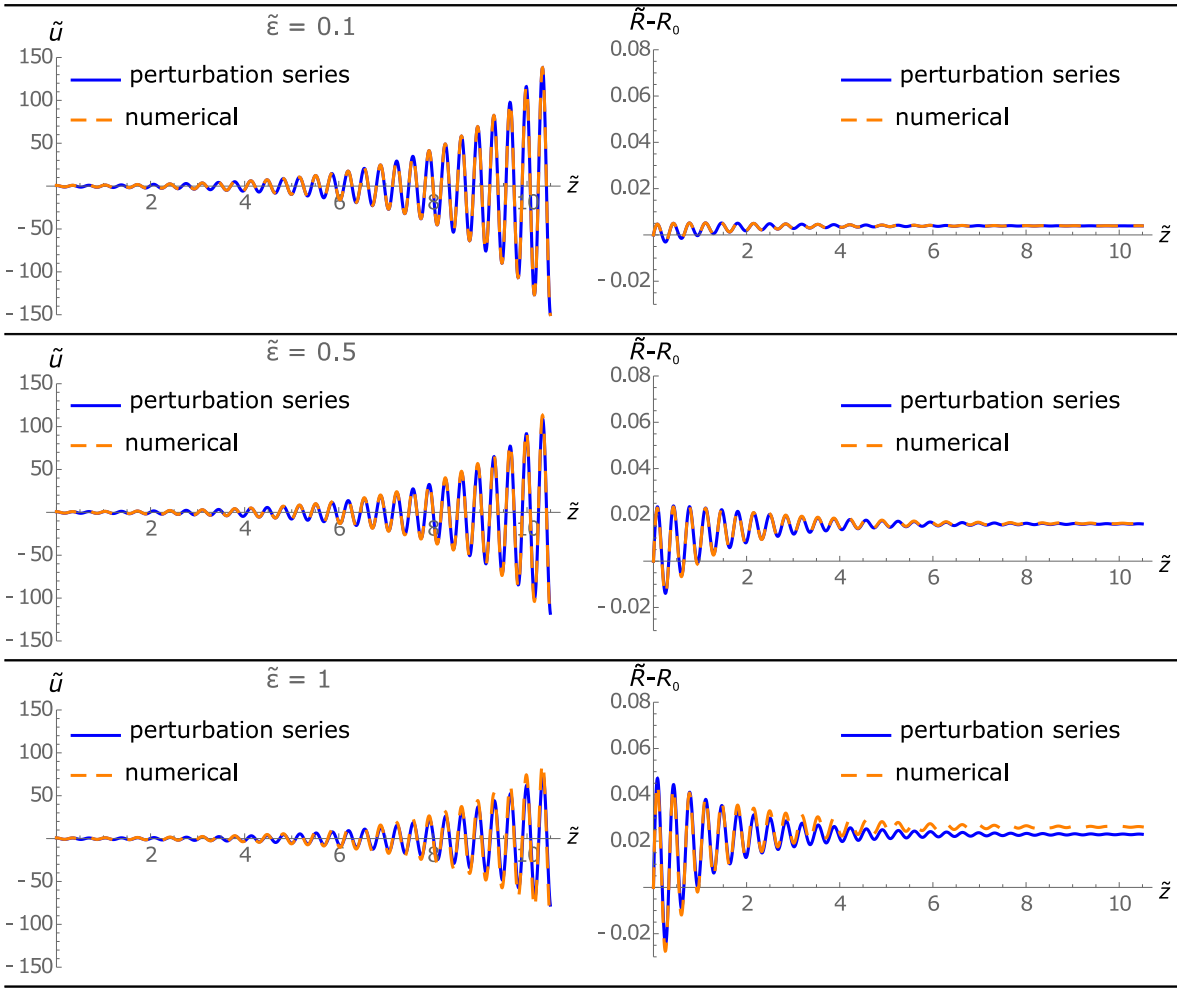


Figure 4.18: Plots of displacement $\tilde{u}$ (left column) and reference radius $\tilde{R}$ (right column), comparing the numerical solution of (4.88) to the series approximation result (4.93) and (4.94). Parameters are as in Figure 4.17, with $\tilde{\varepsilon}$ as indicated in subfigures.

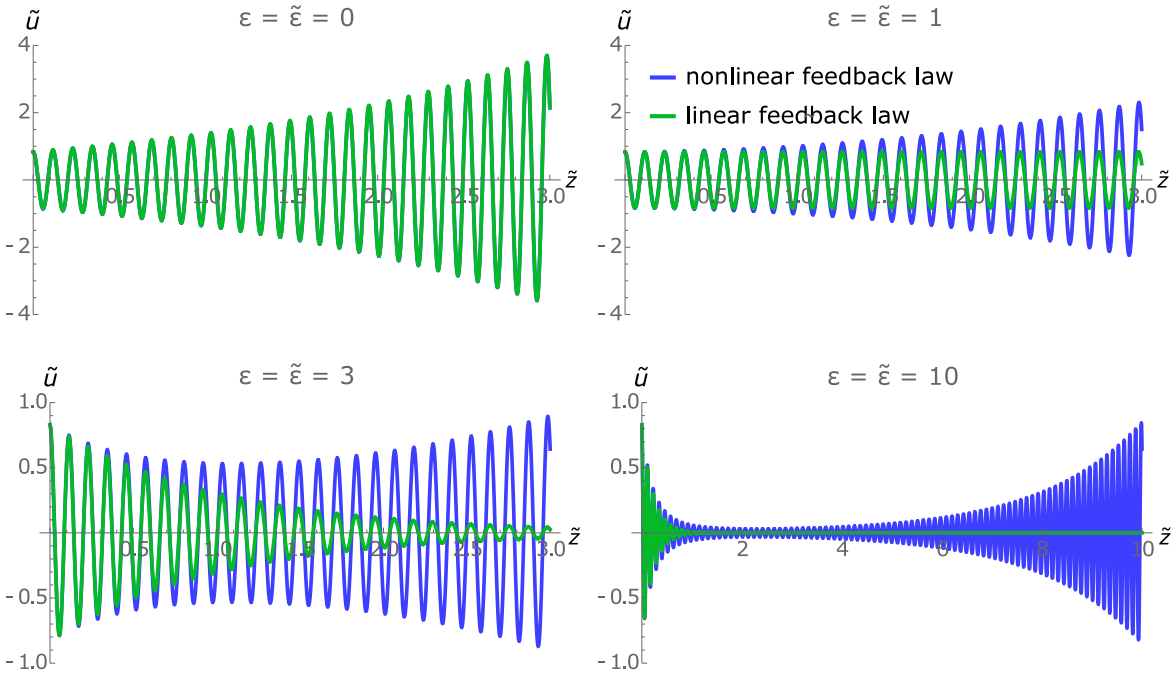


Figure 4.19: Plots of oscillations of displacement $\tilde{u}$ for nonlinear and linear growth laws. For $\varepsilon = \tilde{\varepsilon} = 0$, the solutions coincide, as can be clearly seen from (4.62) and (4.88). As the amplitude of the displacement of the linear growth law scales with $e^{\tilde{z}(1-\varepsilon)/2}$, it grows for $\varepsilon < 1$, remains constant for $\varepsilon = 1$ and decreases for $\varepsilon > 1$. The nonlinear growth law does not share this property. Instead, for approximately $1 < \tilde{\varepsilon} < 1.5$, a local minimum of the amplitude curve appears. The oscillations appear to be growing exponentially, albeit slower than in the case $\tilde{\varepsilon} = 0$. Parameters are as in Figure 4.17, with $\varepsilon$ and $\tilde{\varepsilon}$ as indicated in subfigures.

for tests up to $\tilde{\varepsilon} = 20$).

In summary, Figure (4.19) shows for both growth laws that coupling of the linear expansion model with mechanical feedback (quantified through $\varepsilon$ and $\tilde{\varepsilon}$, respectively) dramatically affects the oscillation amplitude while leaving the frequency unaffected. In case of the linear growth law, the amplitude is modulated by an exponential envelope curve. In the nonlinear growth law, the form of the envelope curve is less clear. The solutions of the nonlinear growth law exhibit some interesting mathematical properties, but the feature of going from ribbed to smooth back to ribbed (because of the additional minimum appearing $1 < \tilde{\varepsilon} < 1.5$) seems to be an unrealistic, whereas the linear growth law captures realistic behaviour: Shells are ribbed in the juvenile stages, then smoothen over the course of their development.

## 4.6 Ammonites' Morphospace and Conclusions

An observation from Ammonites' shells is that rapidly expanding shells in the juvenile stages tend to become smoother during development while the slowly expanding shells tend to remain more strongly ornamented at later stages of the development (see for instance the photographs in Figure 4.20(a)–(c)). The morphomechanical model described in Section 4.3.1.1 supports this observation: In (4.38), the relative amplitude decreases and the ribbing wavelength increases as one moves away from the shell spiral centre (the higher the arc length value $z$, the later the developmental stage).

However, as the simulations results in Figure 4.13 and Figure 4.14 show, the model presented in Section 4.4 predicts that even rapidly expanding shells are not completely smooth in late developmental stages. The photographs in Figure 4.20 show a representative sample of rapidly expanding Ammonites' shell fossils which do appear almost completely smooth in adult stages.

In this Section, we have demonstrated how a mechanical feedback mechanism similar to (1.23) affects the morphology of Ammonites' shells. The coupling of the the morphomechanical model described in Section 4.3.1.1 to the mechanical feedback mechanism described in this Section retains strong ribbing in the juvenile stages of strongly expanding shells, but smoothens the late developmental stages as the coupling strength increases. This morphology is consistent with observation and cannot readily be cap-

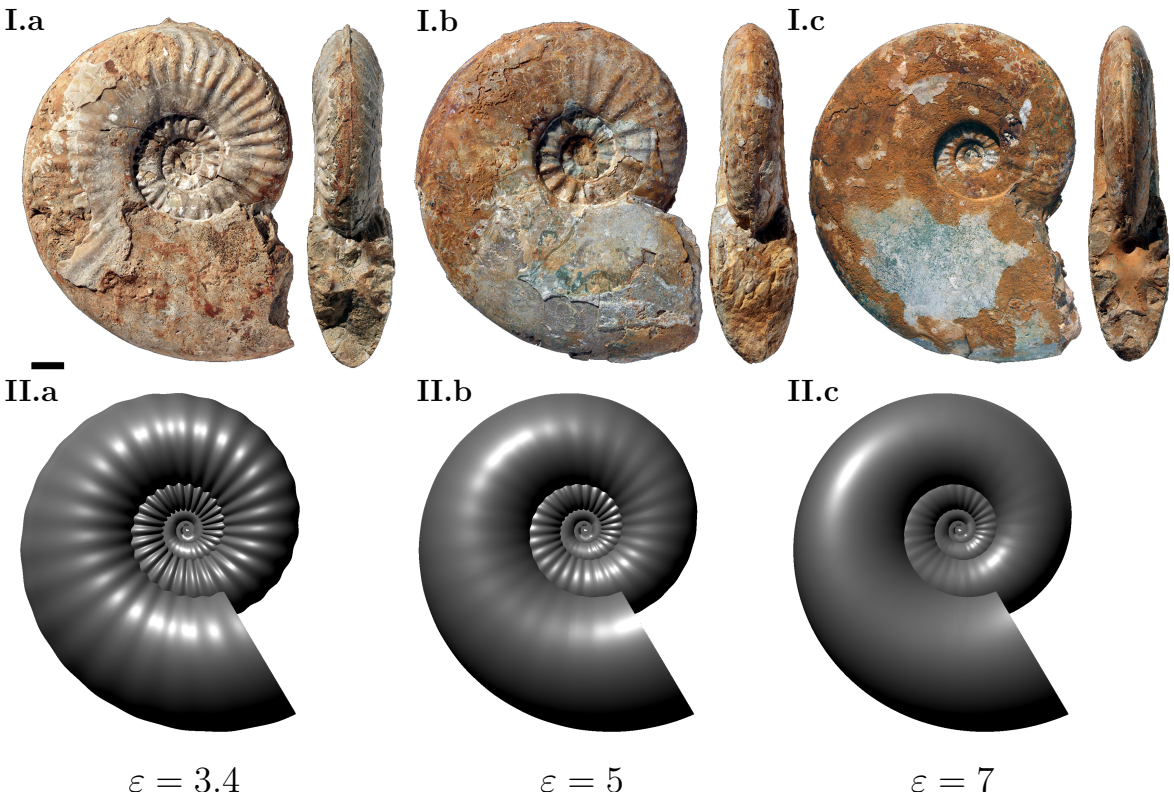


Figure 4.20: Photographs of *Sonninia Propinquans* and modelling results. The parameters for the surface II.a were fitted from the photograph I.a (see Section A.5). The value for $\varepsilon$ was also fitted. The other simulated shells, II.b and II.c, only differ in their increasing $\varepsilon$ parameters, reproducing the trend of the *Sonninia* shells to significantly reduce ribbing while having geometrically very similar properties (coiling, cross-section). Photographs courtesy of Régis Chirat.

tured with previous models.

In Fig. 4.20, we return to the *Sonninia Propinquans* shells from Figure 4.15. The three shells have very similar coiling (i.e. expansion rate $\gamma$) and cross-section shapes (i.e. eccentricity $\hat{e}_0$). Furthermore, since the samples are from the same species, we assume that their stiffness values $k$ are approximately equal. According to Buckman's law the shells should have the same ribbing pattern. However, there are clearly some differences. The shell in Fig. 4.20(**I.c**) has a much smoother outer whorl than the shell in Fig. (**I.a**). At the same time, the inner whorls of all shells show some ribbing. Our model of the linear growth law produces the morphologies (**II.a**–**c**) and is consistent with the observation of a ribbed inner whorl. The outer whorl, on the other hand, depends strongly on the coupling of the linear expansion model to the linear mechanical feedback model, which makes mechanical feedback a good candidate to provide the underlying mechanism for the observation of shells with ribbed juvenile stages and

smooth adult stages.

In Fig. 4.21, we present a set of shapes in the 3-dimensional morphospace that can be investigated with our model. It can be thought of as a summary of Figures 4.13 (in which $\hat{e}$ and $\varepsilon$ are constant), 4.14 (in which $\gamma_a$ and $\varepsilon$ are constant) and 4.20 (in which $\gamma_a$ and $\hat{e}$ are constant). We recover the relationships between the parameters $\gamma_a$, $\hat{e}$ and $\varepsilon$ and the shell shape, as discussed in this chapter: An increase in expansion rate $\gamma_a$ increases the involution of the shell (i.e. makes it coil faster) and makes the ribbing pattern smoother. An increase in eccentricity $\hat{e}$ makes the shell cross-section narrower and smoothens the ribbing pattern. Finally, an increase in mechanical feedback $\varepsilon$ makes the shell smoother, while leaving all other properties of the shape unchanged.

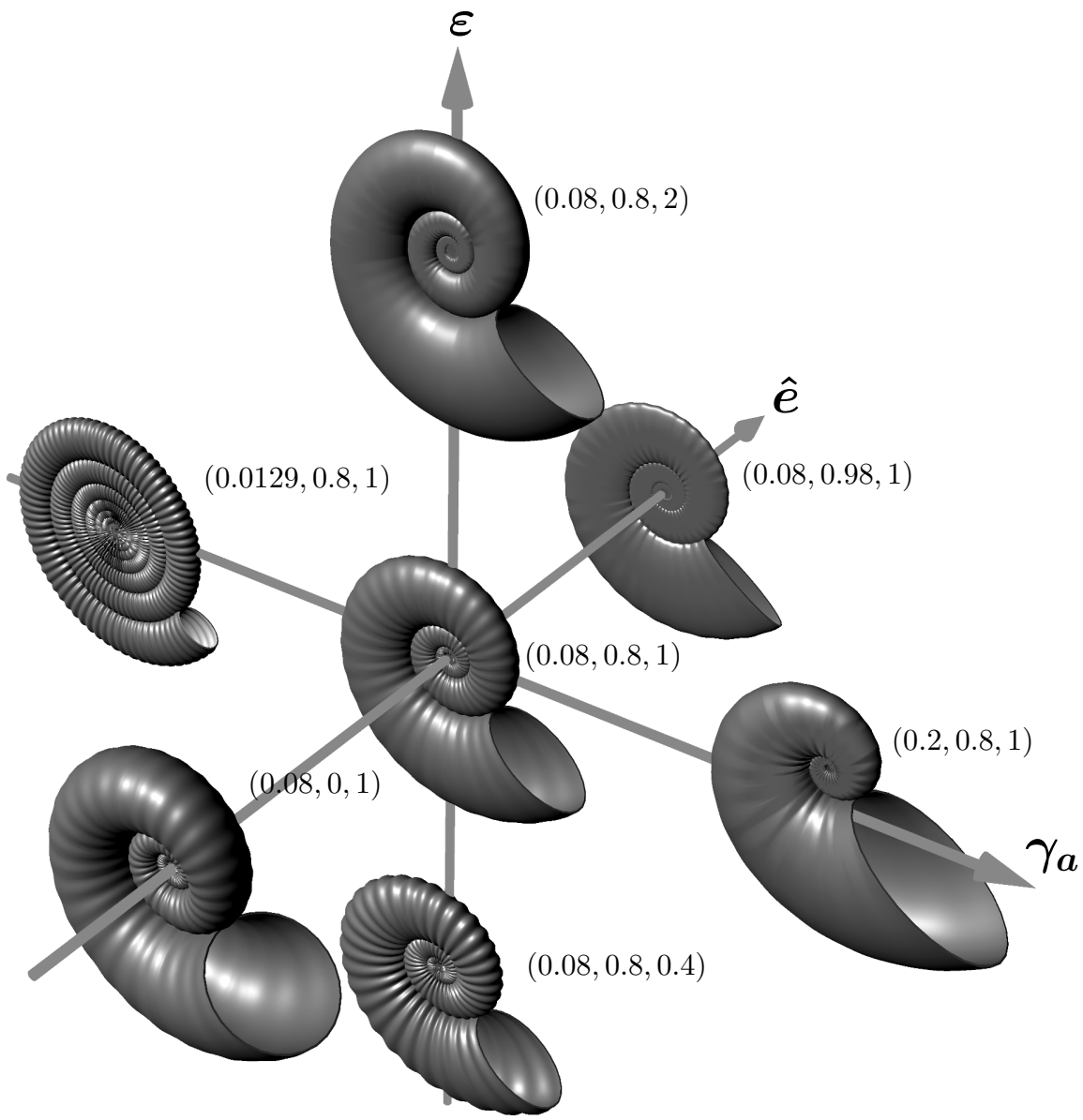


Figure 4.21: 3-dimensional morphospace that can be investigated with our model. The numbers for each surface are given in the form $(\gamma_a, \hat{e}, \varepsilon)$. The expansion rate $\gamma_a$ increases involution and decreases ornamentation. The eccentricity $\hat{e}$ increases compression and decreases ornamentation. The mechanical feedback $\varepsilon$ decreases ornamentation. Individual discussions can be found in Figures 4.21, 4.13 and 4.14.

# Chapter 5

# Conclusion

The primary goal of this thesis has been to to build a mathematical framework for the study of the growth response of soft biological tissues to changes in the mechanical environment. An example from physiology is the wall thickening and ventricular dilation of heart tissue in response to pressure and volume overload. We modeled biological tissue as nonlinear elastic material and described its growth process within the theory of morphoelasticity, which is based on the multiplicative decomposition of the deformation gradient $\boldsymbol{F}$ into an elastic tensor field $\boldsymbol{A}$ and a growth tensor field $\boldsymbol{G}$. We modeled the feedback of changes of the mechanical environment on the tissue growth by prescribing evolution laws to $\boldsymbol{G}$, which we refer to as growth laws. With the notion of growth laws, we can make a more precise statement of the thesis goal. Our goal has been to develop mathematical techniques to analyse macroscopic (tissue-level) growth evolution laws that are biologically plausible, and to explore issues of heterogeneity and growth stability.

We begin by briefly describing how our ideas in the study of growth laws evolved from a fundamental, thermodynamical perspective towards a phenomenological, homeostasis driven perspective. We motivate and summarise the main results of the thesis in Section 5.1. We conclude this Chapter by discussing the impact of our work as well as possible future extensions and applications of our models in Section 5.2.

## 5.1 Evolution of ideas and main results

Our first step in studying growth laws was to review a commonly used analysis of growth laws from the perspective of thermodynamics (Chapter 1). At the centre of this analysis is the Coleman-Noll procedure, which relies on a continuum mechanical statement of the Second Law of Thermodynamics (Clausius-Duhem inequality). Our mathematical analysis of the Coleman-Noll procedure applied to active biological tissue has yielded several interesting insights, as it provides a formal approach to distinguish between active and passive contributions to a growth law, and highlights a specific stress measure (Mandel stress) as a key quantity that emerges very naturally in the Clausius-Duhem inequality. However, our conclusion is that ultimately the thermodynamical approach provides no compelling way to restrict growth evolution laws, and does not offer compelling physical foundation for the frequently used Mandel and Eshelby driven growth laws to model biological growth processes: The tools developed for the study of passive (plastic) material have only a weak impact on active biological material.

The conclusion that growth laws cannot be strongly restricted from thermodynamic principles created the need for an alternative approach to identifying suitable growth laws. The fact that experimental data on evolution of growth and residual stress is sparse makes it difficult to reverse-engineer growth laws directly from observations and lead us towards a phenomenological principle called homeostasis. This principle states that organisms have the ability to self-regulate some of their properties to adapt the conditions for its optimal function in a physiological state, such as the ability of mammals to maintain a constant body temperature. From the perspective of homeostasis, the insight that many biological tissues maintain a residual stress field in physiological operation (which we call homeostatic stress) makes it plausible that growth dynamically evolves to accommodate the homeostatic stress. Our hypothesis is that growth evolves to keep the difference between the actual and homeostatic stress field as small as possible, so that growth stops and the tissue reaches its final observed size and morphology once the homeostatic stress is fully accommodated.

In Chapter 2, we analysed a network of elastic bars connected in a network of series and parallel connections. A biological inspiration comes from the previously mentioned

behaviour of heart tissue: as a response to volume and pressure overload, the mature heart grows by adding sarcomeres in series and parallel, respectively. In our model we analysed a homeostasis-driven growth law of morphoelastic bars deforming in a one-dimensional domain (they cannot bend, twist or shear). The network itself has a particular growth response to loading which is a function of the growth response of individual bars. We have shown that if all bars only undergo small deformations (in the Hookean regime), the full mechanical network will also respond to loading according to an effective Hooke's Law, and its effective Young's Modulus $\mu_{\text{eff}}$ and effective reference length $L_{\text{eff}}$ can be computed as functions of the properties of all individual bars. While such convenient homogenisation applies to static residually stressed networks, the situation for dynamically evolving networks is somewhat more complex. We also showed that if individual bars grow according to a homeostasis-driven growth law (i.e. growth rate and stress are proportional), the dynamics of the overall network cannot in general be broken down to a simple effective homeostasis-driven growth law, i.e. an effective growth rate $K_{\text{eff}}$ and an effective homeostatic stress $T^*_{\text{eff}}$ cannot be obtained in the general case. Growth dynamics has no analogous counterpart in electrical networks and appears to be more complex than the sum of its parts.

Our numerical simulations show that the growth dynamics in the neighborhood of the undeformed state (i.e. in the Hookean regime) exhibits non-monotonic behaviour, but never oscillates. We also show for an example three bar system that the dynamics near the homeostatic equilibrium in the Hookean regime is not always stable and explicitly state under which conditions stability is guaranteed.

In 3, we outlined a growth dynamical framework for the study of tubular structures in biology. As discussed previously, residual stress has been recognised to stabilise and optimise tubular structures, for example by reducing the circumferential stress gradient between arterial walls [23]or through axial residual stress [31]. However, while models focusing on residual stress in tubes can often uncover fine geometric and mechanical details (such as circumferential buckling [54] or axial buckling [60]), they typically cannot quantitatively describe the origin and evolution of such stresses. Our growth model adds an additional layer of description in which the observed stress state is an emergent feature of the homeostasis-driven growth dynamics, and our model enables

us to explore growth towards a particular stress state (the homeostatic stress). The key challenge of modeling the growth dynamics of tubular structures is that stress can be spatially inhomogeneous in a cylindrical geometry. In our model we address the inhomogeneity of the system through a discretisation in which the application of quantitative methods from dynamical systems theory like linear stability analysis becomes feasible. In the system considered, we found that the growth dynamics of tubular structures in the neighborhood of the homeostatic equilibrium nontrivially depends on the anisotropy of the growth response, and that the equilibrium becomes unstable for highly anisotropic growth laws. We show that our model converges as the discretisation becomes finer and we expect that the stable and unstable region represent the true behaviour of the full (inhomogeneous) system.

Having gained some intuition into the complex behaviour of growth dynamics driven of conceptual systems, in Chapter 4 we considered the relevance of mechanical feedback in a particular biological system, the morphogenesis of Ammonites' seashells. An observation from Ammonites' shells is that rapidly expanding shells in the juvenile stages tend to become smoother during development while the slowly expanding shells tend to remain more strongly ornamented at later stages of the development (see for instance the photographs in Figure 4.20(a)–(c)). The morphomechanical model described in Section 4.3.1.1 supports this observation: in (4.38), the relative amplitude decreases and the ribbing wavelength increases as one moves away from the shell spiral centre (the higher the arc length value $z$, the later the developmental stage).

However, as the simulations results in Figure 4.13 and Figure 4.14 show, the model presented in Section 4.3 predicts that even rapidly expanding shells are not completely smooth in late developmental stages. The photographs in Figure 4.20 show a representative sample of rapidly expanding Ammonites' shell fossils which do appear almost completely smooth in adult stages.

In Chapter 4 we demonstrate how a mechanical feedback mechanism similar to (1.23) affects the morphology of Ammonites' shells. The coupling of the morphomechanical model described in Section 4.3.1.1 to the mechanical feedback mechanism described in Section 4.5 retains strong ribbing in the juvenile stages of strongly expanding shells, but smoothens the late developmental stages as the coupling strength increases.

This morphology is consistent with observation and cannot readily be captured with previous models.

## 5.2 Future work and potential impact

### 5.2.1 Growth dynamics in tubes

In most models of tubular structures, residual stress is a result of a prescribed growth field. The model we developed in Chapter 3 provides an underlying mechanism that allows to re-interpret residual stress as an emerging feature of the underlying homeostasis-driven growth dynamics. This point of view opens up new perspectives. We may imagine a scenario in which we are presented with a biological tubular material in physiological condition, of which we know the constitutive law and can measure the pressure at the inner and outer tube wall. From the observed morphology of the tube, our model would allow to fit the anisotropy of the growth rate and the approximate shape of the homeostatic stress profile. These quantities may serve the design of an experimental setup to test the validity of the growth law (1.23) driven by homeostasis for a given tissue. This might be achieved by experimentally quantifying the anisotropy of the growth response of the tissue and by obtaining estimates for the homeostatic stress based on e.g. in vitro cultivated cells. An experimental protocol to assess the validity of the growth law (1.23) to model a given tissue is undoubtedly challenging to design, but the stability result shown in Figure 3.12 (or an adaptation thereof for a particular type of material in particular boundary conditions, see Section 3.3.5) may provide a stepping stone in the quest for the form of growth laws, which is a key piece needed for establishing a mechanical theory of growth [69, 30].

The establishment of solid experimental results narrowing down the functional form of growth laws may take decades to develop. Meanwhile, a more immediate application of our theory may be in the setup and interpretation of computational models of biological tubular structures. When modeling growth dynamics driven by growth laws similar to (1.23), as has been done by many authors (see Section 1.5.4), our homogenisation approach can be applied to inform parameter regimes in which stable dynamics is to be expected (similarly to Figure 3.12). This could potentially inform computational approaches to growth dynamics and provide insight with interpreting results such as

divergent solutions, making it easier to distinguish numerical error from inherently divergent dynamics (e.g. the hyper-restoration curve in Figure 5 of [69]). Models based on the ideas developed here may also assist the development of more computational models, providing a comparative framework in a simple geometry against which more computational code can be tested.

### 5.2.2 Embedding mechanical feedback into a computational framework of accretive growth

The model for growth of Ammonites' shells presented in Chapter 4 discusses circular and ellipse shaped cross sections and their evolution and impact on the shell morphology. An interesting extension would be to consider arbitrary aperture shape. This would allow us to explore the simultaneous formation of commarginal and antimarginal ornamentation. A computational surface growth framework has been proposed in [55, 56] and applied to the model of sharp spines of seashells in proposed in [11]. The application of the framework [55, 56] to growth of seashells with both antimarginal and commarginal ornamentation (see e.g. Figure 4 in [21]) would also allow us to more clearly isolate the impact of mechanical feedback to the morphogenesis of seashells. For instance, modeling an arbitrary aperture shape would allow us to incorporate the contact of the mantle with calcified shell material from the previous whorl, which may have a great effect on the morphogenesis of tightly coiled shells (i.e. if the overlap region in Figure A.5 is significant). Finally, integrating biochemical or biomechanical effects in a single framework would be an important step in bridging between the molecular levels and our tissue level mechanical approach. A starting point to integrating chemistry and mechanics may be to couple the local concentration of a chemical evolving via reaction-diffusion type models with a mechanically relevant parameter. For instance, pigmentation patterns (which can be very realistically reproduced with reaction diffusion models, see [22]) may be coupled to the elastic properties of the mantle, which in turn affects the morphological pattern (see Figure A.9).

### 5.2.3 Growth driven by Cauchy stress vs. Mandel stress

As discussed in Section 1.5.4, a number of authors have advocated Mandel (or Eshelby) stress driven growth laws. The justification for Eshelby driven growth is often based on thermodynamical arguments as outlined in Section 1.6. Growth laws driven by Cauchy stress are also frequently used, as discussed in Section 1.6. Interestingly, in the absence of shear stress in incompressible materials, Mandel and Cauchy stress coincide (see comment before 1.38). A construction of a growth dynamical system in which shear stress is incorporated into the growth law might help highlight interesting features of either growth law family and may reveal whether one or the other produces dynamics in better agreement with physical observation. In [66], fluid shear stress is included into a growth law of type (1.23) in the context of arterial modeling. This setup may serve as a starting point for a focused analysis of what makes Cauchy and Mandel stress driven growth dynamics different.

# Appendix A

# Appendix

## A.1 Numerical study of growth dynamics in three bar network

In this Section, we provide the numerical values and details on the simulations producing Figures 2.9 and (2.8) are given in Section A.1.

For this system ($n = 3$, $r = 2$, $s = 2$) we choose the following initial reference quantities:

$$L_\Sigma^0 = 1, \qquad \boldsymbol{L}^0 = (0.61, 0.39, 0.39)\,. \tag{A.1}$$

We note that the individual initial lengths $L_i^0$ are compatible with the total initial length $L_\Sigma^0$, i.e. $A\boldsymbol{L}^0 = L_\Sigma \boldsymbol{v}^r$.

For the modified Young's Modulus, we choose

$$\tilde{\boldsymbol{\mu}} = (0.62, 4.79, 1.91) \tag{A.2}$$

which implies $\boldsymbol{\mu} = (0.38, 1.86, 0.74)$ (we note that $\tilde{\mu}_i = \mu_i / L_i^0$).

We consider a boundary value problem in which the total length of the system is prescribed $l_\Sigma = 0.95$. The total length is defined as $l_\Sigma = L_\Sigma^0 + \varepsilon \tilde{l}_\Sigma$, and in this particular example we choose a relatively high value of $\varepsilon$, that is

$$\varepsilon = 0.5\,. \tag{A.3}$$

The total displacement is $\tilde{l}_\Sigma = \left(l_\Sigma - L_\Sigma^0\right)/\varepsilon = -0.1$.

Next, we choose the homeostatic stresses

$$\tilde{\boldsymbol{t}}^* = (-3.82, 0.91, -4.74)\,. \tag{A.4}$$

We note that the individual homeostatic stresses $\tilde{t}_i$ are compatible with the network, adding up to a total homeostatic stress $\tilde{t}^*_\Sigma \approx -3.82$ , i.e. $B\tilde{\boldsymbol{t}}^* = \tilde{t}^*_\Sigma \boldsymbol{v}^s$. Finally, we choose the expansion rates

$$\boldsymbol{k} = (2.51, -0.60, 1.86)\,. \tag{A.5}$$

We note that $\boldsymbol{k}$ is chosen so that $S$ has negative eigenvalues. With all the previous information, the values of $S$ and $\boldsymbol{w}$ are

$$S = \begin{pmatrix} -0.89 & -0.63 & -0.25 \\ 0.1 & 0.39 & -0.29 \\ -0.12 & 0.9 & -1.02 \end{pmatrix}, \qquad \boldsymbol{w} = \begin{pmatrix} 5.81 \\ 0.22 \\ 3.42 \end{pmatrix}. \tag{A.6}$$

We note that the linear dynamics near the unstressed state is described by $\dot{\tilde{\boldsymbol{L}}} = S\tilde{\boldsymbol{L}} + \boldsymbol{w}$ . The eigenvalues of $S$ are $\boldsymbol{\lambda} = (-1.1, -0.42, 0)$, i.e. the dynamics of $\tilde{L}_1$ and $\tilde{L}_2$ is stable and the dynamics of $\tilde{L}_3$ depends on the former two. The region of $\boldsymbol{k}$-values in which the dynamics is stable is explored in Fig. 2.7.

## A.2 Analogy between electrical and elastic networks

In this section we develop a formal analogy between growing networks and electrical circuits.

**Parallel connections**

$$\boxed{\tilde{\mu}_\Sigma = \tilde{\mu}_1 + \tilde{\mu}_2} \quad \text{and} \quad \boxed{\tilde{L}_\Sigma = \frac{\tilde{\mu}_1 \tilde{L}_1 + \tilde{\mu}_2 \tilde{L}_2}{\tilde{\mu}_\Sigma}}. \tag{A.7}$$

The addition rule for Young's Modulus of this parallel connection of bars mirrors the addition rule of resistors connected in series in electric circuits. If we consider an

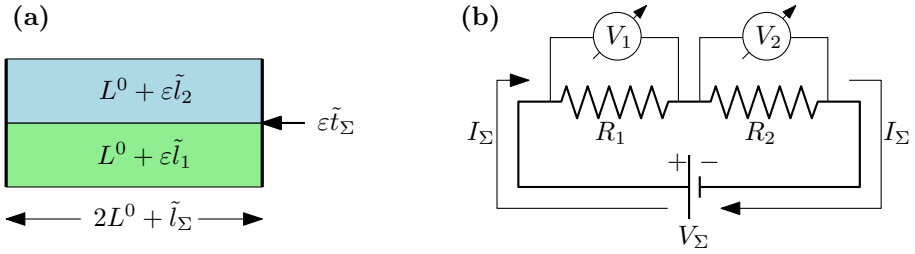


Figure A.1: Relationship between elastic network in series and electric circuit in parallel.

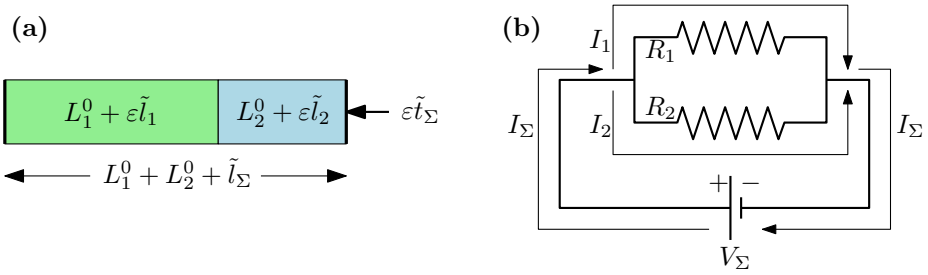


Figure A.2: Relationship between elastic network in parallel and electric circuit in series.

electric circuit just like in the previous case (current $I_\Sigma$ flowing from battery $V_\Sigma$), we find that the individual currents are the same ($I_\Sigma = I_1 = I_2$) but the voltage drop is additive ($V_\Sigma = V_1 + V_2$, where once again $V_1 = R_1 I_2$ and $V_2 = R_2 I_2$). The effective resistance $R_\Sigma$ which satisfies $V_\Sigma = R_\Sigma I_\Sigma$ is

$$\frac{1}{R_\Sigma} = \frac{1}{R_1} + \frac{1}{R_2}, \tag{A.8}$$

which is similar to $(2.69)_1$. Figure A.1 compares these two setups.

**Series connections**

$$\boxed{\frac{1}{\tilde{\mu}_\Sigma} = \frac{1}{\tilde{\mu}_1} + \frac{1}{\tilde{\mu}_2}} \quad \text{and} \quad \boxed{\tilde{L}_\Sigma = \tilde{L}_1 + \tilde{L}_2}. \tag{A.9}$$

The addition rule for Young's Modulus of this series connection of bars mirrors the addition rule of resistors connected in parallel in electric circuits. Consider an electric circuit with a battery with voltage $V_\Sigma$, from which the current $I_\Sigma$ flows. At a parallel connection of two resistors with resistances $R_1$ and $R_2$ the current $I_\Sigma$ splits into two currents $I_\Sigma = I_1 + I_2$. The voltage drop at both resistors is $V_1 = R_1 I_2$ and $V_2 = R_2 I_2$ such that $V_\Sigma = V_1 = V_2$. This allows us to define a rule for an effective resistance $R_\Sigma$

| **elastic networks** | **electrical networks** |
|---|---|
| current displacements $\tilde{l}_i$, $\tilde{l}_\Sigma$ | currents $I_i$, $I_\Sigma$ |
| (small) forces $\tilde{t}_i$, $\tilde{t}_\Sigma$ | voltages $V_i$, $V_\Sigma$ |
| (modified) Young's Modulus $\tilde{\mu}_i$, $\tilde{\mu}_\Sigma$ | (inverse of) resistors $R_i$, $R_\Sigma$ |
| reference displacements $\tilde{L}_i$, $\tilde{L}_\Sigma$ | none |
| Hooke's Law $\tilde{t}_i = \tilde{\mu}_i \left(\tilde{l}_i - \tilde{L}_i\right)$ | Ohm's Law $V_i = R_i I_i$ |
| series connection $\tilde{\mu}_\Sigma = \frac{\tilde{\mu}_1 \tilde{\mu}_2}{\tilde{\mu}_1 + \tilde{\mu}_2}$ | parallel connection $R_\Sigma = \frac{R_1 R_2}{R_1 + R_2}$ |
| parallel connection $\tilde{\mu}_\Sigma = \tilde{\mu}_1 + \tilde{\mu}_2$ | series connection $R_\Sigma = R_1 + R_2$ |
| series connection $\tilde{L}_\Sigma = \tilde{L}_1 + \tilde{L}_2$ | none |
| parallel connection $\tilde{L}_\Sigma = \frac{\tilde{\mu}_1 \tilde{L}_1 + \tilde{\mu}_2 \tilde{L}_2}{\tilde{\mu}_1 + \tilde{\mu}_2}$ | none |

Table A.1: Comparison between elastic and electrical networks.

which satisfies $V_\Sigma = R_\Sigma I_\Sigma$. Similarly to $(2.64)_1$, the effective resistance satisfies

$$\frac{1}{R_\Sigma} = \frac{1}{R_1} + \frac{1}{R_2}\,. \tag{A.10}$$

Figure A.2 compares these two setups.

The fact that a series connection in elastic networks mirrors a parallel connection in electric circuits can be formally understood by comparing the role of resistances $R$ and Young's Modulus $\tilde{\mu}$ in the respective networks. Their relationship is:

$$\boxed{R \longleftrightarrow \frac{1}{\tilde{\mu}}} \tag{A.11}$$

This is a consequence of Hooke's Law and Ohm's Law. The differences between elastic and electrical networks are comprehensively shown in Table A.1.

## A.3 Relative amplitudes of the major and minor axes

In Section 4.3.2, we have shown that the full model displays the same general trends as the reduced model, justifying *a posteriori* the use of the reduced model. Here we demonstrate that no implicit assumptions are made regarding the relative amplitudes of the major and minor axes. In Figure A.3, we plot the relative ribbing amplitude as a function of the reference eccentricity for oscillations around the fixed stress-free states $\hat{b}$ and $\hat{a}$. For each eccentricity, we provide the same initial displacement $\delta$ for both $\hat{b}$ and $\hat{a}$ and observe that the higher curvature side $a(z)$ automatically assumes

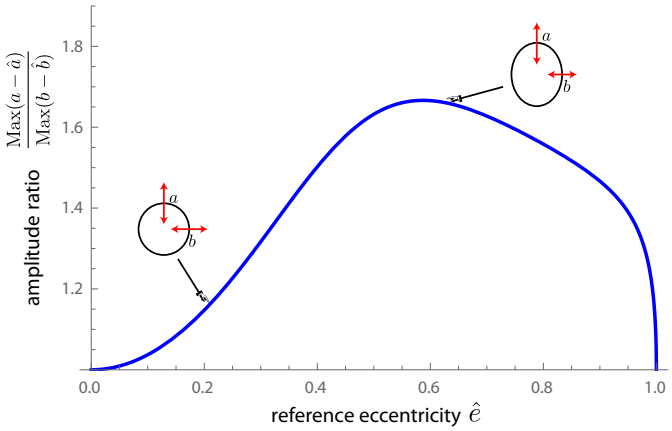


Figure A.3: Relative ribbing amplitude between the high curvature side $a(z)$ and low curvature side $b(z)$ as a function of reference eccentricity. Plot produced through simulations using the full model and with equal initial displacement for $a$ and $b$.

a higher oscillation amplitude than the lower curvature side $b(z)$. In this Section we demonstrate how the nonlinear shape of the curve presented in Figure A.3 is obtained.

In this section we provide details on Figure A.3, which plots the relative ribbing amplitude $\mathrm{Max}(a-\hat{a})/\mathrm{Max}(b-\hat{b})$ as a function of the reference eccentricity $\hat{e}$, for constant reference states $\hat{a}$ and $\hat{b}$ ($\gamma_a = \gamma_b = 0$). We impose equal initial displacements

$$a(0) = \hat{a} + \delta, \quad b(0) = \hat{b} + \delta, \tag{A.12}$$

thus giving no implicit increased amplitude on the major axis. We consider the Euler-Lagrange equations (4.28), and define

$$a\left(z\right) = \hat{a} + a_1\left(z\right), \qquad b\left(z\right) = \hat{b} + b_1\left(z\right). \tag{A.13}$$

Under the assumption of small amplitude oscillations about the reference state, the system can be linearised and exact solutions obtained (similar results may be obtained numerically, but are less illustrative). Assuming that $\delta \ll 1$ and $a_1 \ll 1$, $b_1 \ll 1$, the system (4.28) can be approximated at first order by the matrix equation

$$M\mathbf{x}''\left(z\right) + K\mathbf{x}\left(z\right) = 0 \tag{A.14}$$

where

$$\mathbf{x} = \begin{pmatrix} a_1 \\ b_1 \end{pmatrix}, \tag{A.15}$$

and $M$, $K$ are constant matrices given by

$$M = \begin{pmatrix} -\frac{16\hat{a}\left(\hat{a}+2\hat{b}\right)K_g}{\left(\hat{a}+\hat{b}\right)^2} & -\frac{16\hat{a}\hat{b}K_g}{\left(\hat{a}+\hat{b}\right)^2} \\ 16\hat{a}^5\hat{b}^6K_g & 16\hat{a}^4\hat{b}^6\left(2\hat{a}+\hat{b}\right)K_g \end{pmatrix},$$

$$K = \begin{pmatrix} \frac{-16\hat{b}^3\left(2\hat{a}+\hat{b}\right)K_s\hat{a}^4-\rho K_b}{\hat{a}^5\hat{b}^3\left(\hat{a}+\hat{b}\right)^2} & \frac{\rho K_b-16\hat{a}^4\hat{b}^4K_s}{\hat{a}^4\hat{b}^4\left(\hat{a}+\hat{b}\right)^2} \\ 16\hat{a}^4\hat{b}^5K_s-\rho\hat{b}K_b & 16\hat{a}^4\left(\hat{a}+2\hat{b}\right)K_s\hat{b}^4+\rho\hat{a}K_b \end{pmatrix}.$$

Here we have used the shorthand

$$\rho = \left(\hat{a}+\hat{b}\right)^2\left(2\hat{a}^2\hat{b}^2+7\hat{a}^4+7\hat{b}^4\right). \tag{A.16}$$

The system, (A.14), admits solutions of the form

$$\mathbf{x} = \mathbf{a}\cos\left(\omega z-\varphi\right), \qquad \mathbf{a} = \begin{pmatrix} a_1 \\ a_2 \end{pmatrix}. \tag{A.17}$$

i.e. $a$ and $b$ have the same frequency and phase but a different amplitude. Equation (A.14) then turns into the eigenvalue problem

$$M^{-1}K\mathbf{a} = \omega^2\mathbf{a} \tag{A.18}$$

Here, $\mathbf{a}$ is an eigenvector and $\omega^2$ an eigenvalue. We have a nontrivial solution if and only if $\det\left(M^{-1}K-\lambda 1\right)=0$. This allows us to determine the eigenvalues $\omega_1^2, \omega_2^2$ and the respective eigenvectors

$$\mathbf{e}_1 = \begin{pmatrix} e_1^a \\ e_1^b \end{pmatrix}, \qquad \mathbf{e}_2 = \begin{pmatrix} e_2^a \\ e_2^b \end{pmatrix}. \tag{A.19}$$

Note that the subscript identifies the eigenvector such that $M^{-1}K\mathbf{e}_i = \omega_i^2\mathbf{e}_i$, $i=1,2$, and the superscript identifies the vector component. The general solution is

$$\mathbf{x} = A_1\mathbf{e}_1\cos\left(\omega_1 z-\varphi_1\right)+A_2\mathbf{e}_2\cos\left(\omega_2 z-\varphi_2\right). \tag{A.20}$$

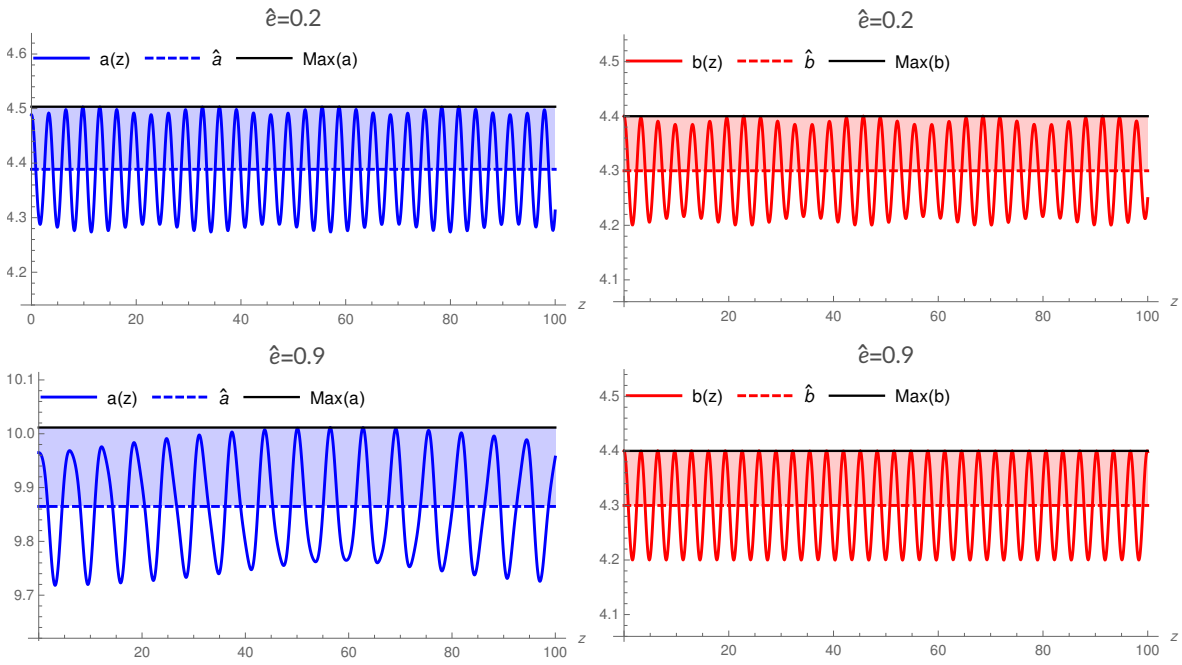


Figure A.4: Oscillations of $a$ and $b$ near reference states $\hat{a}$ and $\hat{b}$ for values of $\hat{e}$, 0.2 and 0.9. The upper limits $\mathrm{Max}\,(a)$ and $\mathrm{Max}\,(b)$ are plotted in red and the shaded regions, which represent $\mathrm{Max}(a_1)$ and $\mathrm{Max}(b_1)$, are drawn side by side for comparison. Parameters for this simulation can be found in Appendix A.5.

The constants $A_1, A_2, \varphi_1, \varphi_2$ are determined from initial conditions

$$a_1\,(0) = b_1\,(0) = \delta, \qquad a_1'\,(0) = b_1'\,(0) = 0\,. \tag{A.21}$$

This gives the following form for the four unknown coefficients:

$$A_1 = \delta\left(\frac{e_2^a - e_2^b}{e_1^b e_2^a - e_1^a e_2^b}\right), \qquad A_2 = -\delta\left(\frac{e_1^a - e_1^b}{e_1^b e_2^a - e_1^a e_2^b}\right), \qquad \varphi_1 = \varphi_2 = 0\,. \tag{A.22}$$

The maximum amplitudes $\mathrm{Max}(a - \hat{a}) = \mathrm{Max}\,(a_1)$ and $\mathrm{Max}(b - \hat{b}) = \mathrm{Max}(b_1)$ are the upper bounds of $a_1$ and $b_1$, which can be computed numerically. The eigenvalues $\omega_1^2$, $\omega_2^2$ and eigenvectors $\mathbf{e}_1$, $\mathbf{e}_2$ are functions of $\hat{a}$ and $\hat{b}$ and therefore can be formulated as functions of $\hat{b}$ and $\hat{e}$. The curve shown in Figure A.3 is a plot of $\mathrm{Max}(a_1)/\mathrm{Max}(b_1)$ over $\hat{e}$. For two values of the reference eccentricity, $\hat{e} = 0.2$ and $\hat{e} = 0.9$, the oscillations $\hat{a} + a_1$ and $\hat{b} + b_1$ are plotted in Figure A.4. The shaded regions represent $\mathrm{Max}(a_1)$ and $\mathrm{Max}(b_1)$ and are drawn side by side for comparison.

## A.4 Coiling and 3D seashell surface

In this section we relate the ribbing oscillations to the coiled 3D shells presented in Figures 4.13 and 4.14 in the main text. We split this task into two parts: First, we introduce coiling via a logarithmic spiral shape that forms the basis for the shell surface (i.e. the shape in the absence of ribbing) and relate the coiling parameters to the expansion rate $\gamma_a$ of the major axis of the ribbing model. Then, we give a parametric representation of the fully ribbed and coiled seashell surface that underlies the figures in the main text.

### A.4.1 Description of shell coiling

A logarithmic spiral is a polar curve with radius $\rho$ and angle $\phi$ by $\rho(\phi) = c_1 e^{c_2\phi}$, characterized by two coiling parameters $c_1$, $c_2$. In Cartesian coordinates $\{x, y\}$, the curve takes the form $x(\phi) = \rho(\phi)\cos\phi$, $y(\phi) = \rho(\phi)\sin\phi$. The (unribbed) Ammonites' shell surface is modeled by three logarithmic spirals: The centreline spiral $\rho_m$, the dorsal spiral $\rho_d$, and the ventral spiral $\rho_v$. In polar coordinates, they are

$$\rho_m(\phi) = c_1 e^{c_2\phi}, \qquad \rho_d(\phi) = (c_1 - \hat{a})\, e^{c_2\phi} \qquad \text{and} \qquad \rho_v(\phi) = (c_1 + \hat{a})\, e^{c_2\phi}. \quad \text{(A.23)}$$

Here $\hat{a} = \hat{a}(\phi)$ is the half-distance between the dorsal and ventral side. If the low curvature side of the elliptical shell margin is oriented along the lateral side, we identify $\hat{a}$ with the reference major axis.

To characterise to what degree the coiling shell overlaps with itself, we introduce a tightness-of-coiling parameter $\tau$, following the ideas of [57] (see Figure 7 of that reference). For coiling in perfect contact, in which the ventral side coincides with the dorsal side of the previous whorl, we have $\tau = 1$. Overlap between each whorl and the previous whorls corresponds to a value of $\tau > 1$. For an illustration see Figure A.5.

From the definition of $\tau$, we have that $\rho_v(\phi) = \tau\rho_d(\phi + 2\pi)$ which implies

$$e^{c_2 2\pi} = \frac{1}{\tau}\left(\frac{c_1 + \hat{a}_0}{c_1 - \hat{a}_0}\right). \quad \text{(A.24)}$$

To relate the coiling to the expansion rate $\gamma_a$, we must first compute the arclength of the centreline spiral $\rho_m$. The centreline is described by the curve $\mathbf{r}_m(\phi) = \rho_m(\phi)\,\mathbf{e}_r(\phi)$

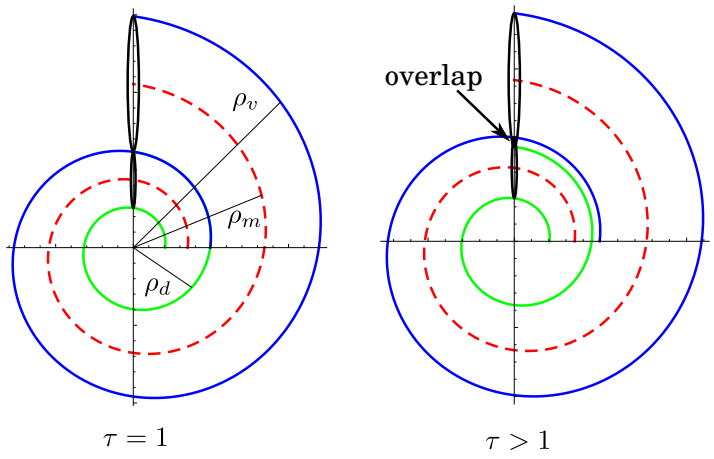


Figure A.5: The logarithmic spirals (A.23) representing the shell centreline $\rho_m$, the dorsal side $\rho_d$ and the ventral side $\rho_v$. In the case of perfect contact between whorls, the tightness of coiling parameter is $\tau = 1$. In the case of overlap, $\tau > 1$. Figure adapted from [57].

where $\mathbf{e}_r$ is the radial direction which in a Cartesian basis $\{\mathbf{e}_x, \mathbf{e}_y, \mathbf{e}_z\}$ is $\mathbf{e}_r(\phi) = \cos\phi\,\mathbf{e}_x + \sin\phi\,\mathbf{e}_y$. Its arclength is

$$z(\phi) = \int_0^{\phi} \left| \frac{\mathrm{d}\mathbf{r}_m(\varphi)}{\mathrm{d}\varphi} \right| \mathrm{d}\varphi = \frac{\sqrt{1+c_2^2}}{c_2} \left[\rho_m(\phi) - c_1\right] \tag{A.25}$$

The reference length of the major axis satisfies by

$$\rho_v(\phi) - \rho_m(\phi) = \hat{a}(z(\phi)), \tag{A.26}$$

where $\hat{a}(z(\phi)) = \hat{a}_0 + \gamma_a z(\phi)$ in the case of linear expansion. Evaluating (A.26) provides the following relationship between $\gamma_a$ and the coiling parameters:

$$\hat{a}_0 c_2 = c_1 \gamma_a \sqrt{1+c_2^2}. \tag{A.27}$$

In order to obtain the coiling parameters $c_1$, $c_2$ in terms of $\gamma$ and $\tau$, the equations (A.24) and (A.27) must be solved simultaneously, which can be achieved numerically.

### A.4.2 Number of ribs per whorl

The above connections, combined with the analytical results of ribbing in Subsection 4.3.1.1 implies a constant number of ribs per whorl. To see this, we consider the result

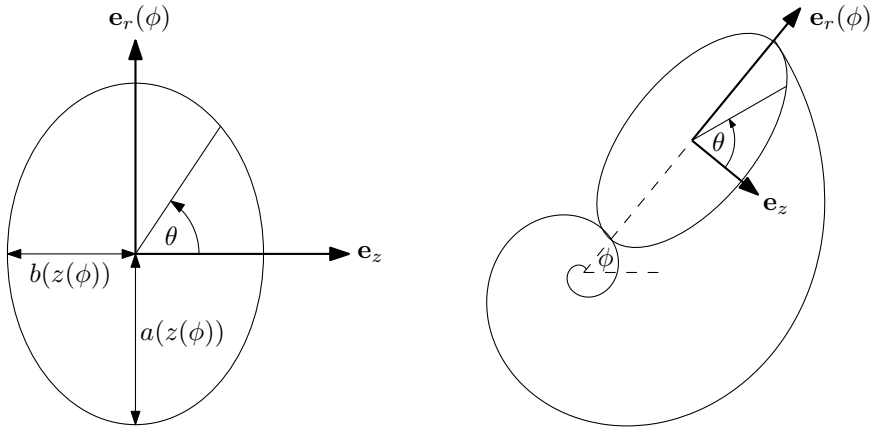


Figure A.6: Cross-section of 3D shell surface. The shell coiling parameter is $\phi$, whereas the ellipse parameter is $\theta$. The surface parameterisation (A.30) can be interpreted as an ellipse with major axis $a$ and minor axis $b$ added on top of the centreline curve $\mathbf{r}_m$ in a local basis $\{\mathbf{e}_z, \mathbf{e}_r\}$.

(4.38) and parameterise it in terms of angle $\phi$ rather than arclength $z$. To do this, we first note that (A.25) together with (A.27) imply $c_1 c_2^{-1}\sqrt{1+c_2^2} = \hat{b}_0/\gamma_b$. With this insight and $\rho_m$ according to A.23$_1$, the arclength expression (A.25) then simplifies to

$$z(\phi) = \frac{\hat{b}_0}{\gamma_b}\left(e^{c_2\phi} - 1\right) . \tag{A.28}$$

Then the result (4.38) transforms to

$$b(\phi) = \hat{b}_0 e^{c_2\phi} + \delta b\, A e^{\frac{1}{2}c_2\phi}\cos\left(\omega c_2\phi - \nu\right) \tag{A.29}$$

which implies a fixed number $N = \omega c_2$ ribs per whorl.

### A.4.3 Parametric form of shell surface

The coiling formulation above enables to find the coiling parameters $c_1$ and $c_2$ in terms of the parameters $\gamma$ and $\tau$, while the morphomechanical ribbing model of Appendix 4.2 provides $a(z)$ and $b(z)$. The full 3D seashell surface is then parameterised by

$$\mathbf{r}(\theta,\phi) = \mathbf{r}_m(\phi) + b(z(\phi))\cos\theta\,\mathbf{e}_z + a(z(\phi))\sin\theta\,\mathbf{e}_r \tag{A.30}$$

where $\theta$ is the cross-section ellipse parameter and $\phi$ is the coiling parameter, see Figure A.6. This surface parameterisation was used to plot all 3D seashells in this paper.

### A.4.4 Shell fitting and 3D printing

When presented with a real life Ammonite, we are interested in extracting the relevant parameters for our model, such as the expansion rate $\gamma_a$ and the stiffness parameter $k$. To do this, we must fit the spirals produced by our model to real life Ammonite photographs. Extracting the relevant parameters allows us to describe a 3D surface, which represents a real life Ammonite through the framework of our model. This also allows us to produce life-size versions of real Ammonites' shells on the basis of our model through 3D printing. The procedure for this fitting is presented in detail in the algorithm below. A visual illustration can be found in Fig. A.7.

**Algorithm A.1** Shell fitting

1. Make a lateral photograph of an Ammonite shell such as the top left image in Fig. A.7
2. Estimate the eccentricity $\hat{e}_0$ of the cross-section.
3. By fitting the three spiral curves (A.23), obtain fit values for the initial major axis $\hat{a}_0$ and coiling parameters $c_1$, $c_2$.
4. By solving the equations (A.24) and (A.27) simultaneously (numerically), compute the expansion rate $\gamma_a$ and the tightness of coiling parameter $\tau$.
5. To fit the stiffness parameter $k$, replace the smooth spirals $\rho_v(\phi)$ and $\rho_d(\phi)$ (see A.23) by the ribbed spirals $\rho_m + a(z(\phi))$ and $\rho_m - a(z(\phi))$. The major axis value $a(z)$ results from a mechanical model, for instance a model of linear expansion ((4.30) and (4.38)), non-linear expansion (Subsection 4.3.1.3), allometric variation (Subsection 4.3.1.2) or mechanical feedback (Section 4.5). Choose the $k$ parameter to best fit the ribbing pattern.
6. The fit is complete. Plot the parametric 3D surface according to (A.30).

### A.4.5 Interactive web simulation of seashell surface

To better illustrate the results of our model, we created an interactive web simulation in which the user can examine the parametric surface (A.30) as a function of various parameters. The user can change the values of the stiffness parameter $k$, the tightness of coiling parameter $\tau$, the expansion rate $\gamma_a$ of the ventral side, and the constant eccentricity $\hat{e}$ (allometric variation is not considered here). The seashell surface updates instantaneously. A screenshot can be seen in Fig. A.8. The simulation can be run from

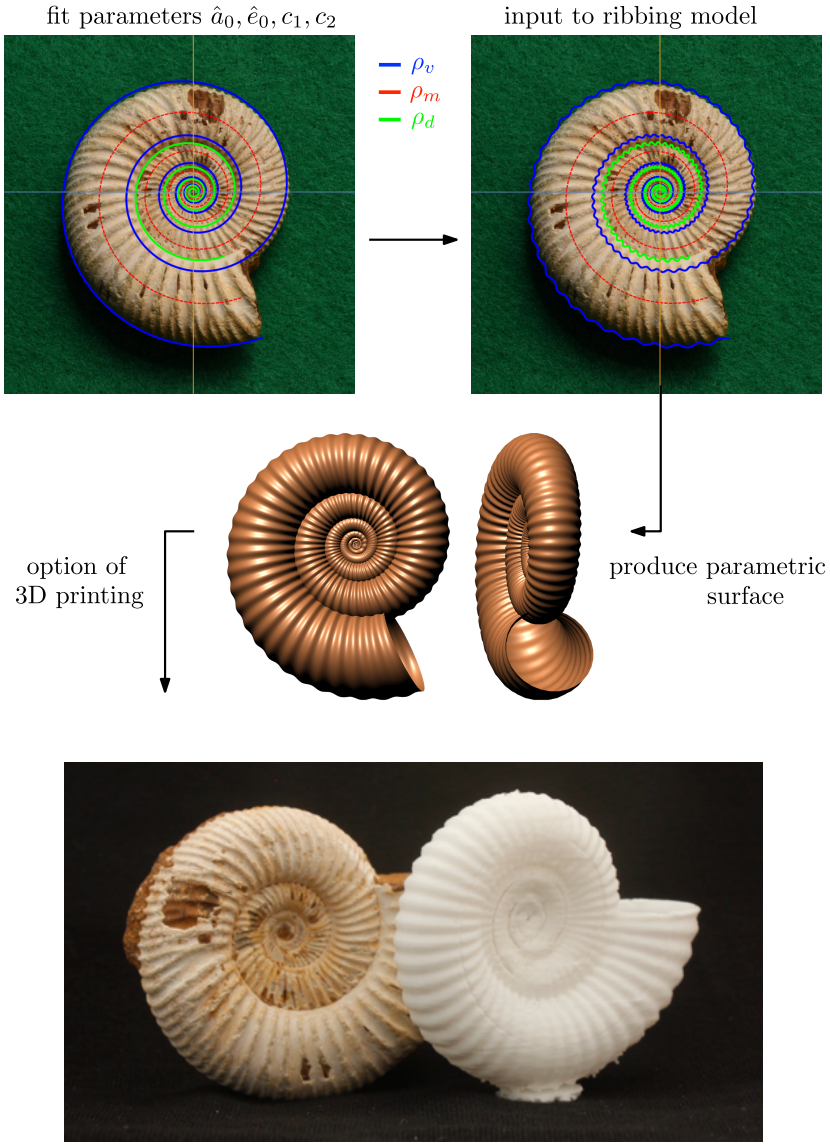


Figure A.7: Illustration of shell fitting method, which allows us to reproduce the three dimensional shape of an Ammonite shell on the basis of our model. **(a)** By fitting the spirals $\rho_m$, $\rho_v$ and $\rho_d$ to the Ammonite photograph, we can extract the parameters $\hat{a}_0$, $\hat{e}_0$, $c_1$ and $c_2$. **(b)** By adding a mechanical model, we obtain a ribbing pattern, which allows us to fit the parameter $k$. **(c)** Once all parameters have been fitted, we obtain a 3D surface. **(d)** With the possibility of 3D printing, we can produce life-size versions of real Ammonites' shells on the basis of our model. Photographs courtesy of Alain Goriely. The details of this shell fitting procedure are given in Algorithm A.1.

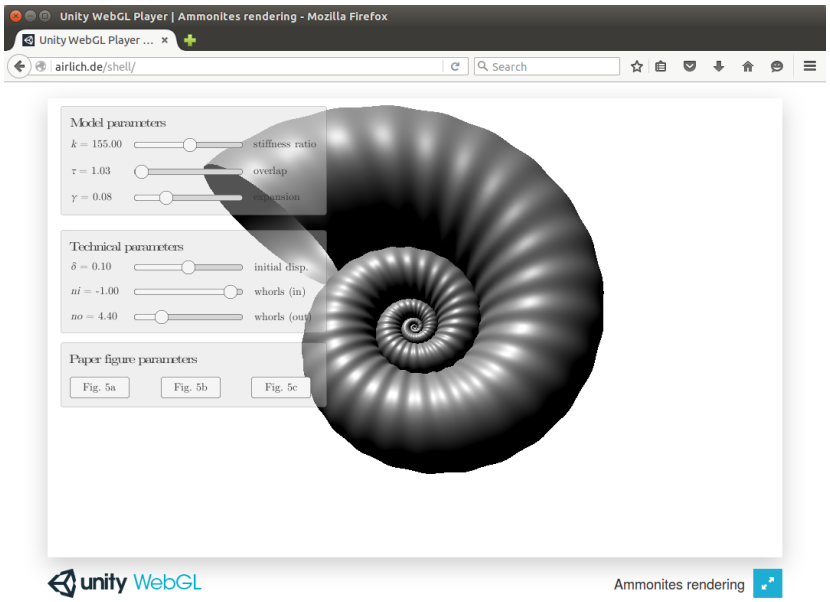


Figure A.8: 3D shell.

any browser on any desktop operating system at airlich.de/shell.

### A.4.5.1 Interactive parameters

The interactive functionality of the simulation can be separated in three categories. This can be seen in the interface categories in Fig. A.8). The categories are: Model parameters, technical parameters and Paper figure parameters. We give details the meaning of the parameters of each category, which also serves to illustrate how the 3D seashell is generated.

#### *Model parameters*

The ribbing pattern is calculated according to (4.38). In order to obtain the logarithmic spirals (A.23), we require the coiling parameters $c_1, c_2$, which we obtain by numerically solving (A.24) and (A.27) simultaneously. The parametric surface is then rendered through (A.30).

#### *Technical parameters*

Note that the parameter $\hat{a}_0$ has a fixed value. The parameter $\delta$, which can be chosen by the user, sets the initial displacement to $a(0) = (1 + \delta)\hat{a}_0$. The parameter $no > 0$ sets the number of whorls in the outside or forward coiling direction (i.e. forward in time),

whereas the parameter $ni < 0$ sets the number of whorls in the opposite direction and can serve as a way to fill the hole in the shell center for shells with small expansion rate $\gamma_a$.

### A.4.6 Computational realisation

In this subsection, we give some brief details on the technical realisation of this simulation. The simulation is created with the Unity game engine (https://unity3d.com/), which is responsible for translating high level code in C# into WebGL code which is uploaded to a server. The mesh of the seashell is procedurally generated from approximately 65.000 vertices 130.000 triangles, half of which are used for the outward facing part of the mesh, the other half facing inward. The shell aperture angle and the shell arc length are discretised in an equidistant manner. Surface normals are calculated from all shared vertices and rendering is performed with Unity's default material shader.

## A.5 Parameters

### A.5.1 Parameter values

Based on a study of images from Peltoceras schroederi, [57] determined a value of $k = 154.75$ based on a least squares analysis determining the best fit of their model to the empirically determined number of ribs produced over a particular shell length. Also, the authors observed that in Peltoceras schroederi *"the shell radius increases from around 1mm to 3.5mm over a length of shell between 40mm and 100 mm"*. On the other hand, shells of the species Echioceras raricostatum have a subcircular cross-section and are slowly expanding, within the range of shell coiling of Peltoceras schroederi, but exhibits ribbing pattern with a wavelength two to three times greater. This interspecific variation of ribbing wavelength among species with similar shell coiling allowed us to determine a second value of $k = 40$ by best fit of the model to an Echioceras shell. Our choice of dimensional parameters (such as $\hat{a}_0$, $\hat{b}_0$) and expansion rates ($\gamma_a$, $\gamma_b$) has been guided by these estimated values of *Peltoceras* and *Echioceras*.

In particular, the parameters used to produce the figures of the main text are:

**Fig. 4.13** $\hat{b}_0 = 5.93\,\mathrm{mm}$, $\delta b = 0.59\,\mathrm{mm}$, $\hat{e}_0 = 0.7$, $k = 155$, $\tau = 1.03$. Expansion rates $\gamma_b$ as indicated in the figure.

**Fig. 4.9** Same as 4.13.

**Fig. 4.14** $\hat{a}_0 = \hat{b}_0 = 8.3\,\mathrm{mm}$, $\delta a = \delta b = 0.83\,\mathrm{mm}$, $k = 40$. Expansion rates $\gamma_a$ and $\gamma_b$ as indicated in the figure.

**Fig. 4.16** $\gamma = 0.16$, $\tau = 1.03$, $k = 155$, $\varepsilon = 0.1$, $R_0 = 8.3\,\mathrm{mm}$, $\varepsilon$ as indicated in the figure.

**Fig. A.4** $\hat{b} = 4.3$, $\delta = 0.1$, $K_s = 70\,\mathrm{Nm}$, $K_b = 100\,\mathrm{Nm}$, $K_g = 1\,\mathrm{Nm}$.

**Fig. A.9** $\hat{a}_0 = \hat{b}_0 = 8.3\,\mathrm{mm}$, $\delta a = \delta b = 0.83\,\mathrm{mm}$, $K_g = 1\,\mathrm{Nm}$, $K_b = 10^5\,\mathrm{Nm}$, $\gamma_a = 0.10$, $\gamma_b = 0.02$. $K_s(z)$ as indicated in the figure.

**Figs. 4.17, 4.18 & 4.19** $\gamma = 0.1$, $k = 30$, $\rho = 0.1$, $R_0 = 8.3\,\mathrm{mm}$, $\varepsilon$ and $\tilde{\varepsilon}$ as indicated in the figure.

**Fig. 4.20** $\gamma = 0.067$, $\tau = 1.5$, $k = 200$, $\rho = 0.7$, $R_0 = 16.32\,\mathrm{mm}$, $\varepsilon$ as indicated in the figure.

### A.5.2 Stiffness variation

A main point of the paper was to explore how the ribbing pattern depends on expansion rate and eccentricity. However, since there is some uncertainty regarding the elastic parameters, we briefly consider whether variations in the elastic parameters might have a significant impact on the pattern. For this purpose, we consider the full nonlinear model (4.28). In Figure A.9, we explore the influence of the stretching stiffness $K_s$ on the ribbing pattern. Here the reference major and minor axis are prescribed as $\hat{a} = \hat{a}_0 + \gamma_a z$ and $\hat{b} = \hat{b}_0 + \gamma_b z$, respectively. The stretching stiffness has the form $K_s = K_s^0 e^{m\,z}$, where $K_s^0$ is the initial stiffness and $m$ is a real number. Note that for $m = 0$, we recover the case presented in Figure 4.11, see Figure A.9 column a. For the case $m < 0$, we obtain a stretching stiffness which decays exponentially, which causes an increase in relative amplitude and wavelength, see column b. Finally, for the case $m > 0$, we obtain an exponentially increasing stiffness, which causes a faster

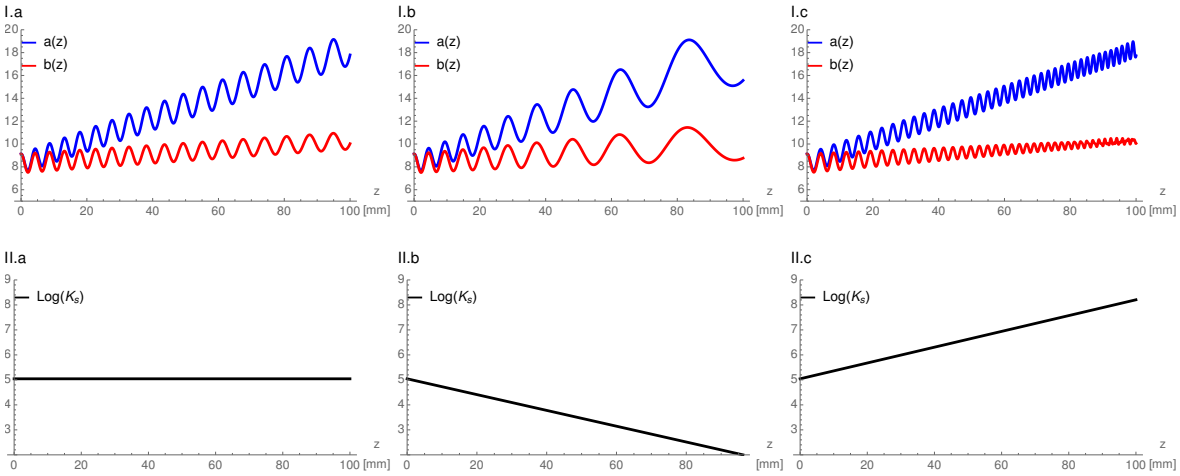


Figure A.9: Influence of stretching stiffness $K_s$ on ribbing pattern. The form of $K_s$ taken in all three columns is $K_s = 155e^{m\,z}$ for different values of $m$. **I.a–II.a**: Case of $m = 0$, which is identical with Figure 4.11, right column. **I.b–II.b**: Case of $m = -10^{\frac{3}{2}}$, which causes an increased amplitude and wavelength. **I.c–II.c**: Case of $m = 10^{\frac{3}{2}}$, which causes a decreased amplitude and wavelength. Other parameters given in Appendix A.5.

decaying relative amplitude and wavelength, column c. These results show a clear effect of stiffness variation on the pattern, though one that is not inconsistent with the functional dependence on stiffness, easily evident for instance in equation (4.39). Physically, increasing stiffness leads to a stronger mechanical feedback, which leads to an increase in ribbing frequency.

# References


[1] D Ambrosi, G a Ateshian, E M Arruda, S C Cowin, J Dumais, A Goriely, G a Holzapfel, J D Humphrey, R Kemkemer, E Kuhl, J E Olberding, L a Taber, and K Garikipati. Perspectives on biological growth and remodeling. *Journal of the Mechanics and Physics of Solids*, **59**(4):863–883, April 2011. [Cited on pages 8 and 18.]

[2] D. Ambrosi and F. Guana. Stress-Modulated Growth. *Mathematics and Mechanics of Solids*, **12**(3):319–342, November 2005. [Cited on page 19.]

[3] D. Ambrosi and A. Guillou. Growth and dissipation in biological tissues. *Continuum Mechanics and Thermodynamics*, **19**(5):245–251, July 2007. [Cited on page 19.]

[4] D. Ambrosi and F. Mollica. The role of stress in the growth of a multicell spheroid. *Journal of Mathematical Biology*, 2004. [Cited on page 5.]

[5] Evren U Azeloglu, Michael B Albro, Vikrum a Thimmappa, Gerard a Ateshian, and Kevin D Costa. Heterogeneous transmural proteoglycan distribution provides a mechanism for regulating residual stresses in the aorta. *American journal of physiology. Heart and circulatory physiology*, **294**(3):H1197–205, March 2008. [Cited on page 5.]

[6] Lev V. Beloussov and Vassily I. Grabovsky. Morphomechanics: Goals, basic experiments and models, 2006. [Cited on page 5.]

[7] Martine Ben Amar and Alain Goriely. Growth and instability in elastic tissues. *Journal of the Mechanics and Physics of Solids*, **53**(10):2284–2319, October 2005. [Cited on page 92.]

[8] L. G. Bowden, H. M. Byrne, P. K. Maini, and D. E. Moulton. A morphoelastic model for dermal wound closure. *Biomechanics and Modeling in Mechanobiology*, **15**(3):663–681, June 2016. [Cited on page 2.]

[9] Silvia Budday, Charles Raybaud, and Ellen Kuhl. A mechanical model predicts morphological abnormalities in the developing human brain. *Scientific Reports*, **4**:5644, 2014. [Cited on page 5.]

[10] Isaac Vikram Chenchiah and Patrick D. Shipman. An energy-deformation decomposition for morphoelasticity. *Journal of the Mechanics and Physics of Solids*, **67**:15–39, July 2014. [Cited on pages 3 and 4.]

[11] R. Chirat, D. E. Moulton, and A. Goriely. Mechanical basis of morphogenesis and convergent evolution of spiny seashells. *Proceedings of the National Academy of Sciences*, **110**(15):6015–6020, 2013. [Cited on pages 98, 100, and 147.]

[12] Bernard D. Coleman and Walter Noll. The thermodynamics of elastic materials with heat conduction and viscosity. *Archive for Rational Mechanics and Analysis*, **13**(1):167–178, December 1963. [Cited on pages 21 and 24.]

[13] Ian Conlon and Martin Raff. Size control in animal development, 1999. [Cited on page 1.]

[14] Steven J. Cooper. From Claude Bernard to Walter Cannon. Emergence of the concept of homeostasis, November 2008. [Cited on page 5.]

[15] M P Coutts and John Grace. *Wind and trees*. Cambridge University Press, 1995. [Cited on page 2.]

[16] S C Cowin and D H Hegedus. Bone remodeling I: theory of adaptive elasticity. *Journal of Elasticity*, **6**(3), 1976. [Cited on page 8.]

[17] Stephen C. Cowin and Keykhosrow Firoozbakhsh. Bone remodeling of diaphysial surfaces under constant load: Theoretical predictions. *Journal of Biomechanics*, **14**(7):471–484, 1981. [Cited on page 27.]

[18] Hilmi Demiray. A note on the elasticity of soft biological tissues. *Journal of Biomechanics*, **5**(3):309–311, 1972. [Cited on page 95.]

[19] M. (Marcelo) Epstein. *The elements of continuum biomechanics*. John Wiley & Sons Inc, 2012. [Cited on pages 12, 14, and 24.]

[20] Marcelo Epstein and Gérard a. Maugin. Thermomechanics of volumetric growth in uniform bodies. *International Journal of Plasticity*, **16**(7-8):951–978, June 2000. [Cited on page 19.]

[21] Alexander Erlich, Derek E. Moulton, Alain Goriely, and Regis Chirat. Morphomechanics and developmental constraints in the evolution of ammonites shell form. *Journal of Experimental Zoology B*, **326**(7):437–450, 2016. [Cited on pages 7, 28, 100, 120, and 147.]

[22] Deborah R. Fowler, Hans Meinhardt, and Przemyslaw Prusinkiewicz. Modeling seashells. *ACM SIGGRAPH Computer Graphics*, **26**(2):379–387, 1992. [Cited on pages 7 and 147.]

[23] Y C Fung. What are the residual stresses doing in our blood vessels? *Annals of biomedical engineering*, **19**(3):237–49, January 1991. [Cited on pages 4, 27, 65, and 144.]

[24] K Garikipati. A continuum treatment of growth in biological tissue: the coupling of mass transport and mechanics. *Journal of the Mechanics and Physics of Solids*, **52**(7):1595–1625, July 2004. [Cited on page 6.]

[25] Serdar Göktepe, Oscar John Abilez, and Ellen Kuhl. A generic approach towards finite growth with examples of athlete's heart, cardiac dilation, and cardiac wall thickening. *Journal of the Mechanics and Physics of Solids*, **58**(10):1661–1680, October 2010. [Cited on pages 2 and 27.]

[26] H. Goldstein, C. Poole, and J. Safko. *Classical Mechanics: Pearson New International Edition*. Pearson Higher Ed, 2014. [Cited on page 134.]

[27] Oscar Gonzalez and A. M. Stuart. *A First Course in Continuum Mechanics*. Cambridge University Press, 2008. [Cited on page 9.]

[28] A. E. Goodship, J. L. Cunningham, V. Oganov, J. Darling, A. W. Miles, and G. W. Owen. Bone loss during long term space flight is prevented by the

application of a short term impulsive mechanical stimulus. *Acta Astronautica*, **43**(3-6):65–75, 1998. [Cited on page 2.]

[29] Richard Gordon and G. Wayne Brodland. The cytoskeletal mechanics of brain morphogenesis - Cell state splitters cause primary neural induction. *Cell Biophysics*, **11**(1):177–238, December 1987. [Cited on page 3.]

[30] A. Goriely. *Mathematics and mechanics of biological growth.* SPRINGER-VERLAG NEW YORK, 2017. [Cited on pages 4, 5, 6, 8, 11, 20, 65, 95, and 146.]

[31] a. Goriely and R. Vandiver. On the mechanical stability of growing arteries. *IMA Journal of Applied Mathematics*, **75**(4):549–570, April 2010. [Cited on pages 4, 27, and 144.]

[32] Alain Goriely and Martine Ben Amar. On the definition and modeling of incremental, cumulative, and continuous growth laws in morphoelasticity. *Biomechanics and Modeling in Mechanobiology*, 2007. [Cited on page 8.]

[33] H. Gregersen, G. S. Kassab, and Y. C. Fung. The zero-stress state of the gastrointestinal tract: Biomechanical and functional implications, 2000. [Cited on page 5.]

[34] J. Guex, Andre Koch, Luis O'Dogherty, and Hugo Bucher. A morphogenetic explanation of Buckman's law of covariation. *Bulletin de la Société géologique de France*, **174**(6):603–606, 2003. [Cited on page 7.]

[35] Morton E Gurtin. *Configurational Forces as Basic Concepts of Continuum Physics.* Springer Science and Business Media, volume 137 edition, 2008. [Cited on page 24.]

[36] Lallit Gurtin, Morton E and Fried, Eliot and Anand. *The mechanics and thermodynamics of continua.* Cambridge University Press, 2010. [Cited on pages 9, 21, 22, and 25.]

[37] John B S Haldane. On being the right size. *Harper's Magazine*, **152**:424–427, 1926. [Cited on page 1.]

[38] Ø. Hammer. A theory for the formation of commarginal ribs in mollusc shells by regulative oscillation. *Journal of Molluscan Studies*, **66**:383–391, 2000. [Cited on page 7.]

[39] Øyvind Hammer and Hugo Bucher. Buckman's first law of covariation – a case of proportionality. *Lethaia*, **38**(1):67–72, 2005. [Cited on page 7.]

[40] Øyvind Hammer and Hugo Bucher. Generalized ammonoid hydrostatics modelling, with application to Intornites and intraspecific variation in Amaltheus. *Paleontological Research*, **10**(1):91–96, 2006. [Cited on pages 100 and 101.]

[41] H. C. Han and Y. C. Fung. Residual strains in porcine and canine trachea. *Journal of Biomechanics*, **24**(5), 1991. [Cited on page 4.]

[42] A. Harris, P Wild, and D Stopak. Silicone rubber substrata: a new wrinkle in the study of cell locomotion. *Science*, **208**(4440):177–179, April 1980. [Cited on page 5.]

[43] Steven R Heidemann and Robert E Buxbaum. Tension as a Regulator and Integrator of Axonal Growth. *Cell motility and the cytoskeleton*, **17**:6–10, 1990. [Cited on page 5.]

[44] Mark H Holmes. *Introduction to perturbation methods*. Springer Science & Business Media, 2012. [Cited on page 128.]

[45] G Holzapfel. *Nonlinear solid mechanics: A continuum approach for engineering*. 2000. [Cited on page 9.]

[46] Gareth Wyn Jones and S. Jonathan Chapman. Modeling Growth in Biological Materials. *SIAM Review*, **54**(1):52–118, January 2012. [Cited on pages 4, 8, 18, and 65.]

[47] Ekkehart Kröner. Allgemeine Kontinuumstheorie der Versetzungen und Eigenspannungen. *Archive for Rational Mechanics and Analysis*, 1959. [Cited on page 9.]

[48] John M. Lawrence. Arm loss and regeneration in Asteroidea (Echinodermata). *Echinoderm Research*, pages 39–52, 1992. [Cited on page 2.]

[49] G. Lebon, D. Jou, and J. Casas-Vázquez. *Understanding Non-equilibrium Thermodynamics*. Springer Berlin Heidelberg, Berlin, Heidelberg, 2008. [Cited on pages 21 and 22.]

[50] E H Lee. Elastic-Plastic Deformation at Finite Strains. *Journal of Applied Mechanics*, **36**(1):1, 1969. [Cited on page 9.]

[51] Jerrold E. Marsden, Thomas J. R. Hughes, and D. E. Carlson. *Mathematical Foundations of Elasticity*, **51**. Courier Dover Publications, 1984. [Cited on page 11.]

[52] Gérard A Maugin. *The Thermomechanics of Nonlinear Irreversible Behaviors*, **27** of *World Scientific Series on Nonlinear Science Series A*. WORLD SCIENTIFIC, October 1999. [Cited on pages 21 and 22.]

[53] Hans Meinhardt. *The algorithmic beauty of sea shells*. Springer Science & Business Media, 2009. [Cited on page 7.]

[54] D E Moulton and A Goriely. Possible role of differential growth in airway wall remodeling in asthma. *Journal of applied physiology (Bethesda, Md. : 1985)*, **110**(4):1003–12, 2011. [Cited on page 144.]

[55] D. E. Moulton and A. Goriely. Surface growth kinematics via local curve evolution. *Journal of Mathematical Biology*, **68**:81–108, 2014. [Cited on pages 100 and 147.]

[56] D. E. Moulton, A. Goriely, and R. Chirat. Mechanical growth and morphogenesis of seashells. *Journal of Theoretical Biology*, **311**(69–79), 2012. [Cited on pages 100 and 147.]

[57] D. E. Moulton, A. Goriely, and R. Chirat. The morpho-mechanical basis of ammonite form. *Journal of Theoretical Biology*, **364**:220–230, 2015. [Cited on pages 7, 28, 97, 99, 102, 103, 112, 113, 123, 156, 157, and 162.]

[58] D. E. Moulton, Th. Lessinnes, and A. Goriely. Morphoelastic rods Part 1: A single growing elastic rod. *Journal of the Mechanics and Physics of Solids*, **61**(2):398–427, 2012. [Cited on pages 104 and 107.]

[59] Raymond W Ogden. *Non-linear elastic deformations*. Courier Corporation, 1997. [Cited on page 9.]

[60] Stephen G. O'Keeffe, Derek E. Moulton, Sarah L. Waters, and Alain Goriely. Growth-induced axial buckling of a slender elastic filament embedded in an isotropic elastic matrix. *International Journal of Non-Linear Mechanics*, **56**:94–104, November 2013. [Cited on page 144.]

[61] J H Omens and Y. C. Fung. Residual strain in rat left ventricle. *Circulation research*, **66**(1):37–45, 1990. [Cited on page 4.]

[62] Ashok Ramasubramanian and Larry a Taber. Computational modeling of morphogenesis regulated by mechanical feedback. *Biomechanics and modeling in mechanobiology*, **7**(2):77–91, April 2008. [Cited on page 19.]

[63] Sean H. Rice. The bio-geometry of mollusc shells, 1998. [Cited on page 7.]

[64] Edward K. Rodriguez, Anne Hoger, and Andrew D. McCulloch. Stress-dependent finite growth in soft elastic tissues. *Journal of Biomechanics*, **27**(4):455–467, April 1994. [Cited on page 9.]

[65] R Skalak, D A Farrow, and A Hoger. Kinematics of surface growth. *J Math Biol*, **35**(8):869–907, 1997. [Cited on page 6.]

[66] LA Taber. Biomechanics of cardiovascular development. *Annual review of biomedical engineering*, pages 1–25, 2001. [Cited on page 148.]

[67] Larry A. Taber. Biomechanics of Growth, Remodeling, and Morphogenesis. *Applied Mechanics Reviews*, **48**(8):487, August 1995. [Cited on pages 5, 6, 8, 17, 18, 20, and 27.]

[68] Larry A Taber. Theoretical study of Beloussov's hyper-restoration hypothesis for mechanical regulation of morphogenesis. *Biomechanics and modeling in mechanobiology*, **7**(6):427–441, December 2008. [Cited on page 19.]

[69] Larry A Taber. Towards a unified theory for morphomechanics. *Philosophical transactions. Series A, Mathematical, physical, and engineering sciences*, **367**(1902):3555–3583, 2009. [Cited on pages 19, 146, and 147.]

[70] R E Taylor, C Zheng, R P Jackson, J C Doll, J C Chen, K R S Holzbaur, T Besier, and E Kuhl. The phenomenon of twisted growth: humeral torsion in dominant arms of high performance tennis players. *Computer methods in biomechanics and biomedical engineering*, **12**(1):83–93, 2009. [Cited on page 2.]

[71] DW Thompson. *On growth and form.* 1942. [Cited on page 1.]

[72] Ramesh N. Vaishnav and Jafar Vossoughi. Residual stress and strain in aortic segments. *Journal of Biomechanics*, **20**(3), 1987. [Cited on page 4.]

[73] Rebecca Vandiver and Alain Goriely. Morpho-elastodynamics: the long-time dynamics of elastic growth. *Journal of biological dynamics*, **3**(2-3):180–95, March 2009. [Cited on page 8.]

[74] Josh Wallman and Jonathan Winawer. Homeostasis of eye growth and the question of myopia. *Neuron*, **43**(4):447–68, August 2004. [Cited on page 6.]

[75] J P Xie, S Q Liu, R F Yang, and Y C Fung. The zero-stress state of rat veins and vena cava. *Journal of biomechanical engineering*, **113**(1):36–41, February 1991. [Cited on page 4.]

[76] Satoshi Yamada, Shigeru Tadano, and Kazuhiro Fujisaki. Residual stress distribution in rabbit limb bones. *Journal of Biomechanics*, **44**(7):1285–1290, April 2011. [Cited on page 5.]

[77] Arash Yavari. A Geometric Theory of Growth Mechanics. *Journal of Nonlinear Science*, **20**(6):781–830, July 2010. [Cited on page 11.]